Development of fluorescent pH-responsive polymeric systems as potential method for CO_2 sensing

by

David A. Londoño de la Cruz

UNIVERSITY OF BIRMINGHAM

A thesis submitted to the University of Birmingham for the degree of DOCTOR OF PHILOSOPHY

School of Chemistry

College of Engineering and Physical Sciences

University of Birmingham

October 2024

Acknowledgements

It feels surreal to be writing this acknowledgment—after a long journey, here I am. First and foremost, I want to express my deepest gratitude to my supervisor, Professor Rachel O'Reilly, for welcoming me into her group, trusting in my abilities, and constantly encouraging me to become a better scientist.

I also want to thank my undergraduate thesis supervisor, Professor Santiago Franco Ontaneda, for sparking my interest in organic chemistry. My thanks go to Dr. Sam Parkinson, Dr. Anissa Khalfa, Dr. Stephen Fielden, Dr. Simon Dale and Dr. Connor Stubbs for their unwavering support during my first year (and even beyond), patiently answering my endless questions and offering their help without hesitation.

Special thanks to Dr. Yujie Xie and Dr. Amrita Sikder for sharing their expertise in fluorescent measurements. I am immensely grateful to Dr. Calum J. Ferguson, Dr. Julia Rho, and Dr. Arianna Brandolese for their guidance, assistance with my project, and their invaluable moral support during challenging times. A special mention goes to Dr. Calum J. Ferguson once again, for proofreading all my chapters and consistently supporting me.

I cannot thank Ms. Tessa Kintail enough for her kindness and unwavering help, always solving problems and making life easier for everyone in the group. Many thanks also to Ms. Julia Valverde and Dr. Daniel Smith for their tremendous support.

I would also like to thank Dr. Thiago O. Machado, Dr. Viviane Chiaradia and Dr. Natalia Reis (my Brazilian familia) for being such an amazing friend and gave those Latino vibes I missed from Colombia.

I am incredibly grateful to all past and present members of the group for the wonderful dinners, BBQs, and outings, but most importantly, for being my family over the last 3.5

years. A special thanks to some extraordinary people: Ms. Bethany Crow, for her endless moral support and being the best EDI representative; Iremita and Marjolinita, for the Drama team and some of the best laughter-filled moments of my life; and Ms. Gabriela Garbonova and Ms. Bige Bati, the magic trident (Gabige and the King) for being two of the best friends I could ever hope for.

I would also like to thank Mr. Daniele Giannantonio (aka Danielito), my companion throughout this entire process, for being my "mate" and daily support until the very last minute. I would also like to thank Dr. Alexis Pierrot, for sharing not only chemistry knowledge but for being a good friend with whom I could share some nice classical music and French lessons.

A very special thanks to my best friends, Eduardo Gil Gonzalez-Madroño (Eduardito), for being my family here in the UK and for being like a brother and mentor over the past 3.5 years, and to my best friend Dr. Alex Martínez Martín (AKA Alexito) for our 11 years of cherished friendship, for chatting with me every single day of this PhD and giving me and outstanding support.

Of course, my deepest gratitude goes to my love, Ms. Claire Morand, for entering my life and standing by my side through both good and tough times—it wouldn’t have been possible without you, bebi.

Lastly, to my mom Claudia Elena de la Cruz Bonfante, for all the love she always gave me and to my dad Gerardo Londoño Saavedra for encouraging me always to be a better version of myself and to my beloved brother Juan Daniel Londoño, for being the best brother and friend in this entire world. I would also like to thank my entire family in Colombia and in the U.S, to the ones who are still there and for the ones who left, for

their constant support, unwavering belief in me, and for always being proud of every step I take in life.

Abstract

Stimuli-responsive polymers that change their fluorescence in response to pH variations have gained significant attention due to their potential applications in sensors, bioimaging, and drug delivery. In particular, for CO_2 sensing, fluorescence-based detection in aqueous environments—triggered by pH changes—offers a promising method for real-time monitoring. This thesis aimed to develop an effective and robust CO_2 sensing system using fluorescent pH-responsive nanoparticles, enhancing the ability to detect carbon dioxide efficiently. The research first focused on the synthesis and characterization of CO_2-responsive polymeric nanoparticles, produced through RAFT emulsion polymerization. These nanoparticles were designed with various fluorescent dyes, enabling them to rapidly "switch on" fluorescence in response to CO_2 exposure. Additionally, a water-soluble polymer functionalized with a pH-sensitive pyrene dye was developed. This system demonstrated a rapid and reversible "off" fluorescence response, and a low detection limit. To further enhance the stability and potential applications of these CO_2-responsive systems, the study explored incorporating the pyrene-based dye (DEAPyMA) into two distinct polymer structures: a cross-linked hydrogel and spherical micelles synthesized *via* RAFT-PISA polymerization. The development of nanoparticles, water-soluble polymers, and hydrogel/micelle structures has led to significant advancements in environmental monitoring, offering fast, reversible, and reliable mechanisms for real-time CO_2 detection.

This thesis is dedicated to Ms. Hortencia Bonfante Pacheco RIP.

List of Figures

Figure 2.6. Synthesis of 5 wt% spherical nanoparticles by RAFT emulsion polymerization with 1 wt% of the total solid content of the dye.

Figure 2.7. (a) FTIR of freeze-dried fluorescent nanoparticles. (b) UV-Vis spectrum of reference nanoparticles (without NBDMA) and fluorescent nanoparticles (with NBDMA) in DI water. Concentration 0.1 mg/mL.

Figure 2.8. (a) DLS analysis of NP-NBDMA at pH 7. (b) Correlogram of NP-NBDMA at Ph 7. (c) TEM image of NP-NBDMA at pH 7, stained with uranyl acetate. (d) Corresponding histogram showing size distribution of NP-NBDMA.

Figure 2.9. DLS graphs of NP-NBDMA: (a) pH 1. (b) pH 2.8. (c) pH 5.6. (c) pH 7. (e) pH 7.6. (f) pH 8. (g) pH 9. (H) pH 10. (i) pH 11. (J) Size variation vs pH of NP-NBDMA.

Figure 2.10. (a) Emission spectrum of NP-NBDMA at pH 1, 2.8, 5.6, 7.0, 7.5, 8.0, 9.0, 10.0, 13.5. (b) Graph representing the relation between fluorescence maximum intensity of NP-NBDMA vs their size variation derived from pH modification.

Figure 2.11. (a) DLS analysis of particles at pH 7. (b) TEM image of nanoparticles at pH 7, stained with uranyl acetate. (c) Corresponding histogram showing size distribution of nanoparticles. (d) Thermogravimetric plot of Loss weight against temperature to calculate the % conversion (67%) in 200 µl of crude nanoparticles of concentration 5.34 wt%.

Figure 2.12. (a) DLS-titration experiment of PDMAPS-b-P(DEAEMA-*co*-EGDMA-*co*-ACMMA) nanoparticles. Concentration 1 mg/mL in DI water. (b) PDMAPS-b-P(DEAEMA-*co*-EGDMA-*co*-ACMMA fluorescence spectrum at pHs 1.0, 2.8, 5.6, 7.0, 10 and 13.5. Concentration 0.3 mg/mL. λ_{exc}= 380 nm. λ_{em}= 500 nm.

Figure 2.13. Representative dry-state TEM images of NP-SPMA.

Figure 3.7. Fluorescence spectrum of PDMAm-*co*-PDMAPyMA at different pHs in aqueous solution. (a) 0.1 mol% of DMAPyMA. (b) 0.5 mol% of DMAPyMA. Concentration of 10 ppm. λ_{exc}= 350 nm.

Figure 3.8. Lifetime spectrum of PDMAm-*co*-DEAPyMA in aqueous solution at different pHs and at r.t. Concentration of 10 ppm. λ_{exc}= 350 nm. λ_{em}= 385, 490 nm. 1 mol% of DEAPyMA in polymer.

Figure 3.9. (a) Fluorescence intensity of P(DMAm-*co*-DEAPyMA). (Concentrations: 100, 10, 5 and 1 ppm, pH 7 and 2, λ_{exc}= 350 nm, λ_{em}= 490 nm) (b) Photograph of P(DMAm-*co*-DEAPyMA) at different concentrations in aqueous solution and different pHs under 365 nm UV-light.

Figure 3.10. pKa of DEAPyMA calculated using the Henderson-Hasselbach-type mass action equation ($pH = pKa + c*\log[(R-Rmin)/(Rmax-R)] + \log(Ia/Ib)$) through analyzing fluorescence intensity ratio changes as a function of pH. Where Rmax (or Rmin) is the maximum (or minimum) ratio value, c is the slope and Ia /Ib is the ratio of absorption intensity in acid to the absorption intensity in base at the wavelength chosen for the denominator of R. The pKa value for DEAPyMA was 4.4.

Figure 3.11. (a) Fluorescence spectra of P(DMAm-*co*-DEAPyMA) after CO_2 kinetics for 150s. Concentration 0.1 mg/mL. λ_{exc}= 350 nm. (b) Kinetics graphic representing a change in fluorescence intensity ratio I_{490nm}/ I_{385nm} of a sample of concentration 0.01 mg/mL as the effect of the volume of CO_2.

Figure 3.12. (a) Fluorescence spectra of P(DMAm-*co*-DEAPyMA) After air kinetics for 60 min. Concentration 0.1 mg/mL. λ_{exc}= 350 nm. (b) Kinetics graphic representing a

UV light (right). (b) SS fluorescence of Cross-Linked P(DMAm$_{100}$-*co*-DEAPyMA$_1$-*co*-EGDMA$_1$) hydrogels after pipeline simulation experiment. λ_{exc}= 350 nm.

Figure 4.6. Swelling test of cross-linked P(DMAm$_{100}$-*co*-DEAPyMA$_1$-*co*-EGDMA$_1$) hydrogel.

Figure 4.7 Rheological test of hydrated cross-linked P(DMAm$_{100}$-*co*-DEAPyMA$_1$-*co*-EGDMA$_1$) hydrogel at 5ºC.

Figure 4.8 Normalized SEC RI (black trace) molecular weight distributions for PGMA$_{35}$ macro-CTA, along with corresponding Mn and Đ values calculated based on PEG standards using DMF containing 4.6 mM of NH_4BF_4 as the eluent.

Figure 4.9. (a) Normalized SEC RI (black trace) molecular weight distributions for PGMA$_{35}$-b-PHPMA$_{50}$ reference nanoparticles, along with corresponding Mn and Đ values calculated based on PEG standards. (b) Normalized DLS graphic of reference nanoparticles in water with corresponding correlogram. (c) Dry-state TEM image of nanoparticles at pH 7, stained with uranyl acetate. (d) Corresponding histogram showing size distribution of nanoparticles.

Figure 4.10. ^{1}H NMR kinetics of synthesis of PGMA$_{35}$-*b*-P(HPMA$_{50}$-*co*-DEAPyMA$_{0.1}$) via RAFT-PISA polymerization at time 0h and time 24h. Solvent DMSO-*d*$_6$.

Figure 4.11 (a) Normalized SEC RI (black trace) molecular weight distributions for PGMA$_{35}$-*b*-P(HPMA$_{50}$-*co*-DEAPyMA$_{0.1}$) nanoparticles, along with corresponding Mn and Đ values calculated based on PEG standards. (b) Normalized DLS graphic of PGMA$_{35}$-*b*-P(HPMA$_{50}$-*co*-DEAPyMA$_{0.1}$) nanoparticles in water with corresponding correlogram. (c) Dry-state TEM image of PGMA$_{35}$-*b*-P(HPMA$_{50}$-*co*-DEAPyMA$_{0.1}$) nanoparticles at pH 7, stained with uranyl acetate. (d) Picture of Schlenk flask containing PGMA$_{35}$-*b*-P(HPMA$_{50}$-*co*-DEAPyMA$_{0.1}$) after 24h of polymerization.

Figure 4.12. (a) Fluorescence spectrum of $PGMA_{35}$-*b*-$P(HPMA_{50}$-*co*-$DEAPyMA_{0.1})$ at pHs 7, 6, 5, 4.5, 4, 3.5, 3 and 2. (b) Graphic representing change in intensity ratio I_{490nm}/I_{385nm} as effect of the pH for $PGMA_{35}$-*b*-$P(HPMA_{50}$-*co*-$DEAPyMA_{0.1})$. Concentration of 0.1 mg/mL of nanoparticles. λ_{exc}= 350 nm. (c) Fluorescence spectrum of $P(DMAm_{99}$-co-$DEAPyMA_1)$ at pHs 7, 6, 5, 4.5, 4, 3.5, 3 and 2. (d) Graphic representing change in intensity ratio I_{490nm}/I_{385nm} as effect of the pH for $P(DMAm_{99}$-co-$DEAPyMA_1)$. Concentration of linear polymer 0.1 mg/mL. λ_{exc}= 350 nm.

Figure 4.13. (a) CO_2 kinetics fluorescence spectrum of $PGMA_{35}$-*b*-$P(HPMA_{50}$-*co*-$DEAPyMA_{0.1})$ (4 minutes kinetics). (b) Graphic representing change in intensity ratio I_{490nm}/I_{385nm} as effect of CO_2 volume for $PGMA_{35}$-*b*-$P(HPMA_{50}$-*co*-$DEAPyMA_{0.1})$ (4 minutes kinetics). Concentration of 0.1 mg/mL of nanoparticles. λ_{exc}= 350 nm. (c) CO_2 kinetics fluorescence spectrum of $PGMA_{35}$-*b*-$P(HPMA_{50}$-*co*-$DEAPyMA_{0.1})$ (60 minutes kinetics). (d) Graphic representing change in intensity ratio I_{490nm}/I_{385nm} as effect of CO_2 volume for $PGMA_{35}$-*b*-$P(HPMA_{50}$-*co*-$DEAPyMA_{0.1})$ (60 minutes kinetics). Concentration of 0.1 mg/mL of nanoparticles. λ_{exc}= 350 nm. (e) CO_2 kinetics fluorescence spectrum of $P(DMAm_{99}$-co-$DEAPyMA_1)$. (f) Graphic representing change in intensity ratio I_{490nm}/I_{385nm} as effect of the CO_2 volume $P(DMAm_{99}$-co-$DEAPyMA_1)$. Concentration of linear polymer 0.1 mg/mL. λ_{exc}= 350 nm.

Figure 4.14. (a) Air kinetics fluorescence spectrum of $PGMA_{35}$-*b*-$P(HPMA_{50}$-*co*-$DEAPyMA_{0.1})$ (50 minutes kinetics). (b) Graphic representing change in intensity ratio I_{490nm}/I_{385nm} as effect of air exposure time for $PGMA_{35}$-*b*-$P(HPMA_{50}$-*co*-$DEAPyMA_{0.1})$ (50 minutes kinetics). Concentration of 0.1 mg/mL of nanoparticles. λ_{exc}= 350 nm. (c) Air kinetics fluorescence spectrum of $P(DMAm_{99}$-co-$DEAPyMA_1)$. (d) Graphic representing change in intensity ratio I_{490nm}/I_{385nm} as effect of air exposure time $P(DMAm_{99}$-co-$DEAPyMA_1)$. Concentration of linear polymer 0.1 mg/mL. λ_{exc}= 350 nm.

Figure 4.15. (a) Graphic representing change in intensity ratio I_{490nm}/I_{385nm} as effect of CO_2 (60 min)/air (60 min) reversibility cycles for $PGMA_{35}$-*b*-$P(HPMA_{50}$-*co*-$DEAPyMA_{0.1})$ nanoparticles. Concentration of 0.1 mg/mL of nanoparticles. λ_{exc}= 350 nm. (b) Pictures of vials of $PGMA_{35}$-*b*-$P(HPMA_{50}$-*co*-$DEAPyMA_{0.1})$ nanoparticles after CO_2/air cycles under 365 nm UV-light. (c) Graphic representing change in intensity ratio I_{490nm}/I_{385nm} as effect of CO_2 (10 min)/air (60 min) reversibility cycles for $P(DMAm_{99}$-co-$DEAPyMA_1)$. Concentration of linear polymer 0.1 mg/mL. λ_{exc}= 350 nm. (d) Pictures of vials of $P(DMAm_{99}$-co-$DEAPyMA_1)$ after CO_2/air cycles under 365 nm UV-light.

Scheme list

Equation list

Table list

List of Symbols and Abbreviations

^{1}H NMR	Proton nuclear magnetic resonance
a_0	Optimal contact between the solvophilic block and the solvent
ACMMA	Aminochloromaleimide methacrylate
ACVA	4,4′-Azobis(4-cyanovaleric acid)
Aq	Aqueous
ATRP	Atom-transfer radical polymerization
CPAD	4-Cyano-4-(phenylcarbonothioylthio)pentanoic acid
CTA	Chain transfer agent
^{13}C NMR	Carbon nuclear magnetic resonance
Da	Dalton
D_{ave}	Average diameter recorded by TEM
DEAEMA	2-(diethylamino)ethyl methacrylate
DMA_m	N,N-dimethyl acrylamide
DMAPyMA	Dimethylaminopyrene methacrylate
DEAPyMA	Diethylaminopyrene methacrylate
D_h	Hydrodynamic diameter
DLS	Dynamic light scattering
$Đ_M$	Dispersity by SEC

DMAPS	*N,N′*-dimethyl(methacryloylethyl)ammonium propane sulfonate
DP	Degree of polymerization
EGDMA	Ethylene glycol dimethacrylate
EtOH	Ethanol
ES	Electrospray
FRP	Free radical polymerization
GMA	Glycidyl methacrylate
HPMA	2-Hydroxypropyl methacrylate
IPA	Isopropanol
KPS	Potassium persulfate
LAMs	Less-activated monomers
lc	Length of the solvophobic block
Macro	Macromolecular
MAMs	More-activated monomers
macroCTA	Macromolecular chain transfer agent
MeOH	Methanol
M_n	Number-average molecular weight
M_w	Weight-average molecular weight
MWCO	Molecular weight cut off
NBDMA	4-Nitrobenzo-2-oxa-1,3-diazole methacrylate

NMP	Nitroxide-mediated radical polymerization
NP	Nanoparticles
OEGMA	Oligo(ethylene glycol) methacrylate
p	Packing parameter
p(DEAEMA)	Poly(2-(diethylamino)ethyl methacrylate)
p(DMA)	Poly(dimethylacrylamide)
p(DMAEMA)	Poly(*N,N*′ -dimethylaminoethyl methacrylate)
p(DMAPS)	Poly(*N,N*′ -dimethyl(methacryloylethyl)ammonium propane-sulfonate)
PD	Dispersity by DLS
PyMA	Pyrene methacrylate
PISA	Polymerization-induced self-assembly
RAFT	Reversible addition-fragmentation chain-transfer
RDRP	Reversible deactivation radical polymerisation
RI	Refractive index
RT	Room temperature
SEC	Size exclusion chromatography
SPMA	Spiropyran methacrylate
TEM	Transmission electron microscopy
TGA	Thermogravimetric analysis
THF	Tetrahydrofuran

TPEMA	Tetraphenylethene methacrylate
TOF	Time of flight
UA	Uranyl acetate
UV	Ultra-Violet
v	Volume of the solvophobic block
Vis	Visible
wt.%	Weight percent
δ	Chemical shift
μ	Viscosity

Table of Contents

1 Introduction

1.1 Polymers

The word polymer is derived from Greek, meaning 'many parts.' A polymer is essentially a large molecule, or macromolecule, made up of numerous subunits called monomers. These monomers are small repeating units connected to each other through covalent or non-covalent bonds.[1, 2] The process by which monomers join to form polymers is known as polymerization. Polymers are characterized by their degree of polymerization (DP), which indicates the number of repeating monomer units they contain. Another important characteristic of polymers is their molecular weight distribution, also referred to as dispersity ($Đ_M$).[3] Dispersity ($Đ_M$) is the ratio of the weight-average molar mass (M_w) to the number-average molar mass (M_n) and represents the spread of molecular masses among polymer chains. When dispersity equals 1, it indicates a monodisperse polymer, meaning all polymer chains have the same molecular weight, which is quite rare. Synthetic polymers are normally “polydisperse”, this means they contain chains with different molecular weights and lengths.[4] The DP and $Đ_M$ of a polymer normally dictate the physicochemical properties of it. Different macroscopic properties such as chemical resistance, mechanical strength and viscosity can be achieved with high molecular masses. Another unique property of polymers is the glass transition temperature (T_g) and is defined as the temperature at which polymer chains lose short range of mobility.[5]

The earliest polymers were natural substances, with deoxyribonucleic acid (DNA) being a prime example. Nowadays, polymers are a cornerstone of the chemical industry and a fundamental element of modern society. They are used in a vast array of applications, ranging from oil recovery and batteries to textiles and aeronautics.[6-8] The increasing focus on polymers has spurred the development of various polymerization techniques with some of them enabling high level of control of the composition and the architecture of the resulting macromolecule.

The composition of polymers can be adjusted by changing their tacticity, which refers to the arrangement of pendant groups along the polymer chain. This can result in isotactic, syndiotactic, and atactic polymers. In isotactic polymers, all pendant groups are on the same side of the polymer backbone. Syndiotactic polymers have alternating pendant groups, while atactic polymers feature randomly arranged pendant groups along the backbone. Moreover, polymers can be designed with various architectures, such as linear, star, or bottlebrush, which impart different properties.[9, 10] Additionally, polymers can be functionalized through reactive components via post-polymerization modifications, leading to diverse characteristics.[11] The ability to synthesize polymers with various architectures allows for their use in a wide range of industrial applications.

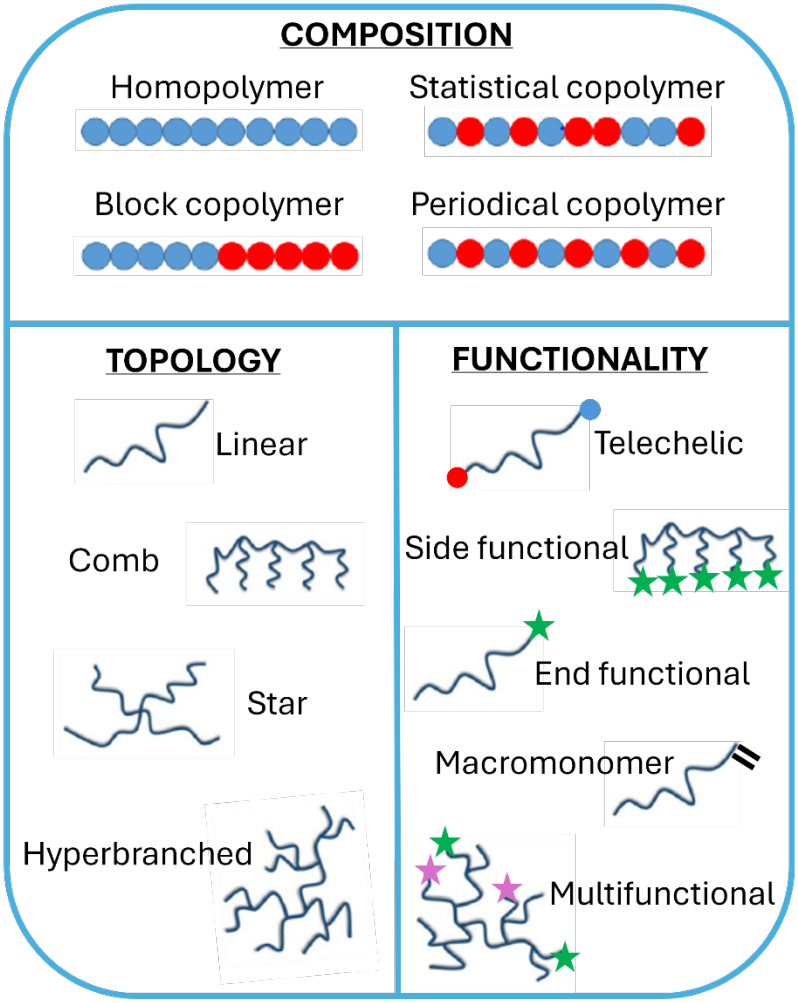

Figure 1.1. Examples of compositions, topologies and functionalization's of polymers. Reproduced from.[12]

1.1.1 Chain-growth polymerization

In contrast, chain-growth polymerization occurs through the sequential addition of monomer units to an expanding polymer chain (Figure 1.2). Unlike the step-growth approach, chain-growth polymerization is divided into three distinct phases: initiation, propagation, and termination.[13] During initiation, monomers are activated, enabling them to propagate. In the propagation phase, these activated monomers react rapidly due to the high reactivity of the active center (such as a radical, cation, or anion). This results in the rapid formation of long polymer chains. Propagation continues until the active center is removed through termination events, which halt further chain growth.[14]

On the other hand, living polymerization differs from the conventional method in that it is a chain-growth polymerization without termination events (Figure 1.2). Consequently, polymer chains continue to grow until all monomer is consumed. Even after complete conversion, the polymer chains remain active, allowing for additional extensions.[15] A key feature of living polymerization is that the initiation rate is faster than the propagation rate, ensuring that all chains grow simultaneously and exhibit a relatively narrow size distribution. Additionally, the molecular weight is directly proportional to the amount of monomer

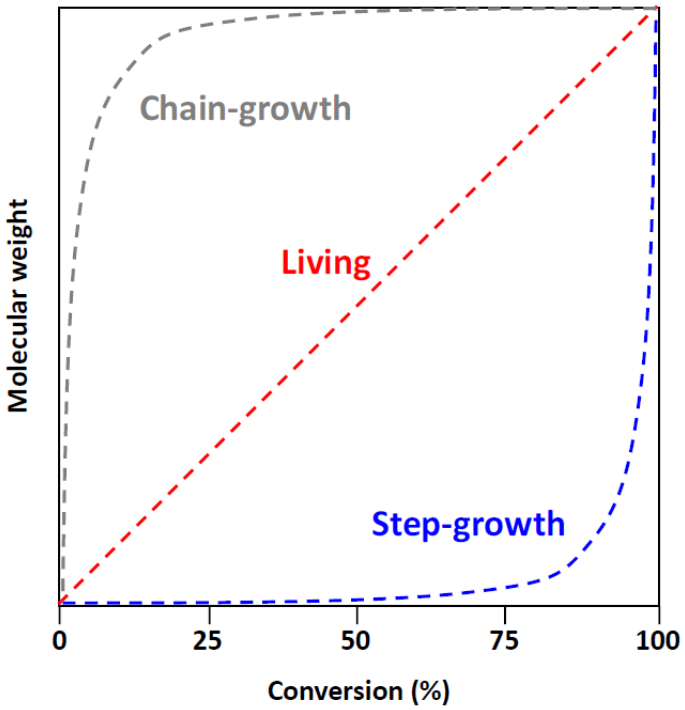

Figure 1.2. Variation of polymer molecular weight against monomer conversion for step-growth, living and chain-growth polymerization. Figure adapted from [8].

As the work conducted in this thesis utilizes chain growth techniques only, an in-depth discussion of step growth is beyond the scope of this chapter.

1.1.2 Radical polymerization

Free radical polymerization (FRP) is one of the most common commercial techniques for polymer synthesis. It can be carried out under mild conditions, obtaining high molecular weight polymers and incorporating a large number of functional groups.[16] The four steps of FRP are: Initiation, propagation, chain transfer and termination, as it can be observed in figure 1.3. Initiation involves the generation of free radicals (I•) through the decomposition of an initiator molecule (I-I), triggered by an external stimulus such as heat or light,[17] at a rate k_d. These free radicals then react with a monomer molecule (M), transferring the radical site to the newly formed monomer (I-M•). During propagation,

this molecule continues to react with additional monomers, shifting the active radical site to the growing chain's new end (Pn•). Chain transfer happens when the active radical site is passed to another molecule, such as a solvent, another polymer chain, or a chain transfer agent (CTA), while simultaneously capping the extending chain. Termination takes place when the active radical species is permanently eliminated. This can happen through combination, this is, when two radical species react with each other to form a covalent bond, or by disproportionation; for example, when a proton is transferred from one polymer chain and leaves an unsaturated double bond.[18]

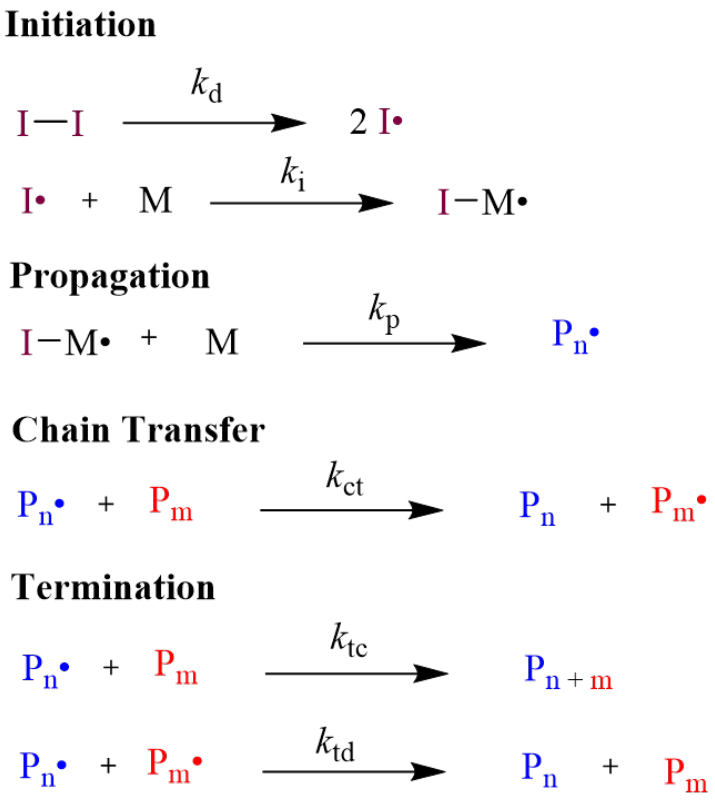

Figure 1.3. The mechanistic steps of free radical polymerization. I represent an initiating molecule, M represents monomer unit, P represents polymer chain with n or m degree of polymerization. Reproduced from.[19]

Nevertheless, some of the limitations of FRP are that termination steps occur at a very rapid pace, with a rate constant nearing the diffusion-controlled limit.[18] This termination

rate is higher than the rate constant for propagation, which itself is greater than the initiation rate. These kinetic factors, combined with the possibility of branching through chain transfer, lead to polymers with poorly defined structures, broad molecular weight distributions ($Đ_M$), and uncontrolled molecular weights.[13, 17] Producing polymers with predictable molecular weights and low dispersity can be achieved if the rates of termination and chain transfer are minimized.

1.1.3 Reversible-Deactivation Radical Polymerization (RDRP)

RDRP offers the benefits of both living polymerization (such as controlled molecular weight and low dispersity) and free radical polymerization (including tolerance to functional groups, scalability, and user-friendly reaction conditions). RDRP is characterized by a low concentration of propagating radicals and a high concentration of dormant polymer chains. Since the equilibrium between active and dormant species is rapid, all polymers have an equal chance to grow. As a result, RDRP produces polymers with controlled molecular weight, degree of polymerization, architecture, and composition. Although termination reactions (such as radical coupling and disproportionation) still occur, they are much less frequent compared to free radical polymerization due to the lower concentration of propagating chains. Therefore, RDRP is considered a controlled polymerization rather than a true living polymerization.[20, 21]

Atom transfer radical polymerization (ATRP) and nitroxide-mediated radical polymerization (NMP) are examples of RDRP techniques that involve deactivation through catalyzed reversible coupling and spontaneous reversible coupling.[22, 23] These polymerizations operate on a principle known as the persistent radical effect (PRE), which ensures that the generated radical species do not self-terminate but instead only terminate by reacting with propagating polymer chains. In the NMP, the concentration of the

propagating chain is controlled by the reversible coupling with stable nitroxide radical species (Scheme 1.1).[24]

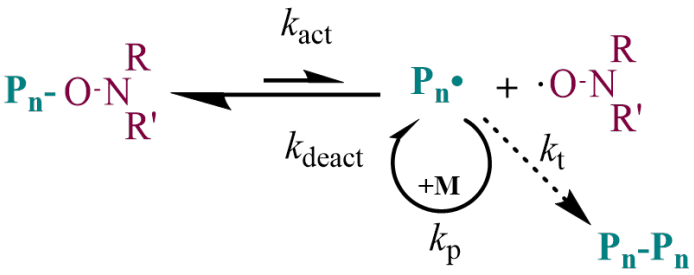

Scheme 1.1. Mechanism of nitroxide-mediated polymerization (NMP). Reproduced from ref.[25]

However in ATRP, the equilibrium is driven by a metal complex (Scheme 1.2).[26] Unlike ATRP, a catalyst is not required, and radicals are formed upon homolysis at high temperatures. Then, the propagating radicals can either react with monomers or with nitroxide radicals resulting in the formation of polymer chains end-capped by nitroxides. In both cases, the dormant species are more stable, which maintains a low concentration of the propagating chains.

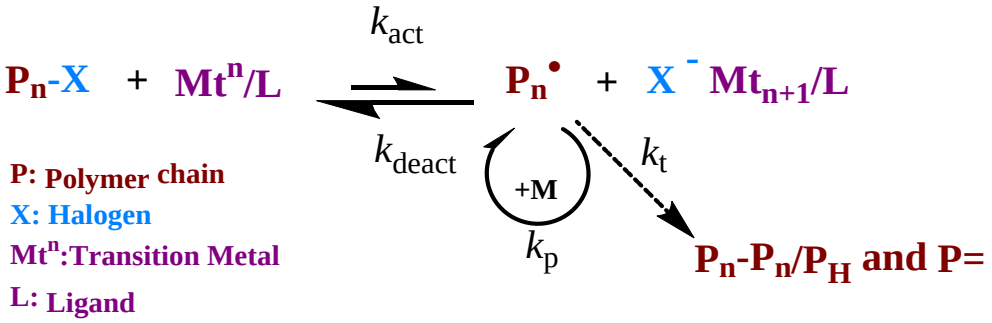

Scheme 1.2. Mechanism of atom-transfer radical polymerization (ATRP). Reproduced from ref.[27]

As in this thesis, RAFT polymerization is mainly used, it will be described in more detail.

1.1.4 Reversible Addition-Fragmentation Chain Transfer (RAFT) Polymerization

RAFT was firstly reported in 1998 and since then has been extensively used due to its notable benefits: it is compatible with a wide range of monomers, enables the production of polymers with low dispersity, and facilitates the straightforward functionalization of polymer end groups.[28, 29] A major advantage of RAFT polymerization compared to other RDRP techniques is that it does not require reagents like metal ligands or harsh conditions such as high temperatures. Besides, another distinction is that the equilibrium between active and dormant species operates under a degenerative chain transfer mechanism. In this system, the number of radicals remains constant during the activation-deactivation process, as radicals are neither generated nor consumed. Consequently, an external radical source is necessary to initiate RAFT polymerization. Another crucial component is the chain transfer agent (CTA), also referred to as the RAFT agent. CTAs are essential in reducing radical-radical terminations by facilitating the quick transfer of radicals between propagating polymer chains and dormant species, this is, ensuring effective control over the polymerization process.[30]

As with conventional FRP, RAFT polymerization is divided into initiation, propagation, chain transfer, and terminations steps. During the initiation step, free radicals (I•) are produced through thermolysis, photolysis, or similar processes of the initiator (I-I) (Scheme 1.3). These radicals then react with vinyl monomers (M) to create an active propagating polymer chain (Pn•). In the RAFT pre-equilibrium step, the active chains reversibly interact with RAFT agents, which contain a thiocarbonylthio group, such as dithioesters and trithiocarbonates, forming intermediate radicals.[30] These intermediates can subsequently fragment into a polymeric CTA (macro-CTA) and a CTA-derived radical (R•). In the reinitiation step, the radical generated from the CTA reacts with

monomers to form propagating polymer chains (Pm•). During the main equilibrium step, this radical intermediate from the CTA quickly fragments, allowing the addition of either Pn• or Pm• chains onto its C=S bond. The rate of this propagation is faster than the rate at which the radical intermediate is initially formed. This reduces termination reactions, such as the bimolecular coupling of Pn• and Pm•, providing relatively good control over polymer dispersity. The symmetrical structure of the CTA-derived radical intermediate ensures that each propagating polymer radical has an equal chance of activation.[31]

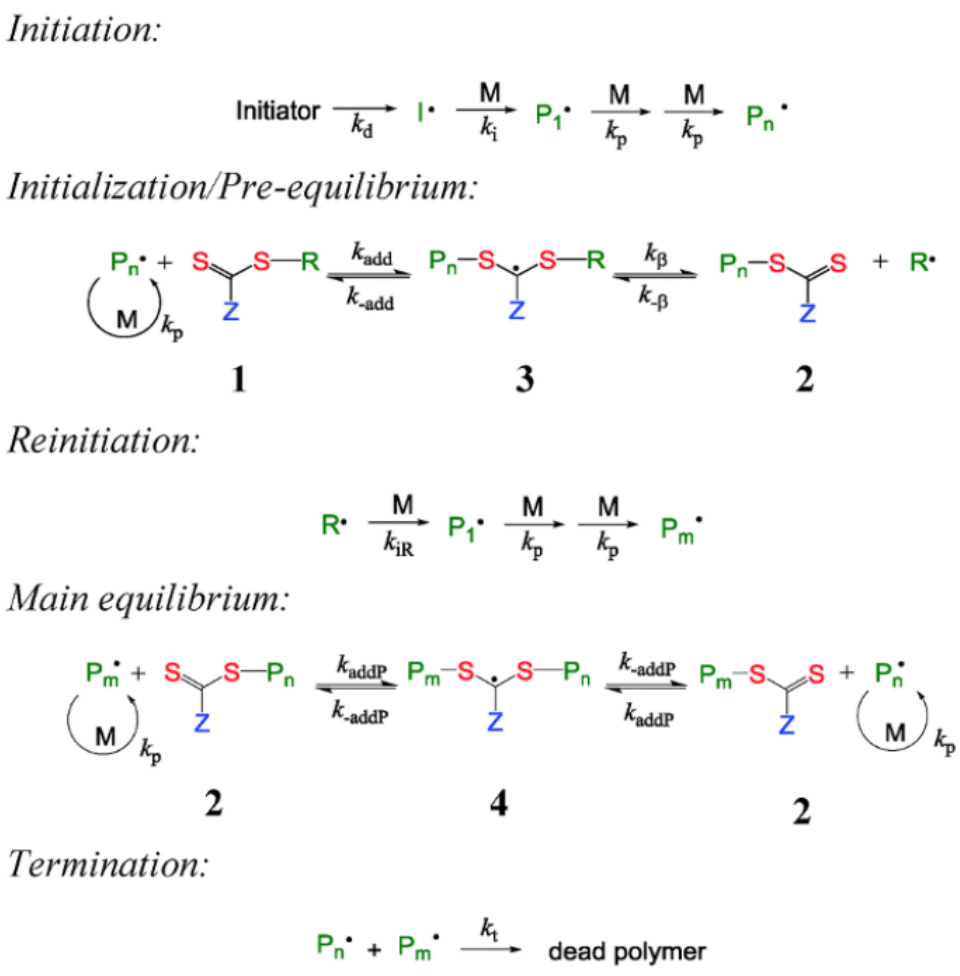

Scheme 1.4. Schematic representation of RAFT polymerization mechanism. Figure reproduced from ref.[31]

The Z and R groups of the RAFT CTA play crucial roles in the mechanism, particularly during the initial chain transfer stage. The Z group regulates the balance between the

dormant and active chains by stabilizing the intermediate radical to prevent it from fragmenting back into the original propagating polymer (Pn•) and CTA species. However, this stabilization must be carefully balanced to permit the desired fragmentation of the R group. An electron-donating Z group will promote fragmentation but may hinder the formation of the intermediate, while an electron-withdrawing Z group will have the opposite effect. To conduct a RAFT polymerization effectively, the rate of addition/fragmentation between polymers and the CTA must be much higher than the rate of propagation. This ensures that fewer than one monomer unit is added during each activation cycle, allowing all chains to grow at the same rate. Since the propagation rate varies significantly depending on the monomer structure.

Therefore, it is important to match appropriate CTAs and monomers when targeting well-defined polymers *via* RAFT polymerization. Regarding the monomer type, we can differentiate two classes of monomers known as more activated monomers (MAMs) and less activated monomers (LAMs) used as RAFT monomers. less-activated monomers (LAMs) result in less stable radicals. In this case, the vinyl group is adjacent to saturated functionalities which increase the reactivity of the vinyl and the resulting radical on the other hand More-activated monomers (MAMs) are linked with vinyl monomers which produce stable radicals. In this case, the vinyl group is often conjugated with other functionalities among those alkenes, aromatics, or nitriles for example (Figure 1.3).

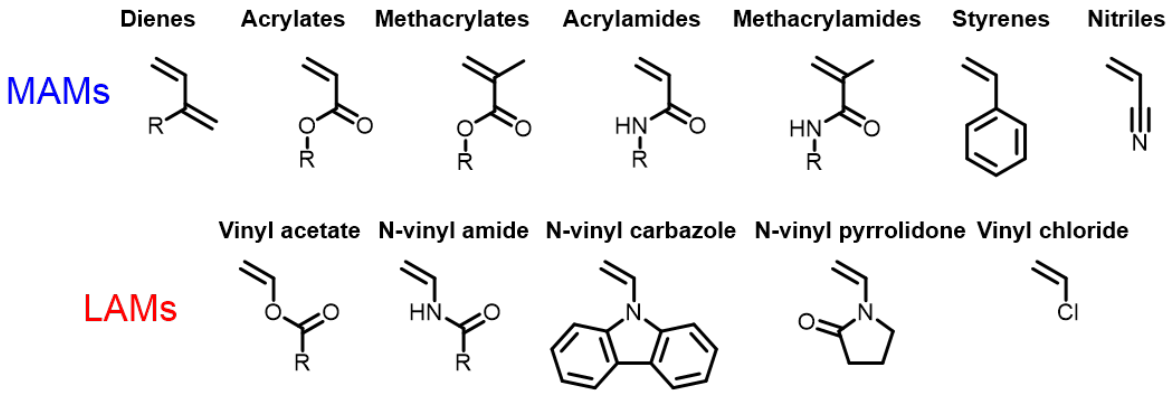

Figure 1.4. Schematic representation of some MAMs and LAMs. Figure adapted from ref[28]

Trithiocarbonates (Z═S-alkyl) and aromatic dithioesters (Z═aryl) are the most effective RAFT agents for achieving well-controlled polymerization of MAMs, as these monomers typically generate more stable radicals during polymerization. However, because these CTAs can hinder the polymerization of LAMs, less reactive xanthates (Z═OR) and dithiocarbamates (Z═NR′2) are preferred for LAMs. Their lower reactivity results in weaker homolytic leaving groups, making them more suitable for these monomers. Using highly reactive CTAs with LAMs or less reactive CTAs with MAMs can lead to polymerization retardation and slow fragmentation, resulting in poor control over the process, or even complete failure of the polymerization. This underscores the importance of choosing an appropriate "Z" group in the CTA, which stabilizes the intermediate radical species. Similarly, the selection of the "R" group is crucial, as it influences the fragmentation of intermediates by serving as an effective homolytic leaving group. A summary table to select both Z and R groups for different polymerizations can be found in figure 1.5.[28]

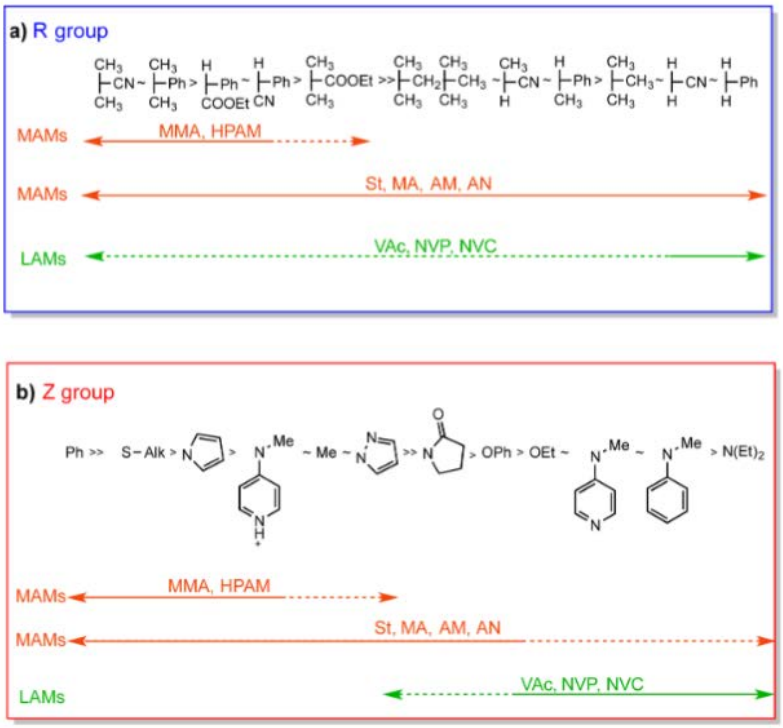

Figure 1.5. Compatibility overview between a selection of (a) R- and (b) Z-groups with a series of MAMs and LAMs vinyl monomers. Figure taken from ref.[28]

In summary, RAFT polymerization is a versatile method for creating well-designed polymers. It works with various monomers and solvents, enables easy post-polymerization functionalization, and avoids the need for metals or harsh conditions. Its high functional group tolerance makes it ideal for applications like paints, cosmetics, lubricants, biosensors, and polymer therapeutics, allowing the construction of complex structures such as block and branched architectures, as well as stimuli-responsive polymers.[32, 33]

1.2 Block copolymer self-assembly

BCPs containing at least one solvophobic and at least one solvophilic block, also known as amphiphilic BCPs, can undergo spontaneous self-assembly in solution.[34] This process is driven by the reduction of unfavorable interactions between the solvophobic block and

the solvent, and this is known as the solvophobic effect.[35] A core-corona structure is formed, where the solvophobic block creates the core, surrounded by the swollen or solvated solvophilic block. Over 20 distinct particle shapes or morphologies have been reported from self-assembly in solution, including spheres, cylinders/worms, lamellae, vesicles, and large compound vesicles.[36] The specific morphology that results from the self-assembly of a BCP in solution is primarily influenced by three key factors: The degree of stretching of the core-forming block, the nature and intensity of the repulsive interactions between the solvophilic blocks, and the interfacial tension between the solvent and the core-forming chain.[37] The morphology of these BCPs self-assembles can be predicted by the unitless packing parameter, p (Equation 1.1).

$$p = \frac{v}{a_o l_c}$$

Equation 1.1. The packing parameter for predicting polymer micelle morphology where v is the volume of the hydrophobic chains, a_o is the optimal area of the corona block, and l_c is the length of the hydrophobic core-forming block.

Typically, spherical micelles are formed when $p \leq ⅓$, cylinders when $⅓ \leq p \leq ½$, and when $p \geq ½$ vesicles are assembled (Figure 1.10).[37, 38] The predominant method for altering the morphology of a BCP is to alter the relative lengths of the hydrophobic and hydrophilic blocks.

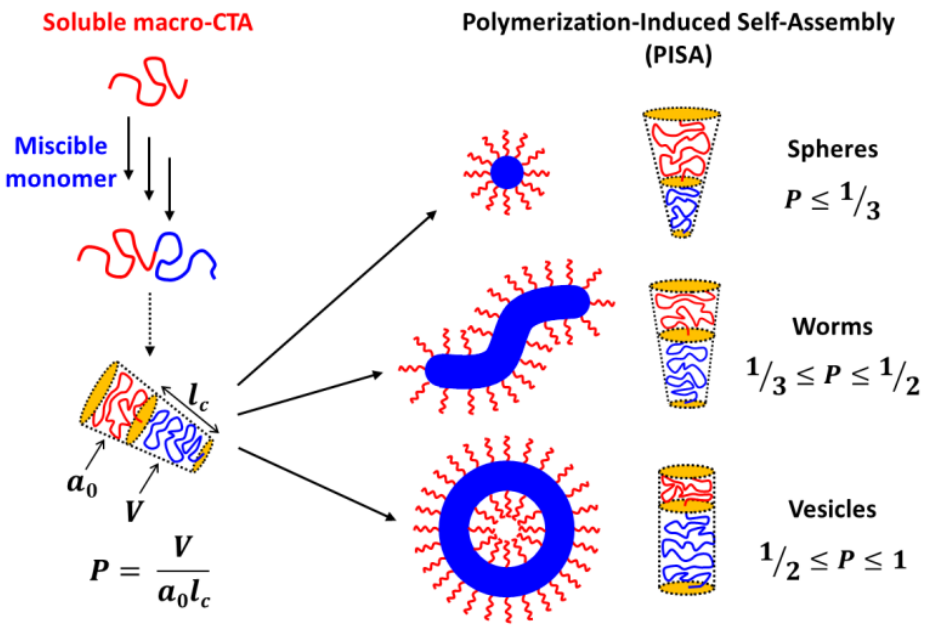

Figure 1.10. Morphologies of amphiphilic polymer self-assemblies according to the packing parameter. Figure taken from.[38]

Polymeric nano-objects can be synthesized using traditional self-assembly techniques like solvent-switch, direct dissolution, and thin-film rehydration, as well as alternative methods such as nanoprecipitation, dispersion/emulsion polymerization, and crystallization-driven self-assembly (CDSA).[39-42] These nano-objects are valuable in fields like imaging, sensing, catalysis, and drug delivery due to their unique properties, including tunable lipophilicity, enhanced therapeutic efficiency, and the ability to control and functionalize their structures.[43] Although conventional BCP self-assembly methods are widely used, they have drawbacks, such as time-consuming multi-step processes involving polymer synthesis and purification before self-assembly, and the need for dilute polymer solutions. Recently, a new method called polymerization-induced self-assembly (PISA) has been developed, which addresses many of the limitations of traditional self-assembly techniques.[44]

1.2.1 Polymerization-Induced Self-Assembly (PISA)

PISA is a method widely used to produce different nanostructures from block copolymers by driving a physical self-assembly process upon an increase of the solvophobic part of the block copolymers as the polymerization progresses.

It is a one-pot synthetic method that offers numerous advantages over traditional self-assembly techniques for creating various morphologies. This method involves polymerizing a solvent-compatible monomer from a pre-synthesized macroCTA, causing the block copolymer to self-assemble as the second block reaches insolubility in the solvent at a certain degree of polymerization[45] PISA can be performed at high solid concentrations (up to 50% w/w), functions in both polar and non-polar organic solvents, as well as in aqueous media, and is compatible with reversible-deactivation radical polymerization techniques such as ATRP,[25] NMP,[24] and RAFT.[29] Additionally, synthesis in concentrated environments is possible, which facilitates industrial scale-up, and a wide range of nano-object morphologies can be achieved (figure 1.11).[46]

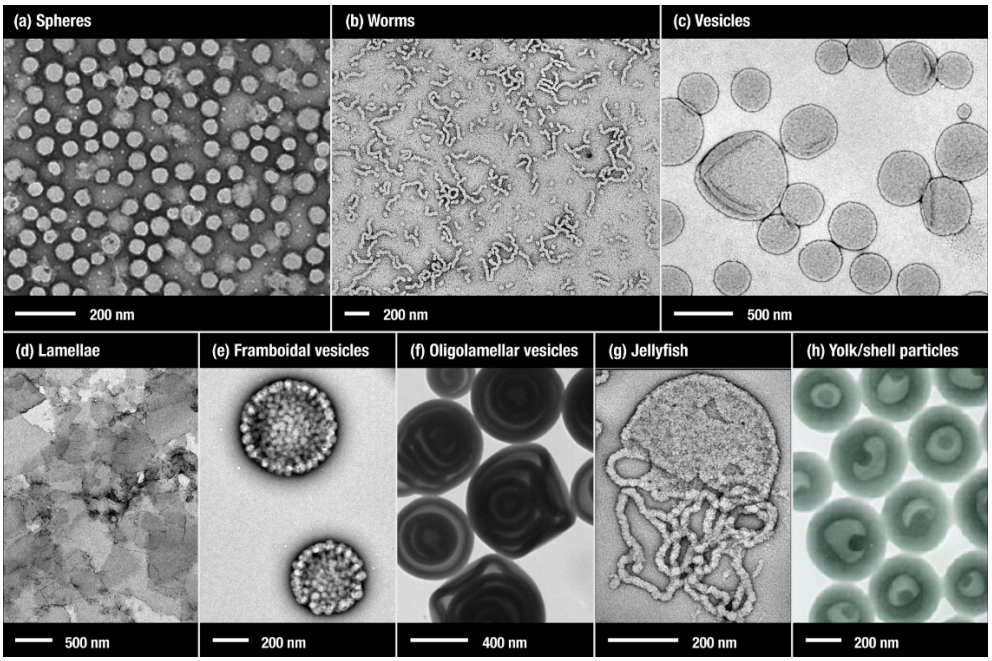

Figure 1.11. Different morphologies obtained *via* RAFT-mediated PISA. Figure taken from ref.[46]

PISA can be carried out using either emulsion polymerization, where the monomers are not miscible, or precipitation polymerization, where the monomers are miscible. Traditional emulsion polymerizations rely on surfactants to stabilize the growing polymer particles in the aqueous phase. However, the use of conventional surfactants can lead to issues like super swelling, poor film formation, degradation of physical properties, and environmental concerns.[47, 48]

In contrast, RAFT-mediated emulsion polymerization offers an alternative approach that avoids these issues. The key to this method is the use of an amphiphilic macroCTA, which can self-assemble in the reaction medium and initiate particle nucleation without the need for traditional low molecular weight surfactants (figure 1.12).[49]

Ferguson et al.[50, 51] were pioneers in demonstrating PISA in emulsion polymerization in 2002, and subsequent research revealed that PISA could be employed to create a variety of complex morphologies, such as worms and vesicles.[43] In these self-assembled structures, the R-group and the solvophilic block of the polymer typically anchor at the particle interface, while the hydrophobic block extends into the particle's interior.[52] This configuration has been utilized to create covalently linked core-shell particles and multilayered particles.[50, 51]

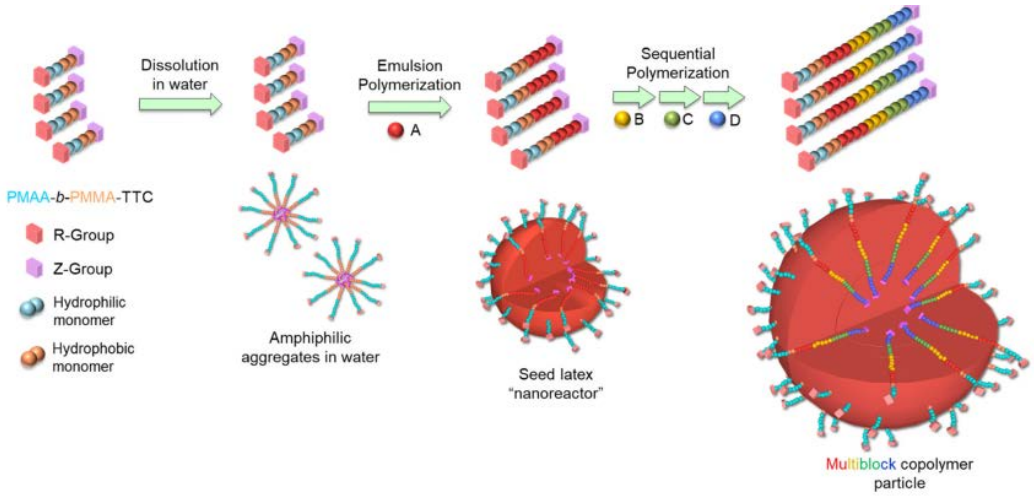

Figure 1.12. Schematic representation of the emulsion polymerisation in the presence of polymeric stabiliser. Figure adapted from.[52]

1.3 Stimuli responsive polymers

Stimuli-responsive polymers have gained enormous attention due to their ability to generate a response when detecting weak changes in their surrounding environment such as pH, CO_2, temperature, enzyme, light, electrical, redox and magnetic fields, ionic strength, etc (figure 1.13).[53-56] These external stimuli usually induce an observable or detectable change in the polymer conformation at the micro- or nanoscale.[57] This often results in a significant change in the solubility, colour, or size; hence, they are of particular interest in fields such as drug delivery, smart surfaces, catalysis and in sensor applications.[58]

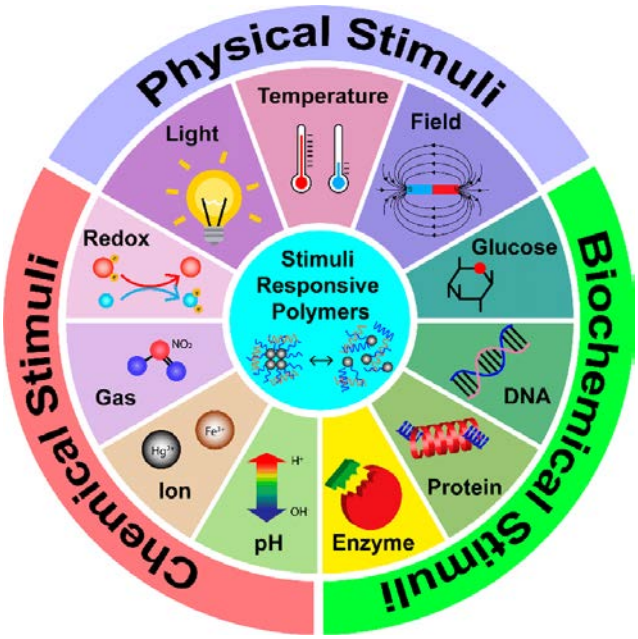

Figure 1.13. Physical, chemical, and biochemical responsiveness of stimuli-responsive polymers. Reproduced from ref.[59]

1.3.1 pH-responsive polymers

pH-responsive polymers are a type of stimuli-responsive polymer that reacts to changes in solution pH by altering their structure and properties, including surface activity, chain conformation, solubility, and configuration. The term "pH-responsive polymers" typically refers to polymers containing ionizable acidic or basic groups, whose ionization state is influenced by the pH of the solution. In recent years, this area of study has gained significant attention, with new research being continually added.[60] These polymers are classified in two main groups.[61]

On one side, pH-responsive acidic polymers, this is, polymers having weak acidic/basic pendant groups that can accept protons at low pH and release them at high pH. These polymers usually contain carboxylic groups, sulfonic acid, phosphonic acid or boronic acids (figure 1.13).

On the other hand, pH-responsive basic polymers, are polymer that undergo ionization/deionization transitions from pH 7-11. These polymers are usually synthesized with monomers containing tertiary amine derivatives that can react with strong and weak acids.[62] Some examples of the most used amine monomers are DMAEMA or DEAEMA (figure 1.14).

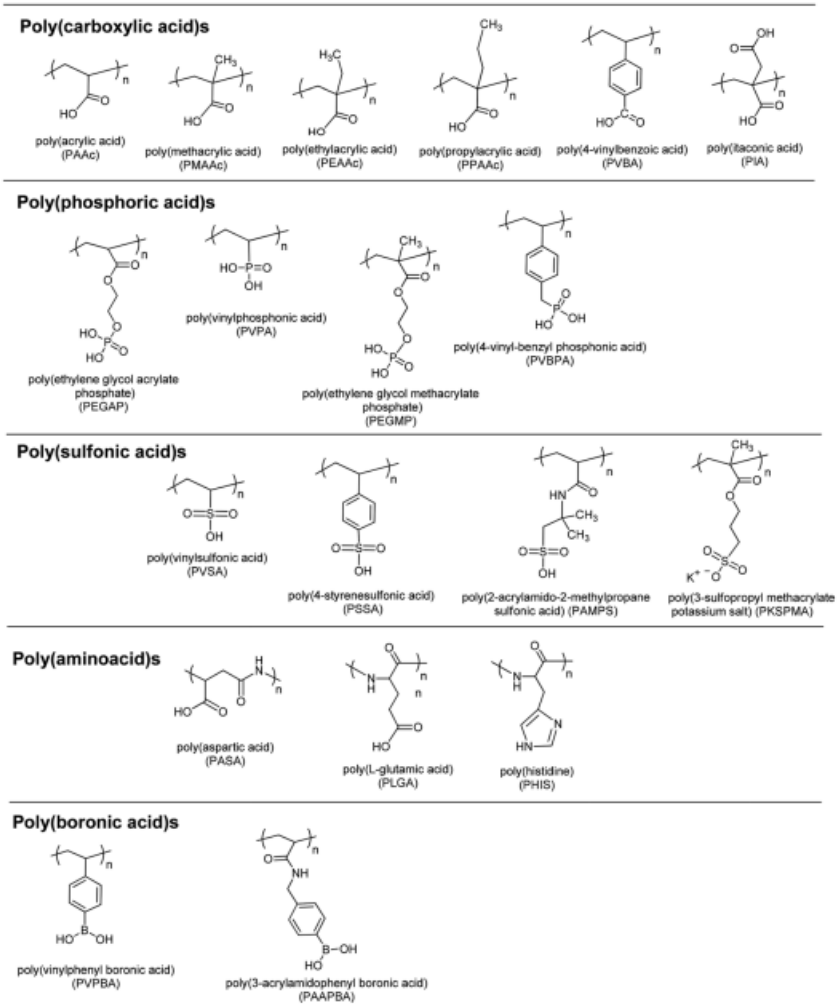

Figure 1.14. Chemical structures of pH-responsive acid polymers. Figure adapted from.[60]

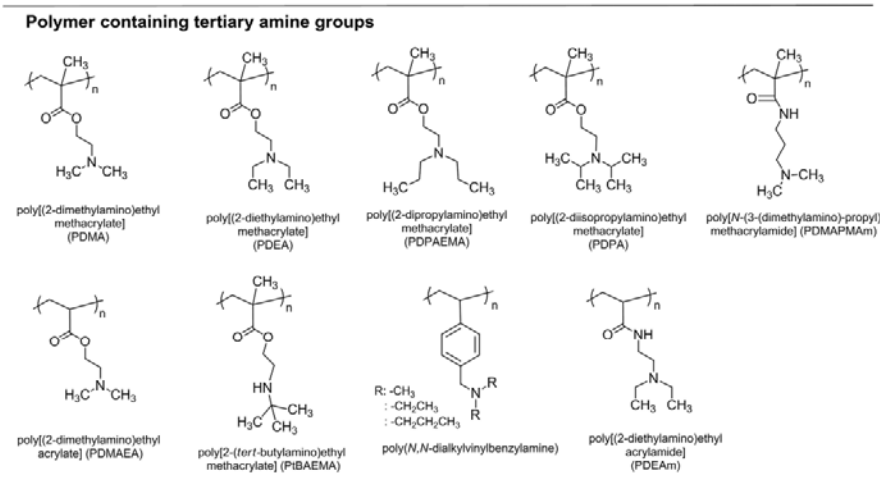

Figure 1.15. Chemical structures of some pH-responsive basic polymers. Figure adapted from.[60]

1.4 Fluorescent polymeric materials

1.4.1 Photoluminescence

Photoluminescence is a key feature that certain responsive polymers can exhibit when they incorporate a dye, reacting to specific stimuli.[63] This photophysical process happens when a molecule absorbs energy at one wavelength and then releases it at another. This type of luminescence typically occurs in the ultraviolet, visible, or near-infrared parts of the electromagnetic spectrum. Luminescence refers to the spontaneous emission of radiation from a species that is either electronically or vibrationally excited and not in thermal balance with its surroundings. For many years, luminescence has been essential in research, finding wide applications in fields such as biological labeling, chemical sensing, medical diagnostics, and the development of photoactive materials for light-emitting technologies. The luminescence behavior of organic compounds, such as fluorescence and phosphorescence, can be understood using the Jablonski diagram (figure 1.17). When a molecule absorbs a photon, it may enter one of two electronic states: a

singlet state (S) with paired electron spins or a triplet state (T) with unpaired spins. Initially, the molecule is excited to a higher singlet state (Sn) and quickly relaxes to the lowest excited singlet state (S1) via internal conversion (IC). From the S1 state, the molecule can either return to the ground state (S0) by emitting a photon through fluorescence or undergo non-radiative internal conversion. In some cases, intersystem crossing (ISC) can take place, where the molecule transitions from S1 to a triplet state (T1). The triplet state can then return to the ground state by phosphorescence, a process that takes longer than fluorescence due to the spin-forbidden nature of the transition.

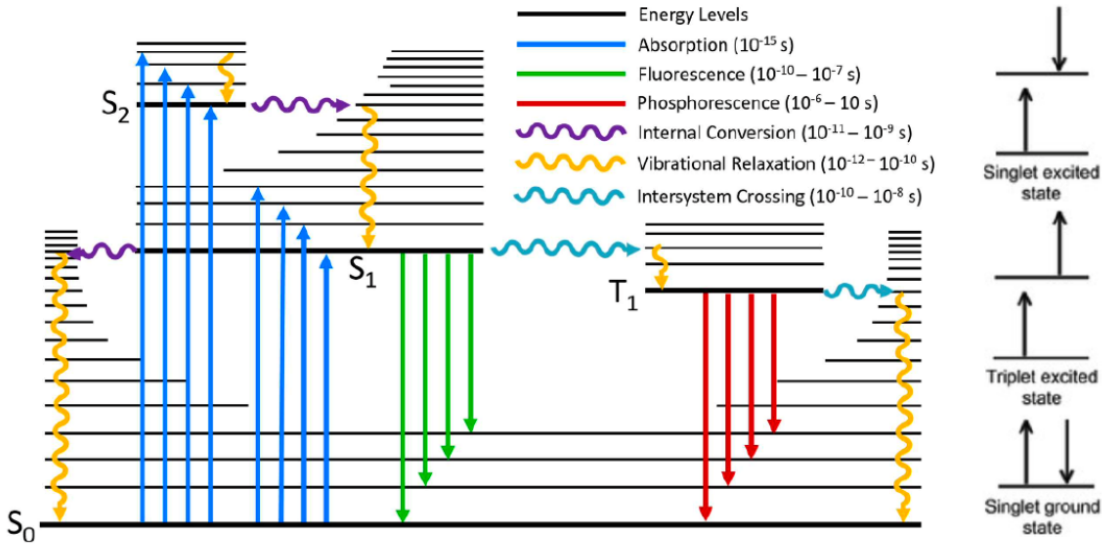

Figure 1.17 Jablonski diagram showing the possible radiative and non-radiative transitions. Figure taken from ref.[64]

1.4.2 Fluorescence emission

Fluorescence emission occurs at a wavelength distinct from the absorption wavelength, and the difference between the two is known as the Stokes shift (Figure 1.18a). This shift is commonly analyzed using steady-state fluorescence spectroscopy, a multiparametric method that examines factors like fluorophore excitation, emission, spectral shifts, and

anisotropy. In most cases, the emission spectrum is independent of the excitation wavelength and can overlap with the excitation spectrum. During these measurements, the light source and detector are usually positioned at a 90-degree angle (Figure 1.18b). The fluorescence intensity (FI) detected by a fluorometer can be impacted by several variables, such as fluorophore concentration, the configuration of the experimental setup, the light source, and environmental factors like solvent, pH, and other conditions. Therefore, fluorescence intensity alone offers limited quantitative insights.

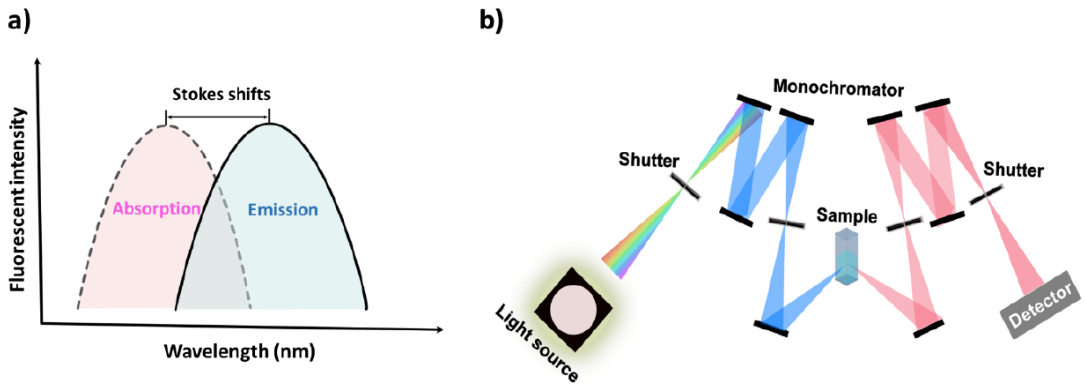

Figure 1.18. a) Schematic representation of the absorption and fluorescence spectra. b) Basic schematic of the fluorescence spectroscopy instrument setup. Figure taken from ref.[65]

1.4.3 Sensing and Detection

Fluorescent materials have found widespread applications across diverse areas such as analytical sensing, optical imaging, and data storage.[66, 67] Through intentional design efforts, these materials have expanded into various forms, ranging from small molecular fluorophores and fluorescent nanoparticles at the microscopic level to large-scale fluorescent films. Among these, fluorescent polymers have gained particular attention due to their versatility and adaptability, inherited from their polymeric structure, as well as the responsive signals generated by their fluorescent components.[68] This has led to

significant advancements in polymers integrated with fluorescent materials, from nanoscale polymeric structures to larger fluorescent hydrogels, which have attracted notable interest within the field of fluorescent materials.

The goal behind developing polymer-based materials with fluorescent properties is to enable the accurate monitoring of changes in polymer chain conformation and dynamics. Furthermore, the ability to adjust the responsiveness of fluorescent polymers has proven highly useful in a variety of sensing applications, including bioimaging and diagnostics.

In addition to their role in imaging, the fast response time and high sensitivity of fluorescence have been utilized in analytical and diagnostic chemistry. Fluorescent chemosensors, which are defined as molecules that detect specific chemical species by producing a fluorescence signal in response to binding or interaction, are especially important for detecting molecules in intracellular conditions.[69] By carefully designing molecular structures and altering the binding sites of fluorophores, the fluorescent response can be precisely adjusted to target specific species with high sensitivity and speed. Additionally, advancements in stimuli-responsive polymer systems have enabled the incorporation of fluorophores, further improving chemosensors by enhancing the interactions within the polymer matrix. To date, a wide range of fluorescent polymer sensors have been created for detecting various species, such as metal ions, small molecules, and biomolecules.

Fluorescent polymer-based sensors can be designed by integrating fluorescent chemosensors with targeted binding sites directly into polymer frameworks.[70-72] Another method involves utilizing polymers as a scaffold or matrix, which offers a solution to common challenges associated with small molecule chemosensors, such as issues with solubility, stability, and certain biological traits like accumulation time and capacity.[73]

Liu et al. created a series of multi-component polymers using the Heck coupling reaction, which demonstrated the ability to detect Hg^{2+}/Hg^{+} in water and various water-miscible solvents. These polymers exhibited strong selectivity and high sensitivity to mercury ions.[74]

A different strategy for creating fluorescent polymeric sensors involves linking fluorophores to polymer structures that have specific interaction sites or display responsive characteristics.[75, 76] These responsive characteristics, including selective swelling, degradation, and assembly/disassembly, enable regulated alterations in the microenvironment and interactions of the embedded fluorophores, thus affecting their photophysical properties. For example, Tuga et al. developed PDEAEMA-based cross-linked polymeric nanoparticles, that could reversibly swell below pH 7.3 and a non pH-responsive dye, rhodamine B isothiocyanate.[77] The dye uptake was carried in acidic media, as they nanoparticles were swollen.

The development of bulk fluorescent sensors using polymeric materials, such as films and hydrogels, is valuable for real-time and in situ detection with visible outputs. Zhou *et* al. developed a hydrogel embedded with CdTe quantum dots (QDs) that exhibited strong luminescence and selective responsiveness to fluoride ions. The ion-exchange functionalized CdTe QDs displayed a rapid sol-gel transition and a selective reaction to fluoride in aqueous solutions.[78] Li and coworkers created a fluorescent hydrogel specifically for detecting Fe^{3+}, using poly(9-fluorenecarboxylic acid) (PFCA) as the sensing component. This hydrogel demonstrated fast and selective recognition of Fe^{3+} when tested against a range of 16 anions and 21 cations.[79] Wu and coworkers developed white fluorescent hydrogels that respond to light and heat by copolymerizing hydrophilic acrylamide with hydrophobic chromophore monomers through micellar copolymerization.[80] Within the hydrogels, both monomers and dimers of the

chromophores were present, emitting complementary blue and yellow fluorescence. When exposed to light or heat, the chromophores underwent a monomer-to-dimer transition, causing the fluorescent color to shift from blue to white and then to yellow. Overall, these bulk polymeric fluorescent materials offer real-time, readable information and have potential applications in displays, biomimetic robotics, and portable sensors.

1.5 Fluorescent pH/CO_2 responsive polymers

Stimuli-responsive polymers, which change their fluorescence properties in response to changes in pH and have attracted a great deal of interest because of their potential applications in sensors, bioimaging, and drug delivery.[81-83] pH-responsive fluorescent polymers can be readily synthesized by incorporating several luminescent and pH-sensitive functional groups into the polymer chains.[84] Benefiting from these advantages, pH-responsive fluorescent polymers have been widely studied as potential sensors.

Moreover, the amine groups present in these pH-responsive systems can be protonated upon a decrease in pH which in turn can be induced by CO_2 as it partially dissolves in water to form an equilibrium with carbonic acid, which is a weak acid that can dissociate into HCO_3^-, CO_3^{2-} and H^+, allowing protonation of the amine monomer. This can be used as a stimulus to trigger a change in the physicochemical properties of the polymer, making them potential CO_2 sensors.[85, 86]

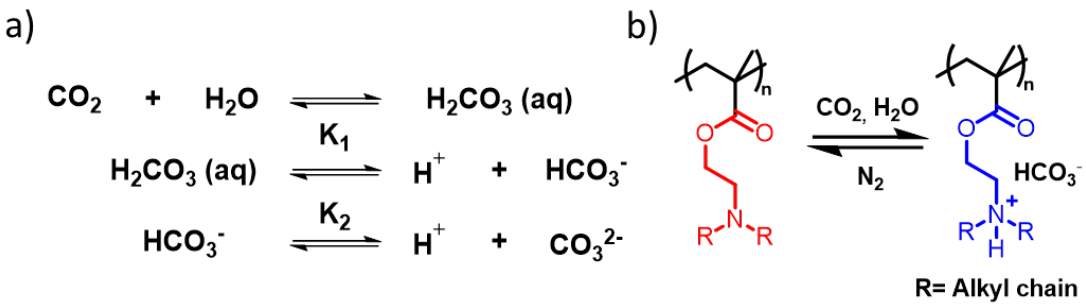

Figure 1.19. a) CO_2 reactivity in water; b) CO_2-switchability of PDRAEMA.

Polymeric tertiary amines exhibit different hydrophobicity based on their protonation state: they are more hydrophobic in their neutral form and become more hydrophilic when protonated.[85, 86] This reversible protonation can be controlled by the addition and removal of CO_2 (figure 1.19). The pK_{aH} values for DEAEMA and its homopolymer are 8.8 and 7.5, respectively, making DEAEMA a CO_2-switchable monomer. Incorporating DEAEMA into a (co)polymer structure imparts CO_2-switchability to the entire polymer. Another CO_2-switchable monomer, DMAEMA, has pK_{aH} values of 8.3 and 7.4 for the monomer and polymer, respectively. Despite their similar chemical structures, DEAEMA and DMAEMA have distinct water solubility properties: DEAEMA and its polymer (PDEAEMA) are hydrophobic, whereas DMAEMA and its polymer (PDMAEMA) are hydrophilic. PDMAEMA precipitates from hexane more readily than PDEAEMA at the same molecular weight. Although both monomers are susceptible to hydrolysis, DEAEMA is more resistant to hydrolysis than DMAEMA under similar pH and temperature conditions.

Fluorescent CO_2 sensors utilizing pH-responsive polymers have progressed quickly, owing to their adjustable water dispersibility, customizable sensitivity, high stability, and ease of integration. For instance, our group previously reported the use of the polarity-sensitive chromophore aminobromomaleimide methacrylate (ABMMA) to detect CO_2 concentration.[87] We developed microgels composed with poly[oligo(ethylene glycol) methacrylate] (POEGMA) forming the shell and crosslinked poly(N,N-diethylaminoethyl methacrylate) (PDEAEMA) as the core forming block, incorporating ABMMA into the nonpolar core. After CO_2 purging for 15 minutes, the PDEAEMA core became protonated and polar, leading to a decrease in fluorescence from the ABMMA chromophores.

Zhang Et. Al. developed fluorescent polymersomes with both aggregation-induced emission (AIE) and CO_2-responsive properties in which the hydrophobic block was a copolymer made of tetraphenylethene functionalized methacrylate (TPEMA) and 2-(diethylamino)ethyl methacrylate (DEAEMA) with unspecified sequence arrangement.[88] Upon CO_2 bubbling these vesicles transformed to small spherical micelles, and upon Ar bubbling micelles returned to vesicles with the presence of a few intermediate morphologies.

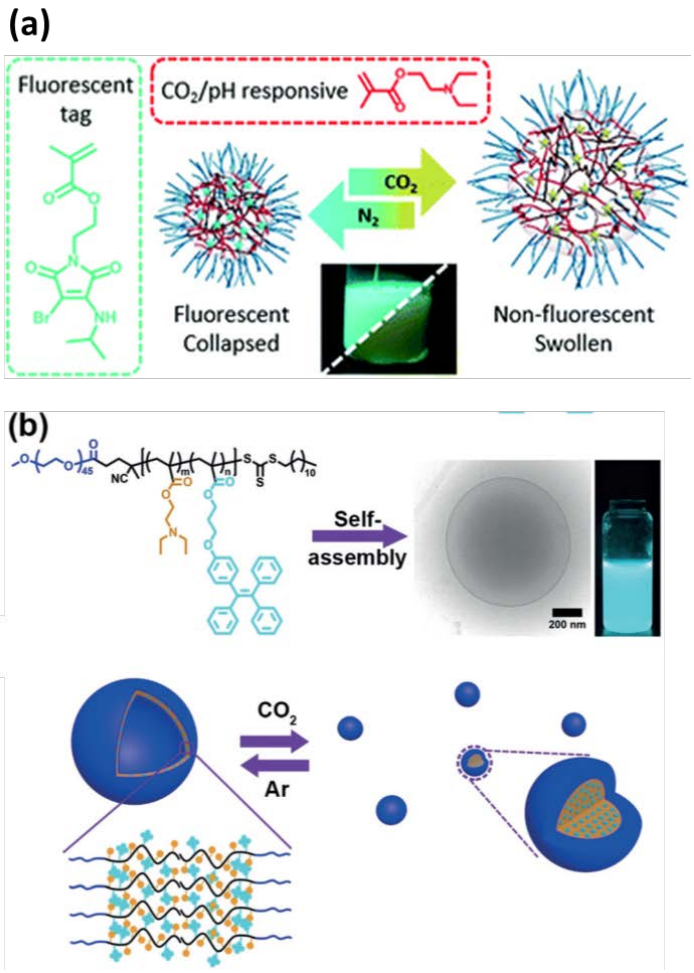

Figure 1.20. a) CO_2-responsive nanoparticles. Picture taken from ref.[87] b) CO_2-responsive polymersomes. Picture taken from ref.[89]

Yuan and coworkers developed an ultrafast CO_2 fluorescent sensor using a block copolymer, [POEGMA-b-P(DEAEMA-r-NBDMA)].[90] In this system, DEAEMA units

served as the CO_2-responsive segment, while 4-nitrobenzo-2-oxa-1,3-diazole (NBD) acted as the chromophore. Upon exposure to CO_2, the micelles disassembled, resulting in an increase in both fluorescence emission and quantum yield (figure 1.20). The sensor also demonstrated recyclability, maintaining its performance over five cycles of CO_2 exposure followed by Ar purging.

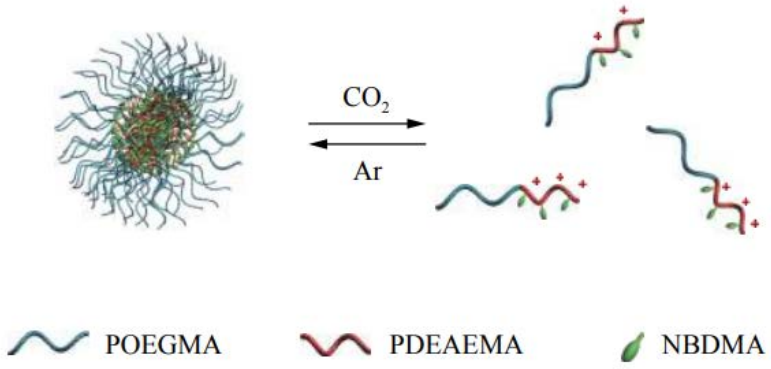

Figure 1.21. Schematic illustration of the micellar sensors' CO_2-sensing behavior. Figure taken from ref.[90]

1.6 BP gas sensing project

BP gas sensing project is a new collaboration between the BP Exploration Operating Company and the O'Reilly group (BP reference: BPX/GPTL/JN/76937 (CW1905016)). BP is looking to monitor and report the release of gases, specifically carbon dioxide (CO_2) that is released into the atmosphere, from pipelines, with a target to reducing emissions. Nitrogen (N_2) is equally of interest as it is pumped through top-side empty pipes, prior to implementation to detect leaks. The challenge with the detection of all these gases are that emission concentrations are low and hence something is needed to magnify the signal. To address this challenge we propose investigating, color-responsive/fluorescence systems to allow for the visualization of a leak and unwanted emissions.

1.7 Aim and objectives

The aim of this collaboration is to develop a new polymeric material able to respond to some gases (CO_2, N_2) while simultaneously change it quantitative and visual fluorescence in a drastic way to be. For that, the main objectives as part of this PhD project are:

- Synthesis of fluorescent cross-linked CO_2 responsive nanoparticles with different fluorescent monomers that can be potentially used in gas sensing.
- Study of the properties, including size, fluorescence, pH, and CO_2 responsiveness of the nanoparticles with the fluorescent monomers.
- Study of delivery methods for the fluorescent nanoparticles depending if they will be dispersed either on the piping (nano/microgels as a paint) or into the gas stream (as an aerosol)

1.8 Summary

This chapter reviews the key concepts explored in the experimental chapters of this thesis. It begins with a brief introduction to the fundamentals of synthetic polymers, followed by an overview of common polymerization techniques, focusing on the mechanisms of controlled polymerizations. RAFT polymerization is discussed in detail, as it is extensively used for preparing block copolymers throughout the thesis. The chapter then touches on the self-assembly of block copolymers, leading into a description of PISA. Stimuli-responsive polymers are introduced, with a detailed explanation of pH-responsive polymers. The chapter also covers fluorescent polymeric materials, along with the basic concepts of photoluminescence and fluorescence, which form the core of the thesis. Finally, fluorescent pH/CO_2-responsive polymers are introduced with some examples published during the last year, as they are synthesized in every chapter of this BP project, highlighting that most self-assembled pH-responsive systems that provide a fluorescent

response to CO_2 involve one pH-responsive moiety and another that is polarity-sensitive, leading to changes in fluorescence properties as the system's polarity shifts.

1.9 References

(1) Parveen, I.; Mahmud, M.; Khan, R. Biodegradable Natural Polymers for Biomedical Applications. *Scientific Review* **2019**, 67-80. DOI: 10.32861/sr.53.67.80.

(2) Brunsveld, L.; Folmer, B. J.; Meijer, E. W.; Sijbesma, R. P. Supramolecular polymers. *Chem Rev* **2001**, *101* (12), 4071-4098. DOI: 10.1021/cr990125q From NLM.

(3) Fang, Z.; Li, B.; Liu, Y.; Zhu, J.; Li, G.; Hou, G.; Zhou, J.; Qiu, X. Critical Role of Degree of Polymerization of Cellulose in Super-Strong Nanocellulose Films. *Matter* **2020**, *2* (4), 1000-1014. DOI: doi.org/10.1016/j.matt.2020.01.016.

(4) Gentekos, D. T.; Dupuis, L. N.; Fors, B. P. Beyond Dispersity: Deterministic Control of Polymer Molecular Weight Distribution. *J. Am. Chem. Soc.* **2016**, *138* (6), 1848-1851. DOI: 10.1021/jacs.5b13565 PubMed.

(5) Mark, J. *Physical Properties of Polymer Handbook*; 2007. DOI: 10.1007/978-0-387-69002-5.

(6) Miclotte, M. P. J.; Lawrenson, S. B.; Varlas, S.; Rashid, B.; Chapman, E.; O'Reilly, R. K. Tuning the Cloud-Point and Flocculation Temperature of Poly(2-(diethylamino)ethyl methacrylate)-Based Nanoparticles via a Postpolymerization Betainization Approach. *ACS Polym. Au* **2021**, *1* (1), 47-58. DOI: 10.1021/acspolymersau.1c00010.

(7) Dyer, W. E.; Kumru, B. Polymers as Aerospace Structural Components: How to Reach Sustainability? *Macromol. Chem. Phys.* **2023**, *224* (24), 2300186. DOI: doi.org/10.1002/macp.202300186.

(8) Mecerreyes, D.; Casado, N.; Villaluenga, I.; Forsyth, M. Current Trends and Perspectives of Polymers in Batteries. *Macromolecules* **2024**, *57* (7), 3013-3025. DOI: 10.1021/acs.macromol.3c01971.

(9) Syrett, J. A.; Haddleton, D. M.; Whittaker, M. R.; Davis, T. P.; Boyer, C. Functional, star polymeric molecular carriers, built from biodegradable microgel/nanogel cores. *Chem. Commun.* **2011**, *47* (5), 1449-1451, 10.1039/C0CC04532B. DOI: 10.1039/C0CC04532B.

(10) Hadjichristidis, N.; Iatrou, H.; Pitsikalis, M.; Mays, J. Macromolecular architectures by living and controlled/living polymerizations. *Prog. Polym. Sci.* **2006**, *31* (12), 1068-1132. DOI: doi.org/10.1016/j.progpolymsci.2006.07.002.

(11) Chen, X.; Michinobu, T. Postpolymerization Modification: A Powerful Tool for the Synthesis and Function Tuning of Stimuli-Responsive Polymers. *Macromol. Chem. Phys.* **2022**, *223* (1), 2100370. DOI: doi.org/10.1002/macp.202100370.

(12) Matyjaszewski, K. Chemistry. Architecturally complex polymers with controlled heterogeneity. *Science* **2011**, *333* (6046), 1104-1105. DOI: 10.1126/science.1209660 From NLM.

(13) Radical Chain Polymerization. In *Principles of Polymerization*, 2004; pp 198-349.

(14) Saleh, T. A. Chapter 3 - Polymer science and polymerization methods toward hybrid materials. In *Polymer Hybrid Materials and Nanocomposites*, Saleh, T. A. Ed.; William Andrew Publishing, 2021; pp 59-103.

(15) Grubbs, R. B.; Grubbs, R. H. 50th Anniversary Perspective: Living Polymerization—Emphasizing the Molecule in Macromolecules. *Macromolecules* **2017**, *50* (18), 6979-6997. DOI: 10.1021/acs.macromol.7b01440.

(16) Baruah, C.; Sarmah, J. K. Chapter 18 - Guar gum-based hydrogel and hydrogel nanocomposites for biomedical applications. In *Micro- and Nanoengineered Gum-Based*

Biomaterials for Drug Delivery and Biomedical Applications, Jana, S., Jana, S. Eds.; Elsevier, 2022; pp 473-492.

(17) Wang, Z.; Cui, F.; Sui, Y.; Yan, J. Radical chemistry in polymer science: an overview and recent advances. *Beilstein J Org Chem* **2023**, *19*, 1580-1603. DOI: 10.3762/bjoc.19.116 From NLM.

(18) Barner-Kowollik, C.; Buback, M.; Egorov, M.; Fukuda, T.; Goto, A.; Olaj, O. F.; Russell, G. T.; Vana, P.; Yamada, B.; Zetterlund, P. B. Critically evaluated termination rate coefficients for free-radical polymerization: Experimental methods. *Prog. Polym. Sci.* **2005**, *30* (6), 605-643. DOI: doi.org/10.1016/j.progpolymsci.2005.02.001.

(19) Matyjaszewski, K.; Gaynor, S. Free radical polymerization. 2000; pp 929-977.

(20) Corrigan, N.; Jung, K.; Moad, G.; Hawker, C. J.; Matyjaszewski, K.; Boyer, C. Reversible-deactivation radical polymerization (Controlled/living radical polymerization): From discovery to materials design and applications. *Prog. Polym. Sci.* **2020**, *111*, 101311. DOI: doi.org/10.1016/j.progpolymsci.2020.101311.

(21) Bagheri, A.; Boniface, S.; Fellows, C. M. Reversible-Deactivation Radical Polymerisation: chain polymerisation made simple. *Chemistry Teacher International* **2021**, *3* (2), 19-32. DOI: doi:10.1515/cti-2020-0025 (acccessed 2024-08-20).

(22) Lorandi, F.; Fantin, M.; Matyjaszewski, K. Atom Transfer Radical Polymerization: A Mechanistic Perspective. *J. Am. Chem. Soc.* **2022**, *144* (34), 15413-15430. DOI: 10.1021/jacs.2c05364.

(23) Lamontagne, H. R.; Lessard, B. H. Nitroxide-Mediated Polymerization: A Versatile Tool for the Engineering of Next Generation Materials. *ACS Applied Polymer Materials* **2020**, *2* (12), 5327-5344. DOI: 10.1021/acsapm.0c00888.

(24) Nicolas, J.; Guillaneuf, Y.; Lefay, C.; Bertin, D.; Gigmes, D.; Charleux, B. Nitroxide-mediated polymerization. *Prog. Polym. Sci.* **2013**, *38* (1), 63-235. DOI: doi.org/10.1016/j.progpolymsci.2012.06.002.

(25) Petton, L.; Ciolino, A. E.; Dervaux, B.; Du Prez, F. E. From one-pot stabilisation to in situ functionalisation in nitroxide mediated polymerisation: an efficient extension towards atom transfer radical polymerisation. *Polym. Chem.* **2012**, *3* (7), 1867-1878, 10.1039/C2PY00444E. DOI: 10.1039/C2PY00444E.

(26) Matyjaszewski, K.; Xia, J. Atom Transfer Radical Polymerization. *Chem. Rev.* **2001**, *101* (9), 2921-2990. DOI: 10.1021/cr940534g.

(27) Pintauer, T.; Braunecker, W.; Collange, E.; Poli, R.; Matyjaszewski, K. Determination of Rate Constants for the Activation Step in Atom Transfer Radical Polymerization Using the Stopped-Flow Technique. *Macromolecules* **2004**, *37* (8), 2679-2682. DOI: 10.1021/ma035634f.

(28) Perrier, S. 50th Anniversary Perspective: RAFT Polymerization—A User Guide. *Macromolecules* **2017**, *50* (19), 7433-7447. DOI: 10.1021/acs.macromol.7b00767.

(29) Ghosh Roy, S.; De, P. Facile RAFT synthesis of side-chain amino acids containing pH-responsive hyperbranched and star architectures. *Polym. Chem.* **2014**, *5* (21), 6365-6378, 10.1039/C4PY00766B. DOI: 10.1039/C4PY00766B.

(30) Keddie, D. J. A guide to the synthesis of block copolymers using reversible-addition fragmentation chain transfer (RAFT) polymerization. *Chem. Soc. Rev.* **2014**, *43* (2), 496-505, 10.1039/C3CS60290G. DOI: 10.1039/C3CS60290G.

(31) Moad, G.; Barner-Kowollik, C. The Mechanism and Kinetics of the RAFT Process: Overview, Rates, Stabilities, Side Reactions, Product Spectrum and Outstanding Challenges. In *Handbook of RAFT Polymerization*, 2008; pp 51-104.

(32) Moad, G.; Rizzardo, E.; Thang, S. H. RAFT Polymerization and Some of its Applications. *Chemistry – An Asian Journal* **2013**, *8* (8), 1634-1644. DOI: doi.org/10.1002/asia.201300262.

(33) Moad, C. L.; Moad, G. Fundamentals of reversible addition–fragmentation chain transfer (RAFT). *Chemistry Teacher International* **2021**, *3* (2), 3-17. DOI: doi:10.1515/cti-2020-0026 (acccessed 2024-08-21).

(34) Wong, C. K.; Qiang, X.; Müller, A. H. E.; Gröschel, A. H. Self-Assembly of block copolymers into internally ordered microparticles. *Prog. Polym. Sci.* **2020**, *102*, 101211. DOI: doi.org/10.1016/j.progpolymsci.2020.101211.

(35) Warr, G. G.; Atkin, R. Solvophobicity and amphiphilic self-assembly in neoteric and nanostructured solvents. *Current Opinion in Colloid & Interface Science* **2020**, *45*, 83-96. DOI: doi.org/10.1016/j.cocis.2019.12.009.

(36) Song, S.; Zhou, H.; Manners, I.; Winnik, M. A. Block copolymer self-assembly: Polydisperse corona-forming blocks leading to uniform morphologies. *Chem* **2021**, *7* (10), 2800-2821. DOI: doi.org/10.1016/j.chempr.2021.08.003.

(37) Karayianni, M.; Pispas, S. Block copolymer solution self-assembly: Recent advances, emerging trends, and applications. *Journal of Polymer Science* **2021**, *59* (17), 1874-1898. DOI: doi.org/10.1002/pol.20210430

(38) Derry, M. J.; Fielding, L. A.; Armes, S. P. Polymerization-induced self-assembly of block copolymer nanoparticles via RAFT non-aqueous dispersion polymerization. *Prog. Polym. Sci.* **2016**, *52*, 1-18. DOI: doi.org/10.1016/j.progpolymsci.2015.10.002.

(39) Lin, H. K.; Yan, T.-H.; Bashir, S.; Liu, J. L. Chapter 3 - Synthesis of nanomaterials using bottom-up methods. In *Advanced Nanomaterials and Their Applications in Renewable Energy (Second Edition)*, Liu, J. L., Yan, T.-H., Bashir, S. Eds.; Elsevier, 2022; pp 61-110.

(40) Song, S.; Zhou, H.; Puzhitsky, M.; Zhang, Y.; Hicks, G.; Lu, Y.; Manners, I.; Winnik, M. A. Crystallization-Driven Self-Assembly of a Block Copolymer with Amphiphilic Pendant Groups. *Macromolecules* **2021**, *54* (2), 930-940. DOI: 10.1021/acs.macromol.0c02521.

(41) Sahoo, S.; Gopalan, A.; Ramesh, S.; Nirmala, P.; Ramkumar, G.; Agnes Shifani, S.; Subbiah, R.; Isaac JoshuaRamesh Lalvani, J. Preparation of Polymeric Nanomaterials Using Emulsion Polymerization. *Advances in Materials Science and Engineering* **2021**, *2021* (1), 1539230. DOI: doi.org/10.1155/2021/1539230.

(42) Martínez Rivas, C. J.; Tarhini, M.; Badri, W.; Miladi, K.; Greige-Gerges, H.; Nazari, Q. A.; Galindo Rodríguez, S. A.; Román, R. Á.; Fessi, H.; Elaissari, A. Nanoprecipitation process: From encapsulation to drug delivery. *Int. J. Pharm.* **2017**, *532* (1), 66-81. DOI: doi.org/10.1016/j.ijpharm.2017.08.064.

(43) Liu, C.; Hong, C.-Y.; Pan, C.-Y. Polymerization techniques in polymerization-induced self-assembly (PISA). *Polym. Chem.* **2020**, *11* (22), 3673-3689, 10.1039/D0PY00455C. DOI: 10.1039/D0PY00455C.

(44) Penfold, N. J. W.; Yeow, J.; Boyer, C.; Armes, S. P. Emerging Trends in Polymerization-Induced Self-Assembly. *ACS Macro Letters* **2019**, *8* (8), 1029-1054. DOI: 10.1021/acsmacrolett.9b00464.

(45) Charleux, B.; Delaittre, G.; Rieger, J.; D'Agosto, F. Polymerization-Induced Self-Assembly: From Soluble Macromolecules to Block Copolymer Nano-Objects in One Step. *Macromolecules* **2012**, *45* (17), 6753-6765. DOI: 10.1021/ma300713f.

(46) Canning, S. L.; Smith, G. N.; Armes, S. P. A Critical Appraisal of RAFT-Mediated Polymerization-Induced Self-Assembly. *Macromolecules* **2016**, *49* (6), 1985-2001. DOI: 10.1021/acs.macromol.5b02602.

(47) Lovell, P. A.; Schork, F. J. Fundamentals of Emulsion Polymerization. *Biomacromolecules* **2020**, *21* (11), 4396-4441. DOI: 10.1021/acs.biomac.0c00769.

(48) Abdelaziz Nasr Moawed Bakr, E.-h. Emulsion Polymerization Mechanism. In *Polymerization*, Nevin, C. Ed.; IntechOpen, 2018; p Ch. 1.

(49) Guimarães, T. R.; Bong, Y. L.; Thompson, S. W.; Moad, G.; Perrier, S.; Zetterlund, P. B. Polymerization-induced self-assembly via RAFT in emulsion: effect of Z-group on the nucleation step. *Polym. Chem.* **2021**, *12* (1), 122-133, 10.1039/D0PY01311K. DOI: 10.1039/D0PY01311K.

(50) Ferguson, C. J.; Hughes, R. J.; Nguyen, D.; Pham, B. T. T.; Gilbert, R. G.; Serelis, A. K.; Such, C. H.; Hawkett, B. S. Ab Initio Emulsion Polymerization by RAFT-Controlled Self-Assembly. *Macromolecules* **2005**, *38* (6), 2191-2204. DOI: 10.1021/ma048787r.

(51) Ferguson, C. J.; Hughes, R. J.; Pham, B. T. T.; Hawkett, B. S.; Gilbert, R. G.; Serelis, A. K.; Such, C. H. Effective ab Initio Emulsion Polymerization under RAFT Control. *Macromolecules* **2002**, *35* (25), 9243-9245. DOI: 10.1021/ma025626j.

(52) Clothier, G. K. K.; Guimarães, T. R.; Thompson, S. W.; Rho, J. Y.; Perrier, S.; Moad, G.; Zetterlund, P. B. Multiblock copolymer synthesis via RAFT emulsion polymerization. *Chem. Soc. Rev.* **2023**, *52* (10), 3438-3469, 10.1039/D2CS00115B. DOI: 10.1039/D2CS00115B.

(53) Wei, M.; Gao, Y.; Li, X.; Serpe, M. J. Stimuli-responsive polymers and their applications. *Polym. Chem.* **2017**, *8* (1), 127-143, 10.1039/C6PY01585A. DOI: 10.1039/C6PY01585A.

(54) Işıkver, Y.; Saraydın, D. Smart Hydrogels: Preparation, Characterization, and Determination of Transition Points of Crosslinked N-Isopropyl

Acrylamide/Acrylamide/Carboxylic Acids Polymers. *Gels* **2021**, *7* (3), 113. DOI: 10.3390/gels7030113.

(55) Gao, S.; Tang, G.; Hua, D.; Xiong, R.; Han, J.; Jiang, S.; Zhang, Q.; Huang, C. Stimuli-responsive bio-based polymeric systems and their applications. *J. Mater. Chem. B* **2019**, *7* (5), 709-729, 10.1039/C8TB02491J. DOI: 10.1039/C8TB02491J.

(56) Yan, Y.; Li, Y.; Wang, J.; Li, L.; Tang, F. A carbon dioxide responsive fluorescent system based on micellar transformation. *Colloids Surf. A Physicochem. Eng. Asp.* **2022**, *641*, 128457. DOI: 10.1016/j.colsurfa.2022.128457.

(57) Guo, J.; Wang, N.; Wu, J.; Ye, Q.; Zhang, C.; Xing, X.-H.; Yuan, J. Hybrid nanoparticles with CO2-responsive shells and fluorescence-labelled magnetic cores. *J. Mater. Chem. B* **2014**, *2* (4), 437-442, 10.1039/C3TB21264E. DOI: 10.1039/C3TB21264E.

(58) Zhao, R.; Fu, C.; Wang, Z.; Pan, M.; Ma, B.; Yin, Q.; Chen, B.; Liu, J.; Xia, H.; Wan, F.; et al. A pH-Responsive Nanoparticle Library with Precise pH Tunability by Co-Polymerization with Non-Ionizable Monomers. *Angew. Chem. Int. Ed.* **2022**, *61* (19). DOI: 10.1002/anie.202200152.

(59) Sun, X.; Agate, S.; Salem, K. S.; Lucia, L.; Pal, L. Hydrogel-Based Sensor Networks: Compositions, Properties, and Applications—A Review. *ACS Applied Bio Materials* **2021**, *4* (1), 140-162. DOI: 10.1021/acsabm.0c01011.

(60) Kocak, G.; Tuncer, C.; Bütün, V. pH-Responsive polymers. *Polym. Chem.* **2017**, *8* (1), 144-176. DOI: 10.1039/C6PY01872F.

(61) Khan, R. U.; Shao, J.; Liao, J.-Y.; Qian, L. pH-triggered cancer-targeting polymers: From extracellular accumulation to intracellular release. *Nano Research* **2023**, *16* (4), 5155-5168. DOI: 10.1007/s12274-022-5252-z.

(62) Jiang, B.; Zhang, Y.; Huang, X.; Kang, T.; Severtson, S. J.; Wang, W.-J.; Liu, P. Tailoring CO2-Responsive Polymers and Nanohybrids for Green Chemistry and Processes. *Ind. Eng. Chem. Res.* **2019**, *58* (33), 15088-15108. DOI: 10.1021/acs.iecr.9b02433.

(63) Teets, T. S. *Photoluminescence*; American Chemical Society, 2021. DOI: doi:10.1021/acsinfocus.7e5014.

(64) Mechanisms and Dynamics of Fluorescence Quenching. In *Principles of Fluorescence Spectroscopy*, Lakowicz, J. R. Ed.; Springer US, 2006; pp 331-351.

(65) Xie, Y. Fluorescent substituted maleimides : from small molecule fluorophore to polymeric barcoding. University of Warwick, 2020.

(66) Wang, H.; Ji, X.; Page, Z. A.; Sessler, J. L. Fluorescent materials-based information storage. *Materials Chemistry Frontiers* **2020**, *4* (4), 1024-1039, 10.1039/C9QM00607A. DOI: 10.1039/C9QM00607A.

(67) Nagarkar, A. A.; Root, S. E.; Fink, M. J.; Ten, A. S.; Cafferty, B. J.; Richardson, D. S.; Mrksich, M.; Whitesides, G. M. Storing and Reading Information in Mixtures of Fluorescent Molecules. *ACS Central Science* **2021**, *7* (10), 1728-1735. DOI: 10.1021/acscentsci.1c00728.

(68) Jiang, J.; Zhang, P.; Liu, L.; Li, Y.; Zhang, Y.; Wu, T.; Xie, H.; Zhang, C.; Cui, J.; Chen, J. Dual photochromics-contained photoswitchable multistate fluorescent polymers for advanced optical data storage, encryption, and photowritable pattern. *Chem. Eng. J.* **2021**, *425*, 131557. DOI: doi.org/10.1016/j.cej.2021.131557.

(69) Nilo, N.; Reyna-Jeldes, M.; Covarrubias, A. A.; Coddou, C.; Artigas, V.; Fuentealba, M.; Aguilar, L. F.; Saldías, M.; Mellado, M. A pH-Sensitive Fluorescent Chemosensor Turn-On Based in a Salen Iron (III) Complex: Synthesis, Photophysical Properties, and

Live-Cell Imaging Application. *Molecules* **2023**, *28* (21). DOI: 10.3390/molecules28217237 From NLM.

(70) Dong, Y.; Wu, Y.; Jiang, X.; Huang, X.; Cheng, Y.; Zhu, C. A polymer based fluorescent sensor for Zn2+ detection and its application for constructing logic gates. *Polymer* **2011**, *52* (25), 5811-5816. DOI: doi.org/10.1016/j.polymer.2011.10.034.

(71) Alam, M. W.; Islam Bhat, S.; Al Qahtani, H. S.; Aamir, M.; Amin, M. N.; Farhan, M.; Aldabal, S.; Khan, M. S.; Jeelani, I.; Nawaz, A.; et al. Recent Progress, Challenges, and Trends in Polymer-Based Sensors: A Review. *Polymers* **2022**, *14* (11), 2164.

(72) Saadatidizaji, Z.; Sohrabi, N.; Mohammadi, R. Development of a simple polymer-based sensor for detection of the Pirimicarb pesticide. *Scientific Reports* **2024**, *14* (1), 10293. DOI: 10.1038/s41598-024-60748-6.

(73) Sanjuán, A. M.; Reglero Ruiz, J. A.; García, F. C.; García, J. M. Recent developments in sensing devices based on polymeric systems. *React. Funct. Polym.* **2018**, *133*, 103-125. DOI: doi.org/10.1016/j.reactfunctpolym.2018.10.007.

(74) Liu, K.; Marin, L.; Xiao, L.; Cheng, X. Fluorescent multi-component polymer sensors for the sensitive and selective detection of Hg2+/Hg+ ions via dual mode fluorescence and colorimetry. *New J. Chem.* **2021**, *45* (48), 22888-22901, 10.1039/D1NJ04286F. DOI: 10.1039/D1NJ04286F.

(75) Guo, B.; Yao, Z.; Liu, L.; Wu, H.-C. Revealing different aggregational states of a conjugated polymer in solution by a nanopore sensor. *Chemical Science* **2016**, *7* (8), 5287-5293, 10.1039/C6SC00296J. DOI: 10.1039/C6SC00296J.

(76) Zlotnikov, I. D.; Ezhov, A. A.; Ferberg, A. S.; Krylov, S. S.; Semenova, M. N.; Semenov, V. V.; Kudryashova, E. V. Polymeric Micelles Formulation of Combretastatin Derivatives with Enhanced Solubility, Cytostatic Activity and Selectivity against Cancer Cells. *Pharmaceutics* **2023**, *15* (6). DOI: 10.3390/pharmaceutics15061613 From NLM.

(77) Tuga, B.; Ligocki, A. T.; Haynes, C. L. Leveraging Swelling Polymer Nanoparticle Reversibility for Cargo Loading. *ACS Applied Nano Materials* **2024**, *7* (6), 6616-6625. DOI: 10.1021/acsanm.4c00571.

(78) Zhou, J.; Li, H. Highly Fluorescent Fluoride-Responsive Hydrogels Embedded with CdTe Quantum Dots. *ACS Appl. Mater. Interfaces* **2012**, *4* (2), 721-724. DOI: 10.1021/am201624u.

(79) Ding, X.; Sheng, L.; Zhang, G.; Ji, M.; Li, Y. Conjugated Polymer-Based Hydrogel Film for a Fast and Sensitive Detection of Fe(III) in Vegetables. *Molecules* **2024**, *29* (5). DOI: 10.3390/molecules29050925 From NLM.

(80) Zhu, C. N.; Bai, T.; Wang, H.; Bai, W.; Ling, J.; Sun, J. Z.; Huang, F.; Wu, Z. L.; Zheng, Q. Single Chromophore-Based White-Light-Emitting Hydrogel with Tunable Fluorescence and Patternability. *ACS Appl. Mater. Interfaces* **2018**, *10* (45), 39343-39352. DOI: 10.1021/acsami.8b12619.

(81) Perera, K.; Nguyen, D. X.; Wang, D.; Kuriakose, A. E.; Yang, J.; Nguyen, K. T.; Menon, J. U. Biodegradable and Inherently Fluorescent pH-Responsive Nanoparticles for Cancer Drug Delivery. *Pharm. Res.* **2022**, *39* (11), 2729-2743. DOI: 10.1007/s11095-022-03317-8 From NLM.

(82) Zhang, A.; Jung, K.; Li, A.; Liu, J.; Boyer, C. Recent advances in stimuli-responsive polymer systems for remotely controlled drug release. *Prog. Polym. Sci.* **2019**, *99*, 101164. DOI: doi.org/10.1016/j.progpolymsci.2019.101164.

(83) Lin, Z.; Pan, H.; Tian, Y.; Tang, J.; Zhang, C.; Zhang, P.; Yang, H.; Chen, J. Photo-pH dual stimuli-responsive multicolor fluorescent polymeric nanoparticles for multicolor security ink, optical data encryption and zebrafish imaging. *Dyes Pigm.* **2022**, *205*, 110588. DOI: doi.org/10.1016/j.dyepig.2022.110588.

(84) Yamada, A.; Hiruta, Y.; Wang, J.; Ayano, E.; Kanazawa, H. Design of Environmentally Responsive Fluorescent Polymer Probes for Cellular Imaging. *Biomacromolecules* **2015**, *16* (8), 2356-2362. DOI: 10.1021/acs.biomac.5b00591.

(85) Darabi, A.; Jessop, P. G.; Cunningham, M. F. CO2-responsive polymeric materials: synthesis, self-assembly, and functional applications. *Chem. Soc. Rev.* **2016**, *45* (15), 4391-4436, 10.1039/C5CS00873E. DOI: 10.1039/C5CS00873E.

(86) Liu, H.; Lin, S.; Feng, Y.; Theato, P. CO2-Responsive polymer materials. *Polym. Chem.* **2017**, *8* (1), 12-23, 10.1039/C6PY01101B. DOI: 10.1039/C6PY01101B.

(87) Mabire, A. B.; Brouard, Q.; Pitto-Barry, A.; Williams, R. J.; Willcock, H.; Kirby, N.; Chapman, E.; O'Reilly, R. K. CO2/pH-responsive particles with built-in fluorescence read-out. In *Polymer Chemistry*, Royal Society of Chemistry: 2016; Vol. 7, pp 5943-5948.

(88) Zhang, D.; Fan, Y.; Chen, H.; Trépout, S.; Li, M.-H. CO2-Activated Reversible Transition between Polymersomes and Micelles with AIE Fluorescence. *Angew. Chem. Int. Ed.* **2019**, *58* (30), 10260-10265. DOI: doi.org/10.1002/anie.201905089.

(89) Zhang, D.; Fan, Y.; Chen, H.; Trépout, S.; Li, M. H. CO2-Activated Reversible Transition between Polymersomes and Micelles with AIE Fluorescence. In *Angewandte Chemie International Edition*, 2019; Vol. 58, pp 10260-10265.

(90) Wang, Y.; Huo, M.; Zeng, M.; Liu, L.; Ye, Q. Q.; Chen, X.; Li, D.; Peng, L.; Yuan, J. Y. CO_2-responsive Polymeric Fluorescent Sensor with Ultrafast Response. In *Chinese Journal of Polymer Science English Edition*, 2018; Vol. 36, pp 1321-1327.

2 Development of fluorescent pH-responsive nanoparticles and their CO_2 responsiveness

2.1 Abstract

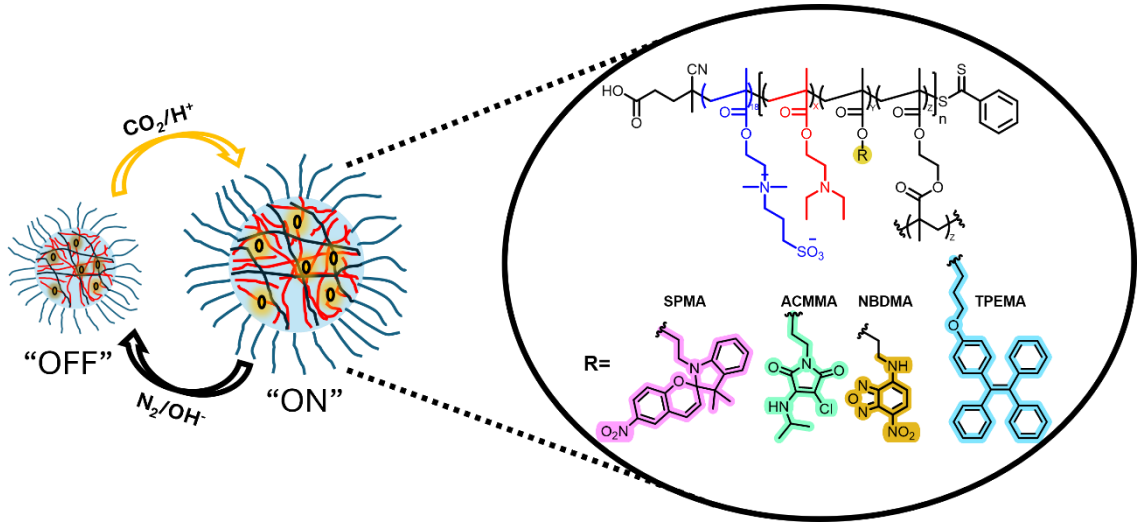

The detection of carbon dioxide is a major challenge in both industrial and domestic environments. Detecting fluctuations in carbon dioxide by switching "on" fluorescence in aqueous environments has often been targeted for efficient monitoring. Moreover, this switching "on" needs to occur over brief time periods to be useful. Here, four different CO_2-responsive polymeric nanoparticles are produced by RAFT emulsion polymerization. Each system shares the same pH responsive unit (DEAEMA), crosslinker (EGDMA) and macro-CTA (PDMAPs) but has a different fluorescent dye. The pH of these polymeric nanoparticles is reduced upon the addition of carbon dioxide to the aqueous environment, due to the chemical equilibrium between the tertiary amine groups and the generated HCO_3^- *in situ*. This can be used as a stimulus to induce conformational changes to the system that in turn enhance fluorescence, allowing easy detection.[1-4] Here, we report the synthesis of four pH-responsive polymer nanoparticles that contain four different dyes moieties (NBDMA, ACMMA, SPMA and TPEMA). These nanoparticles respond the presence of CO_2 and rapidly turn on by changing the polarity of the environment around the dye.

2.2 Introduction

As stated in chapter 1, pH-responsive polymers are recognized for their capacity to accept or donate protons in response to pH changes, leading to structural modifications.[5] These polymers are typically synthesized from monomers containing tertiary amine derivatives, which can react with both strong and weak acids. The literature describes a wide array of pH-responsive polymers, including linear homopolymers, amphiphilic block copolymers,[6] star,[7] branched,[8, 9] polymer brushes,[10] nanogels[11] and hydrogels (microgels),[12, 13] each tailored for specific applications. One way to induce pH changes is by dissolving CO_2 in water, where it forms carbonic acid, a weak acid that can dissociate into bicarbonate, carbonate, and hydrogen ions, facilitating the protonation of the amine monomer. This protonation can function as a stimulus to trigger changes in the polymer's physicochemical properties such as size variation, making it a potential CO_2 sensor.[14, 15]

One of the most used physicochemical properties for sensing pH-responsive polymers is fluorescence. By incorporating fluorescent monomers, these polymers can exhibit emission changes.[14, 16-19] This variation in fluorescence is primarily caused by the change in solution polarity when dissolved CO_2 reacts with the amine monomer DEAEMA. As DEAEMA becomes protonated and more hydrophilic, the hydrodynamic diameter of the particles increases, while fluorescence decreases, as the fluorophore is sensitive to polarity changes within the particle (figure 2.1).

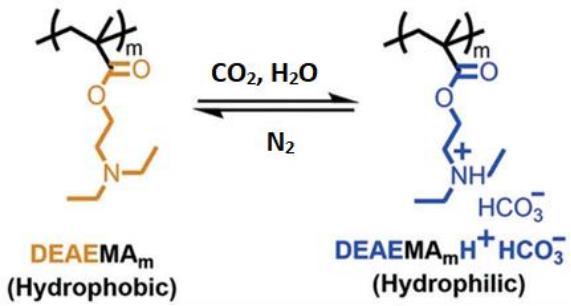

Figure 2.1. Reversible equilibrium of DEAEMA monomer under CO_2 and N_2. Figure taken from ref.

Four fluorescent monomers have been investigated as promising fluorescence probes due to their reported use in several CO_2 fluorescent responsive systems. These include halogen maleimide (AXM) derivatives,[1, 20, 21] spyropyran derivatives (SP),[22] tetraphenylethenil (TPE) derivatives and 7-nitro-2,1,3-benzoxadiazole (NBD) derivatives (Figure 2.2).[23] Most of these molecules share a common feature: they undergo a photoinduced electron transfer (PET) process when employed as fluorescence sensors, a phenomenon that has been extensively studied in recent years.[24]

One of the dye groups we chose to work with is maleimides. These dyes are primarily known for their small size, which allows for easy integration into various polymer and nanoparticle structures without compromising the integrity of the framework.[25] Depending on the solvent, they can emit fluorescence in the range of 458-478 nm due to a solvafluorochromism effect.[20] Moreover, their chemistry is very versatile, their synthesis is facile and particularly, they are characterized by their strong fluorescent properties.[22] As a result, they have been used widely in several fields such as fluorescent linkers in protein-labelling[26] and more recently in gas-sensing.[1] Normally, they undergo quenching of fluorescence when exposed to CO_2 and increase in the quantum yield when purging with an inert gas. In addition, the O'Reilly group has previously worked in the study of maleimide dyes. This experience will be suitable and advantageous for this project.

The second group of dyes we aimed to explore were derivatives of 7-nitro-2,1,3-benzoxadiazole (NBD). These NBD molecules exhibit remarkable characteristics, such as polar sensitivity, compact size, strong fluorescence, and high reactivity.[27, 28] NBD

amines (NBD-NHR) typically emit light above 420 nm, with their fluorescence resulting from intramolecular charge transfer (ICT) transitions.[28] What makes NBD dyes particularly intriguing is their versatility; they can be easily modified by exchanging one of their substituents for various alternatives. This flexibility, combined with their polarity sensitivity, influences their emissive properties. They have previously been incorporated into pH-responsive polymers. For instance, Wang et al. developed a reversible fluorescent micelle sensor that responded rapidly to CO_2, demonstrating enhanced fluorescence, excellent reversibility, and suitability for use in responsive particles as fluorophores.

Another interesting group of dyes we wanted to explore were the spiropyran (SP) derivatives. Spiropyrans are photochromic units that adopt a colorless spiropyran (SP) form in the dark or under visible light, whereas it spontaneously converts to the colored and fluorescent merocyanine (MC) form upon UV irradiation. Moreover, this dye also presents acidochromism, this means, this reversible transition from the SP and MC forms can be induced by pH changes (figure 2.2). For this reason, they have been used in many applications such as polymeric latex particles, modulation of stem cell attachment and, most remarkable, modulation of organic and inorganic nanoparticles fluorescence.[29, 30]

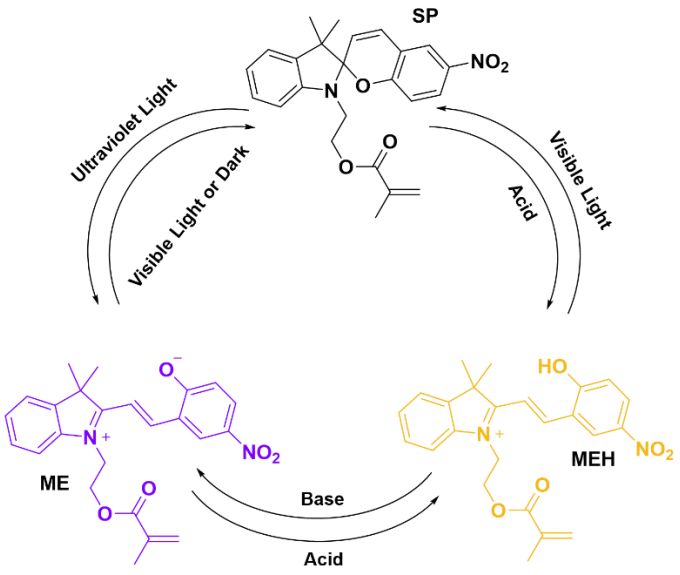

Figure 2.2. Reproduced scheme of equilibrium reactions and different forms of the spiropyran after interaction with light or pH. Figure reproduced from ref.[31]

Finally, tetraphenylethene (TPE) derivatives are one widely studied group of luminogens that undergo a phenomenon called aggregation-induced emission (AIE).[16] An enormous amount of research has been conducted on these systems due to their ease of synthesis, ease of functionalization, high stability, aromaticity and high fluorescence quantum yield.[32] As a result of these features, they have been used in fluorescent sensors for D-glucose detection[33] and OLEDs[33] due to their excellent optical performance. One interesting aspect of these molecules is, that in order to give a fluorescence read-out they have to undergo an AIE[34] process, thus, they are used for inducing an increased fluorescence signal by the formation of aggregates.

The main aim of this PhD is to monitor and report the release of gases, specifically carbon dioxide (CO_2), that are released into the atmosphere, from pipelines, with a target to reduce emissions. Nitrogen (N_2) is equally of interest as it is pumped through top-side empty pipes, prior to implementation to detect leaks. The challenge with the detection of all these gases is that emission concentrations are low and hence something is needed to magnify the signal. To address this challenge, we propose investigating fluorescent responsive nanoparticles that exhibit a notable change in visual fluorescence upon interaction with CO_2, enabling their use as potential sensors for monitoring leaks in pipelines.

To achieve the main goal of this project, this chapter will focus on two main aspects. Firstly, the synthesis of fluorescent cross-linked CO_2-responsive nanoparticles is a primary focus. This involves developing and synthesizing fluorescent nanoparticles using various fluorescent monomers, as illustrated in figure 2.2.

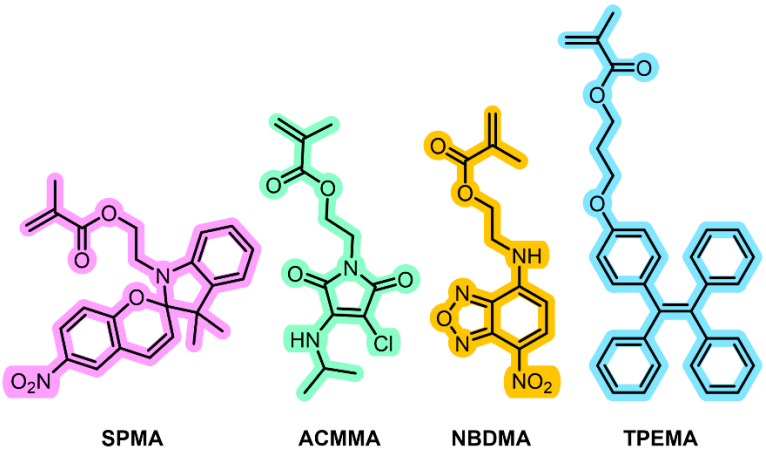

Figure 2.3. Target fluorescent monomers to be synthesized for CO_2 detection.

Secondly, a thorough characterization of the synthesized nanoparticles' properties is essential. This includes measuring and analyzing the size distribution of the nanoparticles. Investigating the pH sensitivity is also crucial to understand how it affects the fluorescence and size properties. Additionally, the fluorescent properties, such as intensity, wavelength, and responsiveness to CO_2 exposure, must be assessed. Moreover, examining their reversibility with N_2.

By addressing these areas, the project aims to develop a robust and effective CO_2-sensing system using fluorescent nanoparticles, enhancing the ability to monitor and detect leaks in pipeline infrastructure.

2.3 Results and Discussion

2.3.1 Synthesis and characterization of crosslinked fluorescent pH responsive nanoparticles

Aiming to incorporate the several fluorescent monomers into a nanoparticle system similar to one our group had developed in previous years,[1] we chose a well-studied pH-responsive nanoparticle system from our earlier research.[35] The initial step was the synthesis of the PDMAPs macro-CTA.

Scheme 2.2. Representation for the synthesis of **mCTA$_{BM}$** by the RAFT polymerization of DMAPS using BM1433 as the CTA and 4,4'-azobis(4-cyanovaleric acid) (ACVA) as the radical initiator.

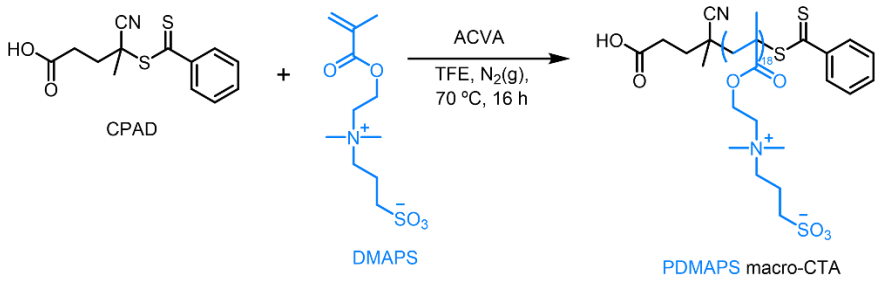

Following purification by dialysis against deionized water and lyophilization, molecular weight and CTA end group fidelity of the resulting **mCTABM** were characterized by aqueous size-exclusion chromatography (SEC) (figure 2.4) and ^{1}H NMR (figure 2.5). This analysis revealed that the **mCTABM** was obtained within the desired range of molecular weight (~18 units of DMAPS), with a narrow molecular weight distribution ($Đ_M$) (M_w = 5.5 kDa, M_n = 5.2 kDa, $Đ_M$ = 1.06). Also, the good overlap between the refractive index (RI) and the ultraviolet (UV) signal confirmed the retention of trithiocarbonate end-group originating from the CTA and which would allow for further chain extension by RAFT process.

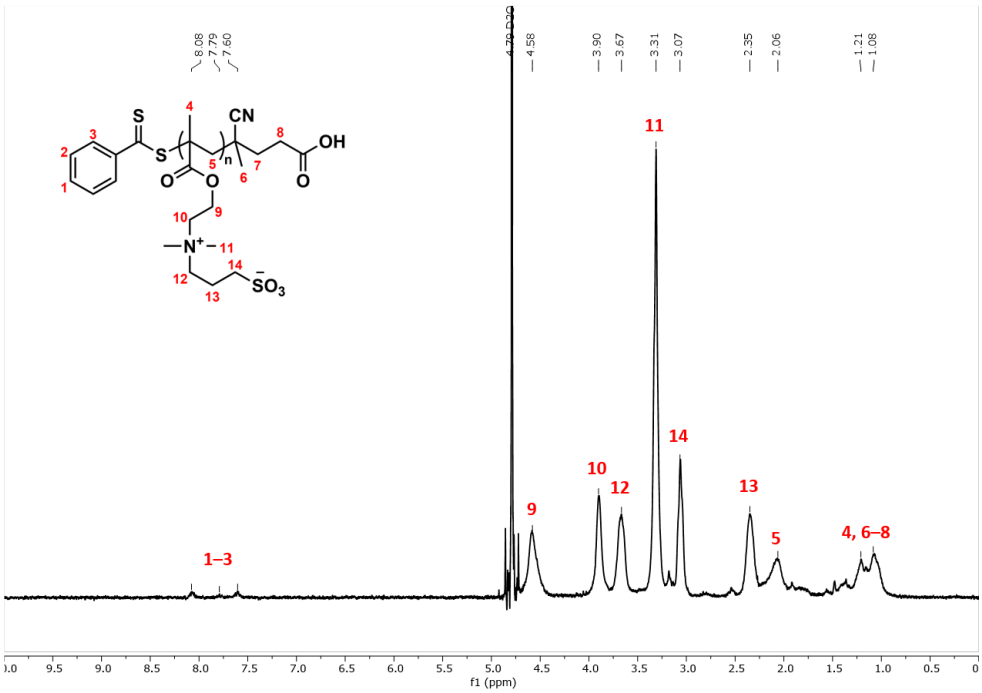

Figure 2.4. ^{1}H-NMR spectrum of poly(N,N'-dimethyl(methacryloylethyl)ammonium propane sulfonate) (PDMAPS) steric stabilizer in D_2O containing 0.5 M NaCl.

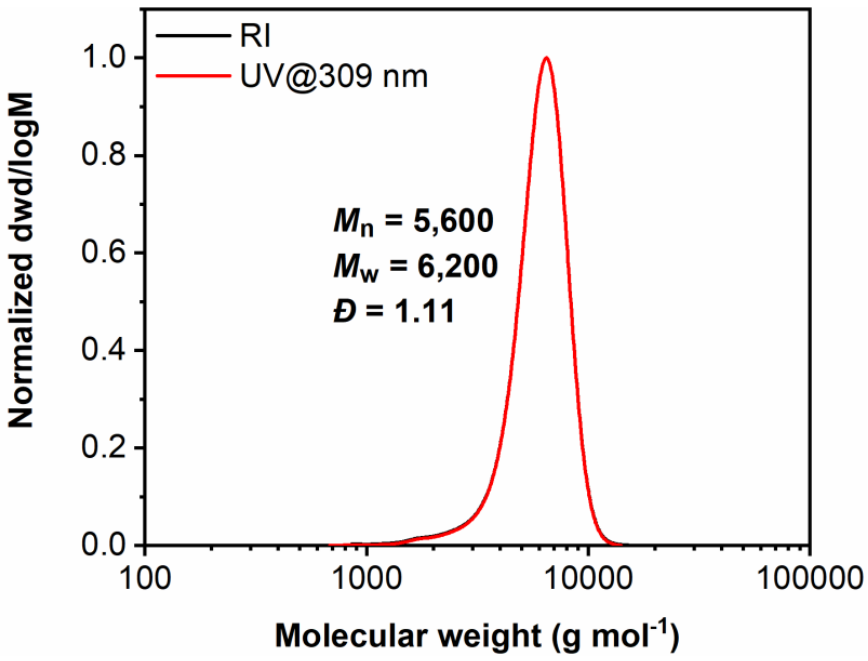

Figure 2.5. Normalized SEC RI (black trace) and SEC UV (red trace, λ = 309 nm) molecular weight distributions for PDMAPS macro-CTA, along with corresponding M_n,

M_w, and Đ values calculated based on PEG standards using H_2O:MeOH (80:20) + 0.1 M $NaNO_3$ as the eluent.

To obtain crosslinked fluorescent nanoparticles, we used the synthesized $PDMAPS_{18}$ macro-CTA as a steric stabilizer in the RAFT-mediated emulsion copolymerization of diethylaminoethyl methacrylate (DEAEMA), ethylene glycol dimethacrylate (EGDMA), and the fluorescent dyes, which comprised 1% of the total solid content (figure 2.5).

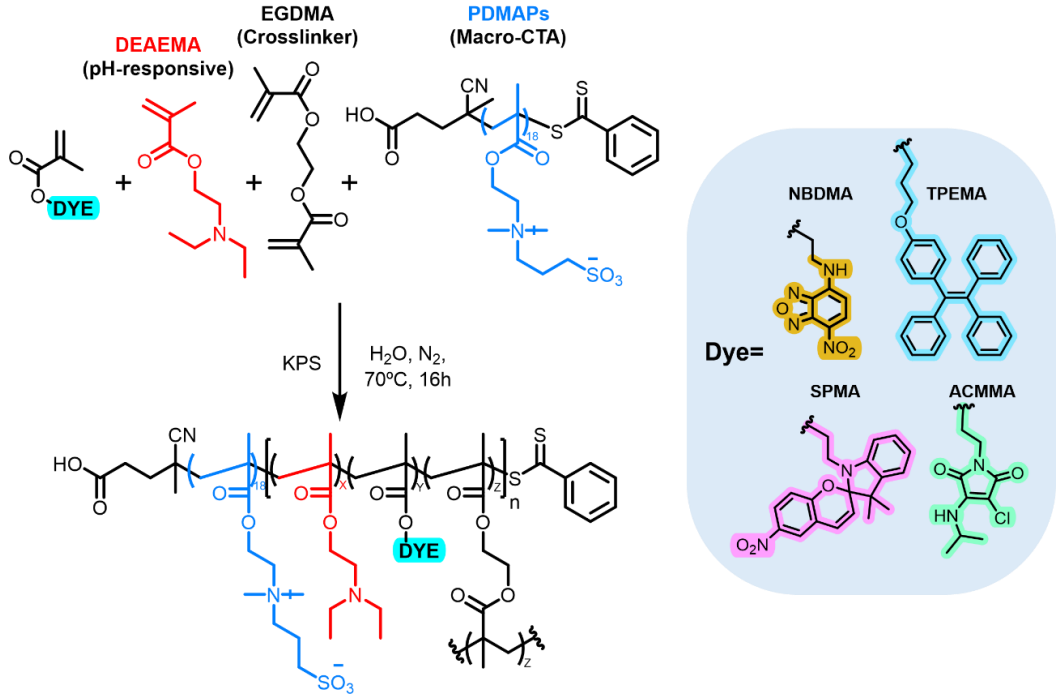

Figure 2.6. Synthesis of 5 wt% spherical nanoparticles by RAFT emulsion polymerization with 1 wt% of the total solid content of the dye.

This polymerization was conducted at 70°C for 16 hours in deionized water, with potassium persulfate (KPS) as the radical initiator, resulting in a yellow aqueous dispersion with a 5 wt. % solids content. DEAEMA provided pH responsiveness, while the different dyes enabled fluorescence read-out of the nanoparticles' state. RAFT-mediated emulsion copolymerization was chosen for its ability to produce well-dispersed nanoparticles in an aqueous medium and for its superior control over the polymerization process and monomer placement compared to other methods.[36]

Table 2.1: Nomenclature of nanoparticles with different dyes.

	Nanoparticles nomenclature
NBDMA	*NP-NBDMA*
ACMMA	*NP-ACMMA*
SPMA	*NP-SPMA*
TPEMA	*NP-TPEMA*

The reaction conversion was determined using TGA by measuring the percentage weight loss of volatiles of 200 µL of crude sample at 250 ºC by triplicate and comparing it to the initial target of 5.34 wt%. The resulting conversions ranged from 50% to 65% across different sets of nanoparticles (Table 2.2). These conversion rates are consistent with those reported in the literature for non-fluorescent pH-responsive systems, which typically reach around 65%. The slightly lower conversion rates observed in some cases may be attributed to differences in the solubility of the fluorescent dye in the reaction medium.

Table 2.2: Comparison of results from thermogravimetric analysis of different nanoparticles.

	NP-NBDMA	***NP-ACMMA***	***NP-SPMA***	***NP-TPEMA***
Target wt%	5.34	5.34	5.34	5.34
Wt % after TGA	2.60 ± 0.03	3.50 ± 0.05	3.10 ± 0.02	2.90 ± 0.03
% conversion (TGA)	50%	65%	58%	54%

The emulsions were purified by extensive dialysis using a 1 kDa membrane. The resulting aqueous particle formation was characterized by dynamic light scattering (DLS) and dry-state transmission electron microscopy (TEM) revealing the successful formation of uniform spherical PDEAEMA-based core-shell nanoparticles.

$$\% \, Conversion = \frac{Final \; wt \; \% \; (TGA)}{Initial \; wt \; \%} x100$$

Equation 2.1. General % conversion equation by TGA of nanoparticles.

To demonstrate the incorporation of the fluorescent dye into the particle formation, Fourier-transform infrared spectroscopy (FTIR) and Ultraviolet-Visible (UV-Vis) absorption analysis were accomplished. In this case we took as example the NP-NBDMA. The FTIR spectrum showed the vibrational energies at 3400 cm^{-1} (N-H) and 1379 cm^{-1} (N-O) of the characteristic bands of the NBDMA dye (figure 2.7a). Moreover, we measured the UV-Vis spectra of both nanoparticles with and without the dye. The first showed a single peak at 299 nm, whereas the second showed an additional peak at 455 nm. This confirmed the incorporation of the NBDMA monomer into the particle system (figure 2.7b). In addition, the obtained yellow emulsion was excited at 470 nm and an emission peak was observed at 550 nm was observed, as stated in the literature.[23]

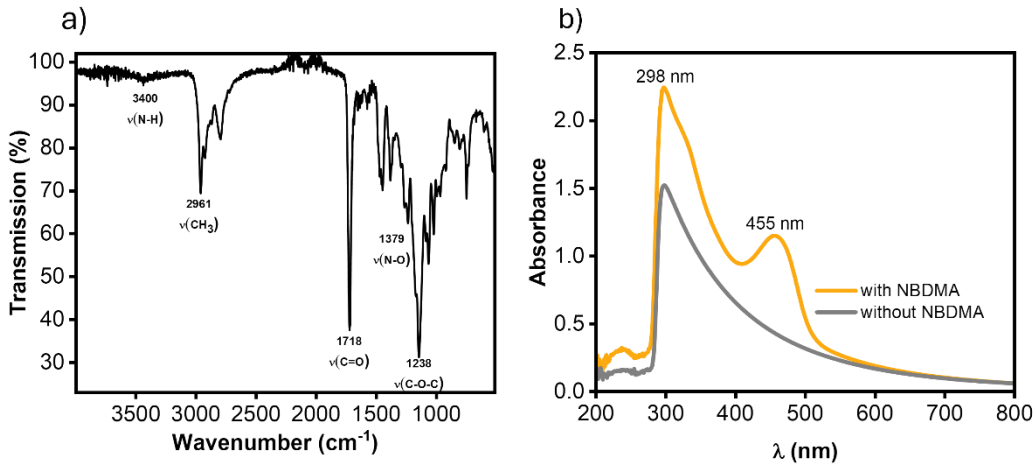

Figure 2.7. (a) FTIR of freeze-dried fluorescent nanoparticles. (b) UV-Vis spectrum of reference nanoparticles (without NBDMA) and fluorescent nanoparticles (with NBDMA) in DI water. Concentration 0.1 mg/mL.

2.3.2 Size properties and pH-responsiveness study of different nanoparticle systems and comparison

2.3.2.1 NP-NBDMA

DLS results at pH=7 showed an average hydrodynamic radius (D_h) of around 226 nm with a parallel polydispersity (PD) of 0.04 showing good concordance between the relative intensity, volume, and number size distributions (figure 2.8a). The uniformity of the particle formulation was confirmed by the autocorrelation function obtained by DLS (figure 2.8b). This data correlates with the acquired dry-state TEM images, which confirmed the formation of spherical nanoparticles of uniform size (figure 2.8c). The corresponding histogram of size distribution for the PDEAEMA-based nanoparticles was obtained by analyzing the TEM data which suggested an average diameter (D_{ave}) of 146 ± 18 nm (figure 2.8d).

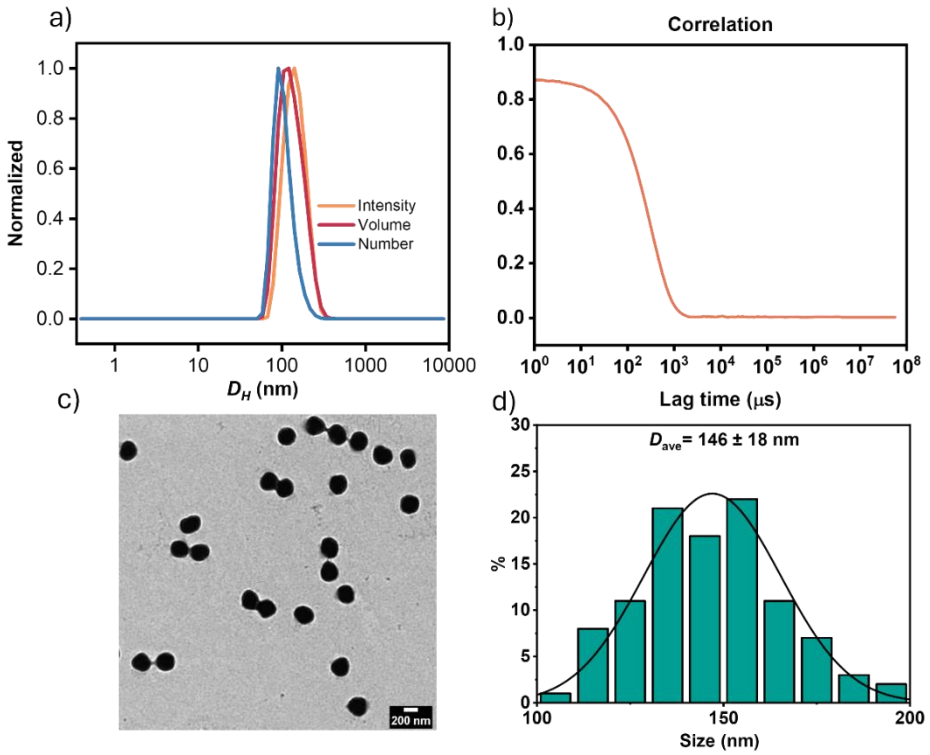

Figure 2.8. (a) DLS analysis of NP-NBDMA at pH 7. (b) Correlogram of NP-NBDMA at Ph 7. (c) TEM image of NP-NBDMA at pH 7, stained with uranyl acetate. (d) Corresponding histogram showing size distribution of NP-NBDMA measured by TEM.

We wanted to observe the size variation against the pH. According to previous systems developed already discussed in the introduction, we expected the diameter to increase at acidic pH and decrease at basic pH. This is, in acidic conditions the tertiary amines present in the core of the particles become protonated, causing them to swell. The opposite effect takes place under basic conditions, where the polymer becomes hydrophobic and the particles collapse. Therefore, a batch of samples with concentration 0.3 mg/ml were prepared at several pHs to study the size behavior. DLS was utilized to monitor changes in the particle diameter in response to pH changes.

DLS analysis showed two different populations in terms of size. One between pH 7.5 to 13.5, where the particle's size collapsed (around 120-140 nm), and at low pH where there is a size variation (210-240 nm). On the other hand, it was expected to get the highest diameter of the particle at pH 1 (211 ± 2 nm), but this was observed at pH 5.6 (251 ± 1 nm) instead (figure 2.9i). This is due to the protonation of the DEAEMA in acidic condition. These amine groups become positively charged, increasing the hydrophilicity of the system, causing electrostatic repulsion between protonated groups and this leads to a swelling effect in the nanoparticles. Once the size variation of the particles against the pH was observed, we moved forward to study their fluorescent behavior against the particle's size due to pH modification.

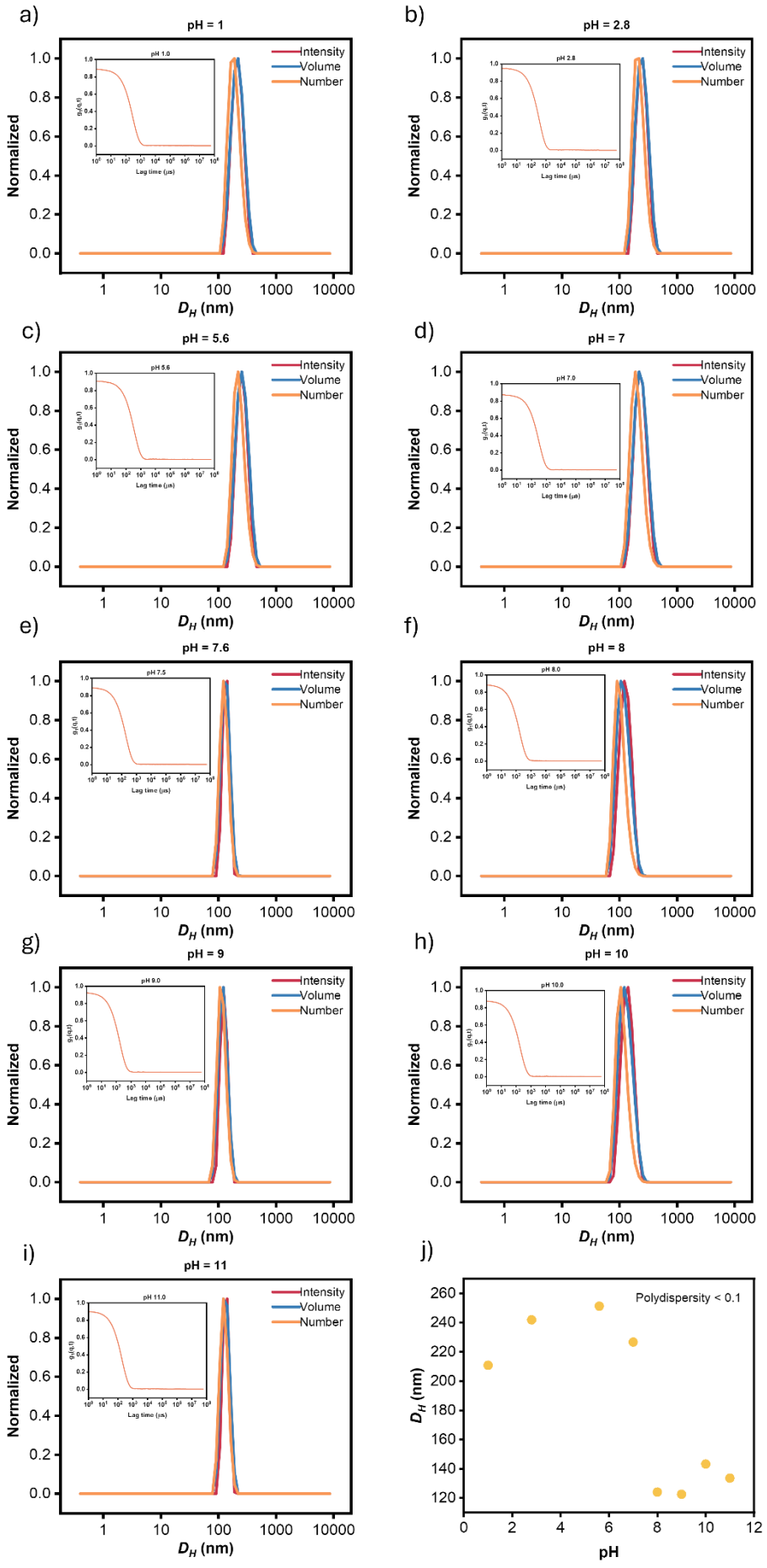
a)
pH = 1
b)
pH = 2.8
c)
pH = 5.6
d)
pH = 7
e)
pH = 7.6
f)
pH = 8
g)
pH = 9
h)
pH = 10
i)
pH = 11
Intensity
Volume
Number
Normalized
D_H (nm)
j)
Polydispersity < 0.1
pH

Figure 2.9. DLS graphs of NP-NBDMA: (a) pH 1. (b) pH 2.8. (c) pH 5.6. (c) pH 7. (e) pH 7.6. (f) pH 8. (g) pH 9. (H) pH 10. (i) pH 11. (J) Size variation vs pH of NP-NBDMA.

Consequently, when we studied the fluorescence properties with pH variation, we observed an increasing tendency in fluorescence when the particle size increased and a decrease of fluorescence when the size decreased (figure 2.10b). As a result, the most emissive particles were the ones at pH 5.6 (251 nm) and the least emissive were the ones at pH 10 (143 nm) (figure 2. 10a). The drop in size was translated into a quenching effect of the fluorescent dye in the particles, inversely, the swell effect of the particles is transcribed in a higher polar solution what for this dye leads to a more fluorescent environment.

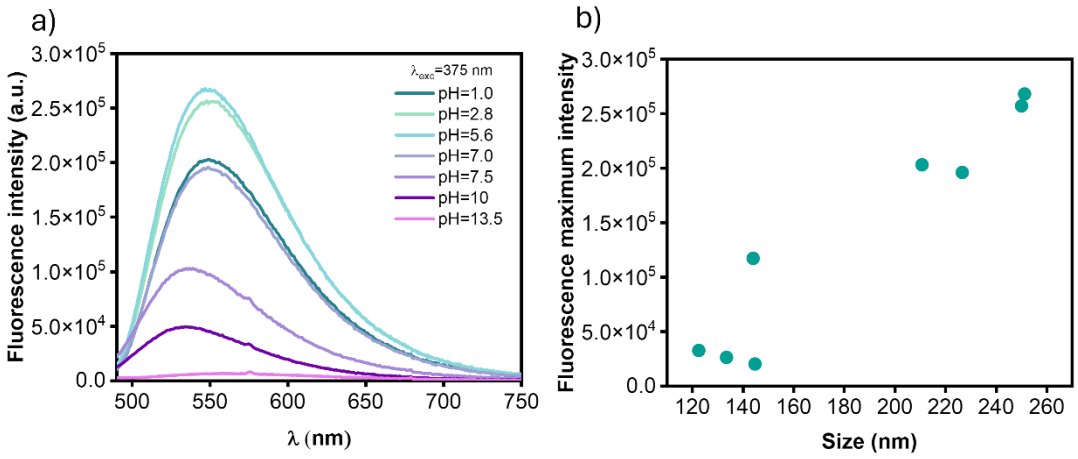

Figure 2.10. (a) Emission spectrum of NP-NBDMA at pH 1, 2.8, 5.6, 7.0, 7.5, 8.0, 9.0, 10.0, 13.5. (b) Graph representing the relation between fluorescence maximum intensity of NP-NBDMA vs their size variation derived from pH modification.

2.3.2.2 NP-ACMMA

The obtention of spherical nanoparticles of average diameter of 268 ± 17 nm (figure 2.11c) was confirmed by DLS (figure 2.11a) and dry-state TEM revealing the successful formation of uniform spherical PDEAEMA-based core-shell nanoparticles (figure 2.11b).

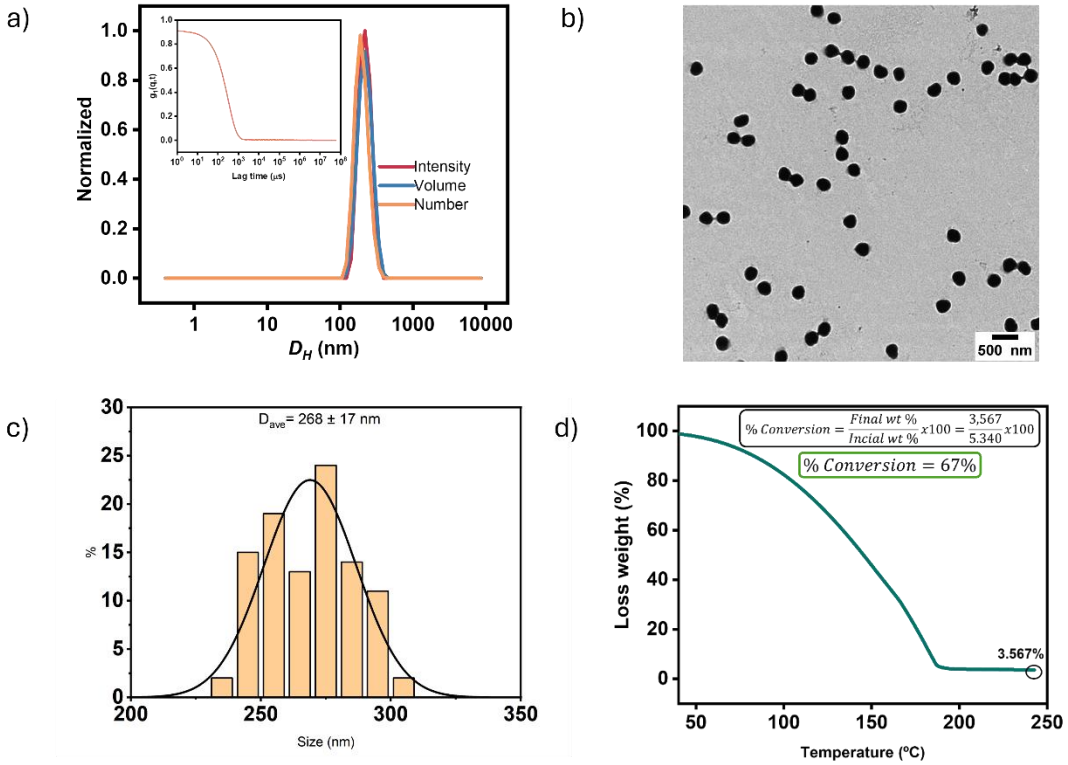

Figure 2.11. (a) DLS analysis of particles at pH 7. (b) TEM image of nanoparticles at pH 7, stained with uranyl acetate. (c) Corresponding histogram showing size distribution of nanoparticles measured by TEM. (d) Thermogravimetric plot of Loss weight against temperature to calculate the % conversion (67%) in 200 µl of crude nanoparticles of concentration 5.34 wt%.

The size variation of the nanoparticles as a function of pH was evaluated by titrating a 0.3 mg/mL sample from acidic to basic pH. Between pH 2.7 and 4.4, the nanoparticles' size ranged from 450 to 480 nm. As the pH increased to more basic values, the size decreased to an average diameter of 218 nm between pH 4.9 and pH 10 (figure 2.12b).

This particle system showed a more uniform response compared to the previous one, suggesting higher stability, likely due to the higher conversion rate obtained.

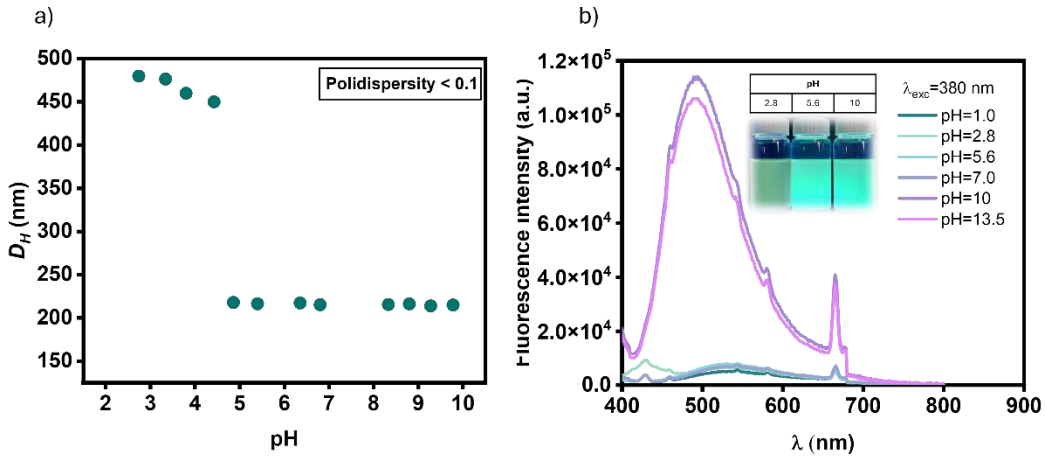

Figure 2.12. (a) DLS-titration experiment of PDMAPS-b-P(DEAEMA-*co*-EGDMA-*co*-ACMMA) nanoparticles. Concentration 1 mg/mL in DI water. (b) PDMAPS-b-P(DEAEMA-*co*-EGDMA-*co*-ACMMA fluorescence spectrum at pHs 1.0, 2.8, 5.6, 7.0, 10 and 13.5. Concentration 0.3 mg/mL. λ_{exc}= 380 nm. λ_{em}= 500 nm.

The fluorescence response with pH showed to be different in this case. While in the previous system the nanoparticles became more fluorescent as the pH was more acidic, in this case the more emissive nanoparticles were the ones at pH 10 and 13.5, therefore the less hydrophilic were the particles, this is the smaller, the more fluorescence they were (figure 2.12a). This is due to the way the change in polarity affects the ACMMA dye.

2.3.2.3 NP-SPMA

The resulting aqueous particle formation was characterized by dynamic light scattering (DLS) at different pHs and dry-state transmission electron microscopy (TEM) revealing the successful formation of uniform spherical PDEAEMA-based core-shell nanoparticles (figure 2.13)

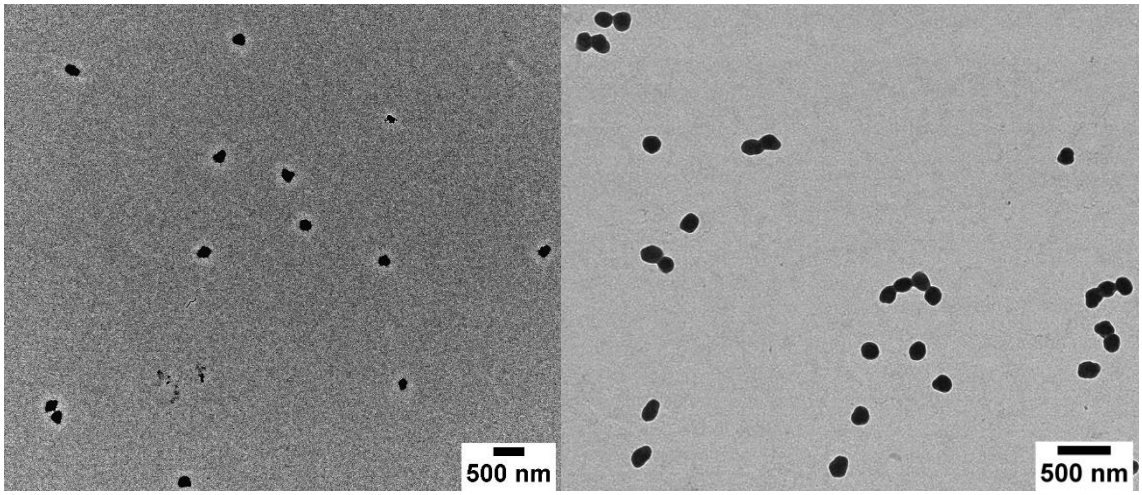

Figure 2.13. Representative dry-state TEM images of NP-SPMA.

In the DLS-titration experiment, we observed how the size of spherical nanoparticles changed with variations in system polarity. Initially, from pH 2.2 to pH 3.9, the nanoparticles maintained a diameter of 278 nm. As the pH increased, their size reached a maximum value of 357 nm between pH 4.4 and 6.8. Finally, at pH levels above 7.8, the average diameter reduced to 163 nm (figure 2.14). This demonstrates that an increase in polarity, associated with a shift from basic to acidic pH, leads to a corresponding increase in nanoparticle size. However, when the pH drops below 4, the particles begin to lose their structural stability and ultimately collapse. This destabilization can be attributed to several factors, including alterations in the buffer concentration, shifts in ionic strength, and the increased incorporation of charged species. These changes disrupt the delicate balance of forces maintaining particle integrity, leading to aggregation or disassembly.

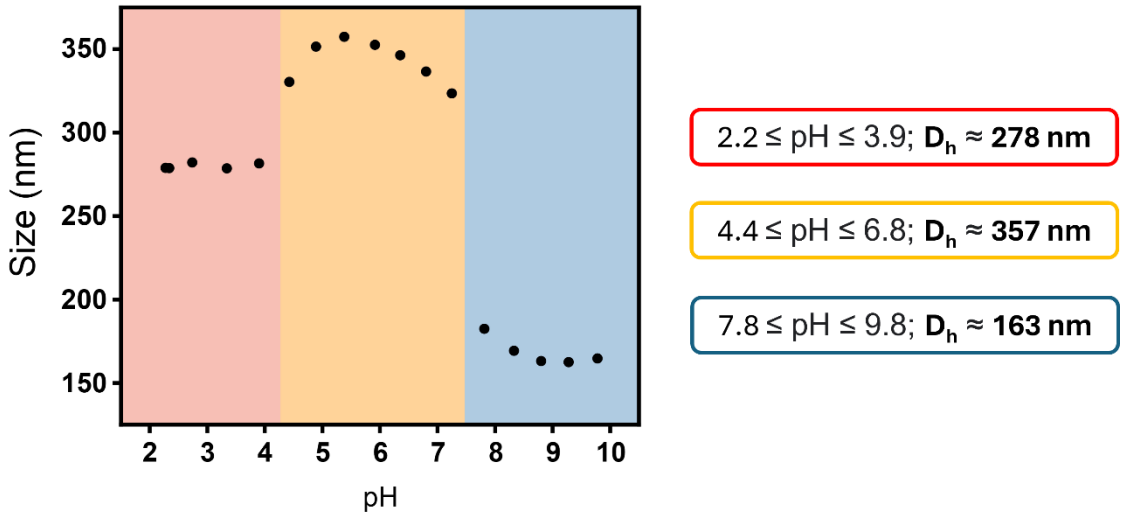

Figure 2.14. DLS-titration experiment of NP-SPMA Fluorescent Nanoparticles. Concentration 1 mg/mL in DI water.

Once the size characterization of the nanoparticles was done, the next step was the study of the possible changes in fluorescence with disruption in pH. For that, we measured the fluorescence intensity of the nanoparticles at concentration 1 mg/mL in DI water at 3 different pHs, 2.5, 4.9 and 7.9 to cover the 3 different regions that we observed in the DLS-titration. We could observe that the fluorescence intensity was decreasing as the pH was decreasing, while also a red shift in wavelength occurred. The qualitative fluorescence of the system seemed to change from a brighter pink to a more 'off' state (figure 2.15). We thought this was due to not only the change in polarity effect in the nanoparticles due to the protonation of the DEAEMA moiety, but also due to an equilibrium between the ring-opened and ring-closed of the SPMA moiety. suggesting higher stability, likely due to the higher conversion rate obtained.

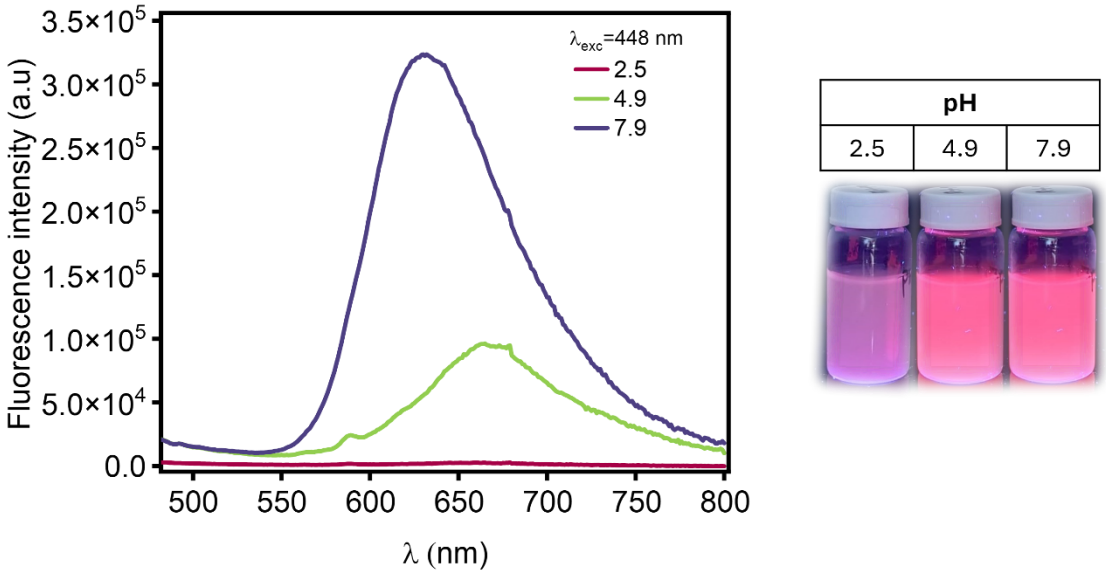

Figure 2.15. Emission spectrum of NP-SPMA pH-Responsive Fluorescent Nanoparticles at pH 2.5, 4.9 and 7.9. Concentration 1 mg/mL. λ_{exc}= 350 nm. λ_{em}= 640 nm.

The fluorescence response with pH showed to be different in this case. While in the previous system the nanoparticles became more fluorescent as the pH was more acidic, in this case the more emissive nanoparticles were the ones at pH 7.9, therefore the less hydrophilic were the particles, the smaller, the more fluorescence they were. We thought this not only by the pH responsiveness of the SPMA dye but algo due to their light switching between the ring-opened and ring-closed forms.

We did not perform a full characterization of this nanoparticle system, as we did for SP-NBDMA and SP-ACMMA, due to interference between fluorescence and color change stability, which made it unsuitable for the application.

2.3.2.4 NP-TPEMA

Continuing with a similar modus-operandi, we proceeded to evaluate the size properties of the NP-TPEMA system as we did for the previous systems. We proceeded to evaluate the changes in morphology with pH and observe a similar response in comparison to the previous systems. As expected, the size increases to a more acidic pH as can be observed in figure 2.16b, where the system becomes more hydrophilic and decreases at basic pHs while the opposite effect takes place.

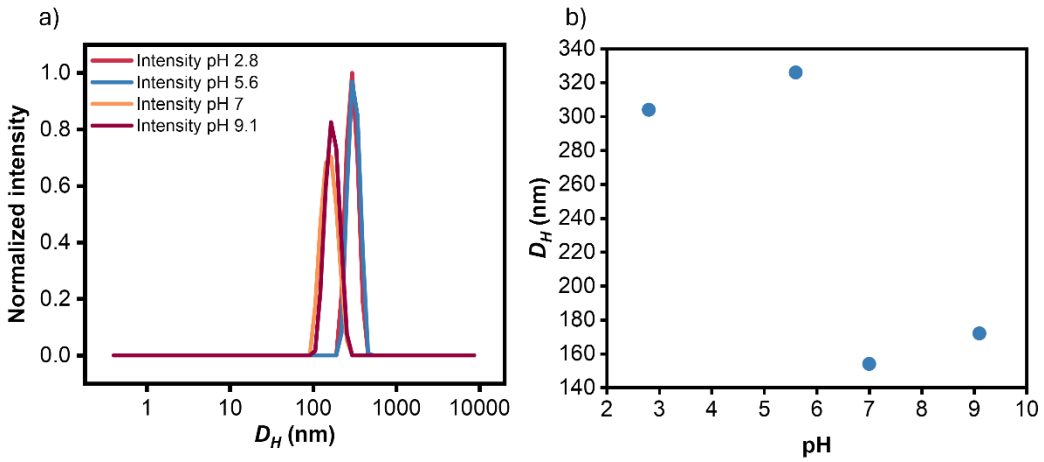

Figure 2.16. (a) DLS normalized intensity of NP-TPEMA at pHs 2.8, 5.6, 7 and 9.1. (b) Size variation of NP-TPEMA with pH. Concentration of 1 mg/mL.

The fluorescence properties of these nanoparticles were also investigated. Samples were prepared at different pH levels, and their emission was measured. The nanoparticles exhibited an emissive peak around 450 nm. The highest fluorescence intensity was observed at pH 7.4 and 5.6. As the pH increased or decreased from these values, the fluorescence intensity diminished, reaching its lowest point at pH 1 (figure 2.17b).

Additionally, the emission curve resolution showed background noise, and the fluorescence did not follow a consistent trend, as shown in figure 2.17a. After leaving the nanoparticles overnight, they precipitated, due to the instability of the system due to the high hydrophobicity of the TPEMA monomer and its aggregation properties (figure 2.18).

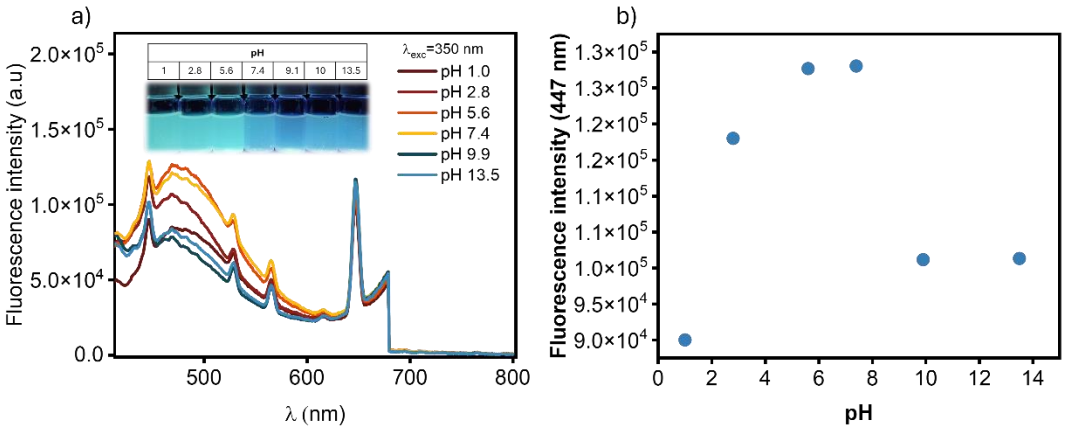

Figure 2.17. (a) Fluorescence spectra of NP-TPEMA at pHs 1.0, 2.8, 5.6, 7.4, 9.9 and 13.5. (b) Graph of Fluorescence intensity of NP-TPEMA at 447 nm vs pH. Concentration of 0.3 mg/mL. λ_{exc}= 350 nm. λ_{em}= 450 nm.

Even though the TPEMA monomer had interesting properties for potential CO_2 sensing, the lack of stability of this system made us discard these nanoparticles to go forward in deep studies.

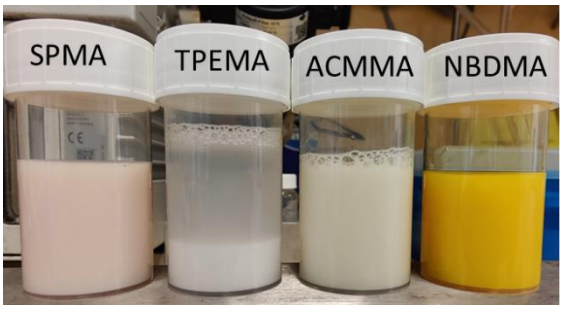

Figure 2.18. Picture of dialyzed nanoparticles without pH modification. From left to right: NP-SPMA, NP-TPEMA, NP-ACMMA and NP-NBDMA.

We did not perform a full characterization of this nanoparticle system, as we did for SP-NBDMA and SP-ACMMA, due to lag of stability of the nanoparticles as we can see in figure 2.18, probably due to the highly hydrophobic character of the TPEMA monomer.

2.3.2.5 Size properties comparison

After examining the responsiveness of the nanoparticle systems, we observed that all four exhibited comparable size variations in response to pH changes. As the pH decreased, leading to increased protonation of DEAEMA, the nanoparticles became more hydrophilic, resulting in an increase in size.

In terms of fluorescence response to pH variation, the nanoparticles could be categorized into two groups. The first group, consisting of NP-ACMMA and NP-SPMA, showed similar behavior where fluorescence intensity increased as pH rose. Specifically, NP-SPMA exhibited a gradual increase in emissions from pH 2.8 to 8, while NP-ACMMA displayed a sharp increase in emission between pH 7 and 10.

On the other hand, NP-NBDMA and NP-TPEMA showed an increase in fluorescence emission as the pH decreased, along with noticeable visual changes in fluorescence. The NP-NBDMA system, which incorporated the NBD-derived dye, experienced a dramatic 40-fold increase in fluorescence emission from pH 13.5 to 5.6, where it reached its maximum. In contrast, NP-TPEMA only exhibited a 1.5-fold increase. Unfortunately, the NP-TPEMA system lacked stability, making it less ideal for further application.

2.3.3 Size properties and CO_2-responsiveness study of different nanoparticles system and comparison

As discussed earlier in the pH-responsiveness study, only the polymers NP-NBDMA, NP-ACMMA, and NP-SPMA demonstrated promising potential for use in CO2 sensing, whereas the NP-TPEMA system lacked stability. Therefore, this section will focus exclusively on the three previously mentioned systems.

2.3.3.1 NP-NBDMA

As previously mentioned, the increasing hydrophilicity of the core upon CO_2 bubbling should shift the fluorescence emission of the particles. To understand the particle's behavior, fluorescence emission, size, and pH of solution of concentration 0.3 mg/mL of the nanoparticles was monitored before and after a constant flow and pressure of CO_2. A fast change in fluorescence intensity was observed after 15s with a corresponding drastic change in pH from 7.4 to 5.6 (figure 2.22). Moreover, a change in size was observed from 134 nm to 303 nm (figure 2.19). The emission and size plateaued after 2 min of CO_2 bubbling figure 20 a and b). The increase in fluorescence emission upon CO_2 bubbling was observed under a UV lamp (λ = 345 nm).

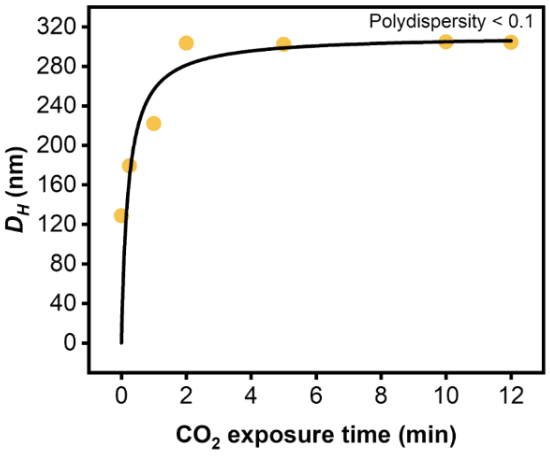

Figure 2.19. Graph representing size variation trend of NP-NBDMA Nanoparticles vs the exposure time of CO_2 at 1 bar of pressure and flowrate 50 cm^3/min.

After comparing the results obtained with pH change made with buffers and the ones obtained with CO_2, we observed a slightly different tendency. Whereas the size of the particles only reached 251 nm as maximum value at pH 5.6 with a buffer solution, it increased to 306 nm when bubbling CO_2 after 2 min and reaching the same pH value. We believed that CO_2 has a bigger impact in tuning the polarity of the system, due to the more hydrophilic nature of the bicarbonate system provides.[37]

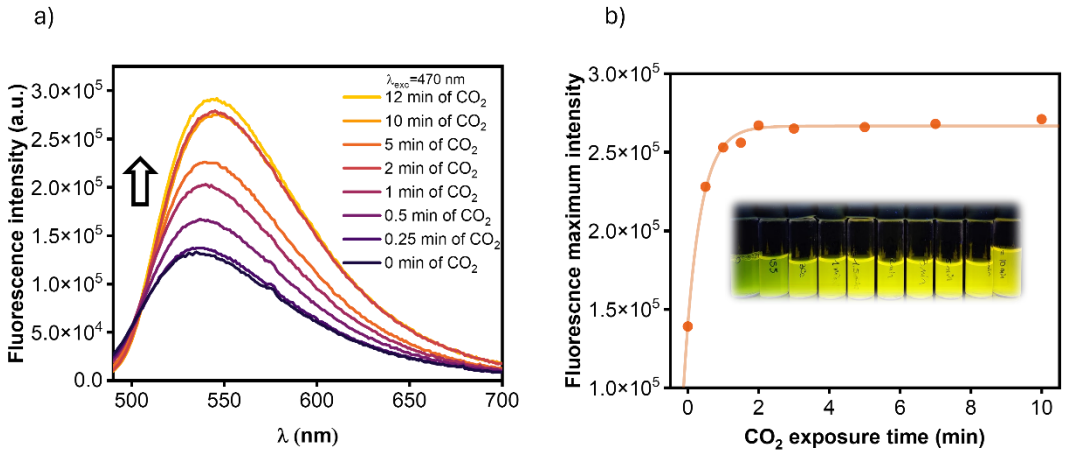

Figure 2.20. (a) Emission spectra of NP-NBDMA following exposure to CO_2 for varying durations. Each curve represents a specific exposure period. (b) Graph representing fluorescence maximum intensity variation trend of NP-NBDMA vs CO_2 exposure time. λ_{ex} = 470 nm; λ_{em} = 550 nm

We aimed to determine if this system was reversible with N_2, as reported for many other systems in the literature. First, we bubbled an aqueous solution of the nanoparticle system (0.5 mg/mL) with CO_2 at a constant flow rate of 50 cm^3/min for 15 minutes. Subsequently, we bubbled the system with pressurized N_2 at a similar flow rate. We observed that the kinetics of this process were significantly slower, taking approximately 10 minutes to

reach its lowest fluorescence emission (figure 2.21a and b). Removing CO_2 from the solution involves the CO_2 molecules diffusing out of the solution, which is a slower process due to its high solubility in water.

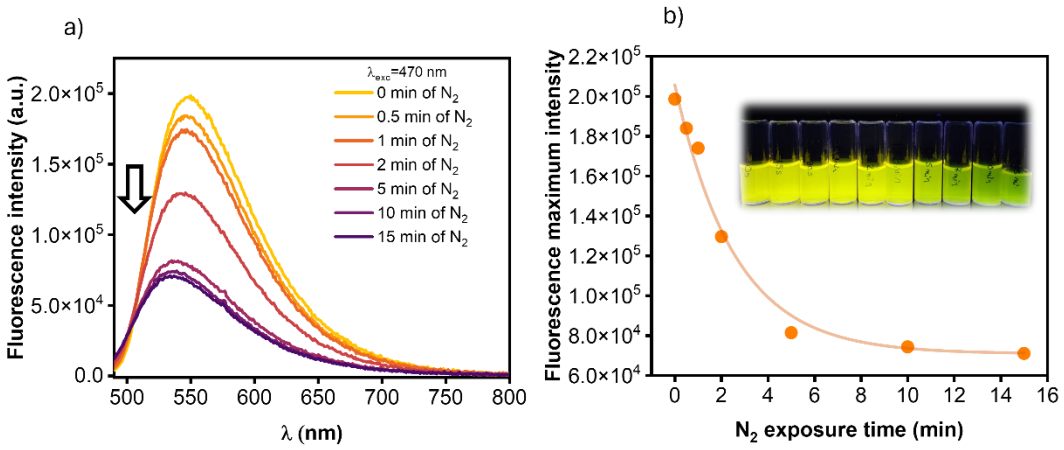

Figure 2.21. (a) Emission spectrum of NP-NBDMA) (previously exposed to 1st CO_2 cycle) after 0, 0.25, 0.5, 1, 2, 5, 10, 12 min of interaction with N_2 (first cycle). (b) Graph representing fluorescence maximum intensity variation trend of NP-NBDMA vs N_2 exposing time. λ_{ex} = 470 nm; λ_{em} = 550 nm.

We repeatedly bubbled CO_2 and N_2 into the particle solution to evaluate its reversibility. Fluorescence spectroscopy was used to monitor purge cycles. The purging time was kept constant for the entire experiment, CO_2 was bubbled for 10 min and N_2 was bubbled for 40 min. The hydrodynamic diameter and the fluorescence emission at 470 nm of the particles were measured after each CO_2 as it can be observed in the experimental part.

The pH of the solution decreased and increased six times, as illustrated in figure 2.22b. Similarly, the intensity of emission alternated between being activated (ON) and quenched (OFF) six times in a reversible manner (figure 2.22a). This characteristic makes the system particularly intriguing for potential applications in lifetime CO_2 sensors, as it can be used over extended periods. Nevertheless, the change in visual fluorescence was not as drastic as we expected.

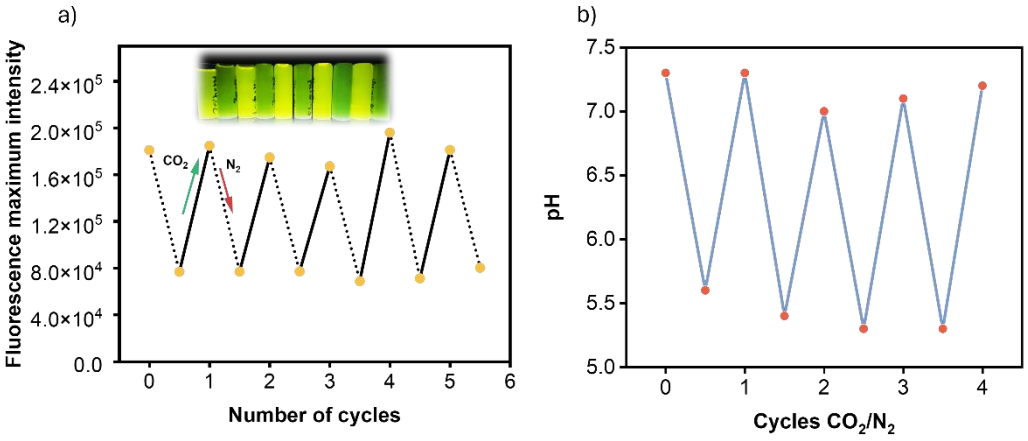

Figure 2.22. (a) Fluorescence intensity of the particles measured after 4 CO_2/N_2 cycles of NP-NBDMA (b) pH variation of NP-NBDMA after 4 CO_2/N_2 cycles. λ_{ex} = 470 nm; λ_{em} = 550 nm.

2.3.3.2 NP-ACMMA

For the ACMMA system the CO_2 responsiveness of the nanoparticles was also evaluated. We bubbled pressurized CO_2 (1 bar, 50 cm^3/min) into a 0.3 mg/mL solution of PDMAPS-b-P(DEAEMA-co-EGDMA-co-ACMMA) for 5 minutes. The fluorescence intensity of the system decreased by approximately 10 times within 2 minutes of CO_2 exposure. The change in visual fluorescence became noticeable after 5 minutes, as shown in figure 2.23.

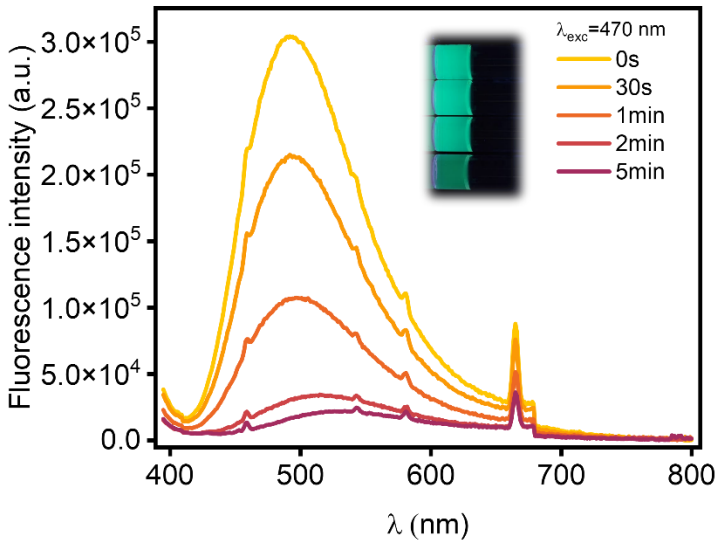

Figure 2.23. Emission spectrum of NP-ACMMA after 0, 0.5, 1, 2, 5 min of interaction with CO_2. λ_{exc}= 380 nm. λ_{em}= 500 nm.

Unlike the previous nanoparticles, this system exhibited a decrease in fluorescence intensity in response to CO_2. Therefore, we expected the fluorescence to increase when exposed to N_2. To assess this, we bubbled pressurized N_2 into a previously CO_2-exposed 0.3 mg/mL solution of the nanoparticles for 15 minutes. The fluorescence intensity of the system gradually increased, with visual fluorescence starting to recover after 7 minutes of N_2 bubbling and reaching its maximum value after 10 minutes. This process was reversible for at least four cycles, demonstrating good reproducibility and lifetime (figure 2.24a and b).

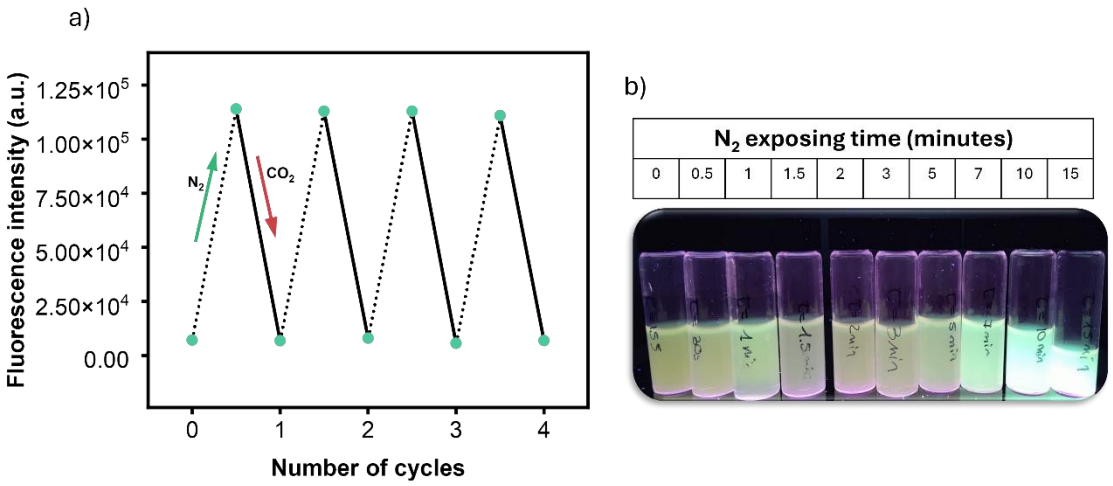

Figure 2.24. (a) Fluorescence intensity of NP-ACMMA measured after 4 CO_2/N_2. Concentration 0.3 mg/mL. λ_{exc}= 380 nm. λ_{em}= 500 nm. (b) NP-ACMMA vials at different N_2 exposures times under a UV lamp (λ = 345 nm).

However, the response to both CO_2 and N_2 was slower than optimal for detection, and the change in visual fluorescence was not as pronounced as expected and was slow.

2.3.3.3 NP-SPMA

Given the nanoparticles' sensitivity to pH changes in both size and fluorescence, the subsequent experiment aimed to assess their responsiveness to CO_2 and the resulting alterations in optical properties. A 1 mg/mL nanoparticle solution was prepared at pH 7.1 and subjected to a continuous CO_2 flow at 1 bar pressure for 10 minutes. A rapid pH decrease was observed within the first minute of CO_2 exposure, and fluorescence was completely quenched after 5 minutes (figure 2.24).

Post-CO_2 exposure, the solution retained its coloration due to the equilibrium between merocyanine forms of spiropyran. This state was reversible, as fluorescence was restored after the solution was kept in darkness for 24 hours, as illustrated in the (figure 2.25).

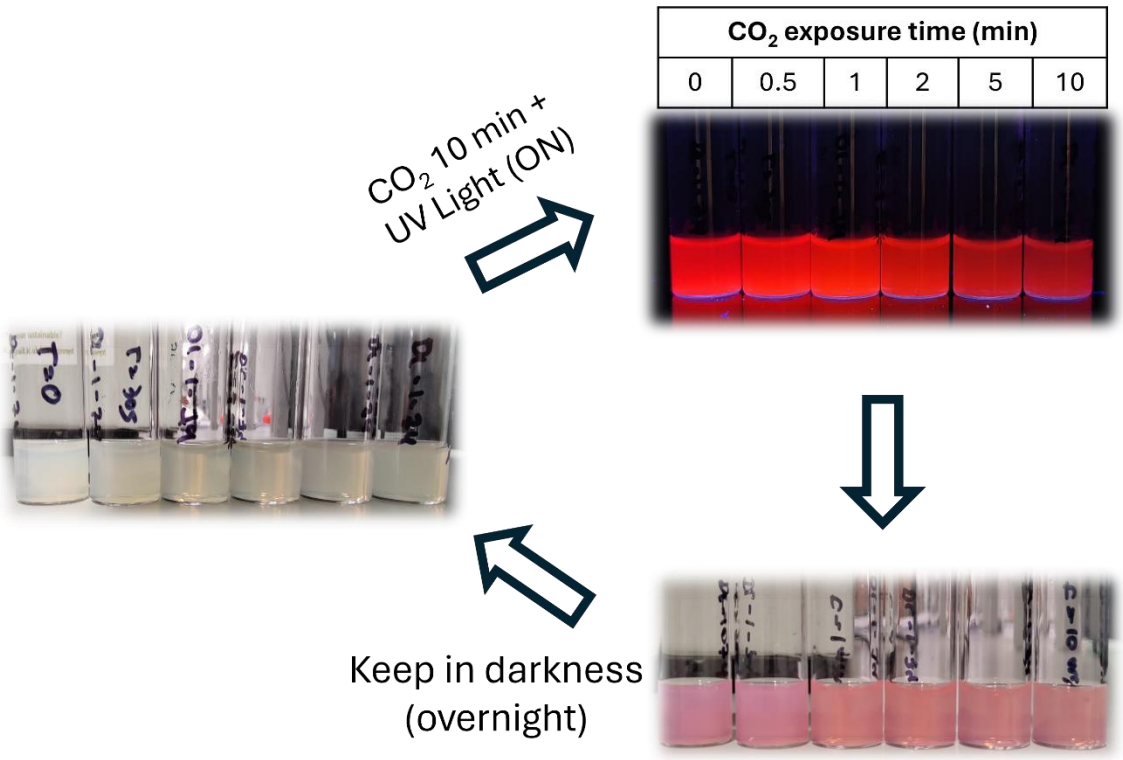

Figure 2.25. Emission spectrum of NP-SPMA at pH 2.5, 4.9 and 7.9. Concentration 1 mg/mL. λ_{exc}= 350 nm. λ_{em}= 640 nm.

Even though we could observe a drastic change not only in qualitative but also quantitative fluorescence for this system, this phenomenon renders this polymeric system intriguing yet challenging to apply in CO_2/pH sensing systems. The difficulty arises from the overlapping effects of the dye's colorimetric response to UV light and the nanoparticle system's pH responsiveness on the effect on the SPMA dye. For this main reason, we decided to discard this dye as a potential fluorescent responsive moiety for this application.

2.4 Conclusion

In this work, we synthesized four different fluorescent monomers—NBDMA, ACMMA, SPMA, and TPEMA—with the aim of developing responsive nanoparticle systems for potential sensing applications. Among these, the NBDMA-based nanoparticles showed the most promising results for CO_2 detection. These particles were synthesized via RAFT emulsion polymerization of DEAEMA and EGDMA in water, using PDMAPS as a steric stabilizer. The resulting system was highly responsive to CO_2, showing a clear fluorescence "turn-on" within 15 seconds of bubbling, which we attribute to the swelling of the DEAEMA-containing core and the resulting suppression of PET due to protonation of the tertiary amine groups.

Importantly, the fluorescence response was fully reversible when switching back to N_2, and this behavior was repeatable over at least six cycles without significant loss of signal, indicating good durability. These results agree with previous studies showing that tertiary amine-based polymers can undergo protonation-induced changes in optical properties upon exposure to CO_2.[38, 39] The rapid response and reversibility suggest real potential for practical sensing applications.

While ACMMA-based particles also exhibited a noticeable change in fluorescence, their response time was slower, possibly due to less effective suppression of PET. Systems incorporating SPMA and TPEMA were not suitable for CO_2 sensing due to instability or inadequate signal change, likely related to the intrinsic properties of the dyes themselves.

Looking ahead, further optimization of the NBDMA system is needed to enhance fluorescence contrast and fine-tune sensitivity. Control experiments in more complex environments—such as varying humidity, pH, and the presence of interfering gases—will be critical to evaluate real-world performance. Additionally, exploring ways to integrate

the responsive nanoparticles into solid supports or membranes could be key to developing portable or wearable sensors for environmental monitoring, industrial safety, or even biomedical use. Overall, the system shows strong potential for real-time CO_2 sensing in aqueous environments, combining fast response, reversibility, and stability. With further refinement, it could become a practical platform for gas detection in various settings.

2.5 Experimental section

2.5.1 Materials

4-Hydroxyl-phenylbenzophenone (99%), 3-bromo-1-propanol (97%), triethylamine (TEA, 99%), methacryloyl chloride, Zn powder (99.995%), benzophenone (99%), 3,4-dichloromaleic anhydride (99%), 4-chloro-7-nitrobenzofurazan (NBD-Cl, 98%), 2,2,2-trifluoroethanol (TFE, ≥99%), ethanolamine (≥98%), *N,N'*-dimethyl(methacryloylethyl)ammonium propane sulfonate (DMAPS) (95%), methacrylic Acid (250 ppm MEHQ, 99%), 4-(dimethylamino) pyridine (DMAP), ethylene glycol dimethacrylate (EGDMA, 98%), 2-(eiethylamino)ethyl methacrylate (DEAEMA, 99%), 4,4'-azobis(4-cyanovaleric acid) (ACVA, 98%), deuterium oxide (D_2O), potassium persulfate (KPS, ≥99.0%), acetonitrile (MeCN, ≥99.9%)**,** and 4-cyano-4-(phenylcarbonothioylthio)pentanoic acid (CPAD) were obtained from Sigma-Aldrich. 1-(3-dimethylaminopropyl)-3 ethylcarbodiimide hydrochloride (EDC-HCl, 98+%) was acquired from Acros-Organics. Ethyl acetate (EtOAc, ≥99%), hexane (Hex, ≥95%), dichloromethane (CH_2Cl_2, 99%), and Na_2SO_4 anhydrous (99+%, Extra Pure) were obtained from Fischer Scientific.1kg CP carbon dioxide-cylinder and pure Nitrogen was obtained from BOC. Spectrum Spectra/Por dialysis tubing with either 1 kDa or 6–8 kDa M_W was supplied by Fisher Scientific. Deionized and 18.2 MΩ·cm ultrapure water was obtained from a Triple Red Alto purification system and was used in all experiments unless stated otherwise.

2.5.2 Instrumentation

Aqueous Size Exclusion Chromatography was performed on an Agilent PL50 instrument fitted with an Agilent PL aquagel-OH MIXED-M column (300 × 7.5 mm × 5 μm) and an aquagel guard column. The mobile phase used was H_2O:MeOH (80:20)

containing 0.1 M $NaNO_3$, at a flow rate of 1.0 mL min-1, a column temperature of 35 °C. 80 μL of sample were injected for each measurement and eluted for 35 min. Samples were prepared at a concentration of 1 mg mL^{-1} and filtered using a 0.45 μm nylon filter prior to analysis. Calibration was conducted in the molecular weight range 100-30000 Da using EasiVial polyethylene glycol (PEG) standards supplied by Agilent Technologies. and detection by both refractive index (RI) and single wavelength UV at 309 nm.

^{1}H, ^{13}C - Nuclear Magnetic Resonance (NMR) spectra were acquired at 400 MHz using a Bruker DPX-400 spectrometer with D_2O containing 0.5 M NaCl as the solvent in the case of PDMAPS, $CDCl_3$ for SPMA and ACMMA, DMSO-d_6 for NBDMA and CH_2Cl_2 for TPEMA. At least 32 scans were recorded for each sample and the proton chemical shifts are reported as chemical shift (δ) in parts per million (ppm) and are relative to solvent residual peaks.

Hydrodynamic diameters (D_h) and size distributions (PD) of particles were determined by dynamic light scattering (DLS) using either a Malvern Panalytical Zetasizer Nano S or Nano ZSP fitted with a 633 nm He-Ne laser operating at 4 or 10 mW. Samples were prepared at a concentration of approximately 1 mg mL^{-1} in 0.3 M NaCl. Measurements were performed at 20 °C using a scattering angle of 173° (backscattering) using the high resolution mode, and the results analysed using Malvern Panalytical Zetasizer software version 7.13. All determinations were repeated 4 times, taking the average of at least 10 measurements for each run. D_h values were calculated using the Stokes-Einstein equation, assuming the particles are spherical in solution.

Thermogravimetric analysis (TGA) was performed using TA Instruments – TGA 550. 200 μL of sample was weighed on a pan and heated from 20 to 250 ºC at a heating rate of 10 ºC min^{-1} under a nitrogen atmosphere.

UV-Vis spectroscopy was performed on an Evolution 350 UV-Vis spectrophotometer equipped with Xenon Flash Lamp light source and Dual Matched Silicon Photodiodes detector. Quartz cells (170 - 2000 nm) from Hellma, with two polished sides, were used for examining the absorption spectral data by using Thermo INSIGHT-2 v.10.0.30319.1 software. A thermostat and 8-cell Peltier system with precise temperature control between 0 ºC and 90 ºC was coupled with an Evolution 350 UV-Vis spectrophotometer to record the LCST behavior, temperature-dependent absorption/transmittance spectra of the sample. All variable temperature analysis experiments were made using samples of concentration 5 mg mL-1 in 0.3 M NaCl, Variable temperature analyses were run from 15-90 ºC at a heating rate of 1 ºC min^{-1}.

pH measurements were conducted in a Mettler Toledo G20 compact titrator equipped with a pH-electrode DGi115-SC. The calibration of the glass pH-electrode was performed using buffer solutions pH 4.01, 7.00, and 9.21 from Mettler Toledo. All data were recorded using the LabX Light Titration 3.1.1.0 software provided by Mettler Toledo.

Dry-state stained transmission electron microscopy imaging was performed on a JEOL 2100 microscope at an acceleration voltage of 200 kV. All samples were diluted with deionized water and then deposited onto formvar-coated copper grids. After 1 min, the excess sample was blotted from the grid and the grid was stained with an aqueous 1 wt% uranyl acetate (UA) solution for 1 min prior to blotting, drying and microscopic analysis.

Titrations Titrations were carried out manually, beginning with the preparation of a basic solution with an initial pH of approximately 13. This was achieved by using a standardized 0.01 M sodium hydroxide (NaOH) solution. Subsequently, 0.01 M hydrochloric acid (HCl) was added incrementally to the basic solution to gradually lower the pH toward the acidic range. The titration proceeded from a strongly basic environment

through neutral pH and into acidic conditions. All experiments were performed under controlled conditions to ensure repeatability and accuracy.

Sample preparation at different pHs Samples at various pH levels were prepared by first preparing phosphate-buffered saline (PBS) solutions. The pH of each PBS solution was then adjusted to the desired value using standardized 0.01 M NaOH and 0.01 M HCl solutions. Adjustments were made incrementally while continuously monitoring the pH to ensure precision. All samples were prepared under consistent conditions to maintain reproducibility across experiments.

2.5.3 CO_2 testing experimental procedure

CO_2 was bubbled into 20 mL of PDMAPS-b-P(DEAEMA-co-EGDMA-co-RMA) micellar dispersion for a period, and the variation of the micelles in diameter and fluorescence emission were studied. The flow rate of CO_2 and N_2 was controlled at 50 mL/min with a glass rotor flowmeter.

2.5.4 Synthesis of fluorescent monomers (SPMA, NBDMA, ACMMA, TPEMA)

2.5.4.1 Synthesis of Spiropyran methacrylate (SPMA). Reproduced from ref.[40]

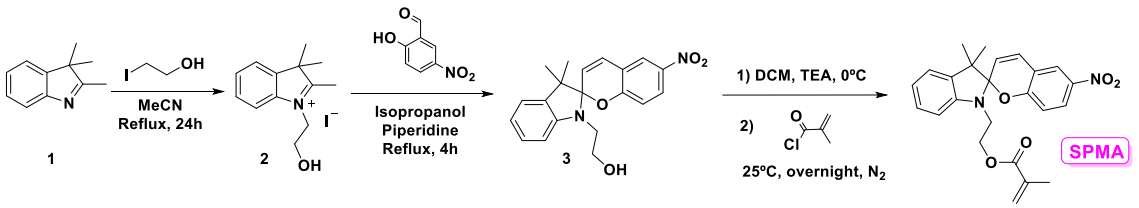

(2). 2,3-trimethyl-3H indole **(1)** (5.01 g, 31.5 mmol) and 2-iodoethanol (7.5 g, 44 mmol) were dissolved in MeCN (50 mL). The solution was refluxed under nitrogen for 24 hours. The reaction mixture was cooled to room temperature and product precipitated by the addition of hexane. The purple solid was filtered and dried without further purification. Yield: 95%.

(3). To a solution of **(2)** (2.17 g, 6.30 mmol) in isopropanol (6 mL) was added 5-nitrosalicaldehyde (1.05 g, 6.28 mmol) and piperidine (0.54 g, 6.30 mmol). The mixture was stirred at reflux for 4 hours under nitrogen. The solvent was evaporated, the residue dissolved in CH_2Cl_2 and passed through a silica column, eluting with more CH_2Cl_2. Then, the portion of product spiropyran which remained on the column was eluted with diethyl ether. Finally, the product was further purified by recrystallization from ethanol, giving a dark purple microcrystalline powder (**3**). The product was dried under vacuum overnight at 30 ºC. (1.53 g, 67%). ^{1}H NMR (400 MHz, Chloroform-d) δ 8.00 – 7.86 (m, 2H), 7.13 (td, J = 7.6, 1.3 Hz, 1H), 7.03 (dd, J = 7.3, 1.3 Hz, 1H), 6.89 – 6.77 (m, 2H), 6.69 (d, J = 8.6 Hz, 1H), 6.60 (d, J = 7.8 Hz, 1H), 5.81 (d, J = 10.4 Hz, 1H), 3.82 – 3.60 (m, 2H), 3.39 (ddd, J = 14.9, 7.4, 5.4 Hz, 1H), 3.26 (dt, J = 14.9, 5.1 Hz, 1H), 1.65 (s, 1H), 1.22 (s, 3H), 1.13 (s, 3H). HR-MS (MaXis) m/z $[M+H]^+$: 353.1503, calculated 353.1501.

(SPMA). A solution of EDC-HCl (0.980 g, 5.10 mmol) in dry CH_2Cl_2 (12 mL) was added dropwise into a mixture of **(3)** (1.50 g, 4.30 mmol), DMAP (53 mg, 0.43 mmol) and methacrylic acid (361 µl, 4.26 mmol) in dry CH_2Cl_2 (15 mL) at 0 ºC. The reaction was allowed to reach room temperature during 24 hours. The crude was diluted with CH_2Cl_2 (50 mL), washed with brine (60 mL x 3), and dried over Na_2SO_4 anhydrous. The reaction mixture was concentrated under vacuum and the residue was purified through flash column chromatography (silica gel) using hexane/ethyl acetate (2:1) as eluent to obtain compound **SPMA** (0.75g, 45 %) as a yellow/purple solid. ^{1}H NMR (400 MHz, Chloroform-*d*) δ 8.01 – 7.87 (m, 2H), 7.17 – 7.10 (m, 1H), 7.02 (dd, *J* = 7.3, 1.3 Hz, 1H), 6.86 – 6.80 (m, 2H), 6.66 (dd, *J* = 19.1, 8.2 Hz, 2H), 6.00 (t, *J* = 1.4 Hz, 1H), 5.80 (d, *J* = 10.3 Hz, 1H), 5.53 – 5.45 (m, 1H), 4.23 (t, *J* = 6.3 Hz, 2H), 3.55 – 3.24 (m, 2H), 1.85 (t, *J* = 1.3 Hz, 3H), 1.21 (s, 3H), 1.09 (s, 3H). ^{13}C NMR (400 MHz, Chloroform-*d*) δ 167.4, 159.5, 159.4, 147.1, 146.8, 141.3, 141.2, 136.2, 136.0, 135.8, 128.4, 128.4, 128.0, 126.1,

126.0, 122.9, 122.1, 122.0, 122.0, 121.9, 120.1, 120.1, 118.7, 118.6, 115.7, 115.7, 107.0, 106.9, 106.7, 106.7, 62.8, 61.0, 53.0, 52.9, 46.3, 42.6, 26.0, 26.0, 20.2, 19.2, 18.5. HR-MS (MaXis) m/z [M+H]+: 421.1760, calculated 421.1763.

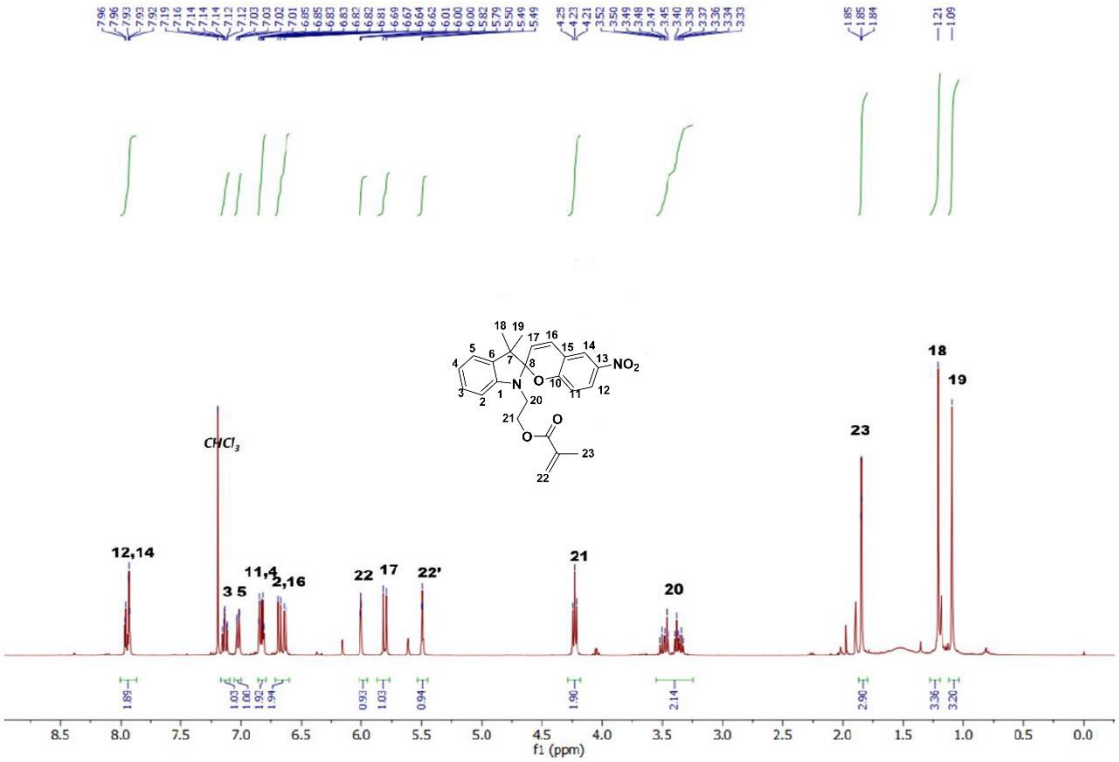

^{1}H-NMR spectrum of SPMA in C*D*Cl$_3$ (400 MHz).

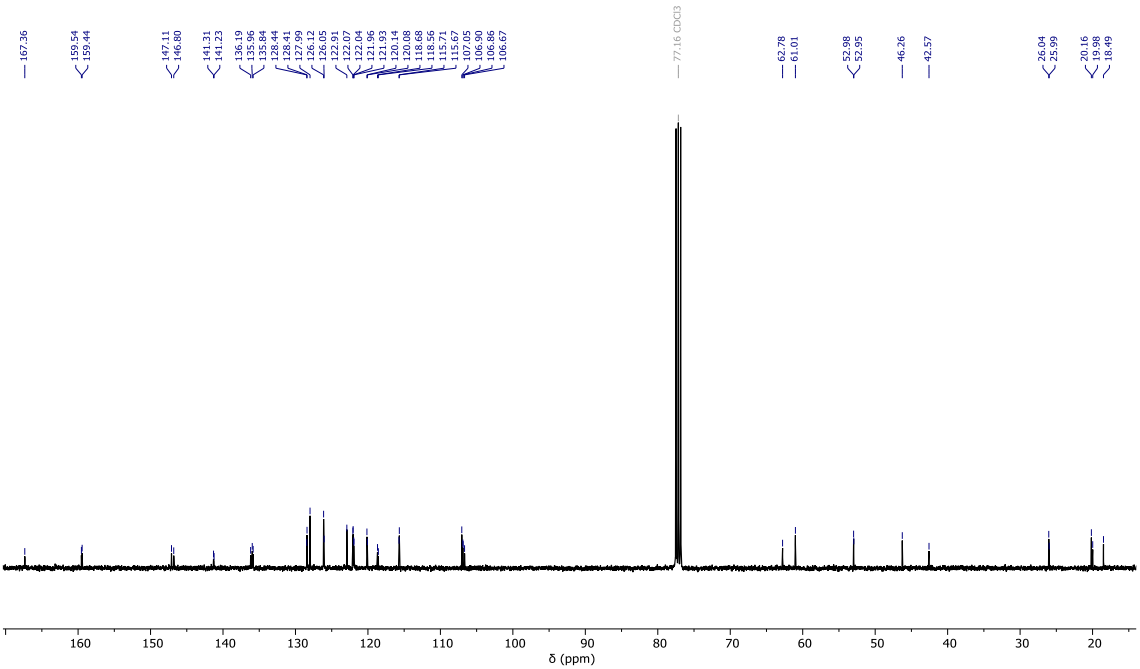

^{13}C-NMR spectrum of SPMA in C*D*Cl$_3$ (400 MHz).

2.5.4.2 Synthesis of 2-(3-chloro-4-(isopropylamino)-2,5-dioxo-2,5-dihydro-1H-pyrrol-yl)ethyl methacrylate (ACMMA). Reproduced from ref.[41]

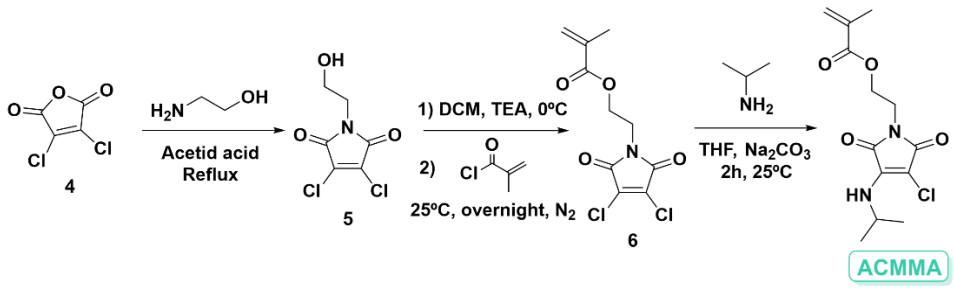

(5). 3,4-dichloromaleic anhydride **(4)** (3.01 g, 18.1 mmol) and 2-ethanolamine (1.62 g, 27.2 mmol) were added to a solution of acetic acid (15 ml) and stirred for 4 hrs at 80 ºC. The reaction became yellow and then cooled to room temperature. The solvent was removed under reduced pressure and then purified by silica-gel column chromatography using hexane/ethyl acetate (2:1, v/v) as eluent to afford product **(5)** as white crystals. (2.35

g, 62%). ^{1}H NMR (400 MHz, $CDCl_3$) δ 4.10 (br s, 1H), 3.80 (t, J = 5.5 Hz, 2H), 3.60 (t, J = 5.5 Hz, 2H).

(6). Product **(5)** (2.03 g. 9.52 mmol) was dissolved in 15 mL dry CH_2Cl_2 and triethylamine (1.18 g, 11.6 mmol) was added to the solution at 0 ºC. Then methacryloyl chloride (1.22 g, 11.6 mmol) dissolved in dry CH_2Cl_2 (10 mL) was added to the above mixture dropwise at 0 ºC under argon. The mixture was allowed to reach the room temperature overnight. The crude solution was washed with water (100 mL) and brine (2 × 100 mL) separately. The CH_2Cl_2 phase was dried over anhydrous sodium sulfate, then the solvent was removed with a rotary evaporator. The crude product was chromatographed on a silica gel using dry-loading technique and petroleum ether/ethyl acetate (9:1, v/v) and slowly increasing the polarity to afford compound **(6)** as a yellow oil. (0.73 g, yield: 28%). ^{1}H NMR (400 MHz, $CDCl_3$) δ 6.40 (dd, J = 17.3, 1.5 Hz, 1H), 6.10 (dd, J = 17.3, 10.5 Hz, 1H), 5.85 (dd, J = 10.5, 1.5 Hz, 1H), 4.35 (t, J = 5.5 Hz, 2H), 3.65 (t, J = 5.5 Hz, 2H).

ACMMA. To a mixture of Compound **(6)** (0.72 g, 2.57 mmol) and anhydrous Na_2CO_3 (0.68 g, 6.44 mmol) in THF (10 mL) a solution of isopropyl amine (0.17 g, 2.83 mmol) in THF (10 mL) was slowly added. The reaction was monitored by TLC. (Consumption of 2,3-dibromomaleimide was monitored by TLC and was completed within 30 min to 1.5 h. The solvent was then evaporated under reduced pressure and the residue was redissolved in CH_2Cl_2 (150 mL). The resultant mixture was washed with water (2 × 150 mL), dried with sodium sulfate anhydrous and purified via column chromatography on silica gel with petroleum ether/ethyl acetate (3:1, v/v). **ACMMA** was obtained as a white powder (0.46 g, 60%). ^{1}H NMR (400 MHz, $CDCl_3$): δ (ppm) 6.15 (1H, s), 5.59 (1H, d), 5.2 (1, m), 4.36-4.27 (1H, m), 4.25 (2H, t), 3.81 (2H, t), 1.90 (3H, s), 1.3 (6H, 2). ^{13}C NMR (400 MHz, $CDCl_3$) δ 167.5, 167.2, 165.7, 139.7, 135.9, 126.4, 88.9, 62.0, 45.2, 37.4, 24.0, 18.4.

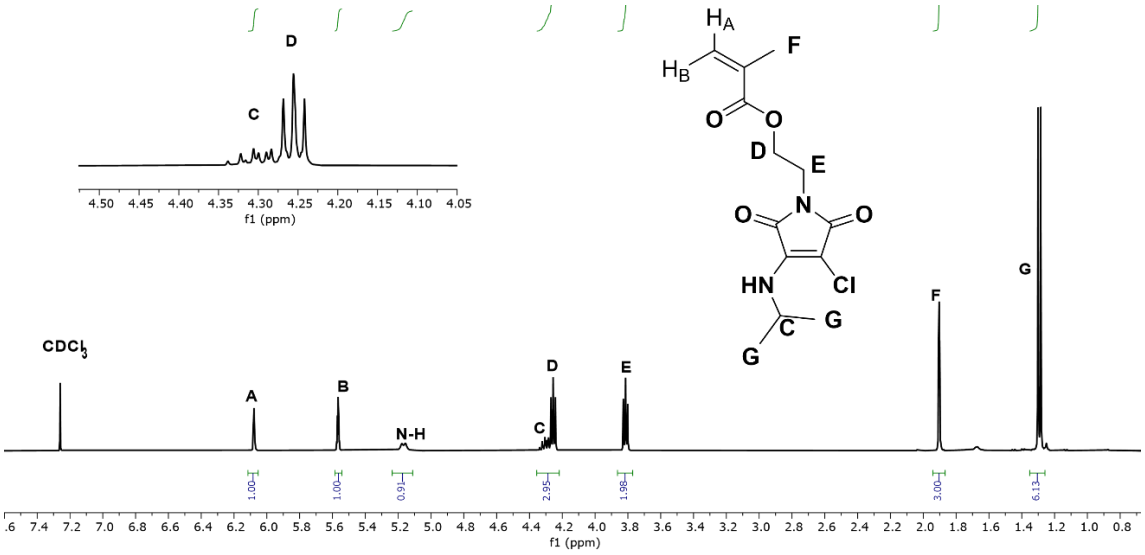

^{1}H-NMR spectrum of ACMMA in C*D*Cl$_3$ (400 MHz).

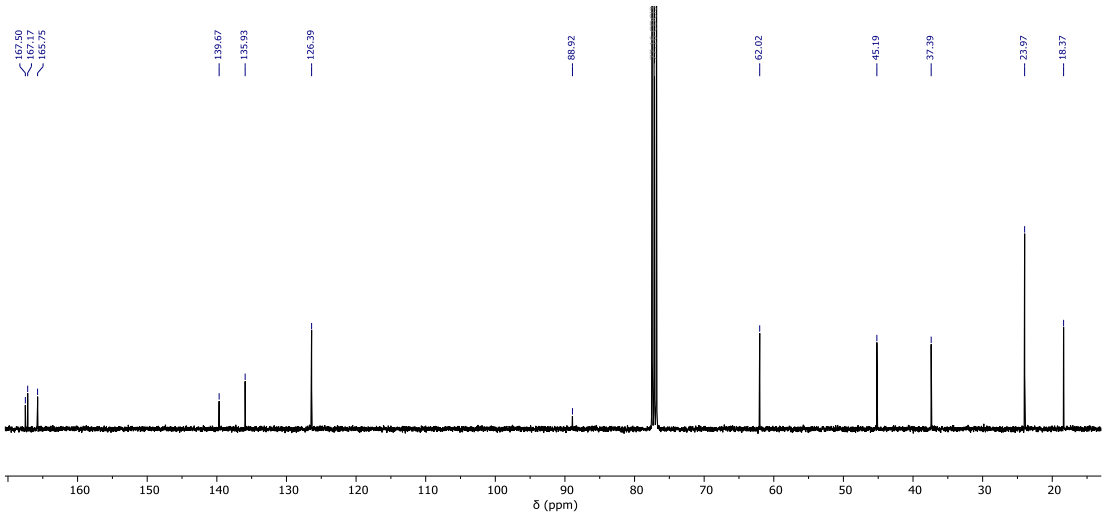

^{13}C-NMR spectrum of ACMMA in C*D*Cl$_3$ (400 MHz).

2.5.4.3 Synthesis of 4-(2-Methacryloyloxyethylamino)-7-nitro-2,1,3-benzoxadiazole (NBDMA). Reproduced from ref.[42]

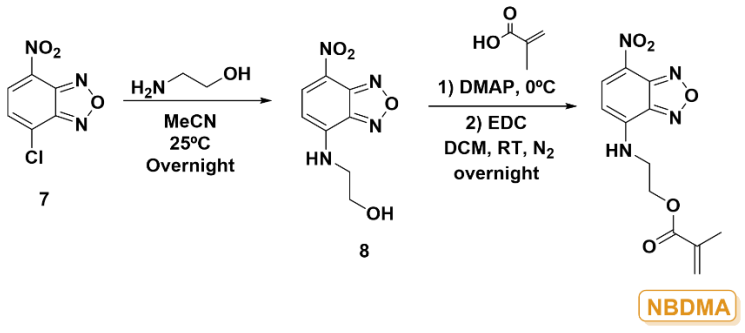

(8). To a solution of 4-chloro-7-nitro-2,1,3-benzoxadiazole **(7)** (1.50 g, 7.52 mmol) in CH_3CN (150 mL) was added a solution of ethanolamine (1.06 mL, 17.45 mmol) dropwise in CH_3CN (30 mL). The resulting solution was stirred at room temperature overnight. Then the reaction mixture was concentrated under vacuum and the residue was purified through liquid chromatography (silica gel) using hexane/ethyl acetate (1:6) as an eluent to afford compound **2** (976 mg, 58 %) as an orange solid. ^{1}H NMR δ (ppm, DMSO-d_6): 3.55 (br, 2H, $NHCH_2CH_2OH$), 3.69 (t, 2H, $NHCH_2CH_2OH$), 4.95 (b, 1H, $NHCH_2CH_2OH$), 6.46 (d, 1H, aromatic), 8.49 (d, 1H, aromatic), 9.43 (b, 1H, $NHCH_2CH_2OH$). MS (DART-TOF): [M + H]+ ion observed at m/z 225.0666.

(NBDMA). A solution of EDC-HCl (410 mg, 2.14 mmol) in dry CH_2Cl_2 (5 mL) was added dropwise into a mixture of **(8)** (400 mg, 1.78 mmol), DMAP (22 mg, 0.18 mmol) and methacrylic acid (153 µl, 1.78 mmol) in dry CH_2Cl_2 (7 mL) at 0 ºC. The reaction was allowed to reach room temperature during 24 h. The crude was diluted with CH_2Cl_2 (50 mL), washed with brine (60 mL x 3), and dried over Na_2SO_4 anhydrous. The reaction mixture was concentrated under vacuum and the residue was purified through flash column chromatography (silica gel) using hexane/ethyl acetate (1:1) as eluent to afford compound **NBDMA** (416 mg, 83 %) as a yellow solid. ^{1}H NMR δ (ppm, DMSO-d_6): 1.83 (s, 3H, C*H*$_3$), 3.82 (b, 2H, $NHCH_2C$*H*$_2$), 4.37 (t, 2H, NHC*H*$_2CH_2$), 5.66 and 6.01 (m, 2H, C=C*H2*), 6.53 (d, 1H, aromatic), 8.53 (d, 1H, aromatic), 9.54 (S, 1H, N*H*CH_2). ^{13}C NMR (400 MHz, DMSO) δ 182.1, 166.7, 138.0, 135.8, 126.9, 62.4, 42.4, 18.2. HR-MS (MaXis) $[M+Na]^+$ - m/z found 315.0712, calculated 315.0705.

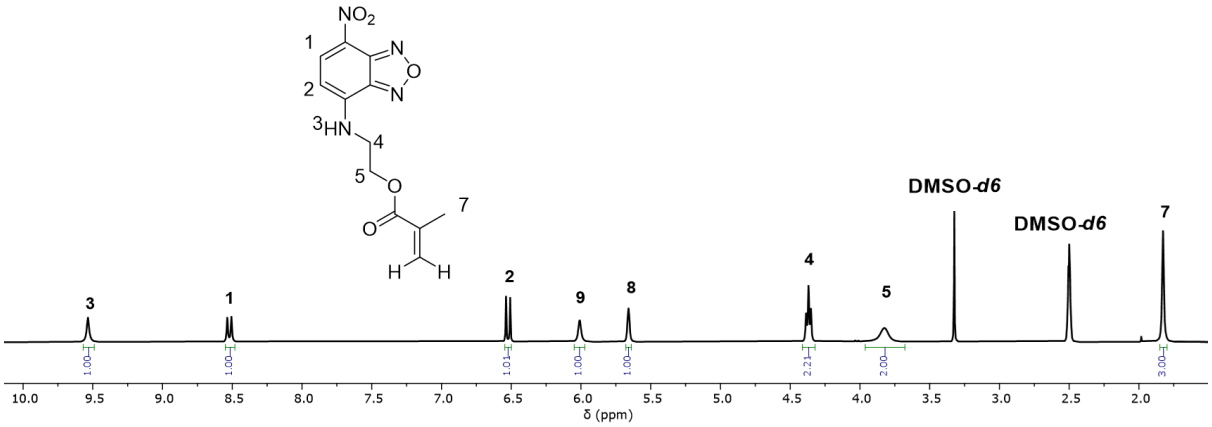

[1]H-NMR spectrum of NBDMA in DMSO-d_6 (400 MHz).

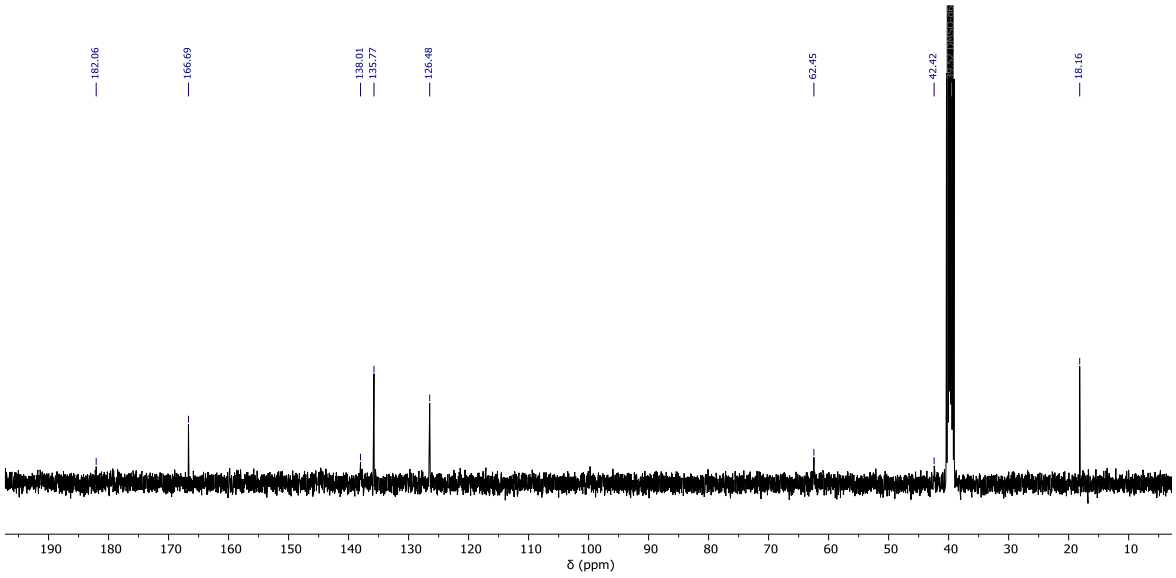

[13]C-NMR spectrum of NBDMA in DMSO-d_6 (400 MHz).

2.5.4.4 Synthesis of 3-(4-(1,2,2-triphenylvinyl)phenoxy)propyl methacrylate (TPEMA). Reproduced from ref.[2]

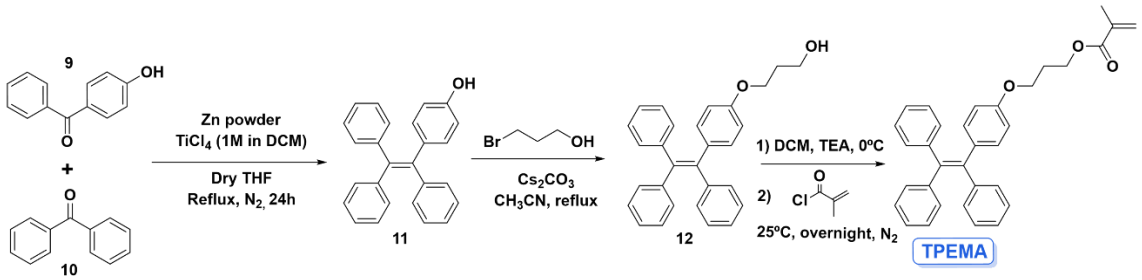

(11). 4-Hydroxyl-phenylbenzophenone **(9)** (4.32 g, 22.0 mmol), benzophenone **(10)** (5.03 g, 27.3 mmol), and Zn powder (6.61 g, 1.20 mmol) were added to a 250 mL two-necked round-bottom flask. The flask was evacuated under vacuum and flushed with nitrogen three times. Then dried THF (137 mL) was added. The solution was cooled to 0 ºC, into which a concentrated solution of $TiCl_4$ (1M in CH_2Cl_2) (50 mL, 50.16 mmol) was added. The mixture was refluxed overnight. After cooling to room temperature, 80 mL dilute hydrochloric acid (1 mol L^{-1}) was added to the mixture, which was extracted with CH_2Cl_2 2 x 100 mL). The collected organic layer was dried over anhydrous magnesium sulfate. After solvent evaporation, the crude product was purified by a silica gel column using hexane/ethyl acetate (9:1, v/v). Product **(11)** was afforded as a white powder (1.2 g, 20%). ^{1}H NMR (400 MHz, $CDCl_3$): δ (ppm) 7.19-6.95 (15H, m), 6.89 (2H, d), 6.56 (2H, d), 4.76 (1H, s).

(12). Compound **(11)** (0.500 g, 1.43 mmol), 3-bromo-1-propanol (0.242 g, 1.72 mmol), Cs_2CO_3 (0.950 g, 2.90 mmol) and dry acetonitrile (CH_3CN, 20 mL) were added to a 50 mL round-bottom flask. The mixture was heated at reflux for 18 h. After cooling to room temperature, the insoluble inorganic salt was removed by filtration. Then the solvent was removed under vacuum. The collected product was further purified by silica-gel column chromatography starting with 100% hexane and gradually increasing the polarity until hexane/ethyl acetate (3:1, v/v). Product **(12)** (white solid, 0.387 g, yield: 67%). ^{1}H NMR (400 MHz, $CDCl_3$): δ (ppm) 7.17-6.97 (15H, m), 6.93 (2H, d), 6.64 (2H, d), 4.05 (2H, t), 3.84 (2H, t), 2.01 (2H, p), 1.70 (1H, s).

(TPEMA). Compound **(12)** (0.451 g. 1.14 mmol) was dissolved in 5 mL dry CH_2Cl_2 and triethylamine (TEA, 0.14 g, 1.37 mmol) was added to the solution at 0 ºC. Then methacryloyl chloride dissolved in dry CH_2Cl_2 (10 mL) was added to the above mixture dropwise at 0 ºC under argon. The mixture was allowed to reach room temperature

overnight. The crude solution was washed with dilute HCl aqueous solution (3%) (3 × 10 mL) and brine (3 × 10 mL) separately to remove water-soluble side products. The CH_2Cl_2 phase was dried over anhydrous magnesium sulfate. Then the CH_2Cl_2 solution was concentrated to 3 mL by rotary evaporation. The crude product was chromatographed on a silica gel using petroleum ether/ethyl acetate (3:1, v/v) to afford the pure **TPEMA** as a light-yellow solid (0.198 g, yield: 40%). ^{1}H NMR (400 MHz, CD_2Cl_2) δ 7.18 – 6.97 (m, 15H), 6.96 – 6.88 (m, 2H), 6.66 – 6.62 (m, 2H), 6.07 – 6.05 (td, *J* = 2.0, 1.0 Hz, 1H) , 5.55 (p, *J* = 1.6 Hz, 1H), 4.28 (t, *J* = 6.3 Hz, 1H), 3.99 (t, *J* = 6.2 Hz, 1H), 2.11 (p, *J* = 6.2 Hz, 1H), 1.92 (dd, *J* = 1.6, 1.0 Hz, 2H). ^{13}C NMR (400 MHz, CD_2Cl_2) δ 144.4, 132.8, 131.6, 131.6, 131.6, 128.1, 128.0, 127.9, 126.7, 126.6, 126.6, 125.4, 113.9, 64.7, 61.9, 29.1, 18.5. HR-MS (MaXis) m/z [M]: 474.2204, calculated 474.219.

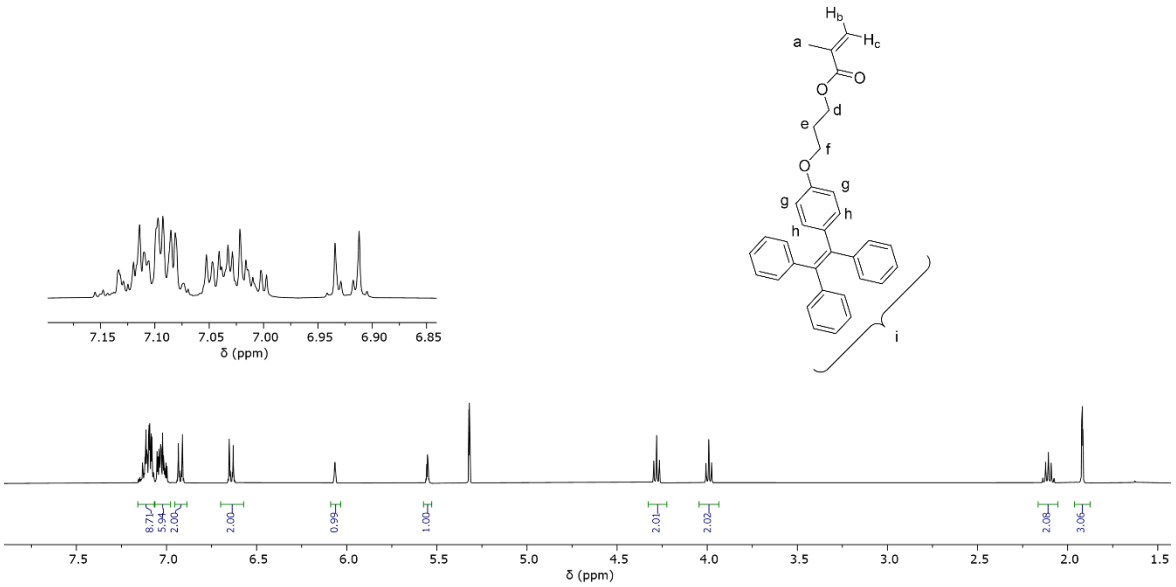

^{1}H-NMR spectrum of TPEMA in C*D*Cl_3 (400 MHz).

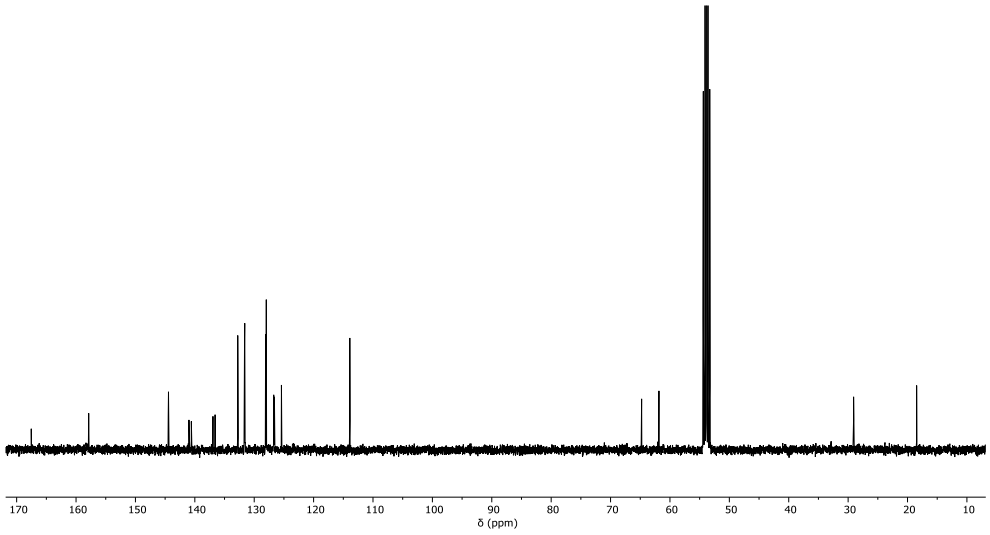

^{13}C-NMR spectrum of TPEMA in CD_2Cl_2 (400 MHz).

2.5.5 General Synthetic procedure for Cross-Linked PDMAPS-b-P(DEAEMA-co-EGDMA-co-dye) CO_2-Responsive Fluorescent Nanoparticles via RAFT-Mediated Emulsion Polymerization using PDMAPS18 as Steric Stabilizer.

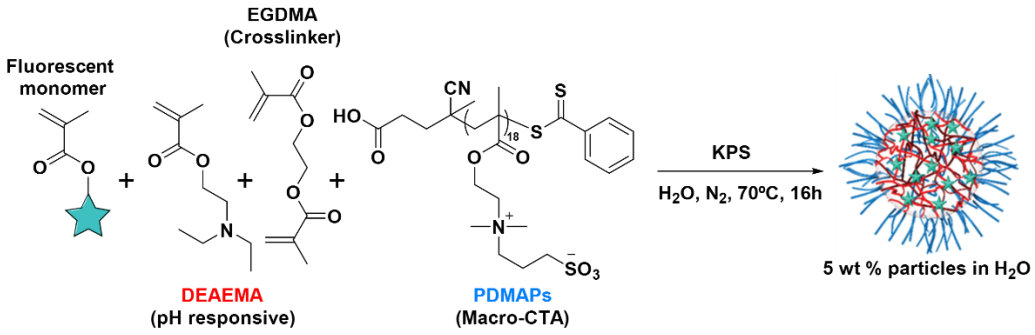

All four nanoparticles with each fluorescent dye were synthesized by the following procedure. PDMAPS$_{18}$ macro-CTA ($M_{n,NMR}$ = 5.2 kDa) (100 mg, 0.02 mmol, 1 equiv), 2-(diethylamino)ethyl methacrylate (DEAEMA) monomer (2.5 mg, 13.5 mmol, 675 equiv), **fluorescent monomer** (1.4 equiv) and ethylene glycol dimethacrylate (EGDMA) cross-linking monomer (25 g, 0.13 mmol, 6.5 equiv) were dispersed in water (47 mL) by rapid stirring. The given mixture was purged with N_2(g) for 30 min under rapid stirring (600 rpm) and then heated for 30 min in an oil bath at 70 °C. The radical initiator potassium

persulfate (KPS) (25 mg, 0.09 mmol, 4.5 equiv) was dissolved separately in water (1 mL) and purged with N_2 (g) for 10 min. The degassed KPS solution was added to the degassed macro-CTA/monomer solution to initiate polymerization. The resulting polymerization mixture was then stirred at 600 rpm at a temperature of 70 °C for 16 h. The polymerization reaction was then terminated upon cooling and exposing the polymerization mixture to air. This procedure resulted in in situ emulsion polymerization-induced self-assembly (PISA), yielding the obtained PDEAEMA-based particles as an aqueous dispersion, which was further analyzed by DLS, UV−Vis spectroscopy, fluorescence spectroscopy, dry-state TEM and TGA, as they are described in the main text.

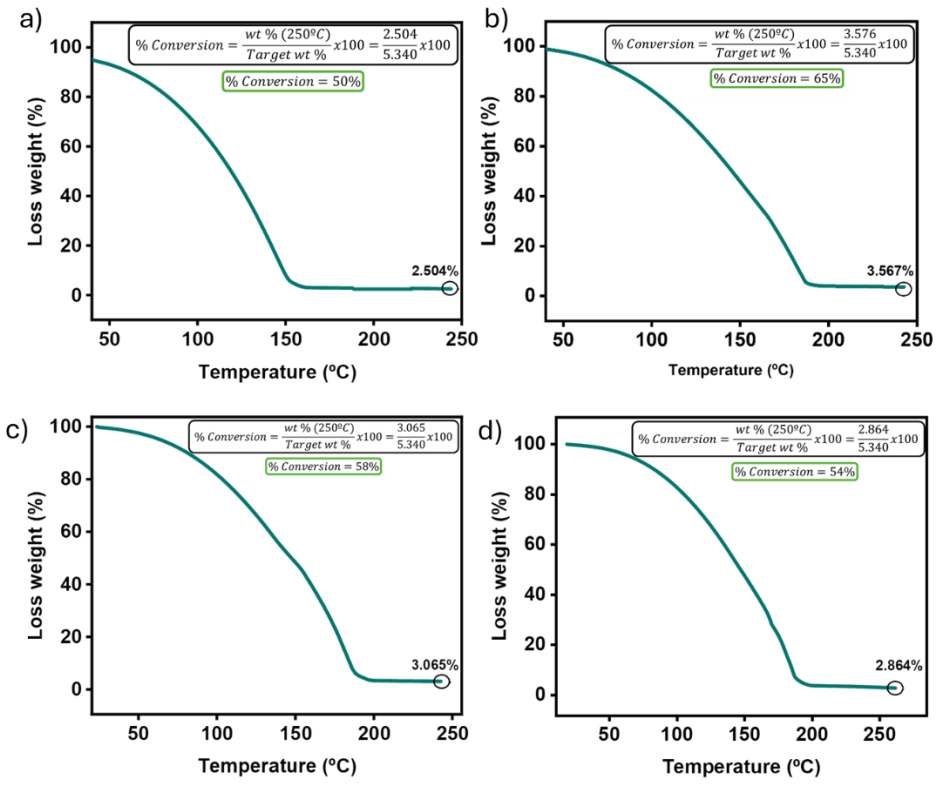

TGA graphics of different nanoparticle systems. a) PDMAPS-b-P(DEAEMA-co-EGDMA-co-NBDMA). b) PDMAPS-b-P(DEAEMA-co-EGDMA-co-ACMMA). c) PDMAPS-b-P(DEAEMA-co-EGDMA-co-SPMA). d) PDMAPS-b-P(DEAEMA-co-EGDMA-co-TPEMA).

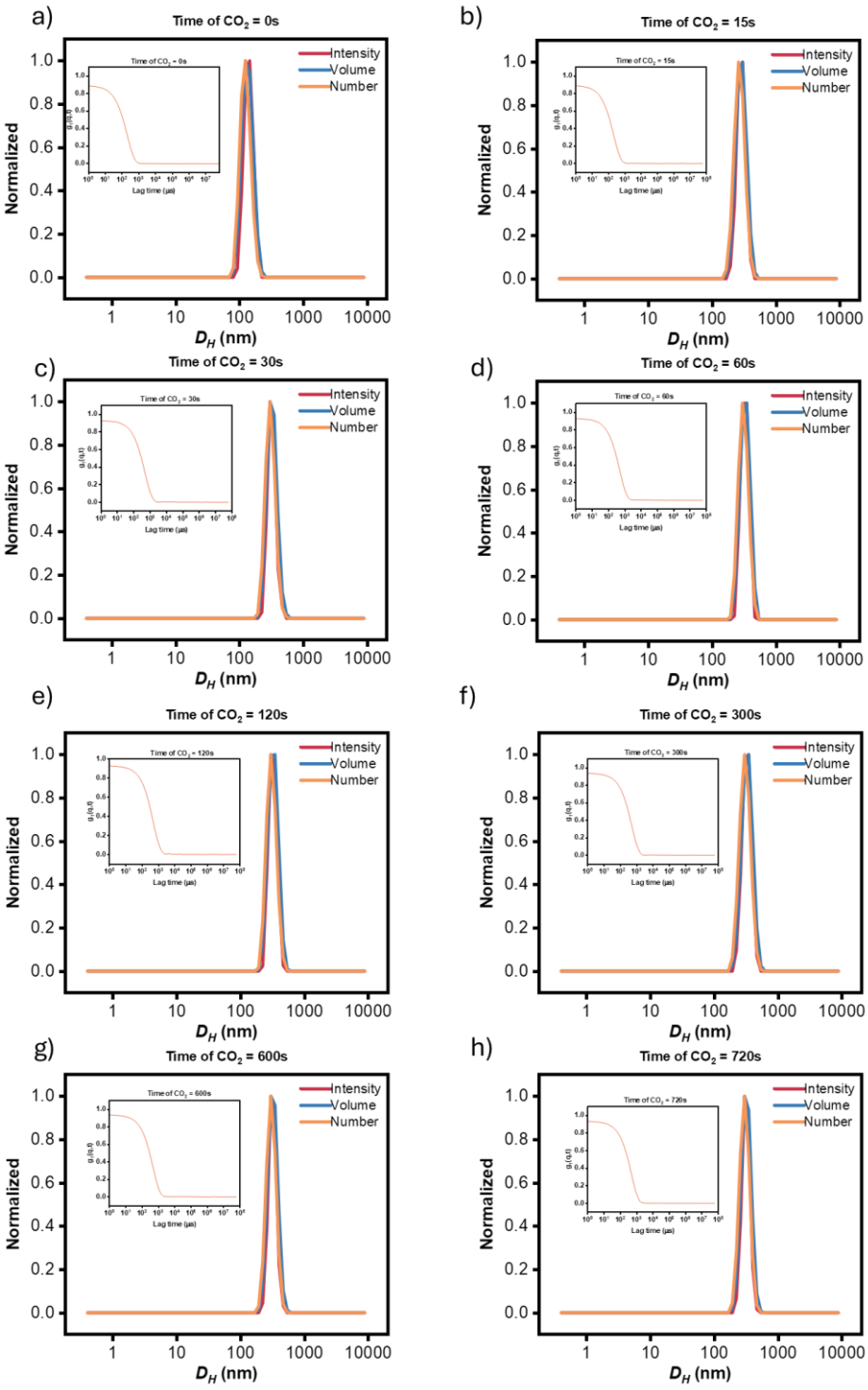

DLS measurements of NP-NBDMA at different times after CO_2 exposure. a) 0s. b) 15s. c) 30s. d) 60s. e) 120s. f) 300s. g) 600s. h) 720s.

2.6 References

(1) Mabire, A. B.; Brouard, Q.; Pitto-Barry, A.; Williams, R. J.; Willcock, H.; Kirby, N.; Chapman, E.; O'Reilly, R. K. CO2/pH-responsive particles with built-in fluorescence read-out. *Polym. Chem.* **2016**, *7* (38), 5943-5948, 10.1039/C6PY01254J. DOI: 10.1039/C6PY01254J.

(2) Zhang, D.; Fan, Y.; Chen, H.; Trépout, S.; Li, M. H. CO2-Activated Reversible Transition between Polymersomes and Micelles with AIE Fluorescence. *Angew. Chem. Int. Ed.* **2019**, *58*, 10260-10265. DOI: 10.1002/anie.201905089.

(3) Qiu, L.; Zhang, H.; Wang, B.; Zhan, Y.; Xing, C.; Pan, C. Y. CO_2-Responsive Nano-Objects with Assembly-Related Aggregation-Induced Emission and Tunable Morphologies. *ACS Appl. Mater. Interfaces* **2020**, *12*, 1348-1358. DOI: 10.1021/acsami.9b18792.

(4) Ma, W.; Dai, S.; Zhu, P.; Zhou, R.; Lu, H. Dual CO_2 Responsiveness of an Oil-In-Water Emulsion by Using Sodium Oleate and Water-Soluble Tertiary Amines. *Langmuir* **2021**, *37*, 750-758. DOI: 10.1021/acs.langmuir.0c03038.

(5) Kocak, G.; Tuncer, C.; Bütün, V. pH-Responsive polymers. *Polym. Chem.* **2017**, *8* (1), 144-176. DOI: 10.1039/C6PY01872F.

(6) Amalvy, J. I.; Unali, G. F.; Li, Y.; Granger-Bevan, S.; Armes, S. P.; Binks, B. P.; Rodrigues, J. A.; Whitby, C. P. Synthesis of Sterically Stabilized Polystyrene Latex Particles Using Cationic Block Copolymers and Macromonomers and Their Application as Stimulus-Responsive Particulate Emulsifiers for Oil-in-Water Emulsions. *Langmuir* **2004**, *20* (11), 4345-4354. DOI: 10.1021/la035921c.

(7) Ghosh Roy, S.; De, P. Facile RAFT synthesis of side-chain amino acids containing pH-responsive hyperbranched and star architectures. *Polym. Chem.* **2014**, *5* (21), 6365-6378, 10.1039/C4PY00766B. DOI: 10.1039/C4PY00766B.

(8) Tai, H.; Duvall, C. L.; Hoffman, A. S.; Stayton, P. S.; Wang, W. pH-Responsive Hyperbranched Copolymers from One-Pot RAFT Copolymerization. *Macromol. Mater. Eng.* **2012**, *297* (12), 1175-1183. DOI: doi.org/10.1002/mame.201200227.

(9) Wang, D.; Zhao, T.; Zhu, X.; Yan, D.; Wang, W. Bioapplications of hyperbranched polymers. *Chem. Soc. Rev.* **2015**, *44* (12), 4023-4071, 10.1039/C4CS00229F. DOI: 10.1039/C4CS00229F.

(10) Demirci, S.; Kinali-Demirci, S.; Caykara, T. Novel pH-responsive mixed-charge copolymer brushes based on carboxylic acid and quaternary amine monomers. *J. Polym. Sci., Part A: Polym. Chem.* **2013**, *51* (7), 1612-1619. DOI: doi.org/10.1002/pola.26532.

(11) Zhang, Y.-X.; Chen, Y.-F.; Shen, X.-Y.; Hu, J.-J.; Jan, J.-S. Reduction- and pH-Sensitive lipoic acid-modified Poly(l-lysine) and polypeptide/silica hybrid hydrogels/nanogels. *Polymer* **2016**, *86*, 32-41. DOI: doi.org/10.1016/j.polymer.2016.01.030.

(12) Li, T.; Yin, X.; Zhai, W.; He, Y.-F.; Wang, R.-M. Enzymatic Digestion of Keratin for Preparing a pH-Sensitive Biopolymer Hydrogel. *Aust. J. Chem.* **2016**, *69* (2), 191-197. DOI: doi.org/10.1071/CH15224.

(13) Yang, X.; Chen, L.; Huang, B.; Bai, F.; Yang, X. Synthesis of pH-sensitive hollow polymer microspheres and their application as drug carriers. *Polymer* **2009**, *50* (15), 3556-3563. DOI: doi.org/10.1016/j.polymer.2009.06.027.

(14) Darabi, A.; Jessop, P. G.; Cunningham, M. F. CO2-responsive polymeric materials: synthesis, self-assembly, and functional applications. *Chem. Soc. Rev.* **2016**, *45* (15), 4391-4436, 10.1039/C5CS00873E. DOI: 10.1039/C5CS00873E.

(15) Liu, H.; Lin, S.; Feng, Y.; Theato, P. CO2-Responsive polymer materials. *Polym. Chem.* **2017**, *8* (1), 12-23. DOI: 10.1039/C6PY01101B.

(16) Zhang, D.; Fan, Y.; Chen, H.; Trépout, S.; Li, M.-H. CO2-Activated Reversible Transition between Polymersomes and Micelles with AIE Fluorescence. *Angew. Chem. Int. Ed.* **2019**, *58* (30), 10260-10265. DOI: doi.org/10.1002/anie.201905089.

(17) Liu, Y.; Tang, Y.; Barashkov, N. N.; Irgibaeva, I. S.; Lam, J. W. Y.; Hu, R.; Birimzhanova, D.; Yu, Y.; Tang, B. Z. Fluorescent Chemosensor for Detection and Quantitation of Carbon Dioxide Gas. *J. Am. Chem. Soc.* **2010**, *132* (40), 13951-13953. DOI: 10.1021/ja103947j.

(18) Gupta, M.; Lee, H.-i. A Pyrene Derived CO2-Responsive Polymeric Probe for the Turn-On Fluorescent Detection of Nerve Agent Mimics with Tunable Sensitivity. *Macromolecules* **2017**, *50* (17), 6888-6895. DOI: 10.1021/acs.macromol.7b01200.

(19) Darwish, T. A.; Evans, R. A.; Hanley, T. L. Spiropyran, chromene and spirooxazine, mélange á trois: Molecular logic systems through selective and reversible deactivation of photochromism mediated by CO2 gas. *Dyes Pigm.* **2012**, *92* (2), 817-824. DOI: doi.org/10.1016/j.dyepig.2011.03.021.

(20) Xie, Y.; Husband, J. T.; Torrent-Sucarrat, M.; Yang, H.; Liu, W.; O'Reilly, R. K. Rational design of substituted maleimide dyes with tunable fluorescence and solvafluorochromism. *Chem. Commun.* **2018**, *54*, 3339-3342. DOI: 10.1039/c8cc00772a.

(21) Husband, J. T.; Torrent-sucarrat, M.; Reilly, R. K. O. Manipulating the fluorescence lifetime at the sub-cellular scale via photo-switchable barcoding. *Nat. Commun.* **2020**, *11*, 2460. DOI: 10.1038/s41467-020-16297-3.

(22) Darwish, T. A.; Evans, R. A.; James, M.; Malic, N.; Triani, G.; Hanley, T. L. CO2 Triggering and Controlling Orthogonally Multiresponsive Photochromic Systems. *J. Am. Chem. Soc.* **2010**, *132* (31), 10748-10755. DOI: 10.1021/ja1013322.

(23) Wang, Y.; Huo, M.; Zeng, M.; Liu, L.; Ye, Q.-Q.; Chen, X.; Li, D.; Peng, L.; Yuan, J.-Y. CO2-responsive Polymeric Fluorescent Sensor with Ultrafast Response. *Chin. J. Polym. Sci.* **2018**, *36* (12), 1321-1327. DOI: 10.1007/s10118-018-2167-y.

(24) Silva, A. P. D.; Moody, S.; Wright, G. D. Fluorescent PET (Photoinduced Electron Transfer) sensors as potent analytical tools. *Analyst* **2009**, *134*, 2385-2393. DOI: 10.1039/b912527m.

(25) Wang, H.; Xu, M.; Xiong, M.; Cheng, J. Reduction-responsive dithiomaleimide-based nanomedicine with high drug loading and FRET-indicated drug release. *R. Soc. Chem.* **2015**, 4807-4810. DOI: 10.1039/c5cc00148j.

(26) Grison, C. M.; Burslem, G. M.; Miles, J. A.; Pilsl, L. K. A.; Yeo, D. J.; Imani, Z.; Warriner, S. L.; Webb, M. E.; Wilson, A. J. Chemical Science. *Chemical Science* **2017**, *8*, 5166-5171. DOI: 10.1039/c7sc01342f.

(27) Ishiguro, K.; Ando, T.; Goto, H.; Brc, R.; Bank, C. Benchmarks Novel application of 4-nitro-7-(1-piperazinyl)-2, 1, 3-benzoxadiazole to visualize lysosomes in live cells. *Biotechniques* **2008**, *45*, 465, 467-468. DOI: 10.2144/000112912.

(28) Jiang, C.; Huang, H.; Kang, X.; Yang, L.; Xi, Z.; Sun, H.; Pluth, M. D.; Yi, L. NBD-based synthetic probes for sensing small molecules and proteins: design, sensing mechanisms and biological applications. *Chem. Soc. Rev.* **2021**, *50* (13), 7436-7495. DOI: 10.1039/D0CS01096K.

(29) Zhu, M.-q.; Zhu, L.; Han, J. J.; Wu, W.; Hurst, J. K.; Li, A. D. Q. Spiropyran-Based Photochromic Polymer Nanoparticles with Optically Switchable Luminescence. *J. Am. Chem. Soc.* **2006**, *128*, 4303-4309.

(30) Zhu, L.; Wu, W.; Zhu, M.-q.; Han, J. J.; Hurst, J. K.; Li, A. D. Q. Reversibly Photoswitchable Dual-Color Fluorescent Nanoparticles as New Tools for Live-Cell Imaging. *J. Am. Chem. Soc.* **2007**, *129*, 3524-3526.

(31) Raymo, M.; Giordani, S.; V, M. D.; Florida, C. G.; Re, V.; Recei, M.; February, V. Signal Processing at the Molecular Level. *J. Am. Chem. Soc.* **2001**, *123*, 4651-4652.

(32) Shi, J.; Wu, Y.; Sun, S.; Tong, B.; Zhi, J.; Dong, Y. Tunable fluorescence conjugated copolymers consisting of tetraphenylethylene and fluorene units: From aggregation-induced emission enhancement to dual-channel fluorescence response. *J. Polym. Sci., Part A: Polym. Chem.* **2013**, *51*, 229-240. DOI: 10.1002/pola.26377.

(33) Liu, Y.; Deng, C.; Tang, L.; Qin, A.; Hu, R.; Sun, J. Z.; Tang, B. Z. Specific detection of D-glucose by a tetraphenylethene-based fluorescent sensor. *J. Am. Chem. Soc.* **2011**, *133*, 660-663. DOI: 10.1021/ja107086y.

(34) Hong, Y.; Lam, J. W. Y.; Tang, B. Z. Aggregation-induced emission: Phenomenon, mechanism and applications. In *Chemical Communications*, 2009; pp 4332-4353.

(35) Miclotte, M. P. J.; Lawrenson, S. B.; Varlas, S.; Rashid, B.; Chapman, E.; O'Reilly, R. K. Tuning the Cloud-Point and Flocculation Temperature of Poly(2-(diethylamino)ethyl methacrylate)-Based Nanoparticles via a Postpolymerization Betainization Approach. *ACS Polym. Au* **2021**, *1* (1), 47-58. DOI: 10.1021/acspolymersau.1c00010.

(36) Perrier, S. 50th Anniversary Perspective: RAFT Polymerization—A User Guide. *Macromolecules* **2017**, *50* (19), 7433-7447. DOI: 10.1021/acs.macromol.7b00767.

(37) Chakraborty, P.; Sharma, A.; Luqman, M.; Khan, M. F.; Sankhydhar, K. Chapter 8 - CO2-triggered switchable polarity solvents and their advancements. In *Green Sustainable Process for Chemical and Environmental Engineering and Science*, Inamuddin, Boddula, R., Asiri, A. M. Eds.; Elsevier, 2022; pp 149-156.

(38) Rezk, M. Y.; Sharma, J.; Gartia, M. R. Nanomaterial-Based CO_2 Sensors. *Nanomaterials* **2020**, *10* (11), 2251. DOI: 10.3390/nano10112251.

(39) Tian, J.; Huang, B.; Xiao, C.; Vana, P. Intelligent CO2- and photo-dual-responsive polymer vesicles with tunable wall thickness. *Polym. Chem.* **2019**, *10* (13), 1610-1618. DOI: 10.1039/c8py01743c.

(40) Xie, Y. Fluorescent substituted maleimides : from small molecule fluorophore to polymeric barcoding. University of Warwick, 2020.

(41) Mabire, A. B.; Brouard, Q.; Pitto-Barry, A.; Williams, R. J.; Willcock, H.; Kirby, N.; Chapman, E.; O'Reilly, R. K. CO2/pH-responsive particles with built-in fluorescence read-out. *Polym. Chem.* **2016**, *7*, 5943-5948. DOI: 10.1039/c6py01254j.

(42) Wang, Y.; Huo, M.; Zeng, M.; Liu, L.; Ye, Q. Q.; Chen, X.; Li, D.; Peng, L.; Yuan, J. Y. CO_2-responsive Polymeric Fluorescent Sensor with Ultrafast Response. *CJPS* **2018**, *36*, 1321-1327. DOI: doi.org/10.1016/j.jbc.2022.102402.

3 pH-responsive polymer-supported pyrene-based fluorescent dyes for CO_2 detection in aqueous environments

3.1 Abstract

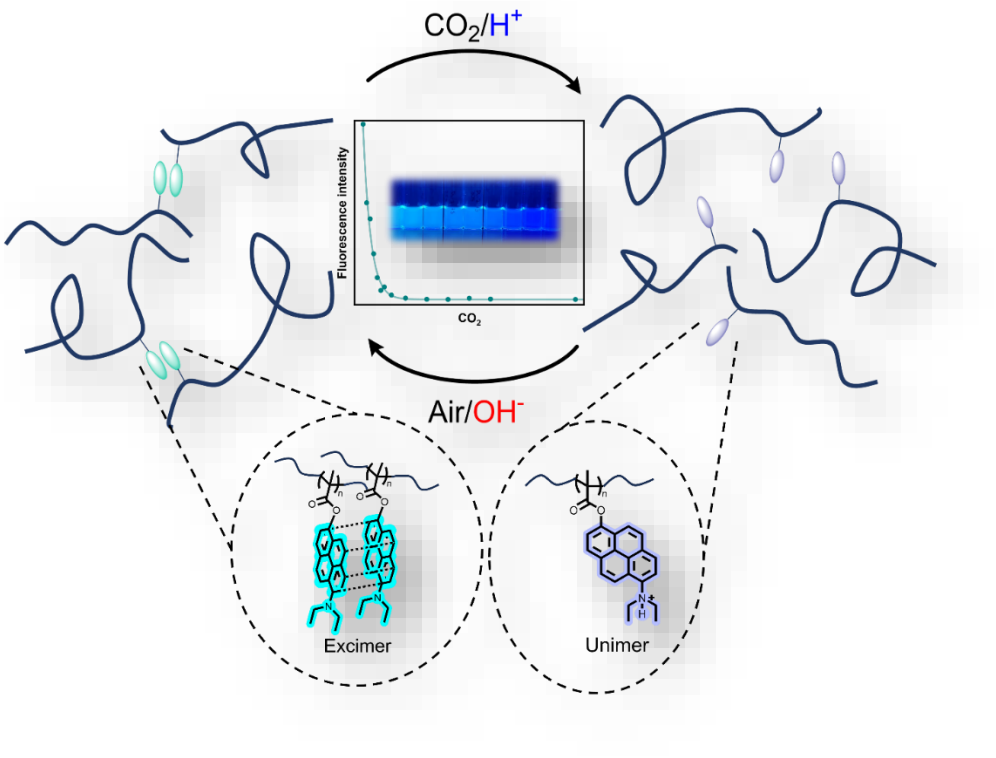

Detecting fluctuations in carbon dioxide by switching ‘on’ or ‘off’ fluorescence in aqueous environments has often been targeted for efficient monitoring. This switch needs to occur in a drastic and fast way that is visually observable to be effective. CO_2 dissolves in water, leading to a reduction in pH, which can be used to trigger a response. Specifically, the modification of fluorescent dyes with pH-responsive units could create a dye that responds to CO_2 and switches "off" fluorescence. Here, we developed a water-soluble polymer functionalized with a CO_2-responsive pyrene dye. This functional dye contains a tertiary amine conjugated to the aromatic pyrene, which can be protonated at pH ~ 6.5 or lower. After only 15s of CO_2 bubbling, a significant fluorescence "off" response was observed, with a drastic reduction in fluorescence at 480 nm as a consequence of breaking excimer bonds. Moreover, the exposure to atmospheric air results in a recovery of the excimer state and, therefore, the fluorescence, demonstrating its reversible nature.

3.2 Introduction

In Chapter 2, we developed nanoparticle systems that showed a response to CO_2 and reversibility with N_2. However, the change in visual fluorescence was not significant enough for use as a visual sensor for CO_2 detection. Therefore, in this chapter, we propose an alternative approach to the one previously used based on a combination of polymer and molecular-based sensors.

Chemical-based sensors, ranging from molecular-based to macromolecular sensors, have been investigated as an alternative strategy for detecting CO_2.[1, 2] These sensors operate by undergoing a compositional change in their chemical structure upon exposure to CO_2, which leads to a response.

Polymer-based sensors offer a stable and easily applicable delivery system, typically comprising a responsive monomer and a dye molecule. Over the past decade, numerous CO_2-responsive polymeric systems with fluorescence read-outs have been reported, commonly consisting of pH-responsive and polar-sensitive fluorescent units.[3-12] They respond to CO_2 by changing the conformation of the polymer, leading to a different microenvironment around the dye molecule, which changes its fluorescence. This response is due to CO_2 forming carbonic acid in water, which can dissociate into HCO_3^-, CO_3^{2-}, and H^+, allowing protonation of amine-based monomers. However, the response rate to CO_2 is often limited by conformational changes in the macromolecular structure.[13]

Molecular-based CO_2 sensors typically involve dye molecules that undergo a chemical transformation when exposed to CO_2, resulting in a detectable signal change. For example, Morandi and coworkers developed a range of deactivated dye molecules that switched on in the presence of CO_2. This highly sensitive and selective molecular sensor

was capable of detecting CO_2 at atmospheric levels (as low as eight ppm).[14] Common dye molecules were modified to include an iminophosphorane group that, in the presence of CO_2, undergoes a cascade aza-Wittig reaction that turns on its fluorescence. However, a significant limitation of this sensor is its non-reversibility, meaning it cannot be reused after detection, which poses challenges for continuous monitoring applications. On the other hand, Lee and coworkers developed an imidazolium-based ionic polymer system for CO_2 detection in both organic and aqueous media. This polymer controlled fluorescence through an ON/OFF mechanism. Upon complex formation, fluorescence was turned "ON" in organic media and solid films, driven by a photo-induced transmission "OFF" photophysical effect. In contrast, the introduction of CO_2 in aqueous media led to fluorescence quenching due to aggregation-caused quenching (ACQ) of polymeric nanoparticles, along with the formation of carbamate anions.[15]

Ideally, a combination of polymer and molecular-based systems should be developed. Such a system would involve a reversibly CO_2-responsive dye molecule that changes fluorescence due to direct fluctuation in CO_2 levels. Incorporating this system into a polymer delivery system would potentially increase its applicability and usability in aqueous environments. The desired characteristics for this system include reversibility, reusability, fast response, low detection limit, and activation in the presence of CO_2 in water and deactivation upon the removal of CO_2.

We reasoned that to establish a robust approach for detecting pH variations induced by CO_2 through fluorescence fluctuations in aqueous solution, we needed to address three essential considerations: First, a fluorescent dye able to switch ON/OFF its fluorescence properties after the interaction with CO_2, second, a CO_2 reactive site able to interact with

it in a reversible manner and finally, an innocuous delivery method to transport the system into water solution.

As fluorescent dye, we turned our attention into pyrene as it is one of the most studied fluorescent dyes in the literature, shows to have remarkable chemical stability under different conditions, and is versatile in terms of modification of its structure and has interesting fluorescent properties that can be modulated.[16-24] The fluorescence emission spectrum of pyrene exhibits five major vibronic bands (Bands I to V) with distinct peaks at approximately 375, 379, 385, 395, and 410 nm, attributed to $\pi \rightarrow \pi^*$ transitions. These collectively form the monomeric emission. Additionally, an unstructured band appears at longer wavelengths (425 to 550 nm, centered around 480 nm) when ground state and excited state pyrene rings are close, resulting in excited state dimer or 'excimer' emission.[17] The long lifetime of pyrene emission (50–90 ns) allows this excited state reaction to occur, either dose-dependently in high concentrations or when two pyrenes are close in an intra-molecular context. This phenomenon can be modulated with the modification of the substituents at various positions and can result in distinct fluorescent properties.[18]

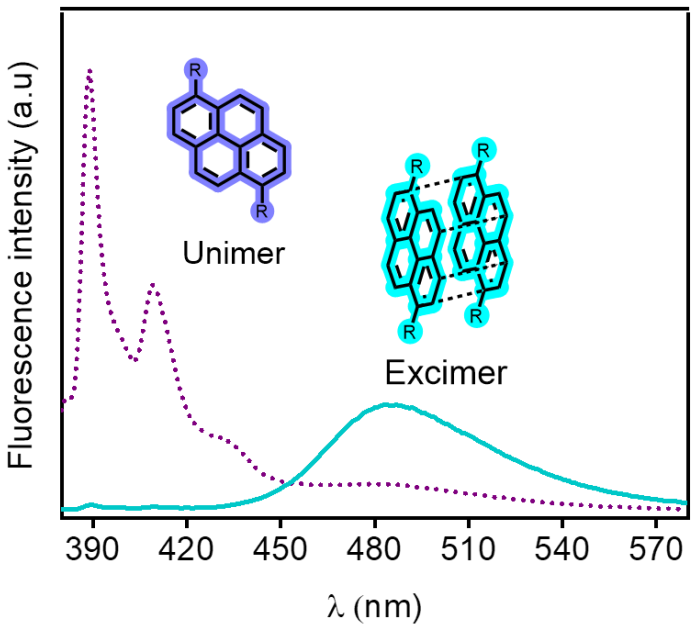

Figure 3.1. Pyrene emission peaks. (Unimer at 385 nm, excimer at 490 nm).

In this study, a modified pyrene-based CO_2 sensing molecule was developed that could be readily incorporated into polymeric supports. Pyrene dye molecules were functionalized with pH-responsive amine functionality, which, upon protonation, turned off fluorescence. This responsive dye-based sensor displayed visible changes in fluorescence, detecting changes in CO_2 as a function of pH at parts per billion concentrations of dye. This pyrene-modified unit was incorporated into linear polymers and displayed a drastic response to changes in pH. Notably, this marks a significant moment as it represents an instance where the fluorescence of pyrene is extinguished by disrupting excimer bonds in the presence of CO_2 within a polymeric system in aqueous solution. Furthermore, the quenching effect is entirely reversible upon exposure to atmospheric air.

3.3 Results and discussion

3.3.1 Design and synthesis of pH-responsive pyrenes

We aimed to modify the chemical structure of pyrene dye to be pH-responsive, creating drastic changes in fluorescence when interacting with CO_2. To achieve this, we wanted to attach an amino pH-responsive unit to the dye that becomes protonated under acidic conditions. This protonation will directly affect its fluorescent properties by decreasing the excimer/unimer ratio due to electrostatic repulsion, drastically changing the dyes emission. However, due to its high hydrophobicity, evaluating its properties in water solution could be challenging. Consequently, we needed to incorporate this modified dye into a polymeric scaffold that enhances its water solubility.

Our aim was to synthesize a water-soluble polymer integrating pyrene derivatives functionalized with N,N-dimethylamino and N,N-diethylamino groups, each offering distinct reactivity and responsiveness to pH and CO_2 variations (figure 1). The selection of these amines was guided by the pKa estimated by chemaxon (5.33 and 6.19, respectively), where we anticipated that the diethylamino group would exhibit optimal reactivity with CO_2, with increased protonation in the HCO_3^-/CO_3^{2-} system, resulting in a more dramatic change in the fluorescence of the probe.

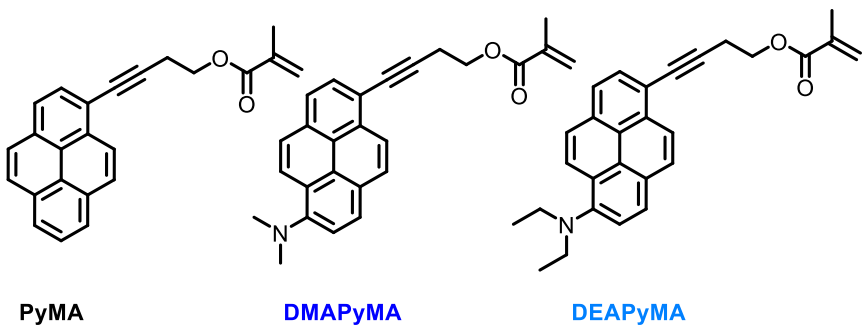

Figure 3.2. Targeted pyrene monomers with and without pH-responsive groups

For the synthesis of the pyrene-based monomers, we proposed a general synthetic route for the two designed monomers. We opted to modify position 1 of pyrene with a tertiary amine and a methacrylate functional group in position 6 (figure 3.2). The most straightforward approach to accomplish this involved dialkylation of the commercially available 1-aminopyrene with the corresponding alkyl iodide, according to a protocol developed in the Wagenknecht laboratory.[25] This was then followed by the addition of a bromo group at position six via bromination with N-bromosuccinimde (NBS). This enabled the subsequent Sonogashira cross-coupling reaction with 3-butyn-1-ol. Esterification with EDC and methacrylic acid was used to obtain the methacrylate monomer diethylamino pyrene methacrylate (DEAPyMA).

We hypothesized that because of the strong repulsion generated from the positive charge of protonated amines in the DEAPyMA moiety it would increase the distance between pyrene units and would consequently break the excimer state. This would be translated in switching the fluorescence from an ‘ON’ to an ‘OFF’ state. We empirically validated our hypothesis by examining the spectral properties of the different pyrene monomers in mixtures of H_2O/MeCN (95:5) at various pH levels (figure. 3.3). As expected, the DEAPyMA dye exhibited distinctive emission peaks in the different mixtures, clearly transitioning from an 'ON' state in basic pH to an 'OFF' state in acidic conditions.

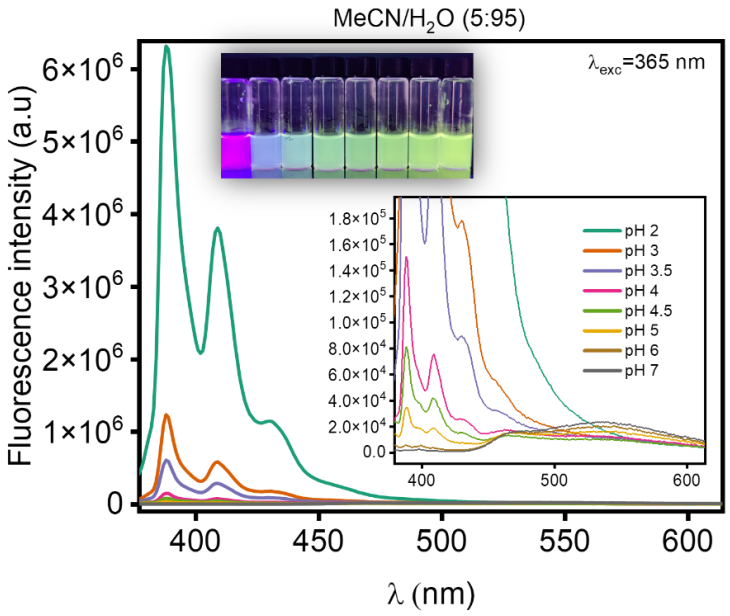

Figure 3.3. Fluorescence spectrum of DEAPyMA at different pHs in MeCN/H_2O (5:95) mixtures. Concentration of 27 nM. λ_{exc}= 365nm.

3.3.2 Synthesis and pH-responsiveness of water-soluble polymers containing pyrene monomers (PyMA, DMAPyMA and DEAPyMA)

Given the hydrophobic nature of the monomer, the subsequent objective involved evaluating its pH sensitivity in an aqueous solution by polymerizing the fluorescent monomer within a water-soluble, non-pH-responsive system. An initial reaction was conducted at 80 ºC by reacting 100 equivalents of N,N-dimethylacrylamide (DMAm) with 1 equivalent of DEAPyMA, 4-[[[(2-carboxyethyl)thio]thioxomethyl]thio]-4-cyanopentanoic acid as chain-transfer agent and 4,4 -azobis(4-cyanovaleric acid) ACVA as radical initiator for 16 hours. The obtained polymer (figure. 3.4a) was purified by extensive dialysis using 3 kDa membrane, in H_2O/THF (1:1). The molecular weight of the polymer was calculated via end-group analysis, showing a 96% of conversion for DMAm whereas a 76% of conversion regarding DEAPyMA, this might be due to the

different nature of the monomers as well as the bigger size of DEAPyMA in comparison to DMAm (approximately 4 times) giving a value of ($M_{n,NMR}$ = 10.1 kDa). We experimentally validated our hypothesis by investigating the optical characteristics of the polymer with a 1 mol% loading of DEAPyMA in an aqueous solution. The addition of the amine to the pyrene structure resulted in a noticeable redshift in both absorption and emission spectra compared to the non-pH-responsive PyMA (figure. 3.4b).

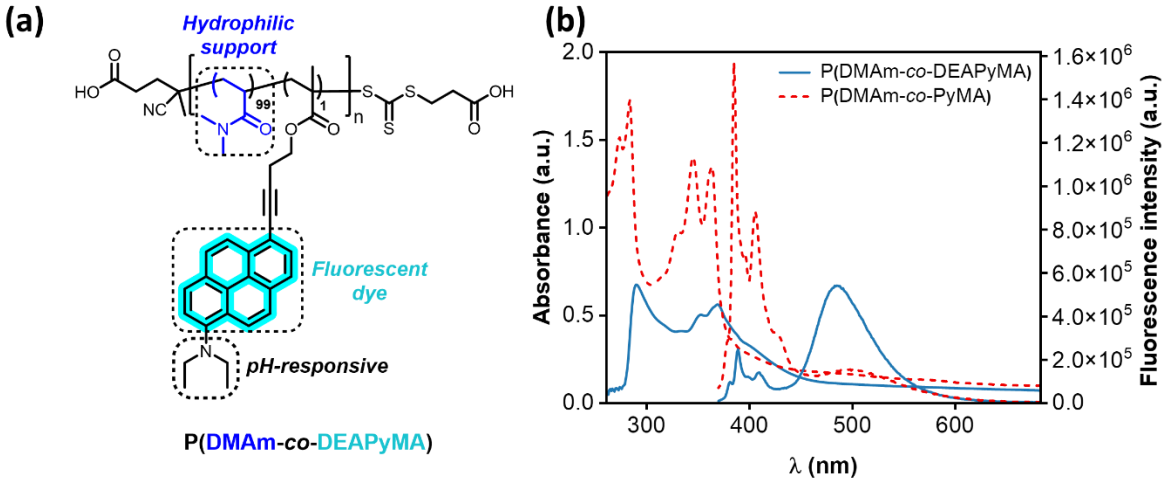

Figure 3.4. (a) Scheme of chemical structure of poly(dimethylacrylamide-co-diethylamino pyrenemethacrylate). (b) UV-Vis and fluorescence spectra of both P(DMAm$_{99}$-co-DEAPyMA$_1$) (continuous line) and P(DMAm$_{99}$-*co*-PyMA$_1$) (discontinuous line) in water at pH 7. Concentration 1 mg/mL. λ_{exc}= 350 nm.

The responsiveness of the polymer containing DEAPyMA was evaluated across the entire pH spectrum. As depicted in figure. 3.4a, the dye exhibited two distinct fluorescent emission bands between 370-420 nm, corresponding to the pyrene unimer, and an additional band at 490 nm indicative of excimer species formation. We synthesized two other control polymers, one integrating a non-pH responsive pyrene unit P(DMAm$_{99}$-*co*-PyMA$_1$) and the other with a dimethylamino moiety as a responsive unit, P(DMAm$_{99}$-*co*-DMPyMA$_1$). The first one showed a constant fluorescence emission through the whole

pH spectrum (figure. 3.5b), whereas the P(DMAm$_{99}$-*co*-DMPyMA$_1$) only showed a response at pH values below 3 (figures 3.6a and b).

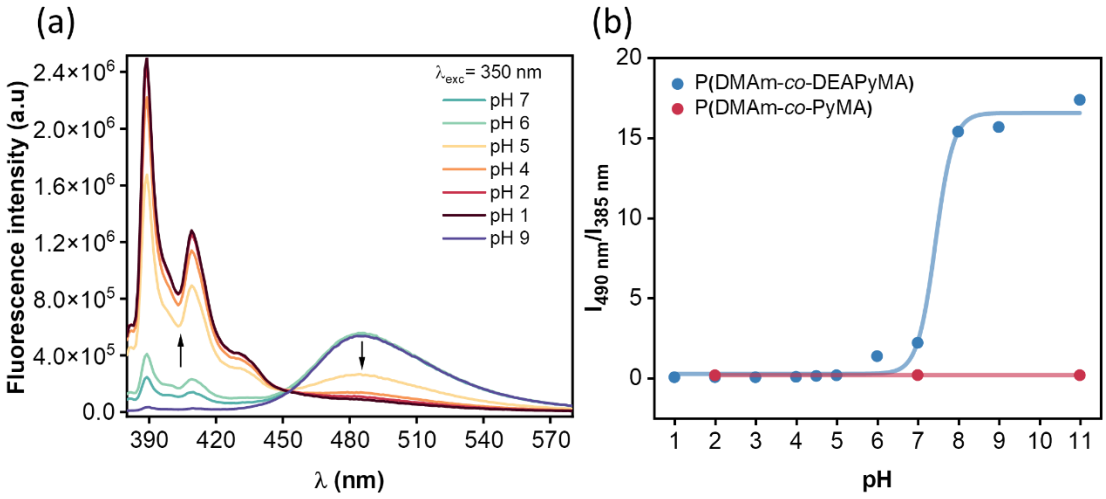

Figure 3.5. (a) Fluorescence spectra of P(DMAm$_{99}$-co-DEAPyMA$_1$) at different pHs 7, 6, 5, 4, 3, 2 and 1. Concentration 0.1 mg/mL. λ_{exc}= 350 nm. (b) Graphic representing change in intensity ratio I_{490nm}/I_{385nm} as effect of the pH for P(DMAm$_{99}$-co-DEAPyMA$_1$) and P P(DMAm$_{99}$-co-PyMA$_1$). Concentration 0.1 mg/mL. λ_{exc}= 350 nm.

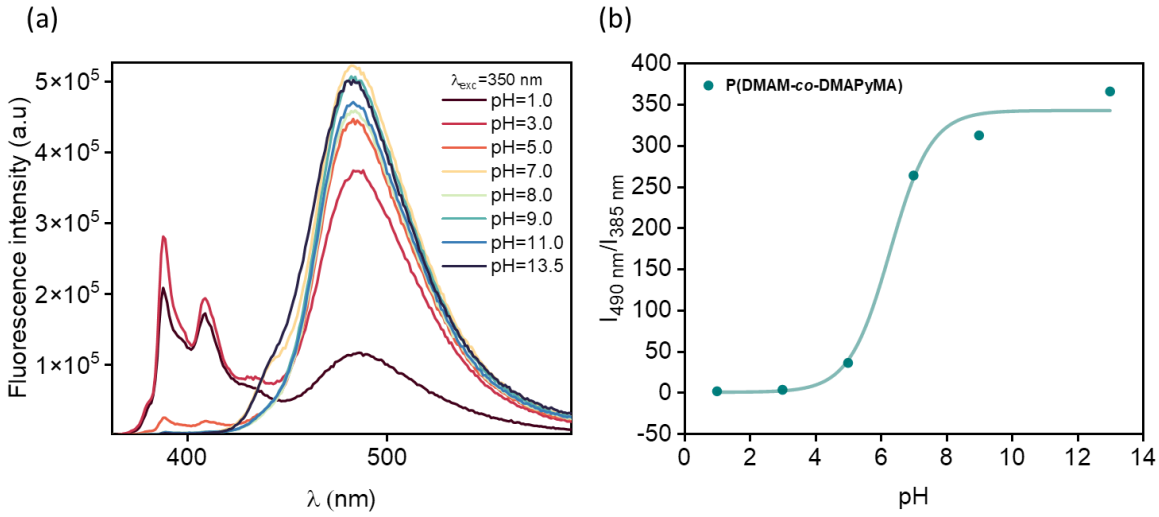

Figure 3.6. (a) Fluorescence spectrum of P(DMAm$_{99}$-*co*-DMPyMA$_1$) at different pHs in aqueous solution. 1 mol% of DMAPyMA. Concentration of 10 ppm. λ_{exc}= 350 nm. (b)

Fluorescence intensity ratio (490 nm/385nm) of P(DMAm$_{99}$-*co*-DMPyMA$_1$) in aqueous solution at different pHs (1, 3, 4, 7, 9 and 13). Concentration of 0.5 mg/mL.

Polymers with 0.1 and 0.5 % of DMAPyMA were prepared and it was confirmed that the fluorescence intensity corresponding to the excimer (490 nm) formation also depended on the concentration of the dye present in the solution (figure. 3.7a and b). We could see that the changes in fluorescence emission were more gradual with the polymer containing 0.1 mol% of dye that with a higher concentration.

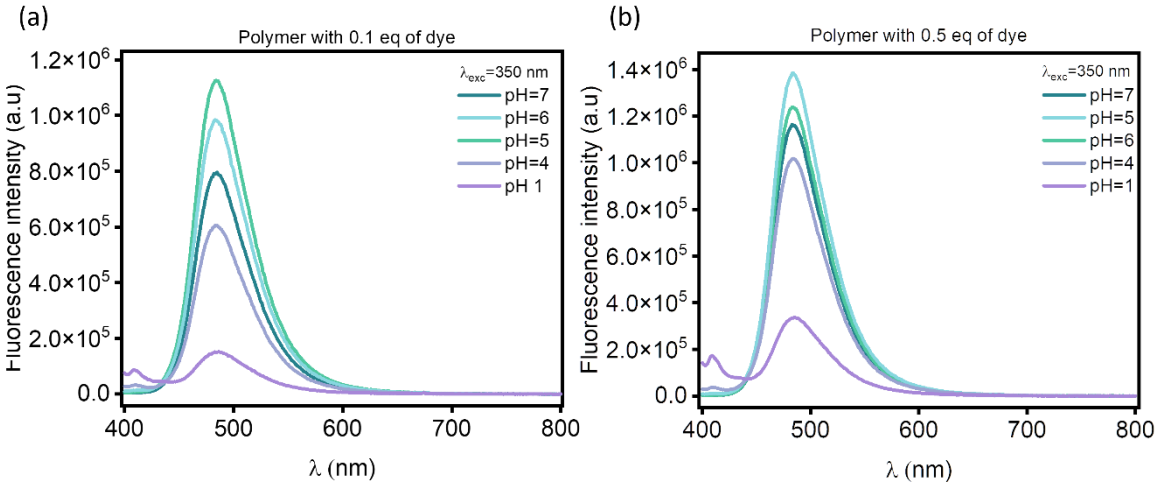

Figure 3.7. Fluorescence spectrum of P(DMAm$_{99}$-*co*-DMPyMA$_1$) at different pHs in aqueous solution. (a) 0.1 mol% of DMAPyMA. (b) 0.5 mol% of DMAPyMA. Concentration of 10 ppm. λ_{exc}= 350 nm.

In contrast, with P(DMAm$_{99}$-*co*-DEAPyMA$_1$), a decrease in pH from basic to acidic led to an increase in the intensity of the unimer pyrene emission peaks, coupled with a decrease in excimer peak intensity (figure. 3.5b). In this case, the changes in the intensity of each peak were observed to be more pronounced than in the free molecule. We think this was due to a solubility issue and the concentration of the dye, as this is lower in the polymer. This suggests that as the amine became protonated, electrostatic repulsion between positively charged amines caused the disruption of π-π interactions between

excimers. This underscores the role of the pyrene unit in the observed pH-dependent fluorescence changes.

We confirmed our hypothesis by conducting fluorescence lifetime measurements on an aqueous solution of P(DMAm$_{99}$-*co*-DEAPyMA$_1$) at pH 2, 4.5, and 7. As anticipated, we observed a decrease in fluorescence lifetime, indicative of excimer formation facilitating non-radiative pathways leading to a faster relaxation to the ground state compared to the unimer. Notably, we observed that the lifetimes corresponding to excimer peaks (490 nm) decreased to half the values compared to those obtained at the same pHs at 385 nm (figure. 3.8).

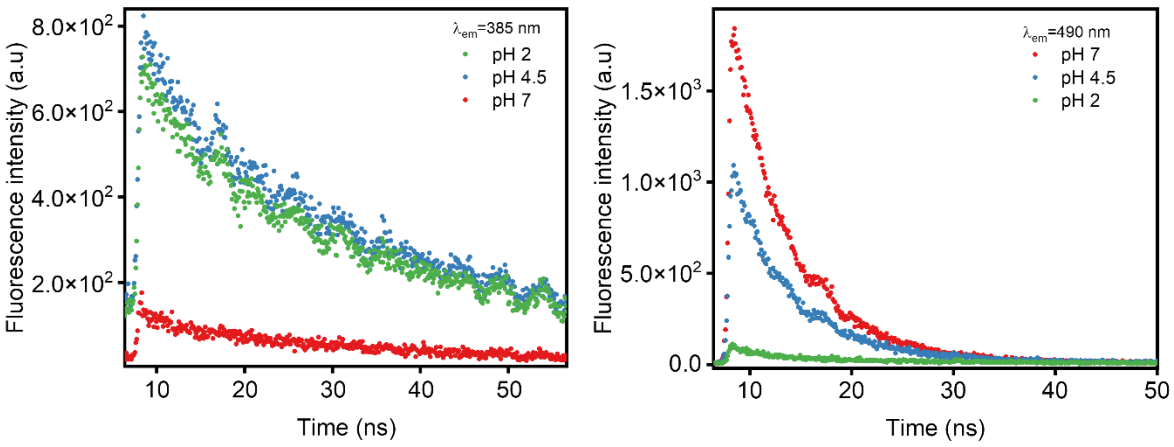

Figure 3.8. Lifetime spectrum of P(DMAm$_{99}$-*co*-DEAPyMA$_1$) in aqueous solution at different pHs and at r.t. Concentration of 0.01 mg/mL (10 ppm). λ_{exc}= 350 nm. λ_{em}= 385, 490 nm. 1 mol% of DEAPyMA in polymer.

Furthermore, we aimed to investigate the detection limit concerning both the polymer and the dye. To achieve this, we prepared samples of P(DMAm$_{99}$-*co*-DEAPyMA$_1$) at five different concentrations and assessed them over a pH range where a significant fluorescence change could be detected (figure 3.9b). The polymer exhibited a noteworthy pH response with a distinct fluorescence ON/OFF transition in the parts per million (ppm)

range (figure 3.9a). Interestingly, the visual response was even more pronounced in the parts per billion (ppb) range for the fluorescent dye, given its presence at around 1 mol% of charge within the polymer chains. This makes DEAPyMA potentially sensitive to CO_2 in aqueous solution. Correspondingly, the fluorescence intensity ratio I_{490nm}/I_{385nm} of P(DMAm$_{99}$-*co*-DEAPyMA$_1$) gradually increases as the pH does.

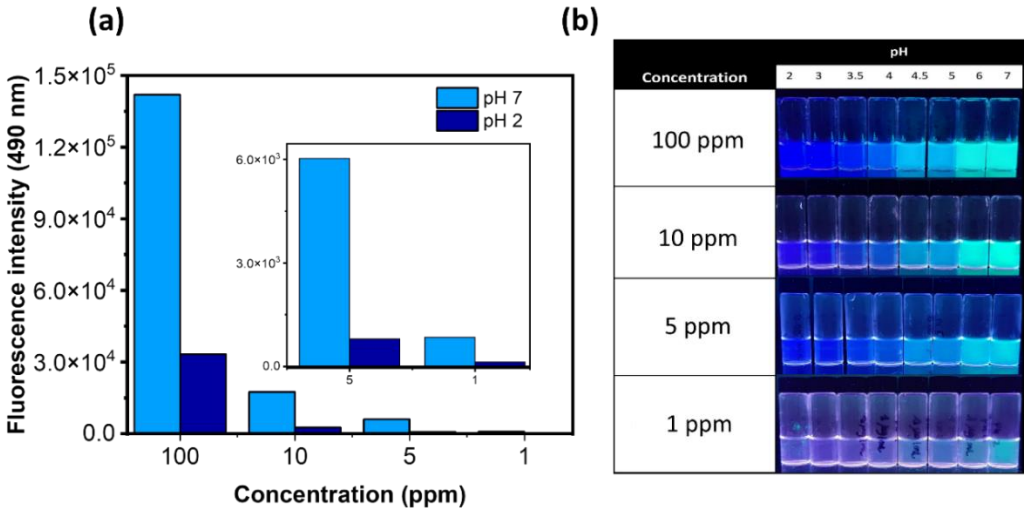

Figure 3.9. (a) Fluorescence intensity of P(DMAm$_{99}$-*co*-DEAPyMA$_1$). (Concentrations: 100, 10, 5 and 1 ppm, pH 7 and 2, λ_{exc}= 350 nm, λ_{em}= 490 nm) (b) Photograph of P(DMAm$_{99}$-*co*-DEAPyMA$_1$) at different concentrations in aqueous solution and different pHs under 365 nm UV-light.

Following the work by Lie et al.,[26] the pKa of DEAPyMA was calculated as 4.4 using the Henderson-Hasselbalch equation (figure 3.10), suggesting its suitability for pH quantification in acidic to neutral environments and CO_2 detection.

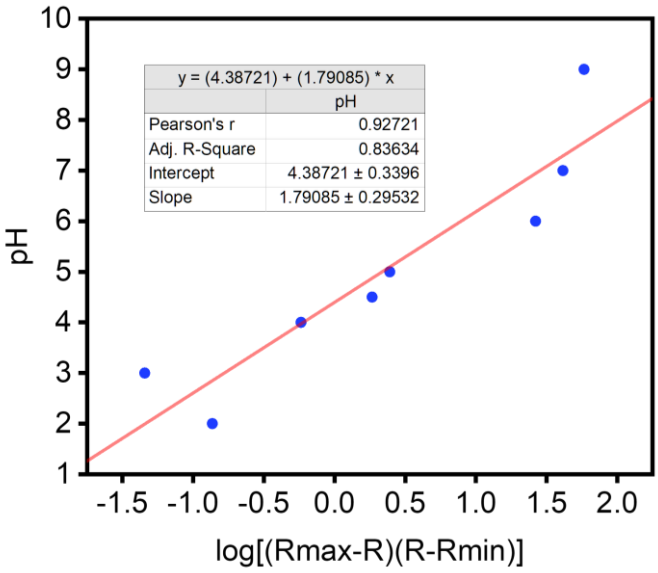

Figure 3.10. pKa of P(DMAm$_{99}$-*co*-DEAPyMA$_1$) calculated using the Henderson-Hasselbach-type mass action equation (pH = pKa + c*log[(R−Rmin)/(Rmax−R)] + log(Ia/Ib)) through analyzing fluorescence intensity ratio changes as a function of pH. Where Rmax (or Rmin) is the maximum (or minimum) ratio value (I_{490nm}/ I_{385nm}), c is the slope and Ia /Ib is the ratio of absorption intensity in acid to the absorption intensity in base at the wavelength chosen for the denominator of R. The pKa value for P(DMAm$_{99}$-*co*-DEAPyMA$_1$) was 4.4.

3.3.3 CO_2, air, and reversibility responsiveness of water-soluble polymers containing pyrene monomers (PyMA, DMAPyMA and DEAPyMA)

To evaluate the system's effectiveness in CO_2 detection, we monitored the fluorescence emission of a 1 ppm sample of P(DMAm$_{99}$-*co*-DEAPyMA$_1$) in water before and after exposing it to a continuous flow and pressure of CO_2. Within minutes, a notable change in visual fluorescence occurred. The reaction kinetics were further investigated by measuring the fluorescence ratio (I_{490nm}/I_{385nm}) at various time intervals with different CO_2 volumes.

Optical characteristics and pH assessments of the polymeric matrix were conducted before and after exposing it to a constant CO_2 flow (50 cm^3/min) and pressure (1 bar). After 15 seconds, an abrupt alteration in fluorescence intensity occurred, accompanied by a significant pH decrease from 7.4 to 5.6. The fluorescence intensity ratio gradually declined from 1.8 to 0.07 as the CO_2 volume reached 25 cm^3, ultimately stabilizing (figures. 3.11a and b).

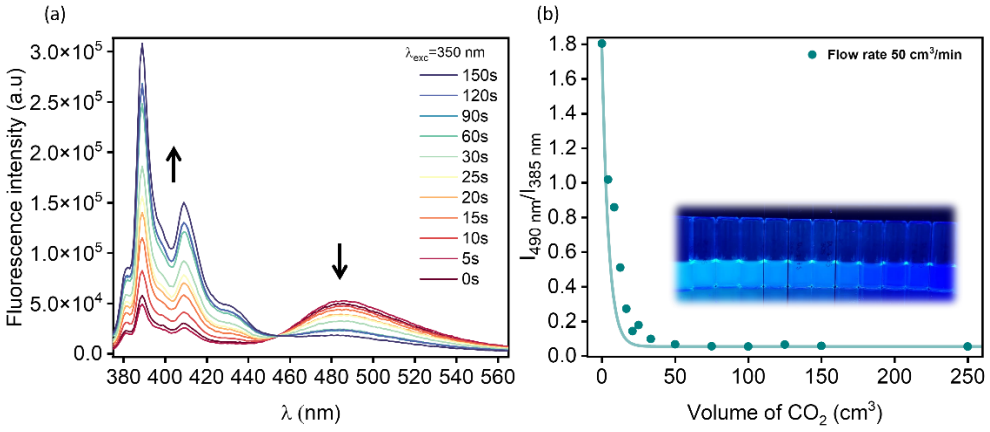

Figure 3.11. (a) Fluorescence spectra of P(DMAm$_{99}$-*co*-DEAPyMA$_1$) after CO_2 kinetics for 150s. Concentration 0.01 mg/mL. λ_{exc}= 350 nm. (b) Kinetics graph represents a change in fluorescence intensity ratio I_{490nm}/ I_{385nm} of a sample of concentration 0.01 mg/mL as the effect of the volume of CO_2.

As the protonation reaction of P(DMAm$_{99}$-*co*-DEAPyMA$_1$) was reversible, we assumed that the fluorescence could be recovered by removing CO_2 by exposing the system to air. The system previously exposed to CO_2 for 10 min, was then exposed to atmospheric air, resulting in a gradual recovery of fluorescence (figure. 3.12a). The fluorescence intensity ratio (I_{490m}/I_{385nm}) gradually increased from 0.07 to 1.56 (figure. 3.12b). The fluorescence intensity at 490 nm exhibited an increase after being exposed to air, while the intensity at 385 nm experienced a sharp decrease. This reversal process took more time compared to the response to CO_2, requiring exposure to air for 25 minutes to observe a substantial

change in fluorescence and 1 hour for complete recovery of the excimer state, as illustrated in figure. 11a. Images of different samples were also taken at various times under 365 nm UV-light (figure. 3.12b), to visualize the reversible fluorescence change.

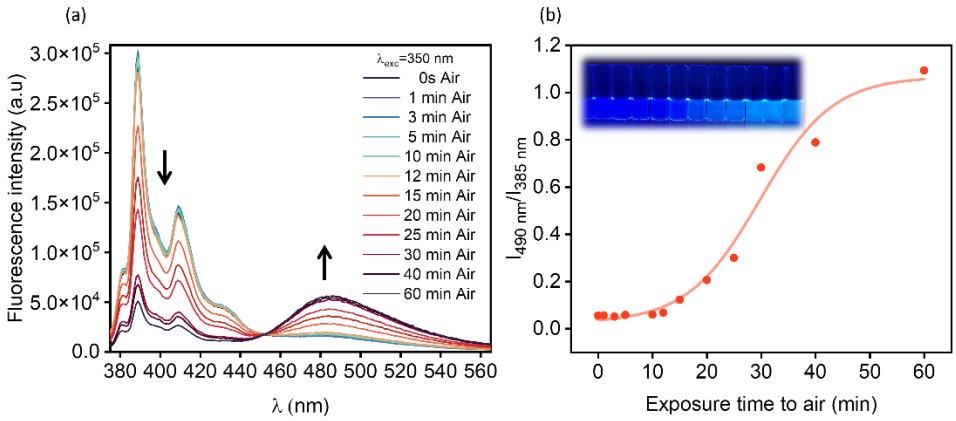

Figure 3.12. (a) Fluorescence spectra of P(DMAm$_{99}$-*co*-DEAPyMA$_1$) after exposure to air for 60 min. Concentration 0.01 mg/mL. λ_{exc}= 350 nm. (b) Kinetics graph representing a change in fluorescence intensity ratio I_{490nm}/ I_{385nm} of a sample of concentration 0.01 mg/mL as the effect aeration of the solution.

Subsequently, the system underwent multiple cycles of CO_2 exposure for 5 minutes (OFF) and air exposure for 1h (ON) to evaluate its reversibility. These results demonstrated that this system's CO_2-responsive fluorescence property was stable and possessed excellent repeatability over at least 6 cycles, transitioning between an ON and OFF state, as shown in figure. 3.13.

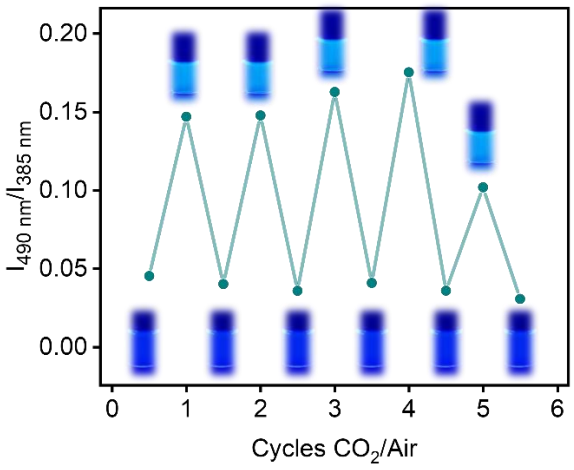

Figure 3.13. Graphic representing the change in fluorescence intensity ratio I_{490nm}/ I_{385nm} of a concentration 0.01 mg/mL sample when being exposed to CO_2 for 5 min and air for 1h for 6 cycles.

3.4 Conclusion

In this study, we developed a new water-soluble linear polymer via RAFT polymerization, incorporating a custom-designed pyrene-based monomer that responds to pH and CO_2. The polymer showed a distinct and highly sensitive fluorescence "turn-off" when exposed to CO_2, with a rapid response time of around 15 seconds, even at concentrations in the ppb range. This sensitivity is likely due to the interaction between CO_2 and the amino group on the pyrene unit, which disrupts intermolecular excimer formation through increased electrostatic repulsion between neighboring pyrene moieties. This fluorescence change was not only quick and pronounced but also fully reversible, with the polymer reliably returning to its initial state after at least six exposure cycles under ambient conditions. These results suggest strong potential for use in real-time CO_2 detection, particularly in aqueous or humid environments where fast and reversible sensing is essential.

The sensing mechanism aligns with previous work on pyrene-based excimer systems[27] and CO_2-responsive amine-containing polymers[28] reinforcing the broader relevance of this approach. Compared to some other CO_2-responsive systems, this polymer stands out due to its combination of solubility, fast kinetics, and sensitivity at low concentrations.

Looking ahead, further experiments are needed to confirm the reproducibility of this behavior in different polymer architectures and under varying environmental conditions, such as temperature, ionic strength, and gas mixtures. Exploring ways to incorporate this

system into coatings, films, or hybrid materials could also open practical applications in smart packaging, industrial safety monitoring, or environmental sensors.

Overall, this work contributes to the growing field of responsive materials by offering a simple yet effective route toward CO_2 detection, and lays the groundwork for future developments in smart, real-time sensing technologies.

.

3.5 Experimental section

3.5.1 Materials

1-Aminopyrene (97%), 1-bromopyrene (98%), triethylamine (TEA), cupper (I) iodide, (98%), 3-butyn-1-ol (97%), methacrylic acid (250 ppm MEHQ, 99%), methacryloyl chloride (250 ppm MEHQ, 97%), N,N-dimethylacrylamide (DMAm, 99%, 500 ppm MEHQ), 4-(dimethylamino) pyridine (DMAP) (≥99%), 4,4'-azobis(4-cyanovaleric acid) (ACVA, 98%), acetonitrile (MeCN, ≥99.9%), methyl iodide (99%), ethyl iodide (99%), and 4-cyano-4-(phenylcarbonothioylthio)pentanoic acid (CPAD) were obtained from Sigma-Aldrich. 1-(3-dimethylaminopropyl)-3 ethylcarbodiimide hydrochloride (EDC-HCl, 98+%) was acquired from Acros-Organics. 1,4-Dioxane (99%), ethyl acetate (EtOAc, ≥99%), hexane (Hex, ≥95%), chloroform ($CHCl_3$, 99%) dichloromethane (CH_2Cl_2, 99%), and Na_2SO_4 anhydrous (99+%, Extra Pure) were obtained from Fisher Scientific.1kg CP carbon dioxide-cylinder and pure nitrogen was obtained from BOC. Spectrum Spectra/Por dialysis tubing with either 1 kDa or 6–8 kDa MWCO was supplied by Fisher Scientific. Deionized and 18.2 MΩ·cm ultrapure water was obtained from a triple red alto purification system and was used in all experiments unless stated otherwise.

3.5.2 Characterization techniques

NMR Spectroscopy. ^{1}H-NMR and ^{13}C-NMR spectra were recorded at 400 MHz on a Bruker DPX-400 spectrometer, using dimethylsulfoxide-d_6 (DMSO-d_6) as the solvent. Chemical shifts of protons are reported as δ in parts per million (ppm) and are relative to solvent residual peaks.

High Resolution Mass Spectra (HR-MS). Were obtained by using Bruker UHR-Q-ToF MaXis spectrometer with electrospray ionization.

Fluorescence Spectroscopy. All steady state emission and excitation were obtained with an Edinburgh Instruments FS5 Spectrofluorometer in matched quartz 3.5 mL cuvettes (Starna Cell, Type: 3/Q/10), and analyzed in Fluoracle (Edinburgh Instruments) and Origin Pro 2022 (Origin Labs). All samples of the pH studies were prepared at concentration of 0.3 mg/ml and different buffers solutions.

Fourier-Transform Infrared Spectroscopy. Fourier-Transform Infrared (FTIR) spectroscopy was conducted using an Agilent Technologies Cary 630 FTIR spectrometer. 16 Scans from 600 to 4000 cm^{-1} were taken at a resolution of 4 cm^{-1}, and the spectra were corrected for background absorbance.

Size Exclusion Chromatography. Molecular weight distributions were determined using aqueous size exclusion chromatography (SEC) on an Agilent PL50 instrument fitted with an Agilent PL aquagel-OH MIXED-M column (300 × 7.5 mm × 5 µm) and an aquagel guard column. The mobile phase used was DMF containing 4.6 mM of NH_4BF_4, at a flow rate of 1.0 mL min^{-1}, a column temperature of 40 °C and detection by refractive index (RI). 80 µL of sample were injected for each measurement and eluted for 35 min. Samples were prepared at a concentration of 1 mg mL^{-1} and filtered using a 0.45 µm nylon filter prior to analysis. Calibration was conducted in the molecular weight range 100-30000 Da using EasiVial polyethylene glycol (PEG) standards supplied by Agilent Technologies.

UV-Vis Spectroscopy. UV-Vis spectroscopy was performed using a Thermo Scientific Evolution 350 UV-Vis spectrophotometer equipped with a Xenon flash lamp light source

and a dual-matched silicon photodiode detector. Quartz cells (360–2500 nm) from Hellma with two polished sides were used for examining the transmittance spectral data by using Thermo INSIGHT-2. All samples were prepared at concentration of 0.3 mg/ml and different buffers solutions.

CO_2 bubbling experiments procedure. In a 50 mL round-bottom flask (RBF), an aqueous solution containing 10 ppm of P(DMAm-*co*-DEAPyMA) polymer is prepared by dissolving 0.4 mg of the polymer in 40 mL of deionized (DI) water. The flask is sealed with a septum, and CO_2 from a 1 kg cylinder (BC) is bubbled into the solution while stirring continuously. This process is conducted at a pressure of 1 bar and a constant flow rate of 50 cm^3/min for a duration typically not exceeding 10 minutes. Samples are taken at different time intervals and their fluorescence is measured in an Edinburgh Instruments FS5 Spectrofluorometer.

Air exposure experiments procedure. A previously CO_2-bubbled (10 min) 10 ppm P(DMAm-*co*-DEAPyMA) solution is exposed to air while rigorous stirring for 1 hour. Samples are taken at different time intervals, and their fluorescence is measured in an Edinburgh Instruments FS5 Spectrofluorometer.

Sample preparation at different pHs Samples at various pH levels were prepared by first preparing phosphate-buffered saline (PBS) solutions. The pH of each PBS solution was then adjusted to the desired value using standardized 0.01 M NaOH and 0.01 M HCl solutions. Adjustments were made incrementally while continuously monitoring the pH to ensure precision. All samples were prepared under consistent conditions to maintain reproducibility across experiments.

3.5.3 Synthetic methods

3.5.3.1 Synthetic routes for different pyrene monomers (PyMA, DMAPyMA and DEAPyMA)

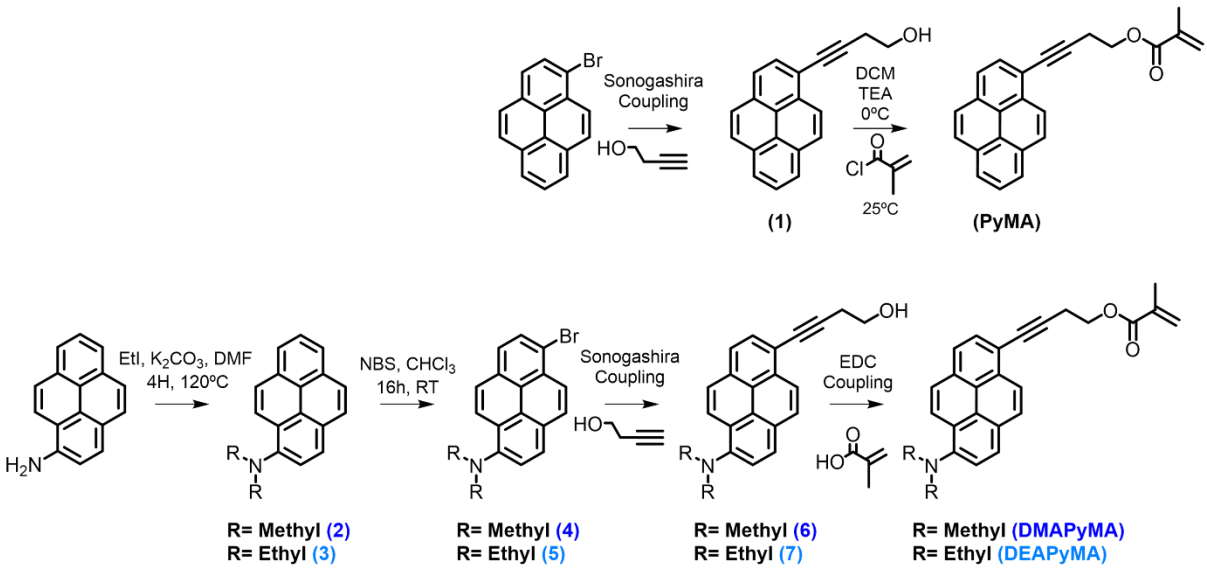

(1). In a dry RBF, 1-bromopyrene (1.00 g, 3.6 mmol) was dissolved in THF (30 mL) and Et_3N (3.01 mL, 21.4 mmol) was added under inert atmosphere. CuI (27.0 mg) and $Pd[Ph_3P]_2Cl_2$ (65.0 mg) were added, followed by 3-butyn-1-ol (0.4 mL, 5.3 mmol). The reaction mixture was heated to reflux and stirred for 18 h.. TLC (hexane/ethyl acetate 1:1) showed the disappearance of starting material. The crude was filtered through celite and washed with CH_2Cl_2. The solvent was removed in vacuo and the residue was loaded on silica gel (3.5 g) and was purified by column chromatography on previously deactivated silica gel in hexane/ethyl acetate (100% hexane to 1:1) and Compound **1** was isolated as a red solid (129 mg, 35%). ^{1}H NMR (400 MHz, chloroform-*d*) δ 8.55 (d, *J* = 9.1 Hz, 1H), 8.21 (ddd, *J* = 8.9, 7.6, 1.1 Hz, 2H), 8.16 (d, *J* = 9.1 Hz, 1H), 8.10 (s, 2H), 8.08 – 8.00 (m, 3H), 3.99 (q, *J* = 6.2 Hz, 2H), 2.95 (t, *J* = 6.3 Hz, 2H), 1.96 (t, *J* = 6.3 Hz, 1H).

PyMA. Compound **(1)** (0.302 g. 1.12 mmol) was dissolved in 5 mL dry CH_2Cl_2 and triethylamine (TEA, 0.191 mL, 1.34 mmol) was added to the solution at 0 ºC. Then

methacryloyl chloride (0.143 mL, 1.46 mmol) dissolved in dry CH_2Cl_2 (5 mL) was added to the above mixture dropwise at 0 ºC under argon. The mixture was allowed to reach room temperature overnight. The crude solution was washed with dilute HCl aqueous solution (3%) (3 × 10 mL) and brine (3 × 10 mL) separately to remove water-soluble side products. The CH_2Cl_2 phase was dried over anhydrous magnesium sulphate. Then the CH_2Cl_2 solution was concentrated to 3 mL by rotary evaporation. The crude product was chromatographed on a silica gel using petroleum ether/ethyl acetate (9:1, v/v) to afford the pure **PyMA** as an orange/yellow solid (0.120 g, yield: 32%). ^{1}H NMR (400 MHz, Chloroform-*d*) δ 8.55 (d, *J* = 9.1 Hz, 1H), 8.20 (ddd, *J* = 9.1, 7.6, 1.2 Hz, 2H), 8.13 (d, *J* = 9.2 Hz, 1H), 8.11 – 8.06 (m, 3H), 8.05 – 8.00 (m, 2H), 6.26 (dq, *J* = 2.1, 1.0 Hz, 1H), 5.64 (p, *J* = 1.6 Hz, 1H), 4.52 (t, *J* = 6.8 Hz, 2H), 3.05 (t, *J* = 6.8 Hz, 2H), 2.03 (dd, *J* = 1.6, 1.0 Hz, 3H), 1.53 (s, 1H). ^{13}C NMR (400 MHz, chloroform-*d*) δ 167.43, 136.35, 132.14, 131.38, 131.20, 131.11, 129.74, 128.27, 128.09, 127.36, 126.31, 126.11, 125.67, 125.60, 125.58, 124.58, 124.57, 124.46, 118.16, 91.44, 81.22, 62.90, 20.64, 18.51, 1.17. TOF MS (ES+) m/z [M]: 339.138, calculated 339.138.

(2). Triethylamine (4.2 ml, 32 mmol) was added to a mixture of 1-aminopyrene (3.0 g, 13.8 mmol) and K_2CO_3 (4.19 g, 30 mmol) previously dissolved in DMF (30 mL) under Ar atmosphere. To this stirring solution, methyl iodide (4.3 ml, 69 mmol) was added dropwise. The reaction mixture was heated at 120 °C for 4 h. The reaction was followed by TLC. After 4 h, TLC analysis showed the completion of the reaction; therefore, it was allowed to cool down to room temperature, and the reaction mixture was evaporated to dryness under reduced pressure. The residue was dissolved in CH_2Cl_2 and washed twice with saturated aq. $NaHCO_3$. The combined aq. phase was extracted with ethyl acetate. The combined organic phase was dried with Na_2SO_4 and evaporated to dryness. The residue was loaded on silica gel (5 g) and purified by column chromatography in

hexane/ethyl acetate (99:1 to 9:1) yielding **(2)** as a yellow solid (2.01 g, 60%). ^{1}H NMR (400 MHz, DMSO-d_6): δ (ppm)8.38 (d, *J* = 9.2 Hz, 1H), 8.20 (td, *J* = 8.7, 2.3 Hz, 3H), 8.14 (d, *J* = 9.2 Hz, 1H), 8.05 (t, *J* = 9.3 Hz, 1H), 8.00 (dd, *J* = 8.3, 4.3 Hz, 2H), 7.82 (d, *J* = 8.3 Hz, 1H), 2.99 (s, 6H).

(4). Previously recrystallized 1-bromo-2,5-pyrrolidinedione (NBS) (1.67 g, 9.4 mmol) was added slowly under stirring to a solution of **2** (2.012 g, 8.1 mmol) in $CHCl_3$ (29 mL) and stirred overnight at rt. After full conversion, which was followed by TLC (hexane/CH_2Cl_2 3:1) the mixture was diluted with CH_2Cl_2 (30 mL) and washed with water and brine, then dried with Na_2SO_4. After removing the solvent, the residue was loaded on silica gel (5 g) and purified by column chromatography on silica gel in hexane/CH_2Cl_2 (19:1 to 9:1) to obtain product **4** (460 mg, 20%) as brown oil. ^{1}H NMR (400 MHz, $CDCl_3$): δ (ppm) 8.55 (d, *J* = 9.5 Hz, 1H), 8.40 (d, *J* = 9.5 Hz, 1H), 8.18 (d, *J* = 8.2 Hz, 1H), 8.13 (d, *J* = 8.3 Hz, 1H), 7.98 (d, *J* = 8.9 Hz, 1H), 7.92 (d, *J* = 8.2 Hz, 1H), 7.86 (d, *J* = 8.9 Hz, 1H), 7.76 (d, *J* = 8.3 Hz, 1H), 3.07 (s, 6H).

(6). In a dry RBF, and with the previous vacuum/nitrogen cycles done. 6-bromo-N,N-dimethylpyren-1-amine **(4)** (0.46 g, 1.4 mmol) was dissolved in THF (13 mL) and Et_3N (1.2 mL, 8.3 mmol) was added under inert atmosphere. CuI (54 mg) and $Pd[Ph_3P]_2Cl_2$ (36 mg) were added, followed by 3-butyn-1-ol (0.2 mL, 2.1 mmol). The reaction mixture was heated to reflux and stirred for 18 h. The reaction mixture was heated to reflux and stirred for 24 h. TLC (hexane/ethyl acetate 1:1) showed the disappearance of starting material. The crude was filtered through celite and washed with CH_2Cl_2. The solvent was removed *in vacuo* and the residue was loaded on silica gel (2.5 g) and was purified by column chromatography on previously deactivated silica gel with TEA, in hexane/ethyl acetate (100% hexane to 1:1) and Compound **6** was isolated as a yellow/orange viscous

oil (195 mg, 44%). ^{1}H NMR (400 MHz, $CDCl_3$): δ (ppm) 8.52 (s, 2H), 8.11 (d, *J* = 8.3 Hz, 1H), 8.04 (d, *J* = 7.9 Hz, 1H), 8.01 – 7.95 (m, 2H), 7.87 (d, *J* = 8.9 Hz, 1H), 7.74 (d, *J* = 8.3 Hz, 1H), 3.99 (t, *J* = 6.2 Hz, 2H), 3.07 (s, 6H), 2.95 (t, *J* = 6.2 Hz, 2H).

DMAPyMA. A solution of EDC-HCl (0.17 g, 0.9 mmol) in dry CH_2Cl_2 (10 mL) was added dropwise into a mixture of **(6)** (0.19 g, 0.6 mmol), DMAP (7 mg, 10 mol %), Et_3N (164 μL, 1.2 mmol) and methacrylic acid (500 μL, 0.6 mmol) in dry CH_2Cl_2 (15 mL) at 0 ºC. The reaction was allowed to reach room temperature for 24 h. The crude was then diluted with CH_2Cl_2 (50 mL), washed with brine (60 mL x 3), and dried over Na_2SO_4 anhydrous. The reaction mixture was concentrated under vacuum and the residue was loaded on silica gel (2 g) and was purified by column chromatography on previously deactivated silica gel in hexane/ethyl acetate (from 100% hexane to 5:1) as eluent to obtain compound **DMAPyMA** (101 mg, 45%). ^{1}H NMR (400 MHz, $CDCl_3$): δ (ppm) 8.50 (d, J = 2.6 Hz, 2H), 8.10 (d, J = 8.3 Hz, 1H), 8.03 (d, J = 7.9 Hz, 1H), 8.01 – 7.95 (m, 2H), 7.87 (d, J = 8.9 Hz, 1H), 7.74 (d, J = 8.2 Hz, 1H), 6.26 (dq, J = 1.9, 1.0 Hz, 1H), 5.64 (p, J = 1.6 Hz, 1H), 4.51 (t, J = 6.8 Hz, 2H), 3.07 (s, 6H), 3.04 (d, J = 6.8 Hz, 2H), 2.03 (dd, J = 1.6, 1.0 Hz, 3H). ^{13}C NMR (400 MHz, CDCl3) δ 167.45, 149.65, 136.36, 132.38, 131.72, 129.81, 128.09, 127.08, 126.10, 126.00, 125.87, 125.39, 125.18, 124.50, 124.44, 124.31, 123.96, 117.26, 116.75, 91.06, 81.41, 62.97, 45.78, 20.65, 18.53, 1.17. TOF MS (ES+) m/z [M]: 381.170, calculated 381.480.

(3). Triethylamine (2.7 mL, 19.2 mmol) was added to a mixture of 1-aminopyrene (1.90 g, 8.7 mmol) and K_2CO_3 (2.66 g, 19.2 mmol) previously dissolved in DMF (18 ml) under an argon atmosphere. To this stirring solution, ethyl iodide (3.20 mL, 43.7 mmol) was added dropwise. The reaction mixture was heated at 120 °C for 4 h. The reaction was followed by TLC. After 4 h, TLC analysis showed the completion of the reaction;

therefore, it was allowed to cool down to room temperature, and the reaction mixture was evaporated to dryness under reduced pressure. The residue was dissolved in CH_2Cl_2 and washed twice with saturated aq. $NaHCO_3$. The combined aq. phase was extracted with ethyl acetate. The combined organic phase was dried with Na_2SO_4 and evaporated to dryness. The residue was loaded on silica gel (5 g) and purified by column chromatography in hexane/ethyl acetate (99:1 to 9:1) yielding **3** as a yellow solid (1.18 g, 50%). ^{1}H NMR (400 MHz, $CDCl_3$): δ (ppm) 8.57 (d, *J* = 9.2 Hz, 1H), 8.16 – 8.08 (m, 3H), 8.05 (d, *J* = 9.3 Hz, 1H), 8.00 (d, *J* = 8.9 Hz, 1H), 7.98 – 7.93 (m, 2H), 7.81 (d, *J* = 8.2 Hz, 1H), 3.35 (q, *J* = 7.1 Hz, 4H), 1.08 (t, J = 7.1 Hz, 6H).

(5). Previously recrystallized 1-bromo-2,5-pyrrolidinedione (NBS) (1.16 g, 6.5 mmol) was added slowly under stirring to a solution of **3** (1.18 g, 4.3 mmol) in $CHCl_3$ (15 mL) and stirred overnight at rt. After full conversion, which was followed by TLC (hexane/CH_2Cl_2 3:1) the mixture was diluted with 30 mL of CH_2Cl_2 and washed with water and brine, dried with Na_2SO_4. After removing the solvent, the residue was loaded on silica gel (4 g) and purified by column chromatography on silica gel in hexane/CH_2Cl_2 (19:1 to 9:1) to obtain product **5** (143 mg, 10%) as brown oil in yield. ^{1}H NMR (400 MHz, $CDCl_3$): δ (ppm) 8.67 (d, *J* = 9.5 Hz, 1H), 8.40 (d, *J* = 9.5 Hz, 1H), 8.19 (d, *J* = 8.2 Hz, 1H), 8.15 (d, *J* = 8.2 Hz, 1H), 8.02 (d, *J* = 8.9 Hz, 1H), 7.94 (d, *J* = 8.2 Hz, 1H), 7.91 (d, *J* = 8.9 Hz, 1H), 7.83 (d, *J* = 8.2 Hz, 1H), 3.36 (q, *J* = 7.1 Hz, 4H), 1.09 (t, *J* = 7.1 Hz, 6H).

DEAPyMA. In a dry RBF, and with the previous vacuum/nitrogen cycles done. 6-bromo-N,N-diethylpyren-1-amine **(5)** (130 mg, 0.4 mmol) was dissolved in THF (4 mL) and Et_3N (330 μL, 2.4 mmol) was added under argon atmosphere. CuI (3 mg) and $Pd[Ph_3P]_2Cl_2$ (7 mg) were added, followed by 3-butyn-1-ol (45 μL, 0.6 mmol). The

reaction mixture was heated to reflux and stirred for 24 h. TLC (hexane/ethyl acetate 1:1) showed the disappearance of starting material. The crude was filtered through celite and washed with CH_2Cl_2. The solvent was removed in vacuo and the residue was loaded on silica gel (2.5 g) and was purified by column chromatography on previously deactivated silica gel in hexane/ethyl acetate (100% hexane to 1:1) and Compound **DEAPyMA** was isolated as a yellow/orange viscous oil (117 mg, 90%). ^{1}H NMR (400 MHz, $CDCl_3$): δ (ppm) 8.64 (d, *J* = 9.4 Hz, 1H), 8.50 (d, *J* = 9.4 Hz, 1H), 8.12 (d, *J* = 8.2 Hz, 1H), 8.05 (d, *J* = 8.0 Hz, 1H), 8.01 (d, *J* = 2.6 Hz, 1H), 7.99 (d, *J* = 3.5 Hz, 1H), 7.91 (d, *J* = 8.9 Hz, 1H), 7.81 (d, *J* = 8.2 Hz, 1H), 3.99 (q, *J* = 6.3 Hz, 2H), 3.36 (q, *J* = 7.1 Hz, 4H), 2.96 (d, *J* = 6.2 Hz, 2H), 1.09 (t, *J* = 7.1 Hz, 6H). ^{13}C NMR (400 MHz, $CDCl_3$) δ 146.97, 136.36, 129.69, 128.03, 126.11, 125.78, 125.63, 124.79, 124.52, 123.97, 120.45, 62.99, 48.88, 20.65, 18.52, 12.85. TOF MS (ES+) m/z [M]: 410.212, calculated 410.212.

3.5.3.2 Synthesis of poly(N,N′-dimethylacrylamide-co-diethylaminopyrene methacrylate) P(DMAm-co-DEAPyMA)

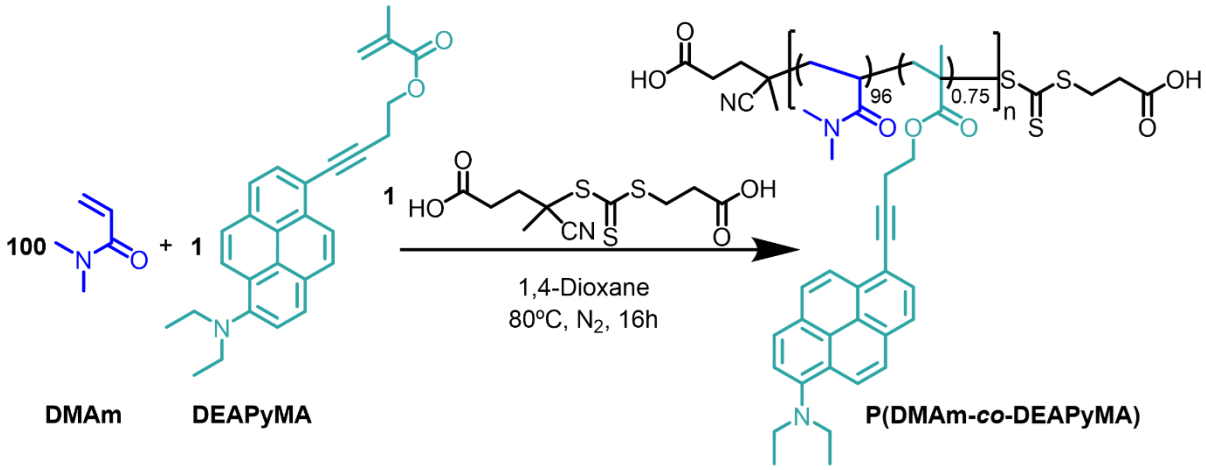

N,N′-Dimethylacrylamide (DMAm) monomer (65 mg, 0.65 mmol, 100 equiv), 4-((((2-carboxyethyl)thio)carbonothioyl)thio)-4-cyanopentanoic acid chain-transfer agent (CTA) (2.0 mg, 65 µmol, 1 equiv), 4-(6-(diethylamino)pyren-1-yl)but-3-yn-1-yl

methacrylate (2.66 mg, 065 μmol, 1 equiv) and 4,4′-azobis(4- cyanovaleric acid) (ACVA) radical initiator (1.0 mg, 06 μmol, 0.1 equiv) were dissolved in 1,4-dioxane (3 mL). After transferring the solution to an ampoule equipped with a magnetic stir bar, the solution was deoxygenated by purging with N_2(g) for 30 min under rapid stirring. The polymerization reaction was initiated upon immersion of the ampoule in an oil bath heated at 80 °C, and the polymerization mixture was stirred at this temperature for 16 h to ensure full monomer conversion. The polymerization reaction was then terminated upon cooling and exposing the polymerization mixture to air. The resulting P($DMAm_{96}$-*co*-$DEAPyMA_{0.75}$) polymer was purified by extensive dialysis against deionized water (MWCO = 1 kDa) and was recovered as a yellow solid by freeze drying (60 mg). The resulting polymer was then characterized by ^{1}H-NMR spectroscopy and aqueous SEC analysis.^{1}H NMR (400 MHz, $CDCl_3$) conv ~96%, $M_{n,NMR}$ = 10.1 kDa. SEC ($CHCl_3$) $M_{n,SEC}$ = 16.2 kDa , $Đ_{SEC}$ = 1.4

3.5.4 Characterization

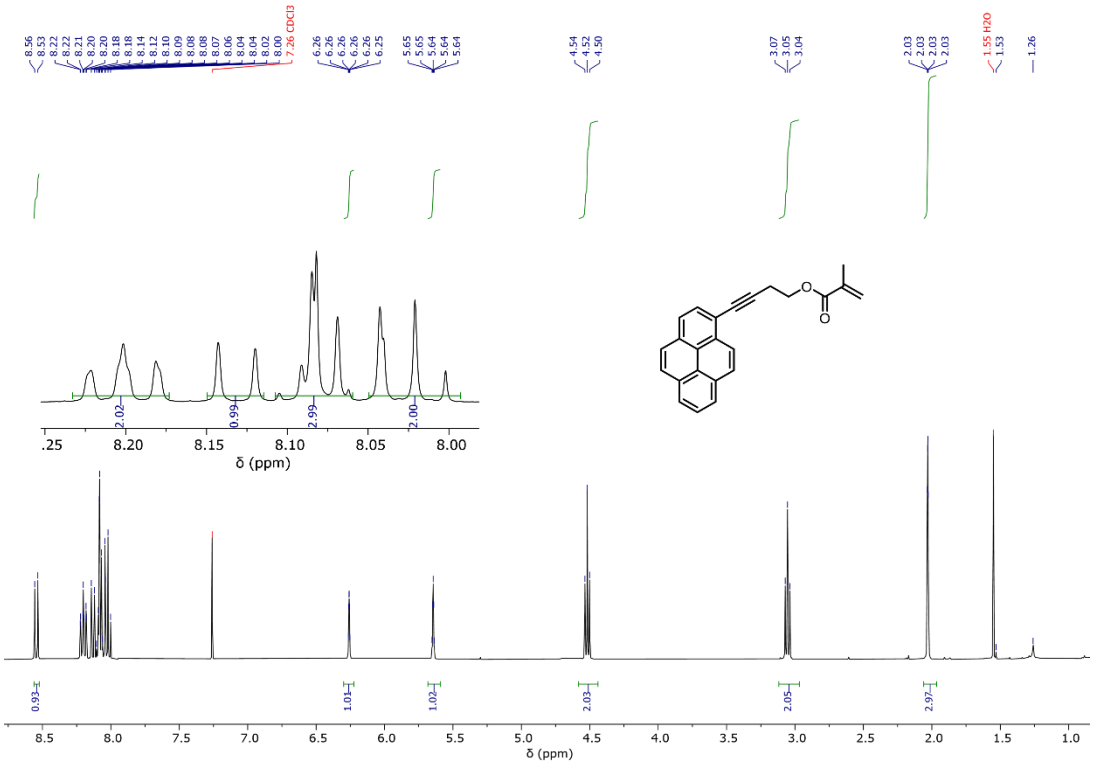

Spectrum S1. ^{1}H NMR spectrum of PyMA in $CDCl_3$

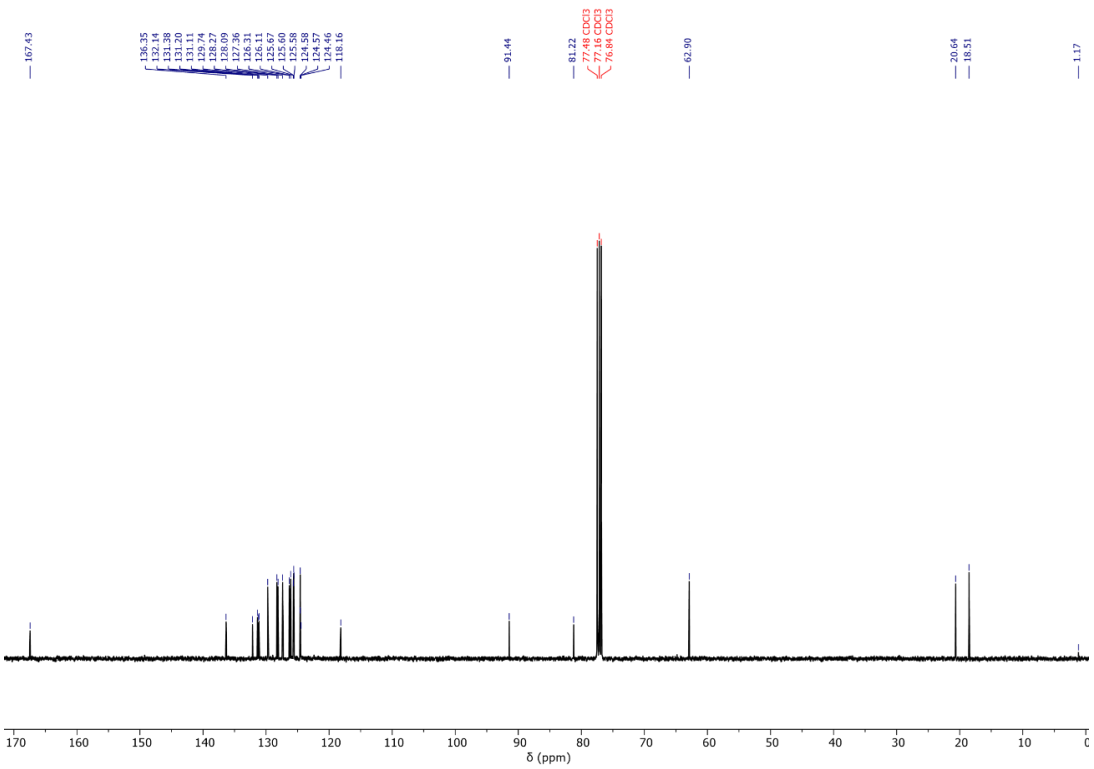

Spectrum S2. ^{13}C NMR spectrum of PyMA in $CDCl_3$

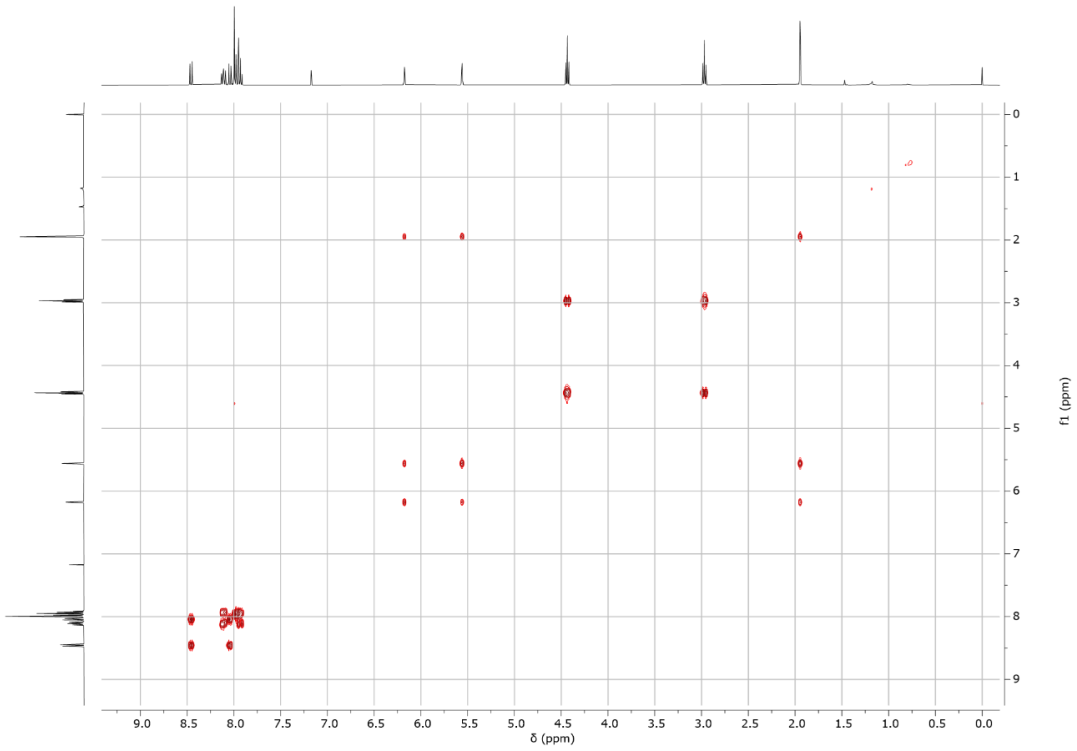

Spectrum S3. COSY 2D spectrum of PyMA in $CDCl_3$

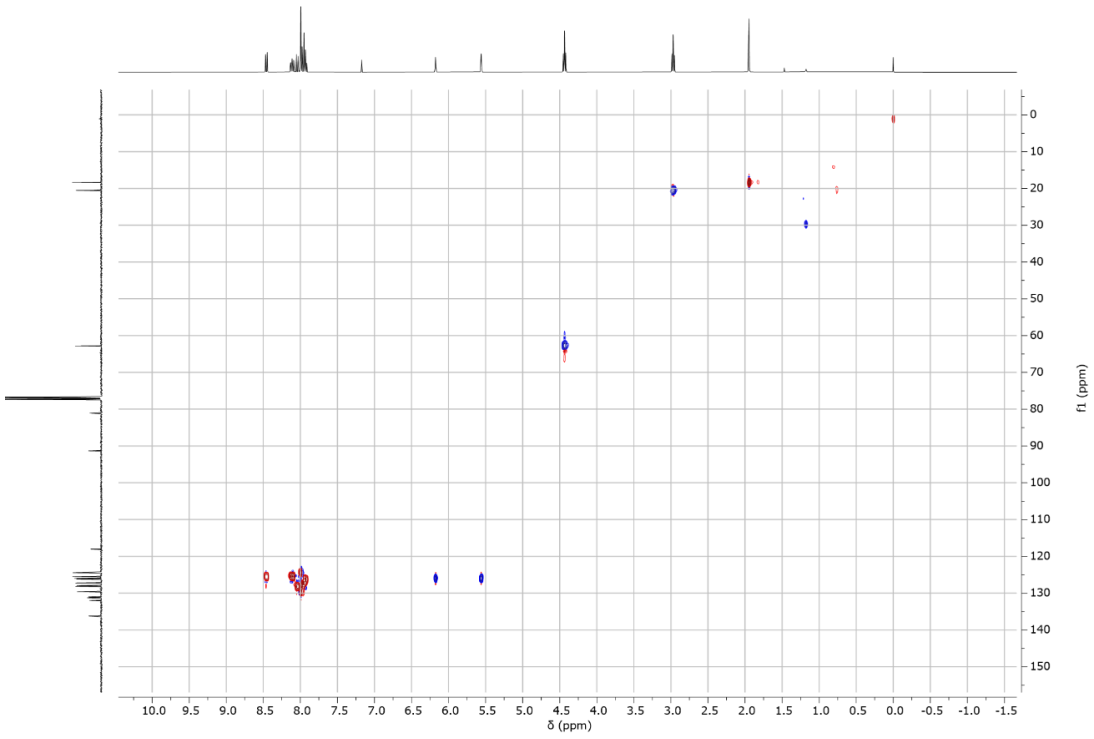

Spectrum S4. HSQC 2D spectrum of PyMA in $CDCl_3$

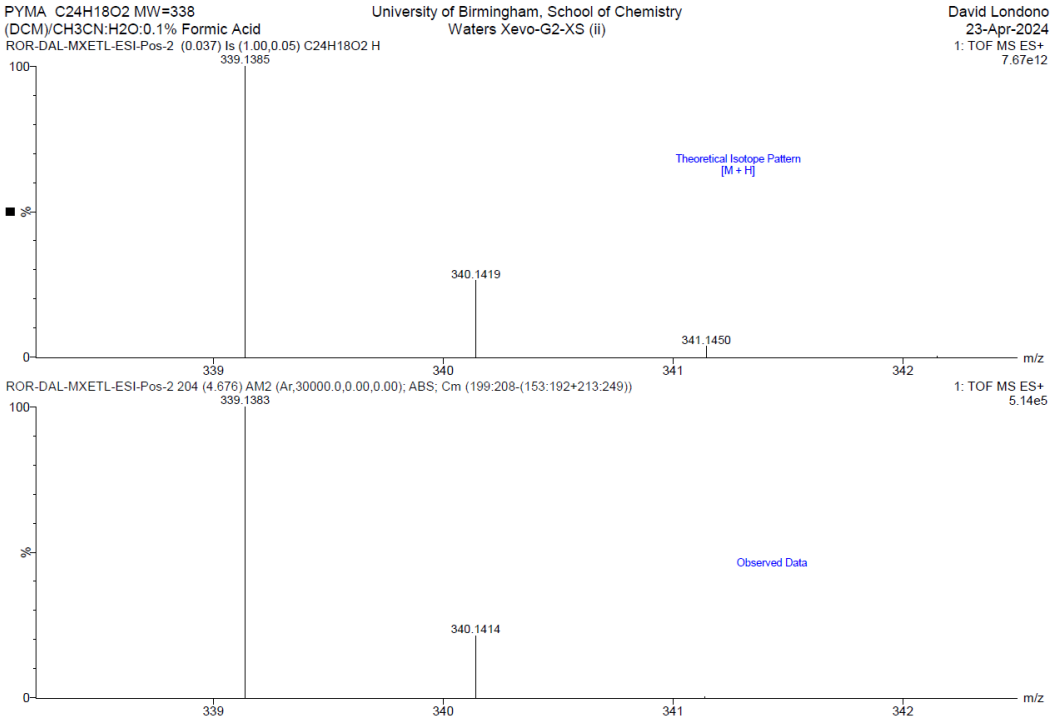

Spectrum S5. TOF mass spectrum of PyMA in $CDCl_3$

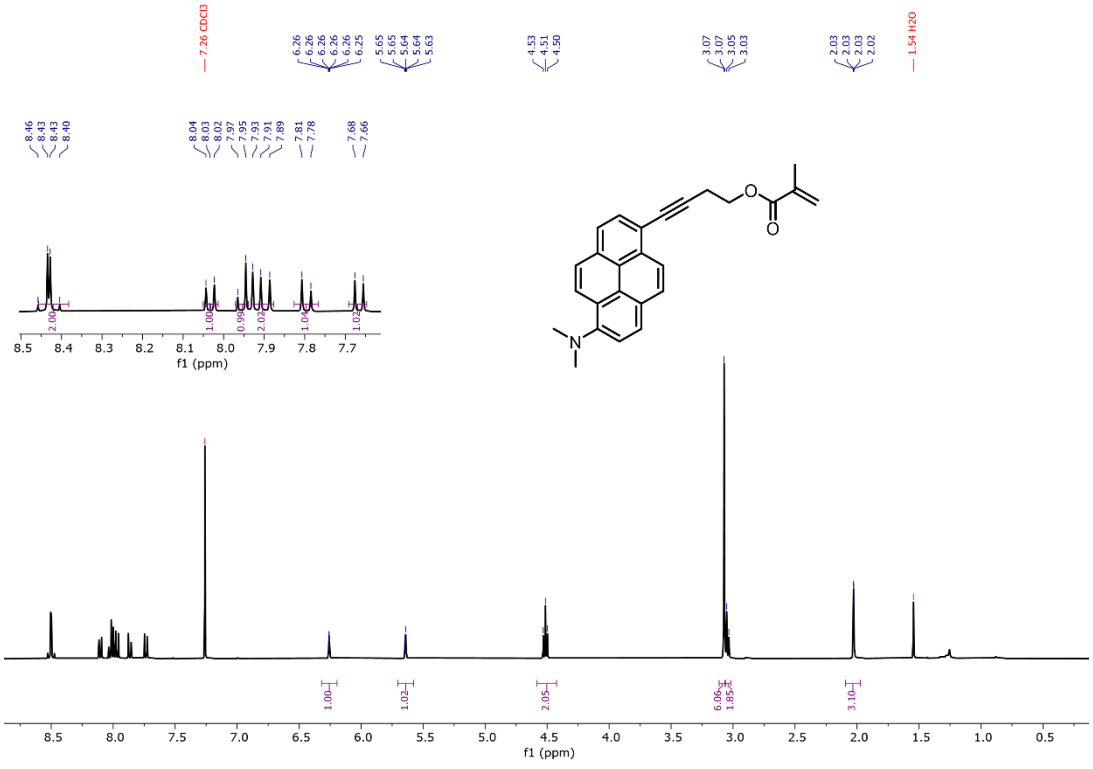

Spectrum S6. ^{1}H NMR spectrum of DMAPyMA in $CDCl_3$

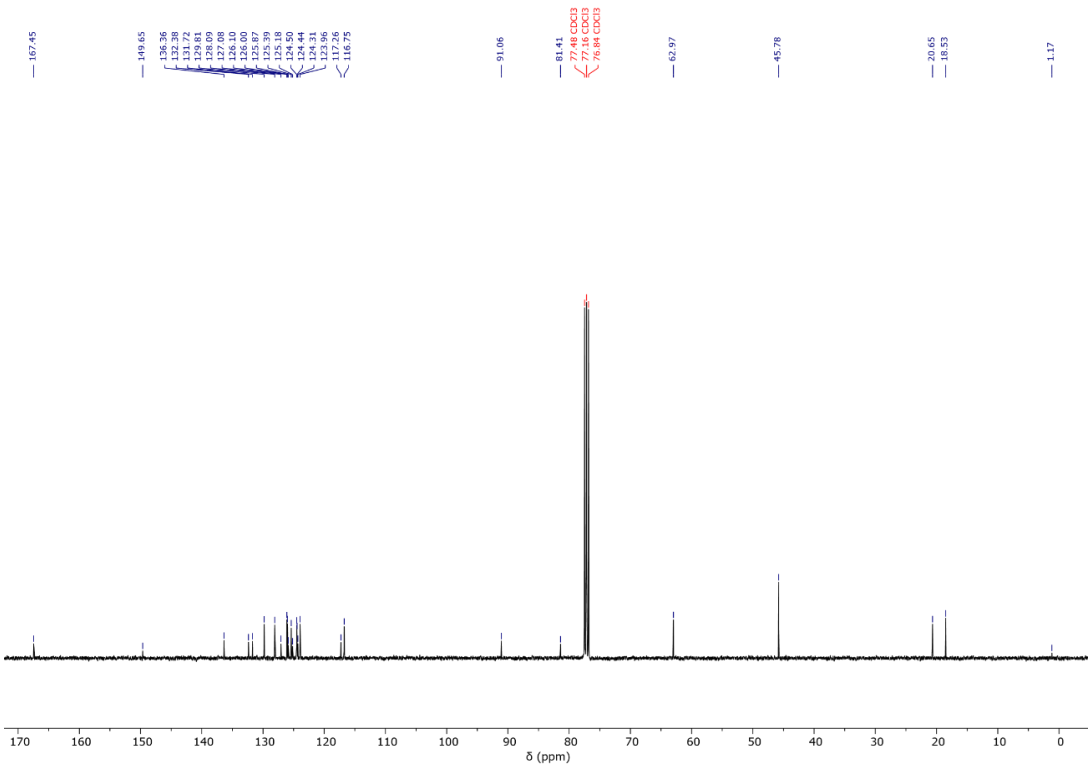

Spectrum S7. ^{13}C NMR spectrum of DMAPyMA in $CDCl_3$

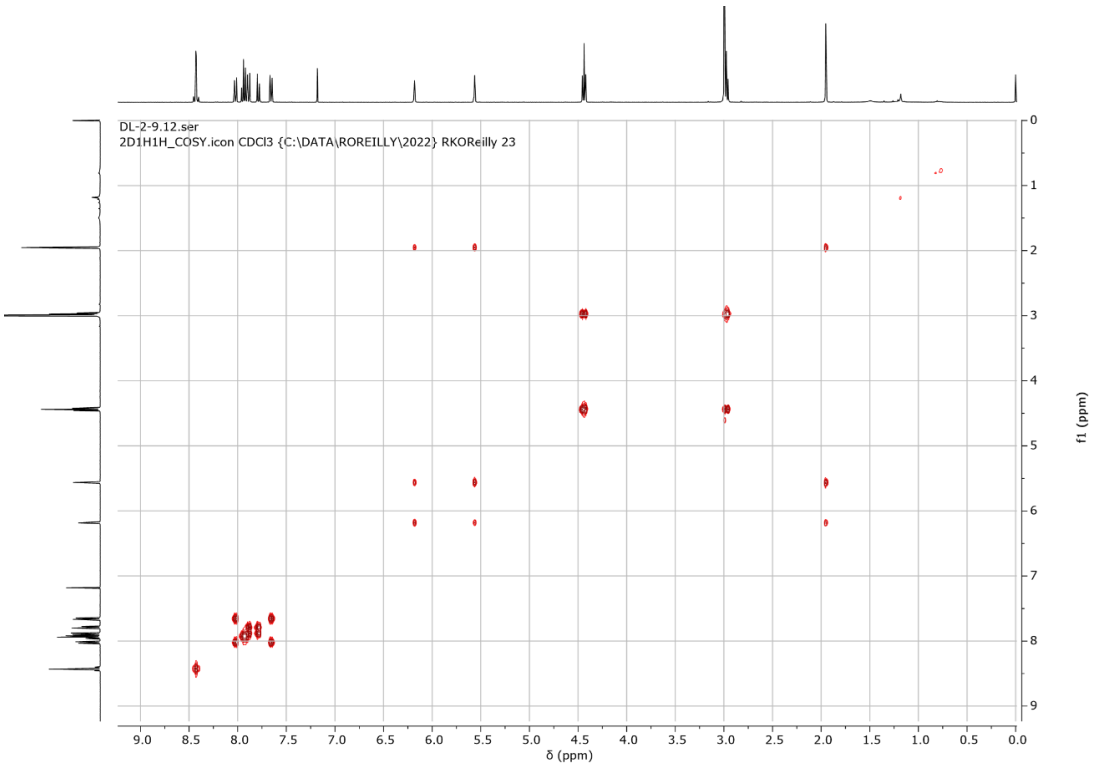

Spectrum S8. COSY 2D NMR spectrum of DMAPyMA in $CDCl_3$

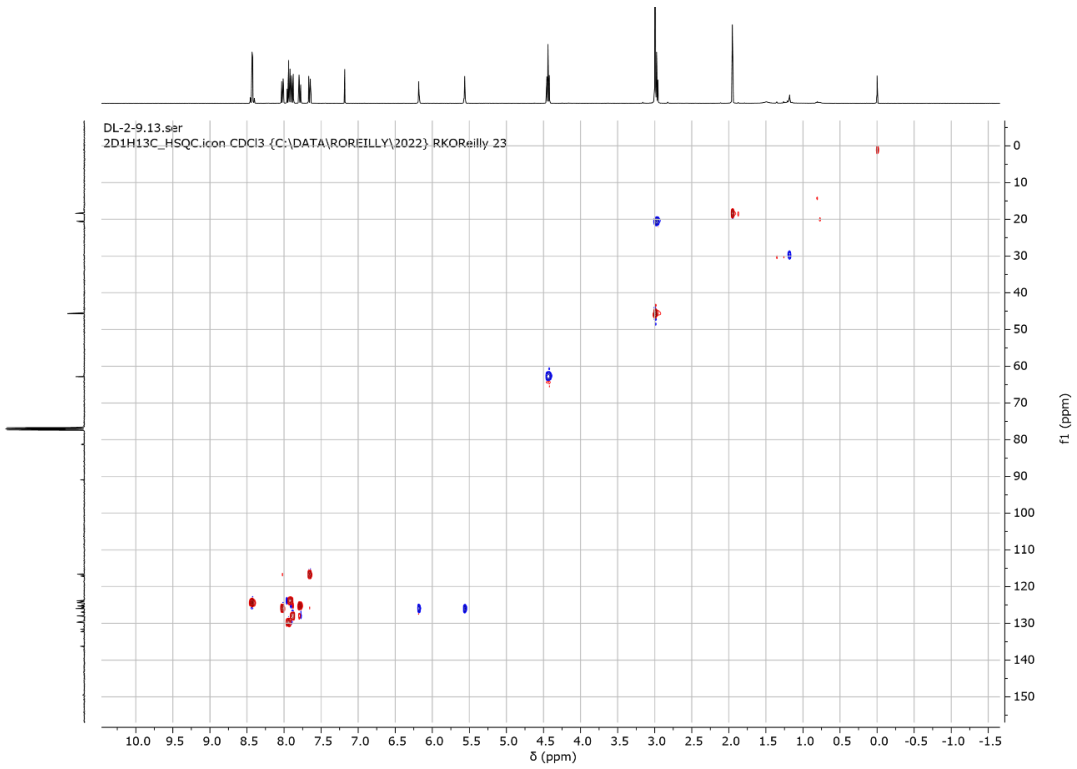

Spectrum S9. HSQC 2D NMR spectrum of DMAPyMA in $CDCl_3$

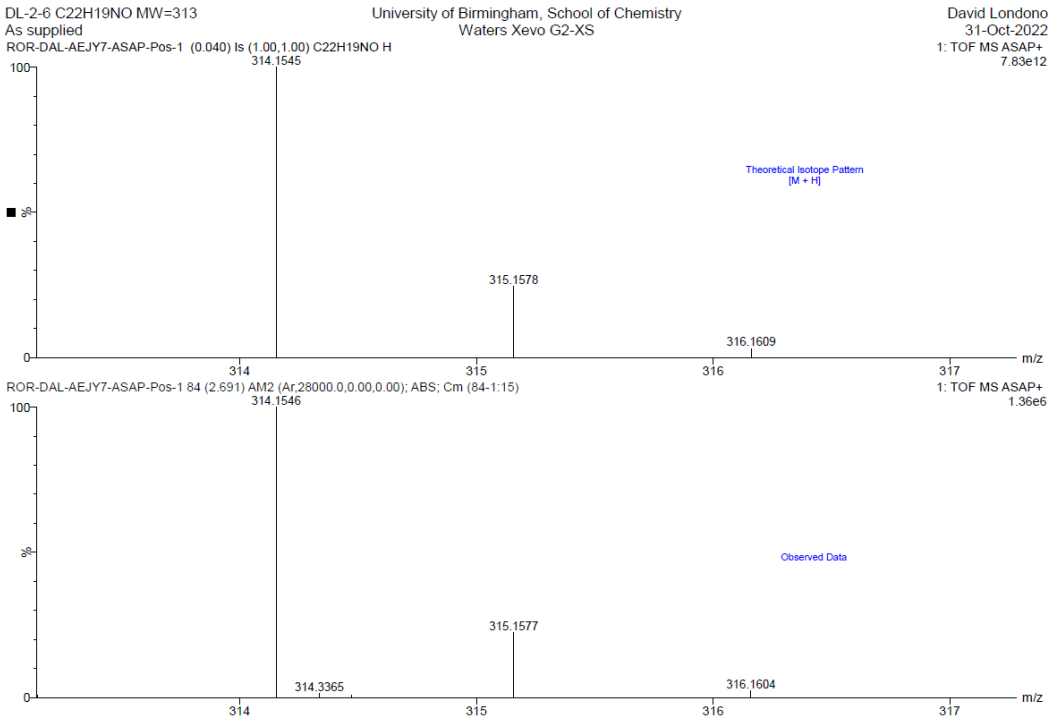

Spectrum S10. TOF Mass spectrum of DMAPyMA in $CDCl_3$

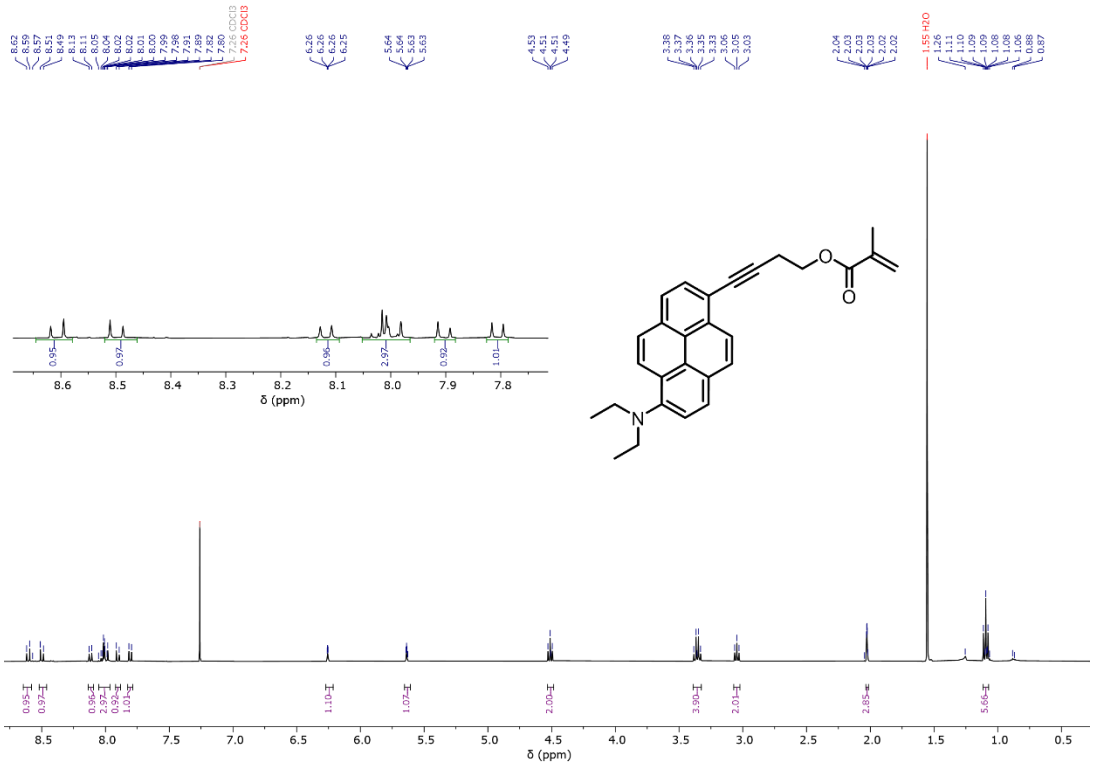

Spectrum S11. ^{1}H NMR spectrum of DEAPyMA in $CDCl_3$

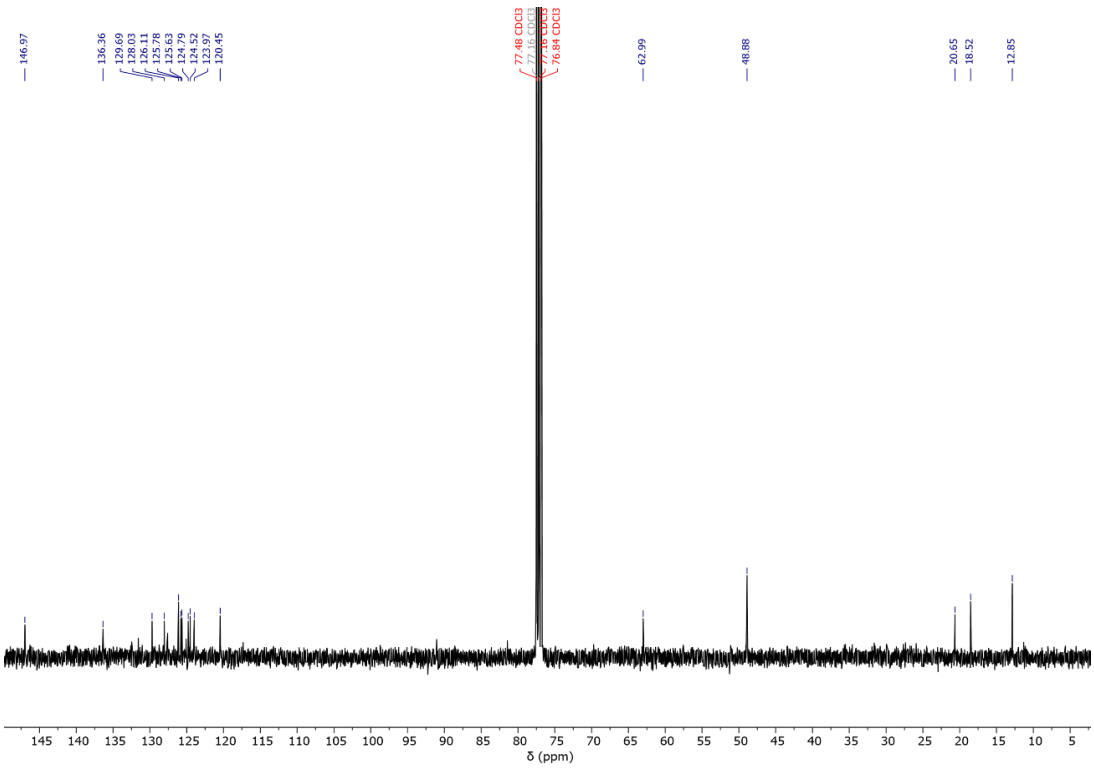

Spectrum S12. ^{13}C NMR spectrum of DEAPyMA in $CDCl_3$

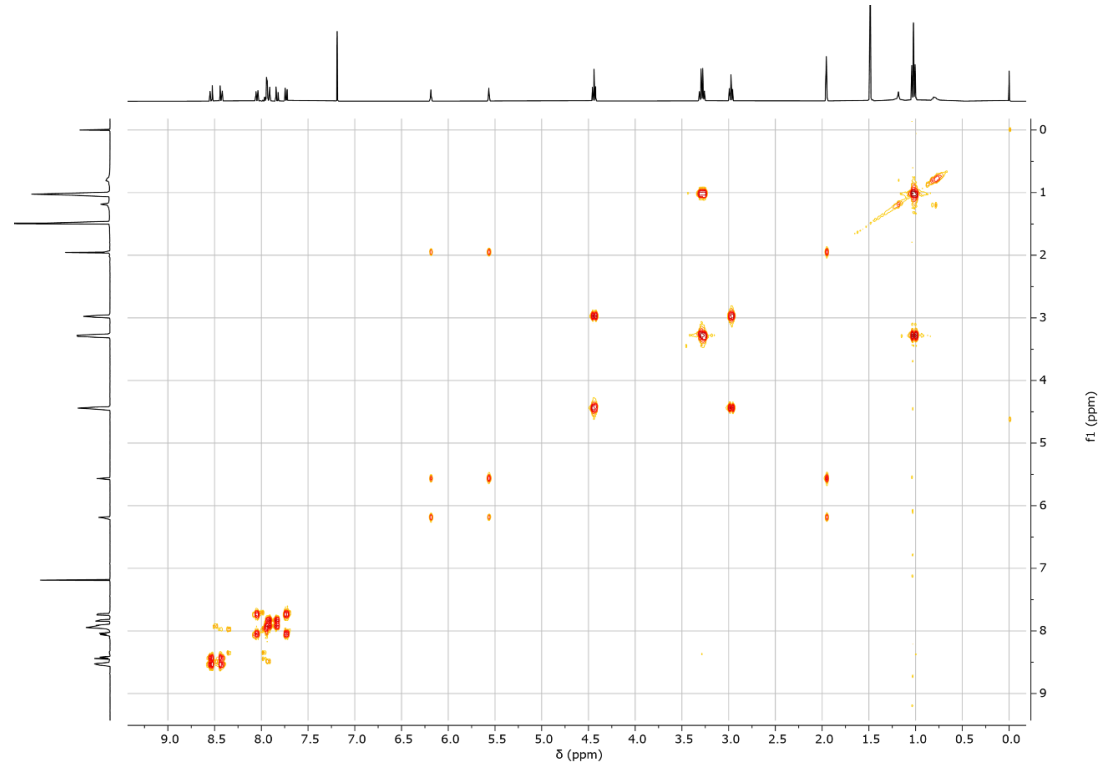

Spectrum S13. COSY 2D NMR spectrum of DEAPyMA in $CDCl_3$

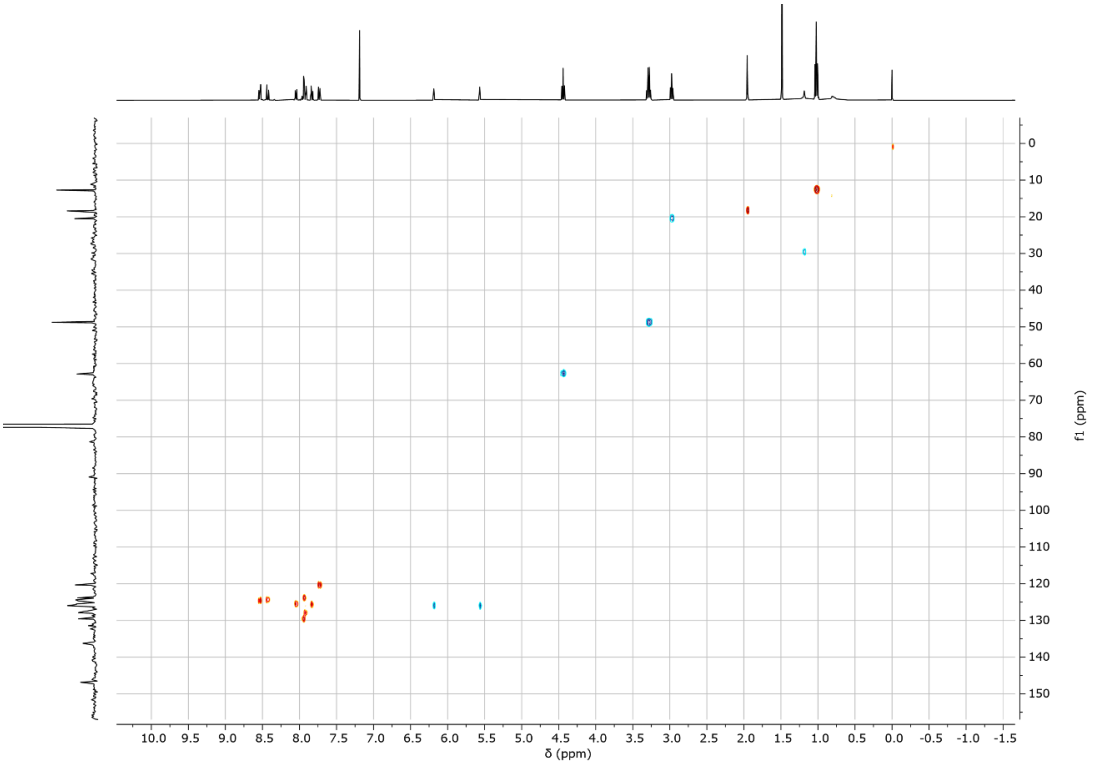

Spectrum S14. HSQC 2D NMR spectrum of DEAPyMA in $CDCl_3$

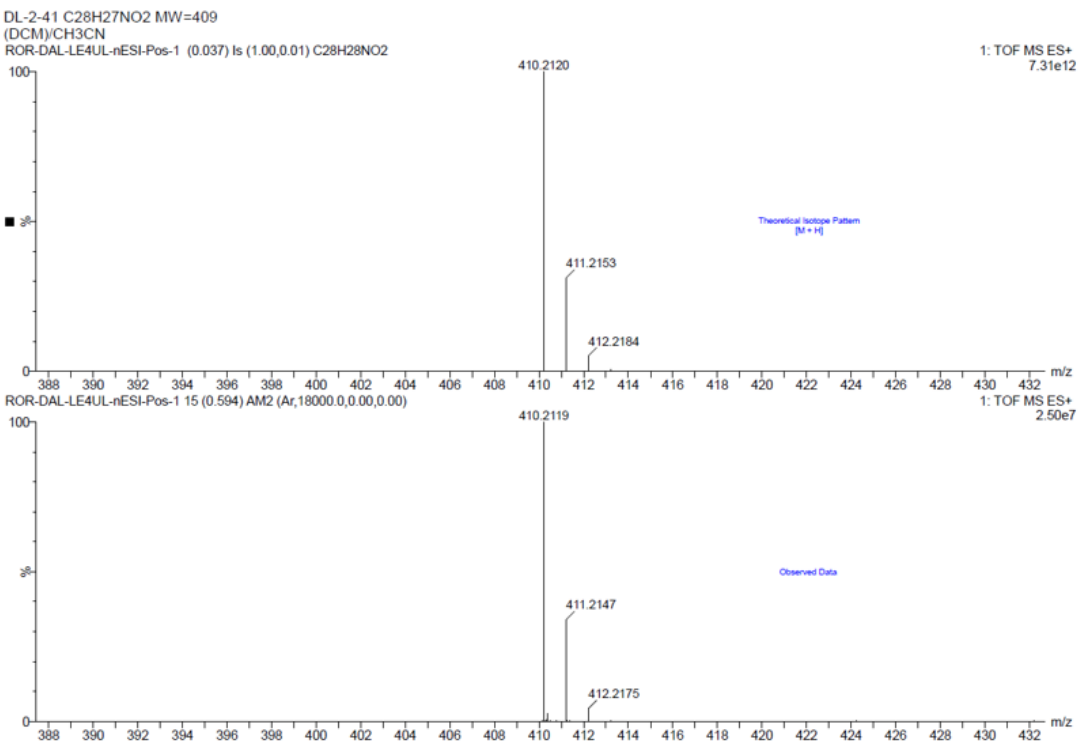

Spectrum S15. TOF mass spectrum of DEAPyMA in CH_2Cl_2

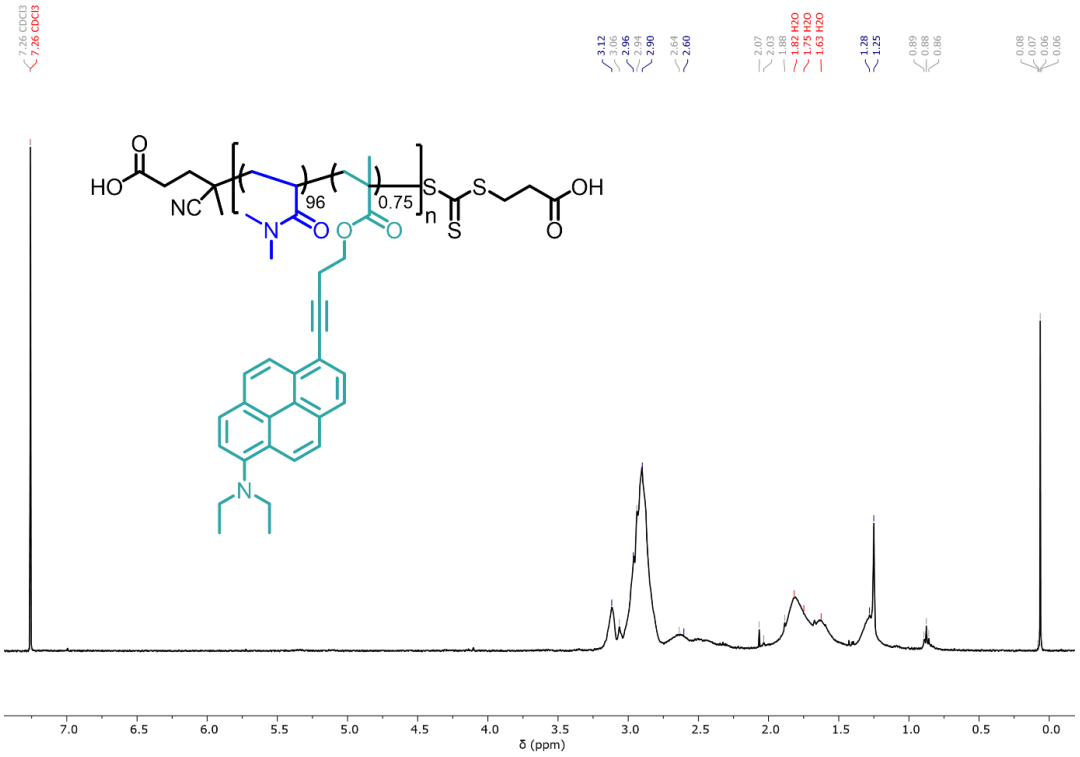

Spectrum S16. ^{1}H NMR spectrum of P(DMAm-*co*-DEAPyMA) in $CDCl_3$

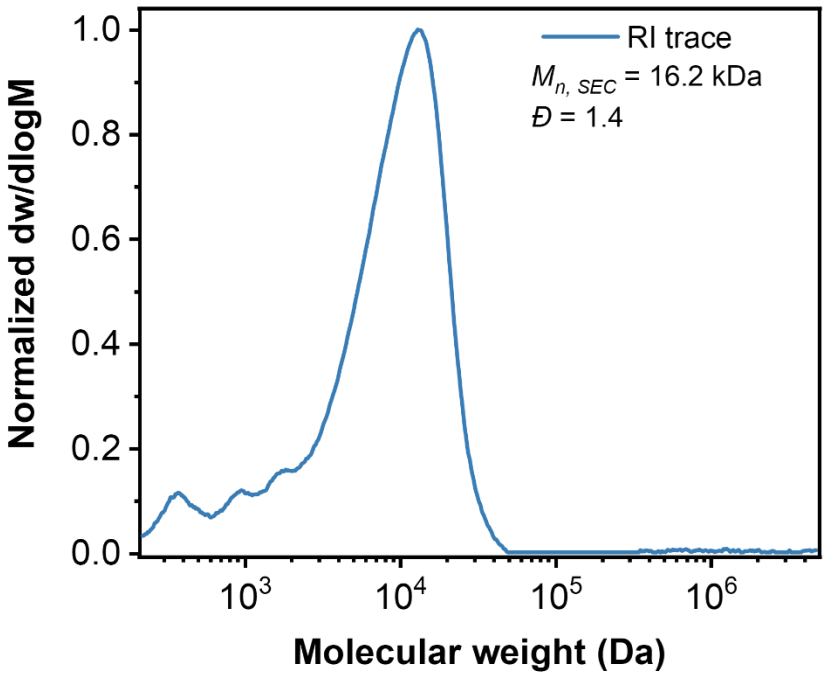

Spectrum S16. $CHCl_3$ SEC spectrum of P(DMAm-*co*-DEAPyMA).

3.6 References

(1) Zhang, C.; Xu, K.; Liu, K.; Xu, J.; Zheng, Z. Metal oxide resistive sensors for carbon dioxide detection. *Coord. Chem. Rev.* **2022**, *472*, 214758. DOI: doi.org/10.1016/j.ccr.2022.214758.

(2) Rath, R. J.; Naficy, S.; Giaretta, J.; Oveissi, F.; Yun, J.; Dehghani, F.; Farajikhah, S. Chemiresistive Sensor for Enhanced CO(2) Gas Monitoring. *ACS Sens* **2024**, *9* (4), 1735-1742. DOI: 10.1021/acssensors.3c01779 From NLM.

(3) Mabire, A. B.; Brouard, Q.; Pitto-Barry, A.; Williams, R. J.; Willcock, H.; Kirby, N.; Chapman, E.; O'Reilly, R. K. CO2/pH-responsive particles with built-in fluorescence read-out. *Polym. Chem.* **2016**, *7*, 5943-5948. DOI: 10.1039/c6py01254j.

(4) Xu, L. Q.; Zhang, B.; Sun, M.; Hong, L.; Neoh, K. G.; Kang, E. T.; Fu, G. D. CO2-triggered fluorescence "turn-on" response of perylene diimide-containing poly(N,N-dimethylaminoethyl methacrylate). *J. Mater. Chem. A.* **2013**, *1*, 1207-1212. DOI: 10.1039/c2ta00482h.

(5) Zhang, D.; Fan, Y.; Chen, H.; Trépout, S.; Li, M. H. CO2-Activated Reversible Transition between Polymersomes and Micelles with AIE Fluorescence. *Angew. Chem. Int. Ed.* **2019**, *58*, 10260-10265. DOI: 10.1002/anie.201905089.

(6) Zhang, Q.; Zhu, S. Oxygen and carbon dioxide dual responsive nanoaggregates of fluoro- and amino-containing copolymer. *ACS Macro Letters* **2014**, *3*, 743-746. DOI: 10.1021/mz500377x.

(7) Yan, Y.; Li, Y.; Wang, J.; Li, L.; Tang, F. A carbon dioxide responsive fluorescent system based on micellar transformation. *Colloids Surf. A Physicochem. Eng. Asp.* **2022**, *641*, 128457. DOI: doi.org/10.1016/j.colsurfa.2022.128457.

(8) Zhu, J.; Jia, P.; Li, N.; Tan, S.; Huang, J.; Xu, L. Small-molecule fluorescent probes for the detection of carbon dioxide. *Chin. Chem. Lett.* **2018**, *29* (10), 1445-1450. DOI: doi.org/10.1016/j.cclet.2018.09.002.

(9) Tian, J.; Huang, B.; Xiao, C.; Vana, P. Intelligent CO2- and photo-dual-responsive polymer vesicles with tunable wall thickness. *Polym. Chem.* **2019**, *10* (13), 1610-1618. DOI: 10.1039/c8py01743c.

(10) Wang, Y.; Huo, M.; Zeng, M.; Liu, L.; Ye, Q. Q.; Chen, X.; Li, D.; Peng, L.; Yuan, J. Y. CO_2-responsive Polymeric Fluorescent Sensor with Ultrafast Response. *CJPS* **2018**, *36*, 1321-1327. DOI: doi.org/10.1016/j.jbc.2022.102402.

(11) Qiu, L.; Zhang, H.; Wang, B.; Zhan, Y.; Xing, C.; Pan, C. Y. CO_2-Responsive Nano-Objects with Assembly-Related Aggregation-Induced Emission and Tunable Morphologies. *ACS Appl. Mater. Interfaces* **2020**, *12*, 1348-1358. DOI: 10.1021/acsami.9b18792.

(12) Mabire, A. B.; Brouard, Q.; Pitto-Barry, A.; Williams, R. J.; Willcock, H.; Kirby, N.; Chapman, E.; O'Reilly, R. K. CO2/pH-responsive particles with built-in fluorescence read-out. *Polym. Chem.* **2016**, *7* (38), 5943-5948, 10.1039/C6PY01254J. DOI: 10.1039/C6PY01254J.

(13) Zhao, R.; Fu, C.; Wang, Z.; Pan, M.; Ma, B.; Yin, Q.; Chen, B.; Liu, J.; Xia, H.; Wan, F.; et al. A pH-Responsive Nanoparticle Library with Precise pH Tunability by Co-Polymerization with Non-Ionizable Monomers. *Angew. Chem. Int. Ed.* **2022**, *61* (19). DOI: 10.1002/anie.202200152.

(14) Green, O.; Finkelstein, P.; Rivero-crespo, M. A.; Lutz, M. D. R.; Bogdos, M. K.; Burger, M.; Leroux, J.-c.; Morandi, B. Activity-Based Approach for Selective Molecular CO 2 Sensing. *J. Am. Chem. Soc.* **2022**. DOI: 10.1021/jacs.2c02361.

(15) Chavan, S. N.; Lee, H.-i. Activity-based molecular CO2 detection by amine-free polymers in organic and aqueous media. *Eur. Polym. J.* **2023**, *196*, 112272. DOI: doi.org/10.1016/j.eurpolymj.2023.112272.

(16) Rutkaite, R.; Swanson, L.; Li, Y.; Armes, S. P. Fluorescence studies of pyrene-labelled, pH-responsive diblock copolymer micelles in aqueous solution. *Polymer* **2008**, *49* (7), 1800-1811. DOI: doi.org/10.1016/j.polymer.2008.02.007.

(17) He, X.; Zhang, S.; Qi, S.; Xu, P.; Dong, B.; Song, B. Enhanced excimer fluorescence emission of pyrene derivatives: Applications in artificial light-harvesting systems. *Dyes Pigm.* **2023**, *209*, 110933. DOI: doi.org/10.1016/j.dyepig.2022.110933.

(18) Zeng, J.; Wang, X.; Song, X.; Liu, Y.; Liao, B.; Bai, J.; Redshaw, C.; Chen, Q.; Feng, X. Steric influences on the photophysical properties of pyrene-based derivatives; mechanochromism and their pH-responsive ability. *Dyes Pigm.* **2022**, *200*, 110123. DOI: doi.org/10.1016/j.dyepig.2022.110123.

(19) Cui, J.; Nie, H.; Liang, X.; Bai, J.; Zhang, X. A pyrene-derived ratiometric fluorescent probe for pH monitoring in cells and zebrafish based on monomer-excimer emission. *J. Mol. Liq.* **2022**, *366*, 120325. DOI: doi.org/10.1016/j.molliq.2022.120325.

(20) Liu, T.; Huang, Z.; Feng, R.; Ou, Z.; Wang, S.; Yang, L.; Ma, L.-J. An intermolecular pyrene excimer-based ratiometric fluorescent probes for extremely acidic pH and its applications. *Dyes Pigm.* **2020**, *174*, 108102. DOI: doi.org/10.1016/j.dyepig.2019.108102.

(21) Ayyavoo, K.; Velusamy, P. Pyrene based materials as fluorescent probes in chemical and biological fields. *New J. Chem.* **2021**, *45* (25), 10997-11017, 10.1039/D1NJ00158B. DOI: 10.1039/D1NJ00158B.

(22) Gou, Z.; Wang, A.; Tian, M.; Zuo, Y. Pyrene-based monomer-excimer dual response organosilicon polymer for the selective detection of 2,4,6-trinitrotoluene (TNT) and

2,4,6-trinitrophenol (TNP). *Materials Chemistry Frontiers* **2022**, *6* (5), 607-612, 10.1039/D1QM01574E. DOI: 10.1039/D1QM01574E.

(23) Pose, M.; Dillon, K. M.; Denicola, A.; Alvarez, B.; Matson, J. B.; Möller, M. N.; Cuevasanta, E. Fluorescent detection of hydrogen sulfide (H2S) through the formation of pyrene excimers enhances H2S quantification in biochemical systems. *J. Biol. Chem.* **2022**, *298* (10), 102402. DOI: https://doi.org/10.1016/j.jbc.2022.102402.

(24) Wang, S.; Zhang, Z.; Huang, Z.; Lei, X.; Wang, Y.; Li, L.; Yang, L.; Liu, H.; Sun, F.; Ma, L.-J. A pyrene-based pH fluorescence probe with continuous multiple responses under acidic conditions and its application for environmental water systems and cells. *J Photochem Photobiol A.* **2021**, *418*, 113438. DOI: doi.org/10.1016/j.jphotochem.2021.113438.

(25) Frommer, J.; Karg, B.; Weisz, K.; Müller, S. Preparation and characterization of pyrene modified uridine derivatives as potential electron donors in RNA. *Org. Biomol. Chem.* **2018**, *16* (41), 7663-7673. DOI: 10.1039/C8OB02246A.

(26) Luo, W.; Jiang, H.; Tang, X.; Liu, W. A reversible ratiometric two-photon lysosome-targeted probe for real-time monitoring of pH changes in living cells. *J. Mater. Chem. B* **2017**, *5* (24), 4768-4773, 10.1039/C7TB00838D. DOI: 10.1039/C7TB00838D.

(27) Li, W.; Yang, P.-P.; Wang, L.; Wang, H. Bis-pyrene based reversibly multi-responsive fluorescence switches. *Journal of Materials Chemistry C* **2015**, *3* (15), 3783-3789, 10.1039/C4TC02987A. DOI: 10.1039/C4TC02987A.

(28) Peng, W.; Cai, Y.; Fanslau, L.; Vana, P. Nanoengineering with RAFT polymers: from nanocomposite design to applications. *Polym. Chem.* **2021**, *12* (43), 6198-6229, 10.1039/D1PY01172C. DOI: 10.1039/D1PY01172C.

4 Synthesis of Hydrogels and Nanoparticles incorporating a pH-Responsive Pyrene: Synthesis, Properties, and Applications

4.1 Abstract

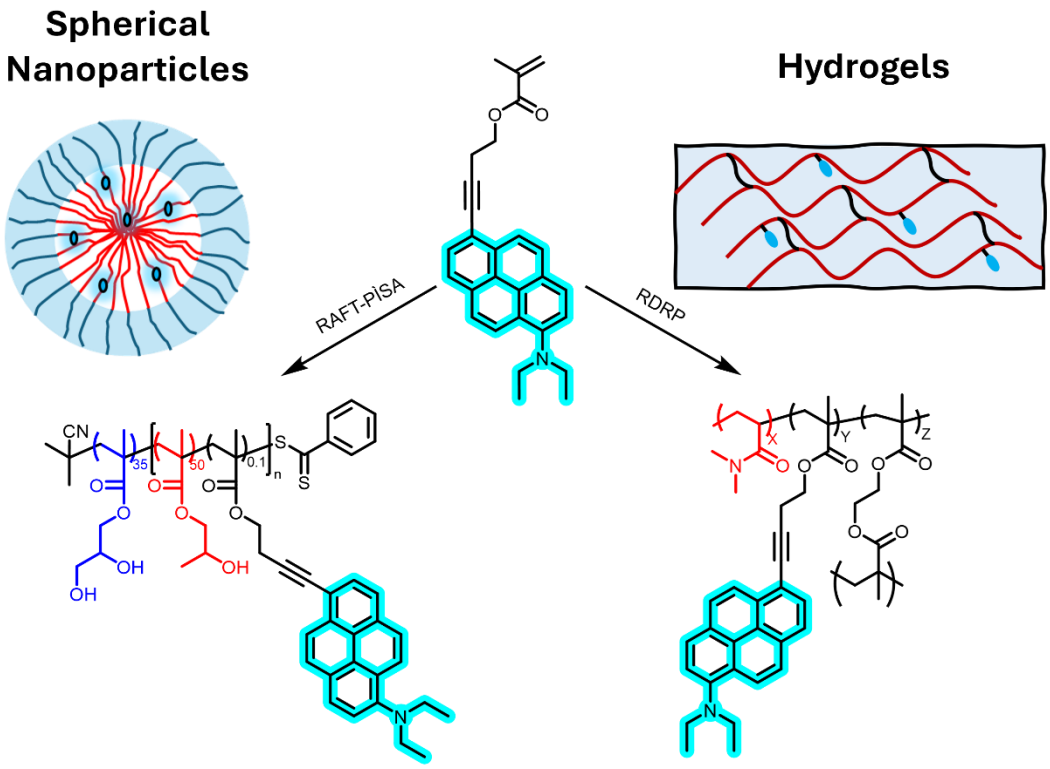

In this study, we developed a stable and minimally disruptive delivery method for the previously synthesized DEAPyMA dye, aimed at potential sensing applications. The goal was to maintain fluorescence properties comparable to the linear polymer P(DMAm$_{99}$-co-DEAPyMA$_1$) to ensure robustness and reproducibility. We incorporated a pH-responsive pyrene monomer into two pH-responsive systems: a cross-linked hydrogel P(DMAm-co-DEAPyMA-co-EGDMA) and spherical micelles PGMA$_{35}$-b-P(HPMA$_{50}$-co-DEAPyMA$_{0.1}$). Our primary focus was on evaluating the pH-responsiveness and CO_2 sensitivity of the DEAPyMA dye within these environments. Continuous spectroscopic assessments during CO_2 exposure revealed that both systems exhibited distinct yet promising responsiveness, indicating their potential in gas sensing applications. The dye in hydrogels responded well to pH, CO_2, and air in a semi-dry state, while the nanoparticle

system showed a slower CO_2 response, and a faster air response compared to the linear polymer system.

4.2 Introduction

As detailed in Chapter 3, we successfully synthesized the pyrene-derived monomer DEAPyMA, which showed notable fluorescence changes in response to pH and CO_2 variations when incorporated into a water-soluble polymer. Building on this achievement, our next goal was to develop a durable and stable polymer system for CO_2 monitoring. An ideal approach involves creating a hybrid system that combines polymer and molecular elements. This system would feature a CO_2-responsive dye molecule that changes its fluorescence directly in response to fluctuations in CO_2 levels. By embedding this system within a polymer-based delivery platform, its practical use and effectiveness in aqueous environments could be significantly enhanced.

The desired characteristics for this system include reversibility, reusability, rapid response, low detection limit, and the ability to activate in the presence of CO_2 in water and deactivate upon CO_2 removal. This chapter focuses on designing effective CO_2 sensing methods using spherical nanoparticles and crosslinked hydrogels, both of which incorporate a fluorescent pH-sensitive dye. The research aims to explore the efficiency and performance of these materials under constant CO_2 pressure conditions.

Hydrogels, known for their soft and hydrated nature, consist of 3D cross-linked networks that can hold up to 90% water. They have recently garnered interest in analytical sensing systems capable of detecting variables such as pressure, temperature, ionic strength, organic compounds, biomolecules, and humidity.[1-3] Hydrogel-based composed of functional polymers, particularly stimuli-responsive types, can undergo specific optical,[4] chemical,[5] colorimetric,[6-8] fluorescence[9] and mechanical changes in response to external

physical and chemical stimuli. pH-sensitive gels exhibit swelling, or shrinkage based on the surrounding pH.[10] These gels contain ionizable groups that either donate or accept protons depending on the pH, leading to a consistent electrical charge (either negative or positive) within the gel.[1, 11] The resulting electrostatic repulsion among these charges facilitates water entry into the gel, causing it to swell. In hydrogels containing basic groups, low pH conditions lead to protonation, generating positive charges that repel each other, promoting water diffusion and resulting in the gel's swelling. These features make them interesting for pH sensing induced by CO_2 in a semi-aqueous environment.

Additionally, CO_2-responsive nano-objects have been the subject of extensive research due to their ability to utilize CO_2 as a trigger,[12-17] distinguishing them from polymers that respond to heat, pH, or light. The removal of CO_2 by purging with an inert gas like nitrogen enables the reversible activation of these polymers without generating harmful byproducts. However, a significant challenge in these systems has been the limited change in visual fluorescence. Moreover, polymer films can be made by spreading a water-based dispersion of these nano-objects onto a substrate, and then evaporating water until the particles come into contact and fuse together to deliver the nanoparticles.[18]

In this study, we report on two distinct polymeric systems: a DMAm-based hydrogel P(DMAm-co-DEAPyMA-co-EGDMA) and HPMA-based spherical nanoparticles PGMA-b-P(HPMA-DEAPyMA), both incorporating varying amounts of the fluorescent pH-responsive dye DEAPyMA- and displaying different interesting responses to pH changes in different states.

4.3 Results and discussion

4.3.1 pH/CO_2 responsiveness of P(DMAm-co-DEAPyMA-co-EGDMA) hydrogels

To develop stable hydrogels with DEAPyMA, we initiated this investigation by focusing on a system like the one described in Chapter 3, based on PDMAm. This approach allowed us to compare the behavior of the dye in two analogous systems and observe any differences in their response. To accomplish this, we copolymerized DMAm with 1% of the previously synthesized DEAPyMA and 1% EGDMA as a crosslinker in aqueous media, maintaining the reaction at 80ºC for 16 hours (Figure 4.1).The resulting 20 wt% hydrogel was too viscous, making it difficult to handle and unsuitable for property studies. Therefore, we reduced the solid content from 20% to 10%, which yielded a more stable and less viscous hydrogel that was easier to characterize. The obtained hydrogel was extensively dialysis in a 6-8 kDa membrane in water/THF (1:1) to remove any residue of unreacted monomer and was then freeze dried to obtain dry gels.

Scheme 4.1. Synthesis of P(DMAm$_{100}$-*co*-DEAPyMA$_1$-*co*-EGDMA$_1$) 10 wt% crosslinked hydrogels via free-radical polymerization with 1 eq of DEAPyMA.

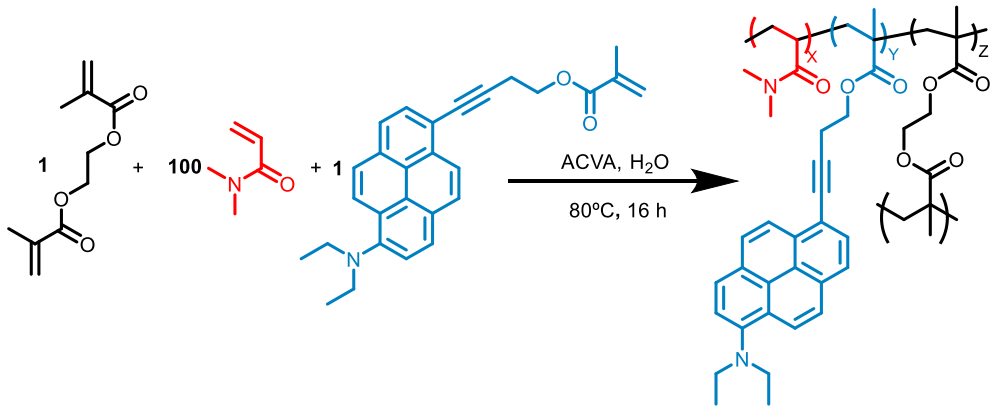

After obtaining the crosslinked system, we encountered that its lack of solubility in different solvents limited its characterization. Therefore, we began by measuring its FTIR

spectrum (Figure 4.1), where we identified the characteristic peaks of the C=O groups and the acrylate groups of DMAm at 1610 cm^{-1}. Additionally, we observed OH peaks at 3500 cm^{-1}, likely due to water absorption, reflecting the gel's high hygroscopic nature.

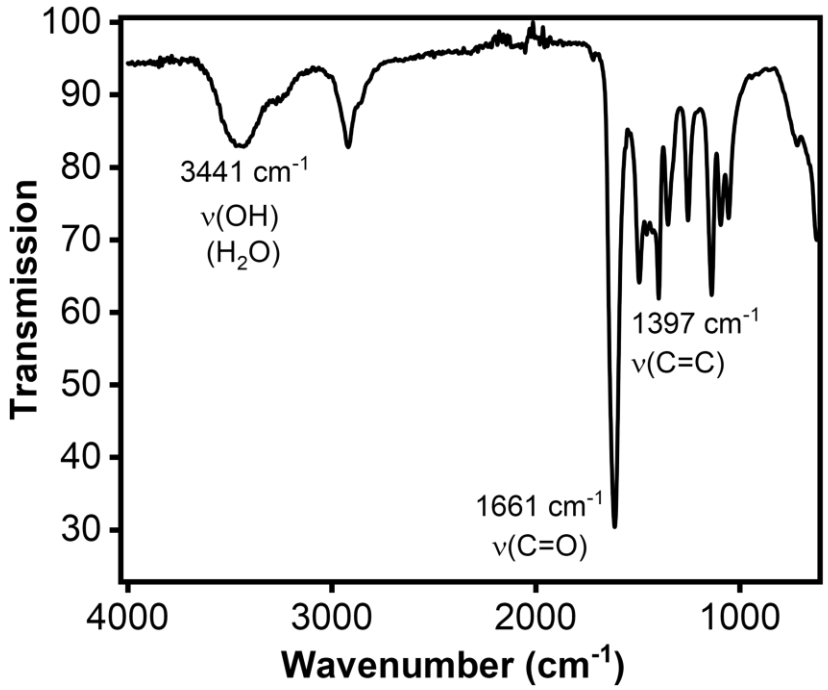

Figure 4.1. FTIR of freeze-dried hydrogels P($DMAm_{100}$-*co*-$DEAPyMA_1$-*co*-$EGDMA_1$).

To investigate the pH-responsiveness of these hydrogels, we wanted to observe any fluctuations in both visual and quantitative fluorescence. A fixed mass of dry hydrogel (0.1 g) was weighed and placed in a vial containing 3 mL of PBS-based pH buffer solution at pH levels of 7, 6, 5, 4, and 2. The hydrogel was incubated for 5 hours in the respective pH solution, after which its solid-state (SS) fluorescence was measured. The results exhibited a trend similar to that observed in the linear polymer described in Chapter 3. Specifically, the fluorescence peak at 385-400 nm, corresponding to the unimer (protonated pyrene), increased in intensity, while the peaks at 500-550 nm, representing the excimer form (non-protonated pyrene), decreased in intensity. Consequently, the $I_{490\ nm}/I_{385\ nm}$ ratio decreased as the pH lowered (figure 4.2b), resulting in a "turn off" of the

visual fluorescence of the system from pH 7 to pH 2, as illustrated in Figures 4.2c and 4.2d. This study confirmed that the DEAPyMA moiety retains its pH responsiveness within the crosslinked system, as well as the drastic change in visual fluorescence, in an analogous manner as we could observed for the linear polymer in the previous chapter.

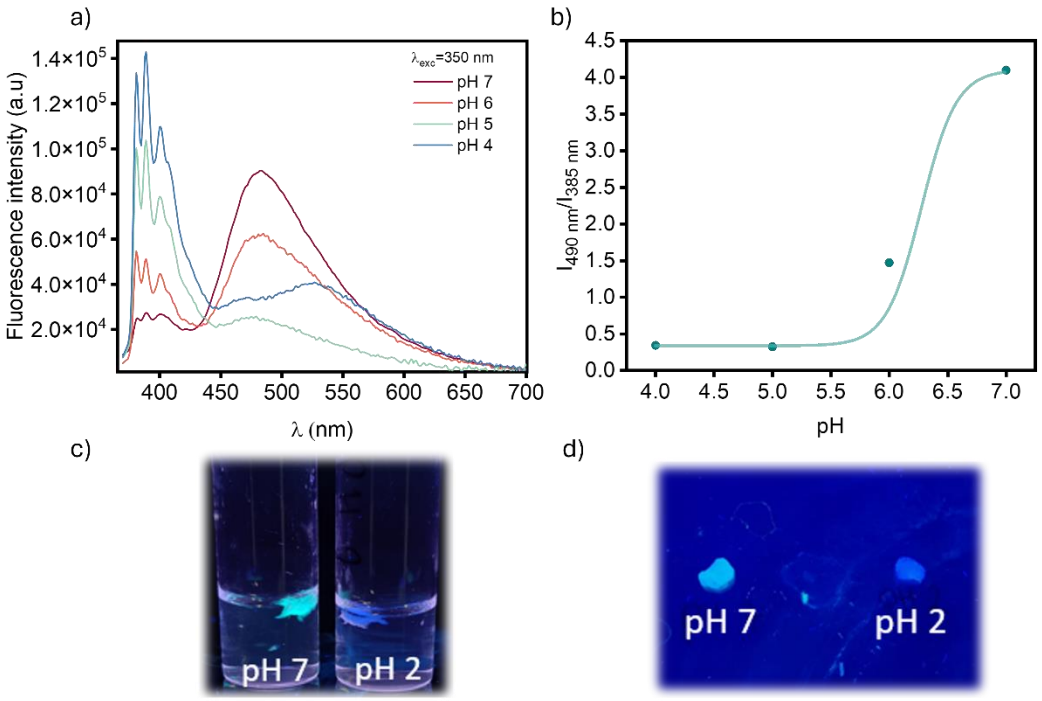

Figure 4.2. (a) Solid state emission spectrum of cross-linked P(DMAm$_{100}$-*co*-DEAPyMA$_1$-*co*-EGDMA$_1$) CO_2-responsive fluorescent hydrogels at pH 7, 6, 5 and 4. (b) Graphic representing change in intensity ratio I_{490nm}/I_{385nm} as effect of the pH for P(DMAm$_{100}$-*co*-DEAPyMA$_1$-*co*-EGDMA$_1$). Concentration 0.1 g of freeze-dried/3 mL PBS buffer solution. λ_{exc}= 350 nm. (c) Picture of vials with incubated hydrogels in buffers at pH 7 and 2 under UV lamp. (d) Picture of hydrogels after incubation in pH 7 and 2 buffers for 5 h under UV lamp.

Given the similarity in pH-responsiveness of the hydrogels to the results observed in Chapter 3, we proceeded to investigate the CO_2 responsiveness of this hydrogel system. A known hydrogel mass was incubated at pH 7 in a sealed vial. The solution was bubbled with CO_2 at a constant flow rate of 50 cm³/min and a pressure of 1 bar for 30 minutes.

Subsequently, the SS fluorescence of the system was measured, revealing an increase in intensity in the unimer emission region (380-400 nm) (figure 4.3a). Notably, the visual fluorescence of the system was completely quenched after CO_2 exposure, as shown in figure 4.3b. We hypothesize that this response is due to the higher permeability of CO_2 into the hydrogel system,[1] attributable to its higher porosity promoting water and CO_2 diffusion and resulting in the gel's swelling[19] compared to the previously studied linear polymer.

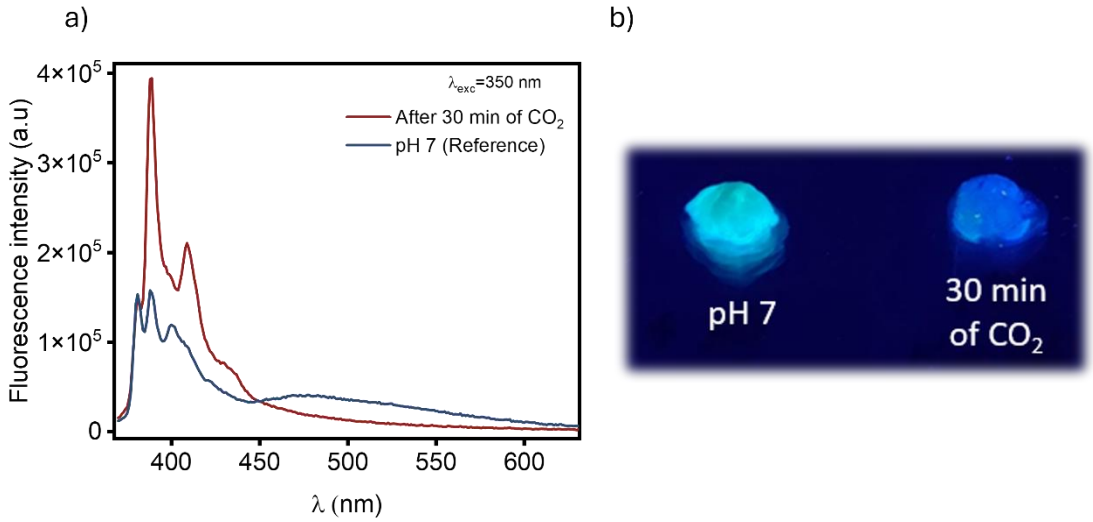

Figure 4.3. (a) Solid state emission spectrum of cross-linked P(DMAm$_{100}$-*co*-DEAPyMA$_1$-*co*-EGDMA$_1$) hydrogel at pH 7 and after 30 min of CO_2 bubbling. λ_{exc}= 350 nm.

Encouraged by the promising results, we proceeded to examine the reversibility of the hydrogel system. First, 0.1 g of hydrogel was introduced into 10 mL of DI water at pH 7. The solid-state (SS) fluorescence was measured and taken as reference. CO_2 was bubbled into the solution for 30 minutes, after which the SS fluorescence was measured again. The previous hydrogel was then exposed to air for 1 hour. The emission was quantified, and this process was repeated three times to assess reversibility (figure 4.4a). The fluorescence intensity ratio ($I_{490\ nm}/I_{385\ nm}$) decreased when CO_2 was bubbled through the

solution and increased when the system was subsequently exposed to air, indicating the removal of CO_2. This reversible behavior was observed over three cycles, as shown in figure 4.4b. Nevertheless, as the SS fluorescence depends on the amount of sample, there were some fluctuations on the values of fluorescence emission.

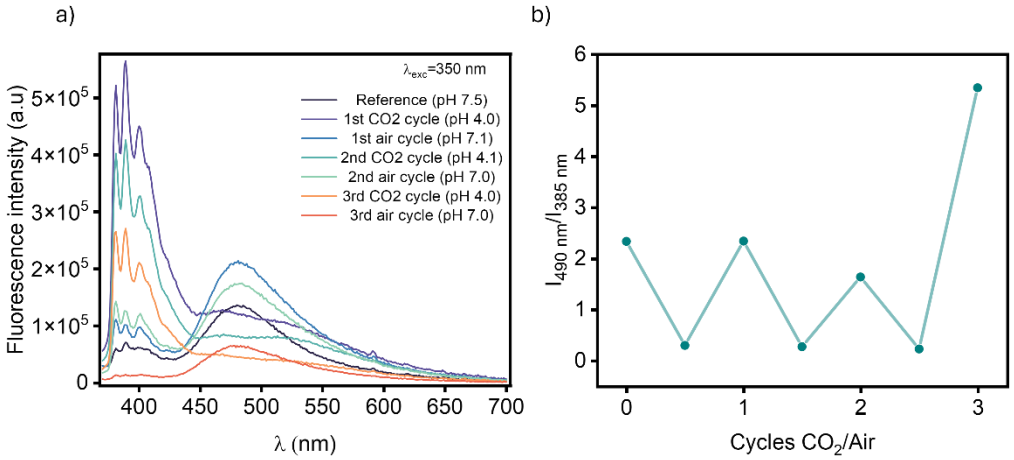

Figure 4.4. (a) Solid state emission spectrum of cross-linked P(DMAm$_{100}$-*co*-DEAPyMA$_1$-*co*-EGDMA$_1$) CO_2-responsive fluorescent hydrogels after several CO_2/air cycles in solution (b) Graphic representing change in intensity ratio I_{490nm}/I_{385nm} after several CO_2/air cycles in solution for P(DMAm$_{100}$-*co*-DEAPyMA$_1$-*co*-EGDMA$_1$). Concentration 0.1 g of freeze-dried/3 mL PBS buffer solution. λ_{exc}= 350 nm.

For CO_2 to dissolve and dissociate, thereby generating protons and reacting with the amines present in DEAPyMA, the reaction needed to take place in a wet/aqueous state. Therefore, as the main purpose of this PhD was to develop responsive polymers for detection in pipelines, we wanted to simulate a pipeline. For that, we used a glass pipette, sealed with a septum, and connected to the CO_2 cylinder with tubing. We then introduced the previously hydrated at pH 7 hydrogel into the system (scheme 4.2), and we flowed CO_2 for 1 hour at a constant flow rate of 50 cm^3/min. We measured its visual changes (figure 4.5a), and we observed a drastic change in fluorescence in comparison to the reference sample at pH 7 (figure 4.5b). This demonstrated that this system could be also

applied in a semi-dried state and did not need to be submerged in a solution to be responsive, amplifying the range of applicability.

Scheme 4.2. Schematic representation of pipeline simulation experiment with CO_2. 0.1g of dye hydrogel, previously hydrated in DI water at pH 7 for 30 min.

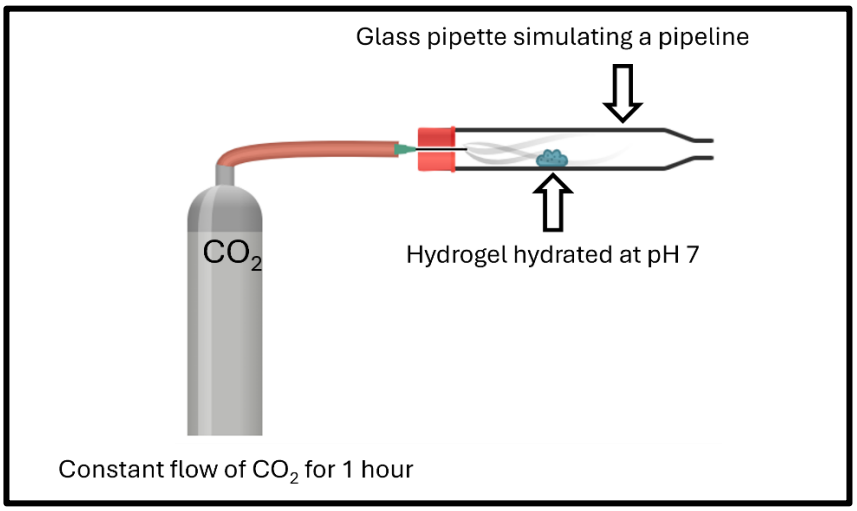

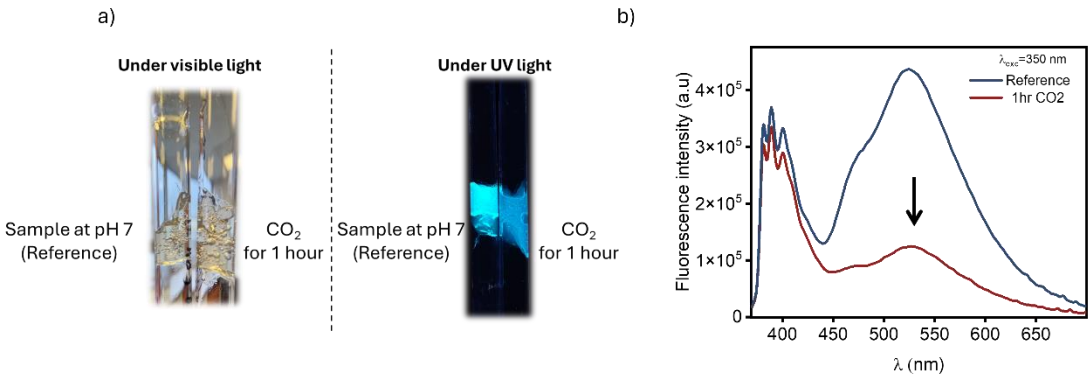

Figure 4.5. (a) Cross-linked P(DMAm$_{100}$-*co*-DEAPyMA$_1$-*co*-EGDMA$_1$) hydrogels in glass pipette, before and after being exposed to CO_2 under visible light (left) and under UV light (right). (b) SS fluorescence of cross-linked P(DMAm$_{100}$-*co*-DEAPyMA$_1$-*co*-EGDMA$_1$) hydrogels after pipeline simulation experiment. λ_{exc}= 350 nm.

Finally, we aimed to investigate additional physical properties of the hydrogel, such as swelling behavior, rheological test and porosity using SEM, to better understand the mechanisms behind its excellent responsiveness.

For the swelling test, the hydrogel was monitored over the course of one week. The results showed a swelling ratio increase of approximately 70% relative to the original dry mass as it can be seen in figure 4.6, indicating a high swelling capacity in aqueous environments. This high swelling capacity is advantageous for CO_2 solution and subsequent reaction within the hydrogel matrix.

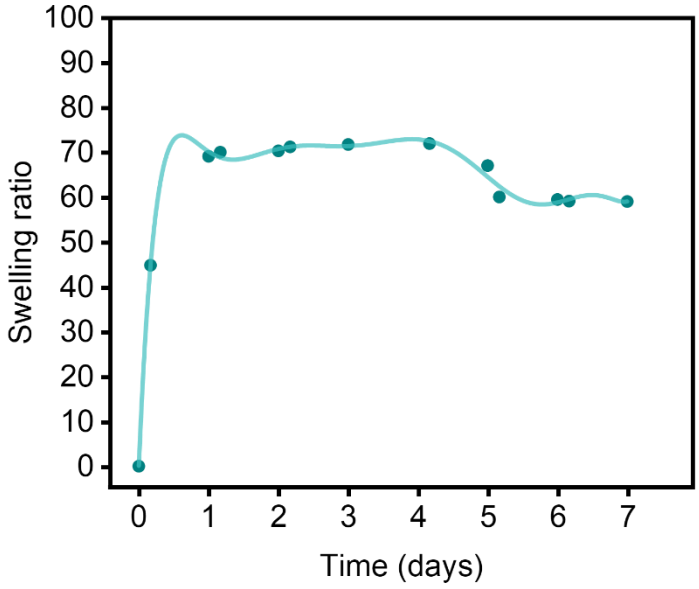

Figure 4.6. Swelling test of cross-linked P(DMAm$_{100}$-*co*-DEAPyMA$_1$-*co*-EGDMA$_1$) hydrogel.

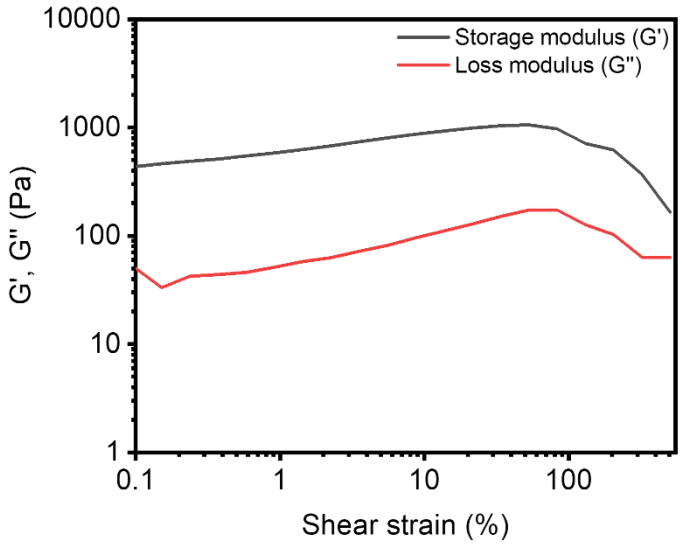

Figure 4.7. Rheological test of hydrated cross-linked P(DMAm$_{100}$-*co*-DEAPyMA$_1$-*co*-EGDMA$_1$) hydrogel at 5ºC.

The rheological analysis shows the storage modulus (G') higher than the loss modulus (G") across the range of shear rates. It indicates that hydrogel has a predominantly elastic nature. The material exhibits shear-thinning behavior: the hydrogel can maintain its structure under low stress but becomes less viscous and flow more easily under high stress. This means, these hydrogels could be applied as coating for CO_2 sensing as they are shear-thinning materials.

The hydrogel system demonstrated to have promised for CO_2 sensing. It performed not only a remarkable response to CO_2 but also a high swelling ratio and interesting rheological properties for their potential applicability as CO_2 sensors in pressurized systems.

4.3.2 pH/CO_2 responsiveness of PGMA-b-P(HPMA-DEAPyMA) spherical nanoparticles.

Scheme 4.3. $PGMA_{35}$ macro-CTA 2-step synthesis starting from glycidyl methacrylate.

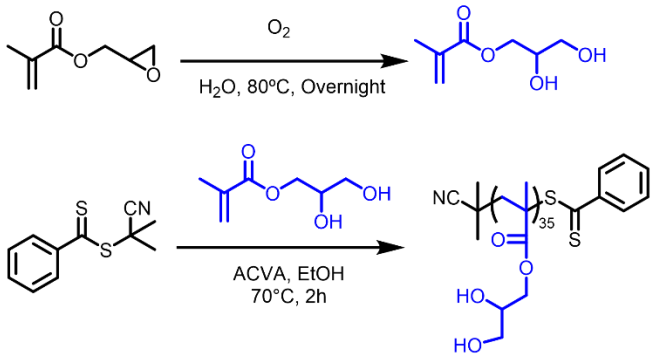

From the previous system, we observed how the structural properties of the hydrogel could affect CO_2 permeation and, as consequence, the fluorescence response of the dye. For the nanoparticle system we wanted to observe how the hydrophobicity of the core would affect its performance. We started this investigation by finding a well-known water-dispersible spherical nanoparticle scaffold that could be used as a potential delivery method for our previously synthesized dye DEAPyMA. For that we chose to be used, a similar system based on one previously reported by Armes and coworkers.,[20] synthesized by RAFT aqueous dispersion polymerization. Subsequently, a well-defined poly(glycerol methacrylate)$_{35}$ ($PGMA_{35}$) macro-CTA was synthesized by RAFT polymerization in ethanol at 70ºC for 2 h. (DMF GPC, M_n = 11,800 g mol^{-1}, M_w/M_n = 1.27; vs poly(methyl methacrylate) calibration standards) of glycerol methacrylate (GMA) and 2-Cyano-2-propyl benzodithioate (CPBD) as RAFT agent.

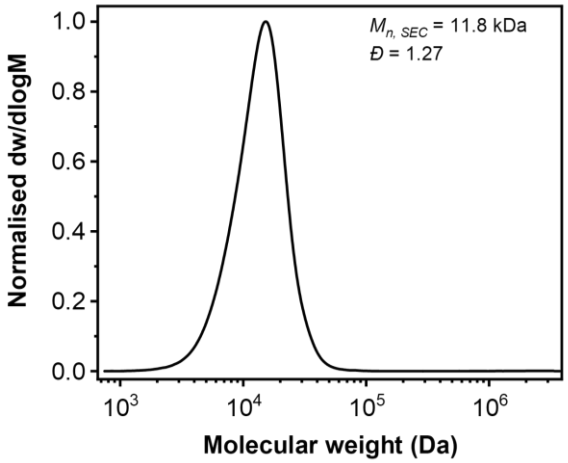

Figure 4.8. Normalized SEC RI molecular weight distribution for $PGMA_{35}$ macro-CTA, along with corresponding M_n and Đ values calculated based on PEG standards using DMF containing 4.6 mM of NH_4BF_4 as the eluent.

To obtain spherical nano-objects we first synthesized a reference system by chain-extension of the previously synthesized $PGMA_{35}$ with 2-hydroxypropyl methacrylate (HPMA) via RAFT dispersion polymerization in a H_2O/EtOH (1:1) dual solvent system. The use of this dual solvent system was necessary due to the highly hydrophobic nature of the DEAPyMA dye.

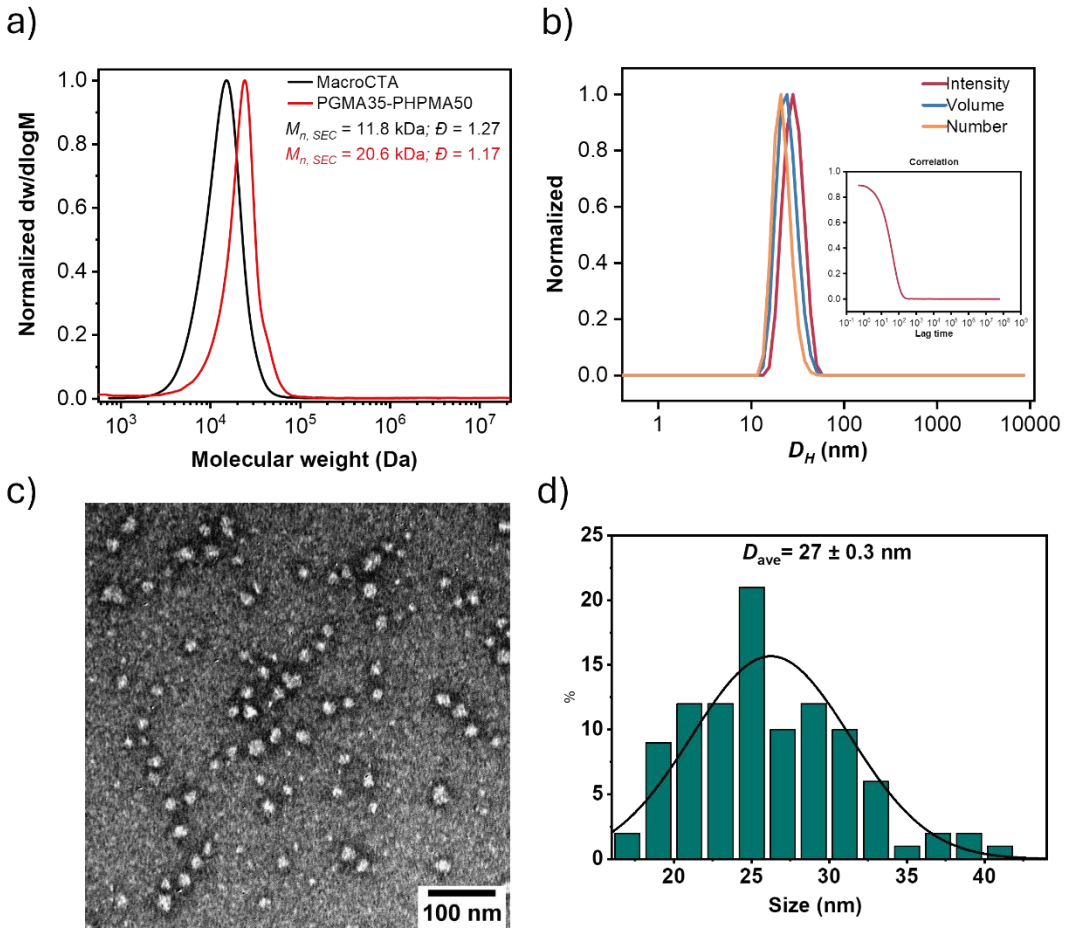

Figure 4.9. (a) Normalized SEC RI molecular weight distributions for $PGMA_{35}$-b-$PHPMA_{50}$ reference nanoparticles and macroCTA, along with corresponding M_n and Đ values calculated based on PEG standards. (b) Normalized DLS particle size distribution of reference nanoparticles in water with corresponding correlogram. (c) Dry-state TEM image of nanoparticles at pH 7, stained with uranyl acetate. (d) Corresponding histogram showing size distribution of nanoparticles.

$PGMA_{35}$-*b*-$PHPMA_{50}$ spherical nanoparticles were obtained and the resulting polymer had a molecular weight (M_n) of 20,600 g/mol and a narrow molecular weight distribution (Mw/Mn = 1.17) (figure 4.9a), according to DMF GPC analysis using poly(methyl methacrylate) standards. The reaction achieved a high monomer conversion rate of over 98%, as indicated by the disappearance of vinyl proton signals at 5.6 and 6.2 ppm in the

^{1}H NMR spectrum (see figure 4.10). Dynamic Light Scattering (DLS) studies showed that the average hydrodynamic diameter of the PGMA$_{35}$-*b*-PHPMA$_{50}$ copolymer nano-objects was approximately 30nm (see figure 4.9b). Additionally, dry TEM analysis confirmed the formation of well-defined spherical nanoparticles as it can be observed in figures of size average size 27 nm (4.9c and d).

Scheme 4.4. Synthetic scheme of synthesis of both reference and fluorescence pH-responsive nanoparticles via RAFT-PISA polymerization in H_2O/EtOH (1:1)

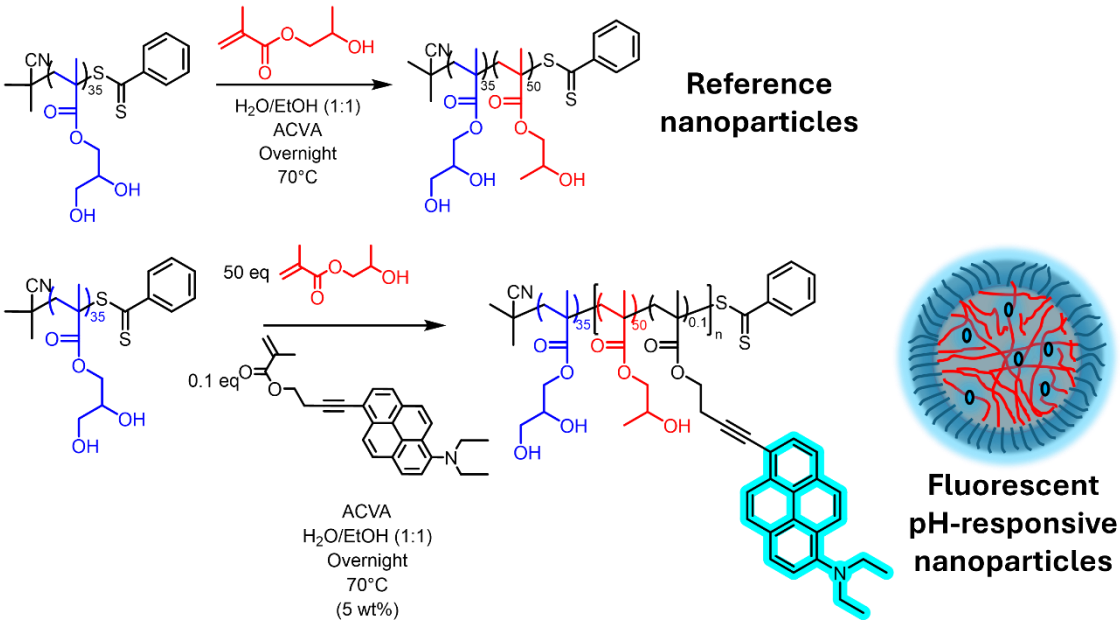

After synthesizing the reference nanoparticles, our goal was to incorporate the DEAPyMA dye into the hydrophobic core to compare its reactivity with CO_2 to previously developed systems. For that, we used the same synthetic method as for the reference particles, but copolymerizing DEAPyMA with HPMA in the second step on a ratio 50/1 (HPMA/DEAPyMA). However, during the first polymerization attempt, the hydrophobic nature of DEAPyMA disrupted the process, leading to gelation. To resolve this issue, we reduced the HPMA/DEAPyMA ratio to 50/0.1. This adjustment was feasible due to the high sensitivity of the DEAPyMA moiety, around the ppb range, as discussed in Chapter 3 for P(DMAm$_{100}$-*co*-DEAPyMA$_1$).

We successfully obtained the self-assembled system PGMA$_{35}$-*b*-P(HPMA$_{50}$-*co*-DEAPyMA$_{0.1}$) at 5 wt.% solids via RAFT-PISA polymerization, this time without gelation process occurring as it can be seen in figure 4.11d.

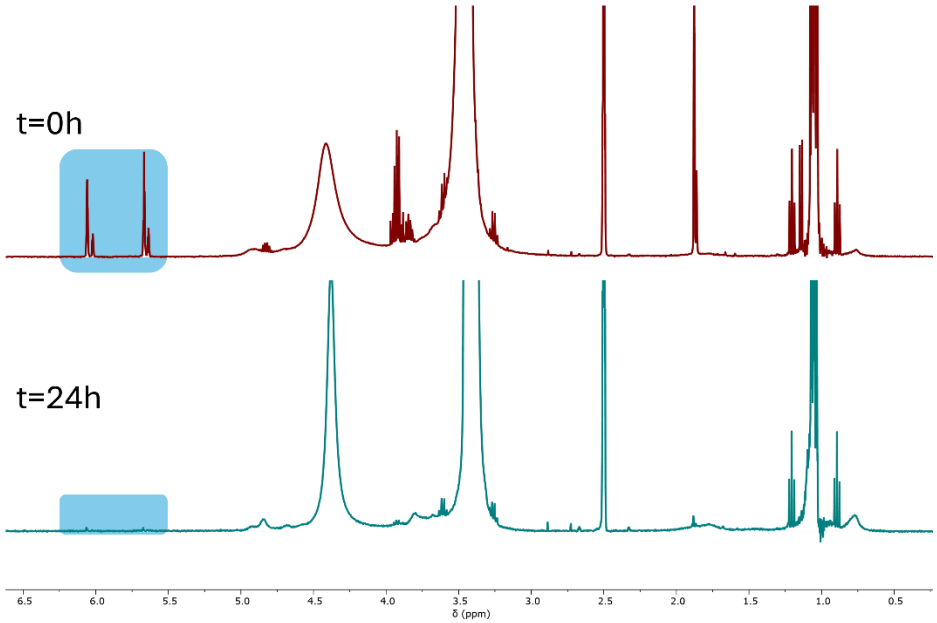

Figure 4.10. ^{1}H NMR spectra of synthesis of PGMA$_{35}$-*b*-P(HPMA$_{50}$-*co*-DEAPyMA$_{0.1}$) via RAFT-PISA polymerization at time 0 h and time 24 h. Solvent DMSO-d_6.

The obtention of the polymer was confirmed by ^{1}H NMR spectroscopy, which showed over 95% conversion (figure 4.10), and size exclusion chromatography, which indicated the resulting polymer had a molecular weight (M_n) of 24,900 g/mol and a narrow molecular weight distribution (M_w/M_n = 1.12) as it is shown in figure 4.11a. The nanoparticles were dispersed in water and DLS analysis revealed one single distribution in intensity, number, and volume with an average particles size of 61 nm (figure 4.11b), almost double the size of the reference nanoparticles. Dry-state TEM confirmed that the spherical morphology was maintained (figure 4.11c). We attributed this increase in size to the incorporation of the voluminous DEAPyMA molecule into the core and the overall increased of the hydrophobicity which expanded the core and, consequently, the average size of the nanoparticles.

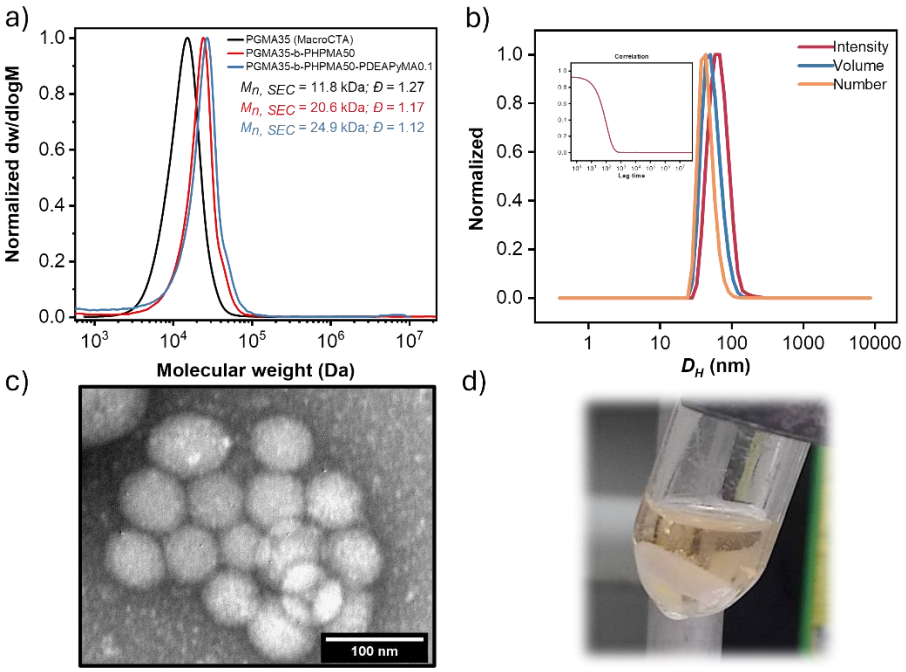

Figure 4.11. (a) Normalized SEC RI (black trace) molecular weight distributions for PGMA$_{35}$-*b*-P(HPMA$_{50}$-*co*-DEAPyMA$_{0.1}$) nanoparticles, along with corresponding Mn and Đ values calculated based on PEG standards. (b) Normalized DLS graphic of PGMA$_{35}$-*b*-P(HPMA$_{50}$-*co*-DEAPyMA$_{0.1}$) nanoparticles in water with corresponding correlogram. (c) Dry-state TEM image of PGMA$_{35}$-*b*-P(HPMA$_{50}$-*co*-DEAPyMA$_{0.1}$) nanoparticles at pH 7, stained with uranyl acetate. (d) Picture of Schlenk flask containing PGMA$_{35}$-*b*-P(HPMA$_{50}$-*co*-DEAPyMA$_{0.1}$) after 24 h of polymerization.

Once we obtained the spherical nanoparticles, the next step was to study their optical properties and how these properties changed with variations in pH or CO_2 concentration in the solution, just as we did with the previous systems. This time, we aimed to compare the responses of this nanoparticle system with the results obtained for the linear polymer P(DMAm$_{99}$-co-DEAPyMA$_1$). Despite the differences in composition between these systems, we wanted to observe the behaviour of the pyrene monomer in two different environments. We studied the fluorescence emission of the self-assembled system across a pH range of 7 to 2 at a concentration of 0.1 mg/mL. DEAPyMA exhibited a more

distinct response in the nanoparticles compared to the linear system (figure 4.12a vs 4.12c); specifically, each emissive peak changed gradually. The intensity ratio I_{490}/I_{I385} trend observed was consistent with previous systems: as the pH became more acidic, the intensity of the unimer peak at 385 nm increased, while the peak at 490 nm decreased. This is, the ratio I_{490}/I_{I385} increased as the pH increased (figure 4.12b vs 4.12d)

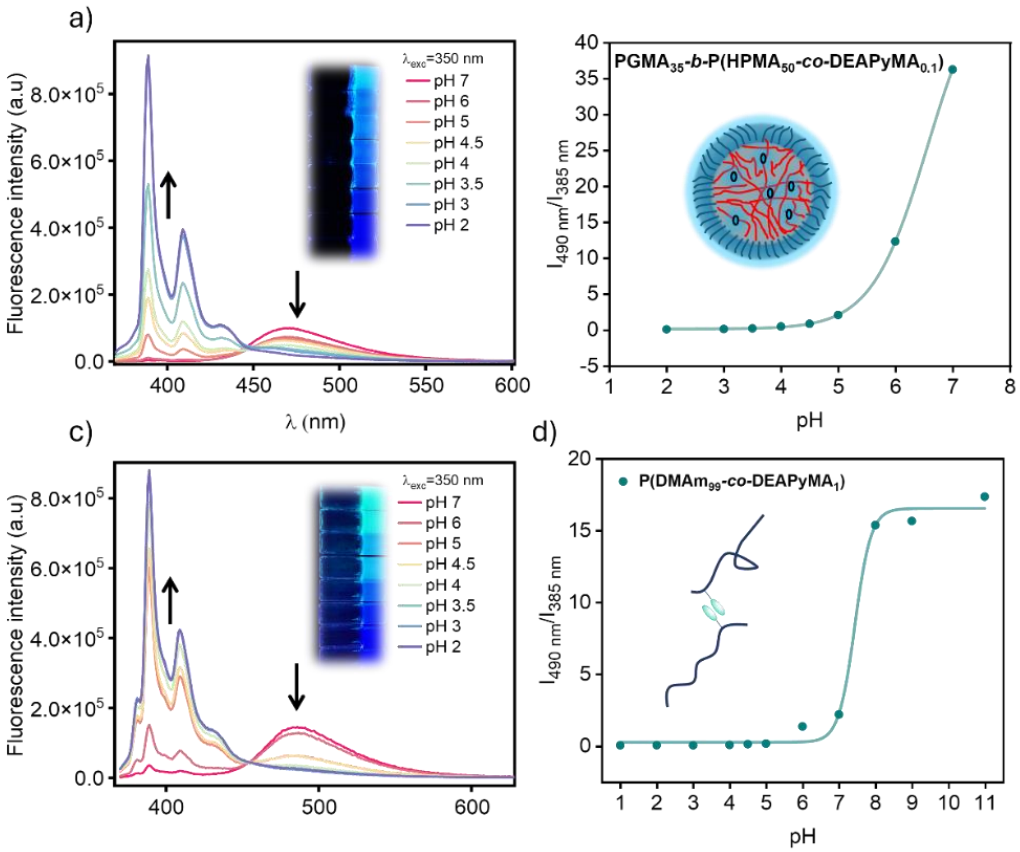

Figure 4.12. (a) Fluorescence spectrum of $PGMA_{35}$-*b*-$P(HPMA_{50}$-*co*-$DEAPyMA_{0.1})$ at pHs 7, 6, 5, 4.5, 4, 3.5, 3 and 2. (b) Graph representing change in intensity ratio I_{490nm}/I_{385nm} as effect of the pH for $PGMA_{35}$-*b*-$P(HPMA_{50}$-*co*-$DEAPyMA_{0.1})$. Concentration of 0.1 mg/mL of nanoparticles. λ_{exc}= 350 nm. (c) Fluorescence spectrum of P(DMAm99-co-$DEAPyMA_1$) at pHs 7, 6, 5, 4.5, 4, 3.5, 3 and 2. (d) Graph representing change in intensity ratio I_{490nm}/I_{385nm} as effect of the pH for P(DMAm99-co-$DEAPyMA_1$). Concentration of linear polymer 0.1 mg/mL. λ_{exc}= 350 nm.

To assess the CO_2 responsiveness of the particles, we first evaluated a 0.1 mg/mL solution of the nanoparticles in water at pH 7, using a CO_2 flow rate of 50 cm^3/min for 5 minutes, consistent with our previous experiments on the linear polymer. As shown in figure 4.13a, the intensities of both unimer and excimer peaks change gradually with increasing CO_2 exposure time. The change in intensity for the peak at 490nm was less anticipated, resulting in no visible change in fluorescence despite a notable change in the intensity ratio I_{490}/I_{I385} (figure 4.13b). For a better understanding of the system's behavior, we extended the kinetics time to 1 hour. The fluorescence intensity measured over this period revealed a decrease in the 490 nm peak intensity, similar to what we observed for the linear polymer (figures 4.13c and 4.13e). Figures 4.13d and 4.13f indicate that a higher volume of CO_2 was required to 'turn off' the fluorescence of the nanoparticles compared to the linear polymer. Specifically, while the linear polymer required approximately 50 cm^3 of CO_2, the nanoparticles required 1000 cm^3 to achieve fluorescence quenching, The lowest I_{490}/I_{I385} ratio achieved for the nanoparticles was 0.28, compared to 0.05 for the linear polymer.

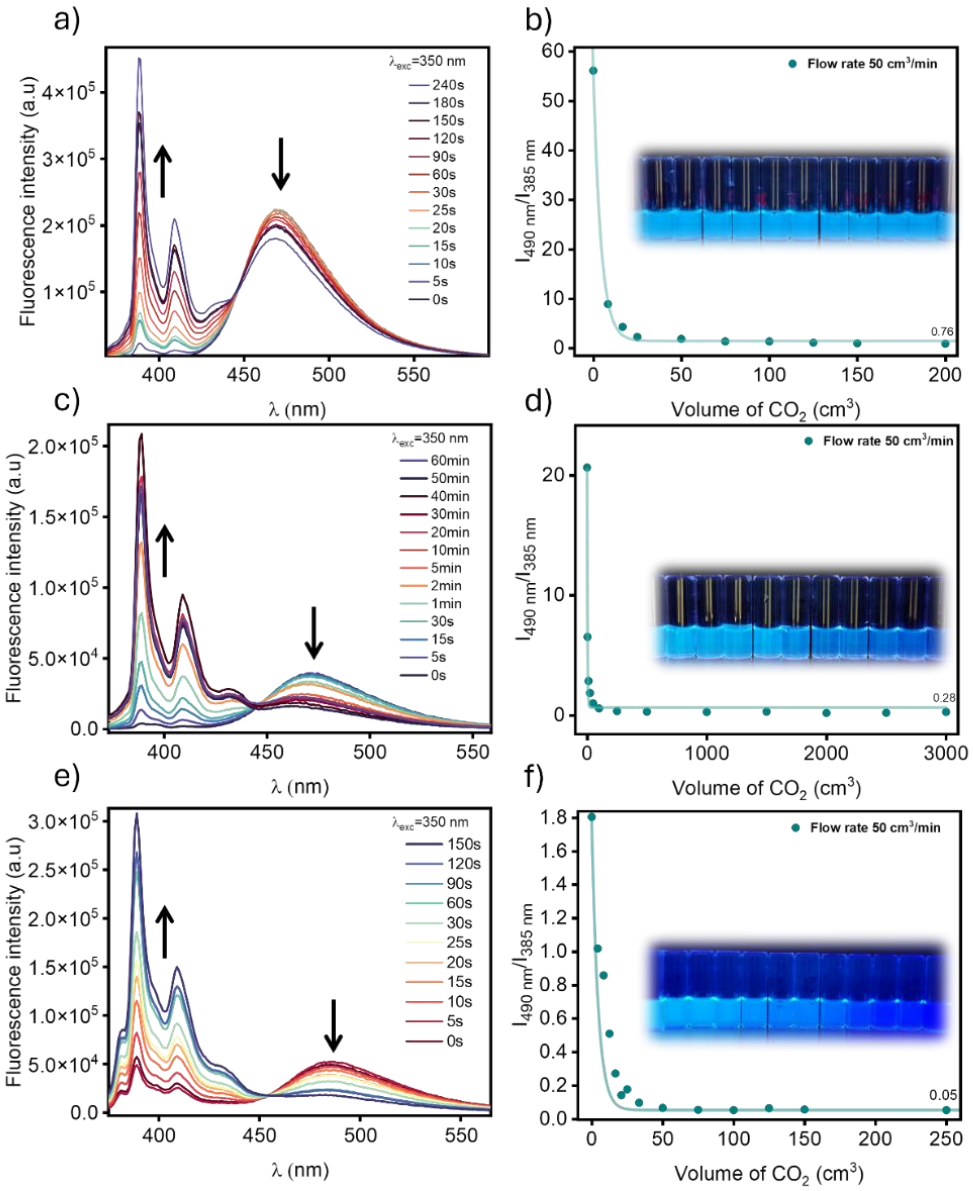

Figure 4.13. (a) CO_2 kinetics fluorescence spectrum of PGMA$_{35}$-*b*-P(HPMA$_{50}$-*co*-DEAPyMA$_{0.1}$) (4 minutes kinetics). (b) Graph representing change in intensity ratio I_{490nm}/I_{385nm} as effect of CO_2 volume for PGMA$_{35}$-*b*-P(HPMA$_{50}$-*co*-DEAPyMA$_{0.1}$) (4 minutes kinetics). Concentration of 0.1 mg/mL of nanoparticles. λ_{exc}= 350 nm. (c) CO_2 kinetics fluorescence spectrum of PGMA$_{35}$-*b*-P(HPMA$_{50}$-*co*-DEAPyMA$_{0.1}$) (60 minutes kinetics). (d) Graph representing change in intensity ratio I_{490nm}/I_{385nm} as effect of CO_2 volume for PGMA$_{35}$-*b*-P(HPMA$_{50}$-*co*-DEAPyMA$_{0.1}$) (60 minutes kinetics). Concentration of 0.1 mg/mL of nanoparticles. λ_{exc}= 350 nm. (e) CO_2 kinetics fluorescence spectrum of P(DMAm$_{99}$-co-DEAPyMA$_1$). (f) Graphic representing change in intensity

ratio I_{490nm}/I_{385nm} as effect of the CO_2 volume P(DMAm$_{99}$-co-DEAPyMA$_1$). Concentration of linear polymer 0.1 mg/mL. λ_{exc}= 350 nm.

To evaluate the air kinetics, a previously CO_2 bubbled sample was exposed to atmospheric air while stirring at 1000 rpm for 1 h. this resulted in a recovery of the 'ON' state, the unimer peak in this case was decreasing in intensity while the excimer peak was increasing simultaneously (figure 4.14a), as effect of the removal of CO_2 from the system and increase of the pH from 4.3 to 7. In the case of the nanoparticles the I_{490}/I_{I385} ratio gradually increased and the 'ON' process was a much faster process than expected, just after 1 minute of exposure (figure 4.14b), while it took around 25 minutes in the linear polymer to recover the same state of visual fluorescence. (figure 4.14c and 4.14d).

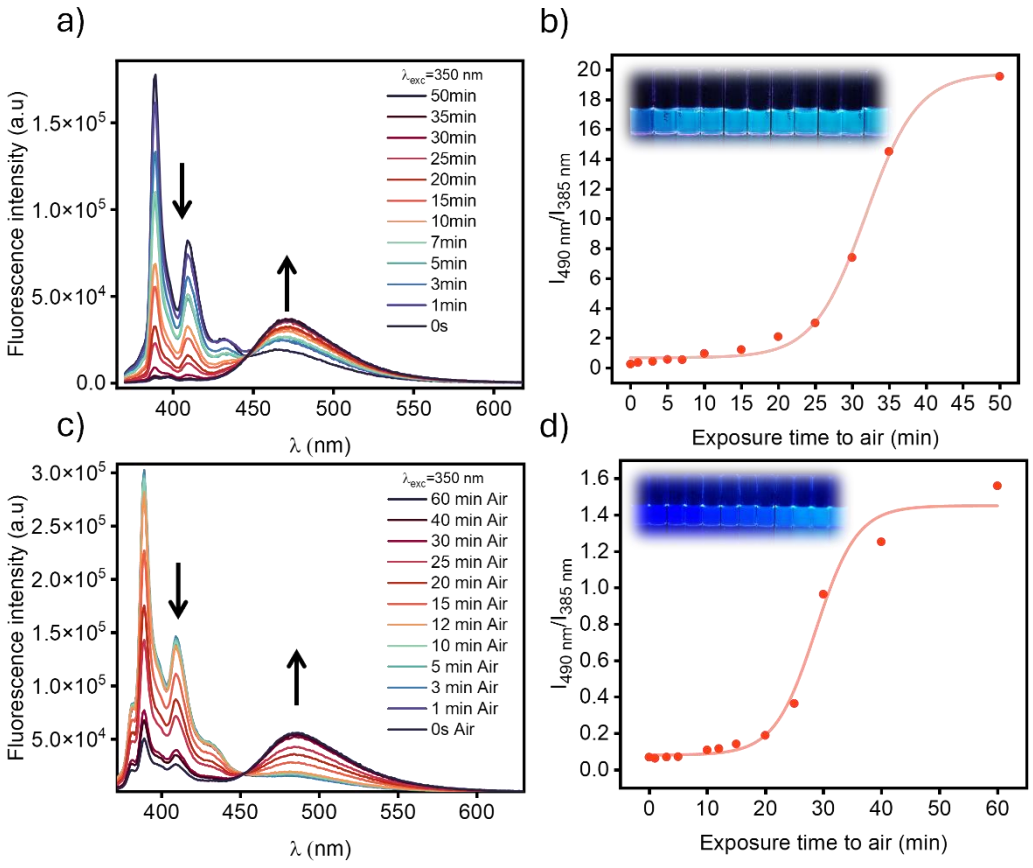

Figure 4.14. (a) Air kinetics fluorescence spectrum of PGMA$_{35}$-*b*-P(HPMA$_{50}$-*co*-DEAPyMA$_{0.1}$) (50 minutes kinetics). (b) Graph representing change in intensity ratio I_{490nm}/I_{385nm} as effect of air exposure time for PGMA$_{35}$-*b*-P(HPMA$_{50}$-*co*-DEAPyMA$_{0.1}$)

(50 minutes kinetics). Concentration of 0.1 mg/mL of nanoparticles. λ_{exc}= 350 nm. (c) Air kinetics fluorescence spectrum of P(DMAm$_{99}$-co-DEAPyMA$_1$). (d) Graph representing change in intensity ratio I_{490nm}/I_{385nm} as effect of air exposure time P(DMAm$_{99}$-co-DEAPyMA$_1$). Concentration of linear polymer 0.1 mg/mL. λ_{exc}= 350 nm.

We hypothesized that the process occurs much faster in the self-assembled system due to the hydrophobic core of the particles. Since the pyrene moiety is located within this core, it is more challenging for CO_2 and water to permeate, necessitating a longer exposure to CO_2 to protonate the pyrene moieties and disrupt the excimer state. Conversely, when the system is exposed to air, the process is rapid for the same reason. The hydrophobic core resists interaction with hydrophilic compounds, so as soon as air exposure begins, the CO_2 dissolved in the core quickly escapes, this is the excimer state is recovered.

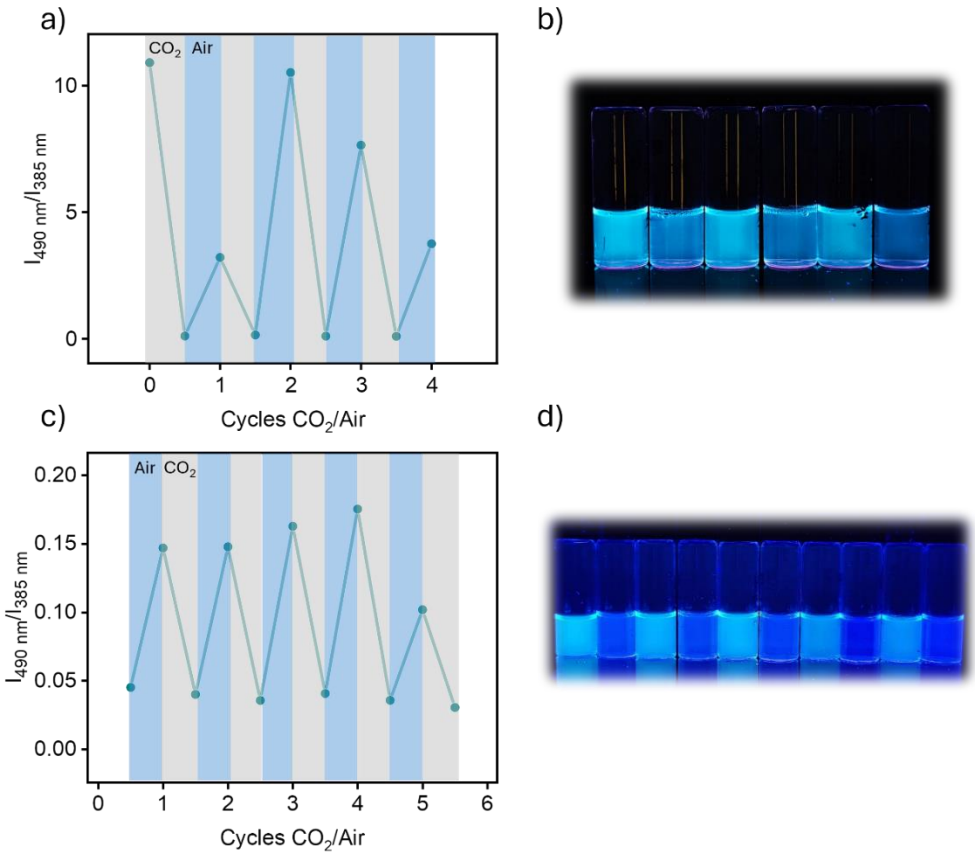

Figure 4.15. (a) Graph representing change in intensity ratio I_{490nm}/I_{385nm} as effect of CO_2 (60 min)/air (60 min) reversibility cycles for PGMA$_{35}$-*b*-P(HPMA$_{50}$-*co*-DEAPyMA$_{0.1}$)

nanoparticles. Concentration of 0.1 mg/mL of nanoparticles. λ_{exc}= 350 nm. (b) Pictures of vials of $PGMA_{35}$-*b*-$P(HPMA_{50}$-*co*-$DEAPyMA_{0.1})$ nanoparticles after CO_2/air cycles under 365 nm UV-light. (c) Graph representing change in intensity ratio I_{490nm}/I_{385nm} as effect of CO_2 (10 min)/air (60 min) reversibility cycles for $P(DMAm_{99}$-co-$DEAPyMA_1)$. Concentration of linear polymer 0.1 mg/mL. λ_{exc}= 350 nm. (d) Pictures of vials of $P(DMAm_{99}$-co-$DEAPyMA_1)$ after CO_2/air cycles under 365 nm UV-light.

Finally, the reversibility test involved exposing the nanoparticle system to CO_2 for 1 hour and to air for 50 minutes, continuously, while measuring the fluorescence intensity ratio and pH. Comparing the results, the nanoparticles did not exhibit as robust reversibility as the linear polymer, mainly due to difficulty of permeation of CO_2 into the system. Additionally, the change in fluorescence was significantly more pronounced for the linear polymer than for the nanoparticles, which did not exhibit the expected level of change. We believe that the particles' permeability and hydrophobicity, as previously mentioned, play a crucial role in these cycles. One way of further investigation would be to synthesize analogue nanoparticles with a less hydrophobic core to observe the differences in response of the dye within the system.

4.4 Conclusion

Conclusion

In this study, we successfully integrated the DEAPyMA monomer into two distinct polymeric platforms with potential for CO_2-responsive applications. Both systems showed behaviours consistent with the linear polymer analogue described in Chapter 3, while also revealing new characteristics influenced by their structural environments. The P(DMAm-co-DEAPyMA-co-EGDMA) hydrogel system demonstrated strong fluorescence modulation under pH, CO_2, and air exposure, particularly in a semi-dry state. This enhanced response is likely due to improved gas permeability, facilitating the interaction between CO_2 and the dye-functionalized matrix—an effect similarly reported in gas-permeable hydrogel-based sensing systems.[21]

On the other hand, nanoparticles incorporating the pyrene-functional DEAPyMA exhibited a more delayed response to CO_2 and a quicker one to air. This difference can be attributed to the pyrene unit being embedded in the hydrophobic core, which limits CO_2 and water diffusion—behaviour consistent with findings in polymeric micelle systems where core-localized dyes show attenuated interactions with external stimuli.[22]

These results highlight the versatility and reliability of the DEAPyMA fluorophore across varying architectures. While the kinetics and sensitivity vary depending on the physical structure, the core sensing mechanism remains robust. The distinct advantages offered by each system—whether faster signal change in semi-dry hydrogels or encapsulated protection and tunability in nanoparticle systems—suggest a broad range of future applications in real-time CO_2 sensing.

Moving forward, optimization of these materials' mechanical and physicochemical properties will be critical. Enhancing aspects like swelling behaviour, particle permeability, and photostability will allow better adaptability to complex environments, including industrial CO_2 leak detection, environmental monitoring, and potentially biomedical scenarios such as respiratory diagnostics, where accurate and timely CO_2 detection is crucial.[23]

By refining these systems, we aim to lay the groundwork for multifunctional, scalable, and application-ready CO_2 sensing materials capable of real-world implementation.

4.5 Experimental section

4.5.1 Materials

N,N-Dimethylacrylamide (DMAm, 99%, 500 ppm MEHQ), ethylene glycol dimethacrylate (EGDMA, 98%), glycidyl methacrylate (97%, 100 ppm MEHQ), 4,4'-azobis(4-cyanovaleric acid) (ACVA, 98%), hydroxypropyl methacrylate (97%, mixture of isomers, 180-22 ppm MEHQ), 2-cyano-2-propyl benzodithioate (CPBD, 97%) were supplied by Sigma Aldrich. Ethanol (EtOH, ≥99.5%) was supplied by Fisher Scientific. 4-(6-(diethylamino)pyren-1-yl)but-3-yn-1-yl methacrylate (DEAPyMA) was previously synthesized in chapter 3. 1kg CP carbon dioxide-cylinder and pure nitrogen was obtained from BOC. Spectrum Spectra/Por dialysis tubing with either 1 kDa or 6–8 kDa MWCO was supplied by Fisher Scientific. Deionized and 18.2 MΩ·cm ultrapure water was obtained from a Triple Red Alto purification system and was used in all experiments unless stated otherwise.

4.5.2 Instrumentation

***Size Exclusion Chromatography*.** Molecular weight distributions were determined using size exclusion chromatography (SEC) on an Agilent PL50 instrument. The mobile phase used was DMF containing 4.6 mM of NH_4BF_4, at a flow rate of 1.0 mL min^{-1}, a column temperature of 40 °C and detection by refractive index (RI). 80 µL of sample were injected for each measurement and eluted for 35 min. Samples were prepared at a concentration of 1 mg mL^{-1} and filtered using a 0.45 µm nylon filter prior to analysis. Calibration was conducted in the molecular weight range 100-30000 Da using EasiVial polyethylene glycol (PEG) standards supplied by Agilent Technologies.

^{1}H, ^{13}C - Nuclear Magnetic Resonance (NMR) spectra were acquired at 400 MHz using a Bruker DPX-400 spectrometer with D2O containing 0.5 M NaCl as the solvent in the

case of PDMAPS, $CDCl_3$ for SPMA and ACMMA, DMSO-d6 for NBDMA and CH_2Cl_2 for TPEMA. At least 32 scans were recorded for each sample and the proton chemical shifts are reported as chemical shift (δ) in parts per million (ppm) and are relative to solvent residual peaks.

Hydrodynamic diameters (D_h) and size distributions (PD) of particles were determined by dynamic light scattering (DLS) using either a Malvern Panalytical Zetasizer Nano S or Nano ZSP fitted with a 633 nm He-Ne laser operating at 4 or 10 mW. Samples were prepared at a concentration of approximately 1 mg mL^{-1} in 0.3 M NaCl. Measurements were performed at 20 °C using a scattering angle of 173° (backscattering) using the high resolution mode, and the results analysed using Malvern Panalytical Zetasizer software version 7.13. All determinations were repeated 4 times, taking the average of at least 10 measurements for each run. D_h values were calculated using the Stokes-Einstein equation, assuming the particles are spherical in solution.

UV-Vis spectroscopy was performed on an Evolution 350 UV-Vis spectrophotometer equipped with Xenon Flash Lamp light source and Dual Matched Silicon Photodiodes detector. Quartz cells (170 - 2000 nm) from Hellma, with two polished sides, were used for examining the absorption spectral data by using Thermo INSIGHT-2 v.10.0.30319.1 software. A thermostat and 8-cell Peltier system with precise temperature control between 0 ºC and 90 ºC was coupled with an Evolution 350 UV-Vis spectrophotometer to record the LCST behaviour, temperature-dependent absorption/transmittance spectra of the sample. All variable temperature analysis size experiments were made using samples of concentration 5 mg mL^{-1} in 0.3 M NaCl(aq), Variable temperature analyses were run from 15-90 ºC at a heating rate of 1 ºC min^{-1}.

Fluorescence Spectroscopy. All steady state emission and excitation were obtained with an Edinburgh Instruments FS5 Spectrofluorometer in matched quartz 3.5 mL cuvettes

(Starna Cell, Type: 3/Q/10), and analyzed in Fluoracle (Edinburgh Instruments) and Origin Pro 2022 (Origin Labs). All samples of the pH studies were prepared at concentration of 0.3 mg/mL and different buffer solutions.

pH measurements were carried out in a Mettler Toledo G20 compact titrator equipped with a pH-electrode DGi115-SC. The calibration of the glass pH-electrode was performed using buffer solutions pH 4.01, 7.00, and 9.21 from Mettler Toledo. All data were recorded using the LabX Light Titration 3.1.1.0 software provided by Mettler Toledo.

Transmission Electron Microscopy. Dry-state-stained transmission electron microscopy (TEM) imaging was performed on a JEOL JEM-1400 microscope at an acceleration voltage of 80 kV. All samples were diluted with deionized water to appropriate analysis concentration and then deposited onto formvar-coated copper grids. After approximately 1 min, excess sample was blotted from the grid and the grid was stained using an aqueous 1 wt % uranyl acetate (UA) solution for 1 min prior to blotting, drying and microscopic analysis. Average particle diameters (D_{ave}) were determined by measuring 100 particles per sample using the ImageJ software.

Fourier-Transform Infrared Spectroscopy. Fourier-Transform Infrared (FTIR) spectroscopy was carried out using an Agilent Technologies Cary 630 FTIR spectrometer. 16 scans from 600 to 4000 cm^{-1} were taken at a resolution of 4 cm^{-1}, and the spectra were corrected for background absorbance.

Sample preparation at different pHs Samples at various pH levels were prepared by first preparing phosphate-buffered saline (PBS) solutions. The pH of each PBS solution was then adjusted to the desired value using standardized 0.01 M NaOH and 0.01 M HCl solutions. Adjustments were made incrementally while continuously monitoring the pH

to ensure precision. All samples were prepared under consistent conditions to maintain reproducibility across experiments.

4.5.3 CO_2 testing experimental procedure

CO_2 experiments procedure for hydrogels in solution. In 20 mL vial, a previously hydrated freeze-dried P(DMAm$_{100}$-*co*-DEAPyMA$_1$-*co*-EGDMA$_1$) hydrogel with DI H_2O at pH 7, is bubbled with CO_2 at flow rate 100 cm^3/min for 30 min. The sample is taken, and the solid-state fluorescence is measured in an Edinburgh Instruments FS5 Spectrofluorometer. Then, the same hydrogel is put back into solution and the solution is bubbled with pressurized air for 1 h, and the fluorescence is measured the same way, for several cycles.

CO_2 bubbling experiments procedure for nanoparticles. In a 50 mL round-bottom flask (RBF), an aqueous solution containing 0.1 mg/mL of PGMA$_{35}$-*b*-P(HPMA$_{50}$-*co*-DEAPyMA$_{0.1}$) polymer is prepared by dissolving dispersing the nanoparticles in DI water and adjusting the pH to 7 by the addition of NaOH (0.1M). The flask is sealed with a septum, and CO_2 from a 1 kg cylinder (BC) is bubbled into the solution while stirring continuously. This process is conducted at a pressure of 1 bar and a constant flow rate of 50 cm^3/min for a duration typically not exceeding 10 minutes. Samples are taken at different time intervals and their fluorescence is measured in an Edinburgh Instruments FS5 Spectrofluorometer.

Air exposure experiments procedure. A previously CO_2-bubbled (1 hr) 0.1 mg/mL of PGMA$_{35}$-*b*-P(HPMA$_{50}$-*co*-DEAPyMA$_{0.1}$) solution is exposed to air while rigorous stirring for 1 h. Samples are taken at different time intervals and their fluorescence is measured in an Edinburgh Instruments FS5 Spectrofluorometer.

4.5.4 Synthetic procedure for 10 wt % cross-linked P(DMAm$_{100}$-co-DEAPyMA$_1$-co-EGDMA$_1$) hydrogels

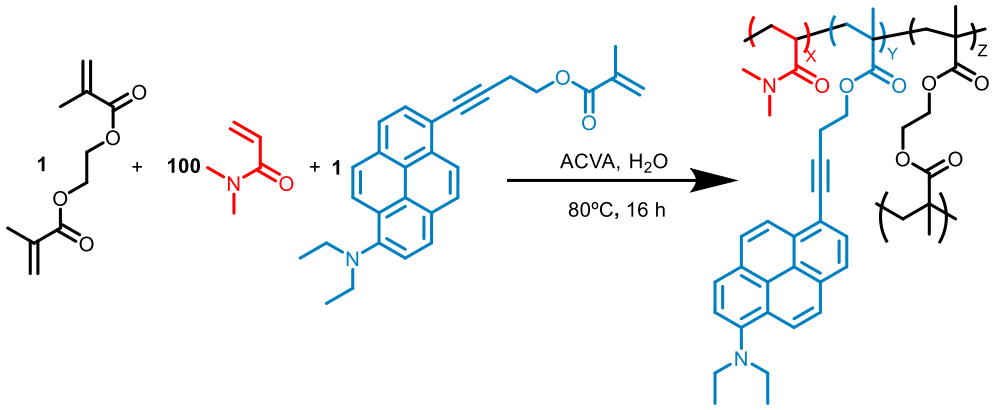

DMAm (0.22g; 0.013 mmol), DEAPyMA (2.0 mg; 0.049 mmol), EGDMA (2 mg; 0.006 mmol) were weighted into a 20 mL vial and dissolved in DI water (1.8 mL). Then ACVA (0.002g, 0.007 mmol) was added into the, and the solution was degassed using N_2 mixture. The mixture was heated at 80 ºC for 16 h. The resulting hydrogel was thoroughly washed with THF and purified via dialysis against pure water. The resulting purified hydrogel was freeze-dried to obtain 0.21g of dry gel.

4.5.5 Synthetic procedure for 5 wt% PGMA$_{35}$-*b*-P(HPMA$_{50}$-*co*-DEAPyMA$_{0.1}$) spherical nanoparticles

4.5.5.1 Synthesis of PGMA$_{35}$ macroCTA

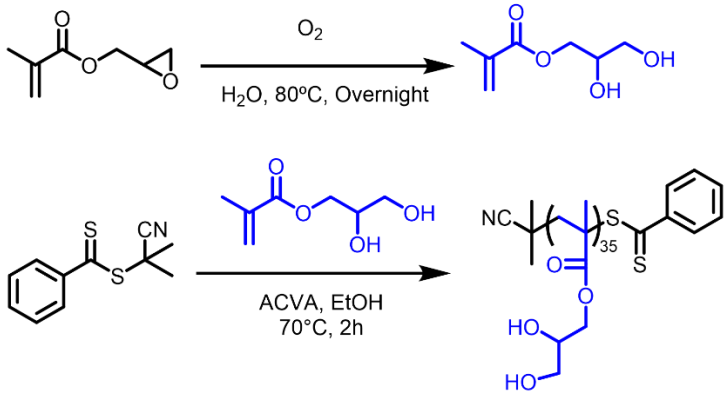

Glycerol methacrylate (GMA). In a 50 mL RBF, 2.64 mL of glycidyl methacrylate (2.84g, 20.0 mmol) were dissolved in DI water (28 mL). The mixture was bubbled with pressurized O_2 overnight at 80ºC. The resulting solution was washed with EtOAc (3 x 75 mL), and the organic phase was dried over $MgSO_4$ anhydrous, and solvent was removed under vacuum. A thick, colorless oil was obtained (2.23g, 70%). ^{1}H NMR (400 MHz, DMSO-d_6) δ 6.06 (dq, J = 1.9, 1.0 Hz, 1H), 5.74 – 5.70 (m, 1H), 4.46 (dd, J = 12.4, 2.7 Hz, 1H), 3.92 (dd, J = 12.4, 6.4 Hz, 1H), 3.26-3.22 (m, 1H), 2.80 f(dd, J = 5.1, 4.2 Hz, 1H), 2.66 (dd, J = 5.1, 2.6 Hz, 1H), 1.90 (dd, J = 1.6, 1.1 Hz, 3H).

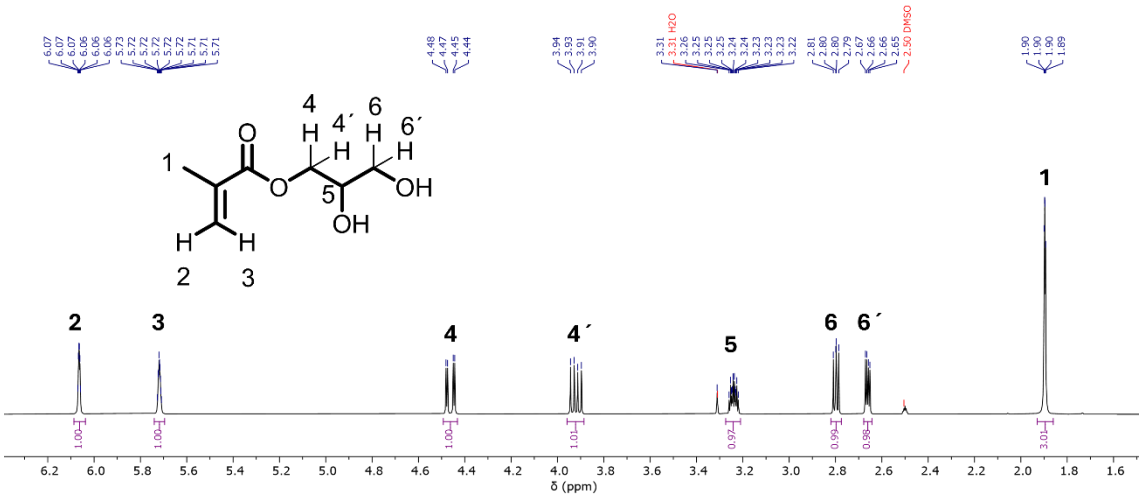

$PGMA_{35}$. CPDB RAFT agent (0.25 mg; 0.11 mmol) and the glycerol methacrylate (GMA) monomer (0.902 g; 5.62 mmol), which had been previously synthesized, were combined in a 7 mL vial. This mixture was then purged with nitrogen for 30 minutes. Following this, ACVA initiator (6.3 mg; 22 µmol), corresponding to a CTA/ACVA molar ratio of 5.0, along with anhydrous ethanol (1.77 mL) (also purged with nitrogen for 30 minutes), was added to the vial. The resulting pink solution underwent an additional nitrogen purge for 10 minutes. The vial was subsequently sealed and placed in an oil bath at a temperature of 70 °C. After a polymerization duration of 120 minutes, the reaction was terminated by immersing the vial in liquid nitrogen and diluting it with 3 mL of methanol. The final conversion of GMA was measured at 75% using ^{1}H NMR spectroscopic analysis. To precipitate the product, the methanolic solution was combined with an excess of diethyl ether (ten times the volume). After filtration and rinsing with diethyl ether, the crude homopolymer was dissolved in water, and residual CH_2Cl_2 was removed under vacuum. The resulting solution was then freeze-dried overnight, yielding a pink powder. Analysis of the purified solid using ^{1}H NMR spectroscopy showed an average polymerization degree of 35 for the PGMA macro-CTA. Its M_n and M_w/M_n were 11,800 g mol^{-1} and 1.27, respectively, as judged by DMF GPC (using a refractive index detector and a series of near-monodisperse poly(methyl methacrylate) calibration standards).

4.5.5.2 Synthesis of $PGMA_{35}$-b-$PHPMA_{50}$

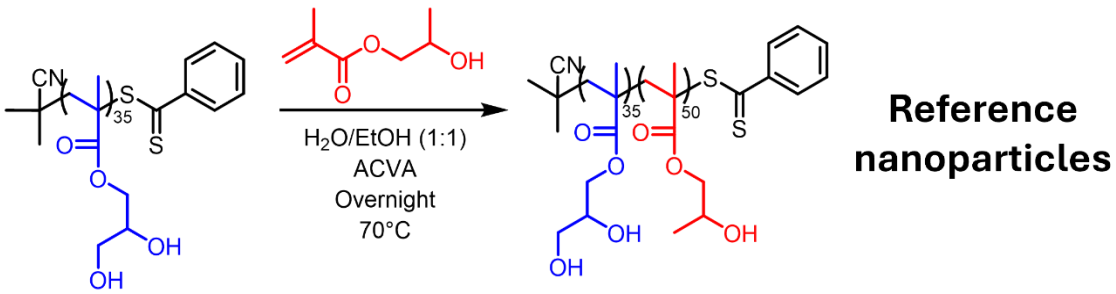

$PGMA_{35}$ macroCTA (20 mg, 3.43 μmol), HPMA monomer (24.74 mg, 0.172 mmol; target DP = 50), ACVA (0.32 mg, 1.1 μmol, CTA/ACVA molar ratio = 3.0) were introduced into a 5 mL Schlenk flask. 0.9 μL of mixture deionized water/ethanol (1:1) were added (producing a 5.0% w/w solution). The resultant mixture was freeze-pump thawed for 3 cycles and immersed in an oil bath set at 70 °C. The reaction solution was stirred for 24 h before the RAFT polymerization was quenched by exposure to air. ^{1}H NMR analysis of the solution indicated a mean degree of polymerization of 50 for this $PGMA_{35}$-b-$PHPMA_{50}$. Its M_n and M_w/M_n were 20,600 g mol^{-1} and 1.17, respectively, as judged by DMF GPC (using a refractive index detector and a series of near-monodisperse poly(methyl methacrylate) calibration standards).

4.5.5.3 Synthesis of $PGMA_{35}$-b-P($HPMA_{50}$-co-$DEAPyMA_{0.1}$)

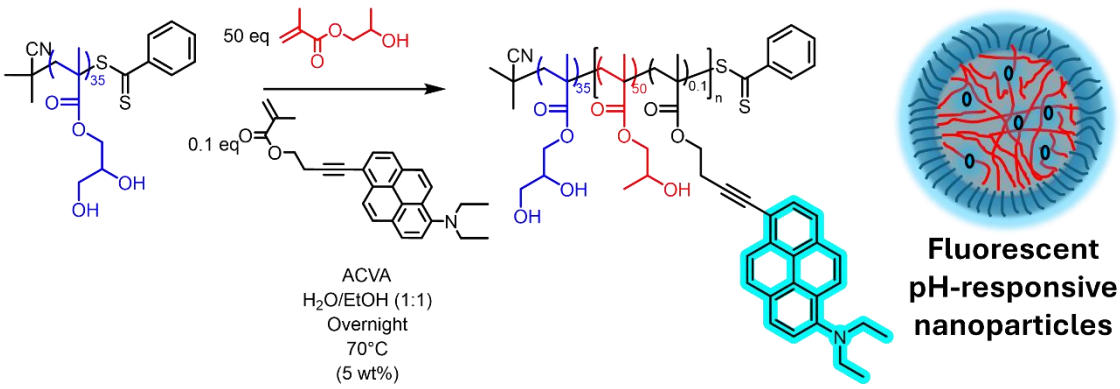

DEAPyMA monomer (0.141 mg; 0.34 μmol), $PGMA_{35}$ macroCTA (20 mg, 3.4 μmol), HPMA monomer (24.74 mg, 0.172 mmol; target DP = 50), ACVA (0.32 mg, 1.13 μmol, CTA/ACVA molar ratio = 3.0) were introduced into a 5 mL Schlenk flask. 0.9 μL of mixture deionized water/ethanol (1:1) were added (producing a 5.0% w/w solution). The resultant mixture was freeze-pump thawed for 3 cycles and immersed in an oil bath set at 70 °C. The reaction solution was stirred for 24 h before the RAFT polymerization was quenched by exposure to air. ^{1}H NMR spectroscopic analysis of the solution indicated a

mean degree of polymerization of 50.1 for this $PGMA_{35}$-b-P($HPMA_{50}$-*co*-$DEAPyMA_{0.1}$). Its M_n and M_w/M_n were 24,900 g mol^{-1} and 1.12, respectively, as judged by DMF GPC (using a refractive index detector and a series of near-monodisperse poly(methyl methacrylate) calibration standards).

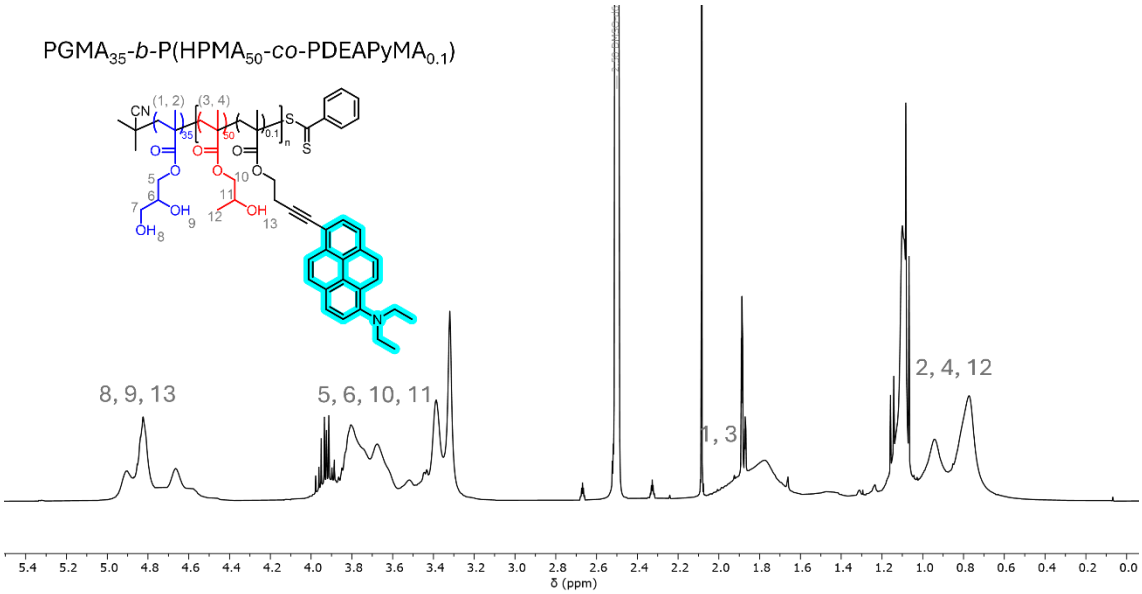

Figure 4.16. ^1H NMR spectra recorded in DMSO-d_6 for the $PGMA_{35}$-b-P($HPMA_{50}$-*co*-$DEAPyMA_{0.1}$) diblock copolymer prepared by RAFT-mediated PISA.

4.6 References

(1) Işıkver, Y.; Saraydın, D. Smart Hydrogels: Preparation, Characterization, and Determination of Transition Points of Crosslinked N-Isopropyl Acrylamide/Acrylamide/Carboxylic Acids Polymers. *Gels* **2021**, *7* (3), 113. DOI: 10.3390/gels7030113.

(2) Kocak, G.; Tuncer, C.; Bütün, V. pH-Responsive polymers. *Polym. Chem.* **2017**, *8* (1), 144-176. DOI: 10.1039/C6PY01872F.

(3) Sun, X.; Agate, S.; Salem, K. S.; Lucia, L.; Pal, L. Hydrogel-Based Sensor Networks: Compositions, Properties, and Applications—A Review. *ACS Appli. Bio. Mater.* **2021**, *4* (1), 140-162. DOI: 10.1021/acsabm.0c01011.

(4) Elsherif, M.; Hassan, M. U.; Yetisen, A. K.; Butt, H. Glucose Sensing with Phenylboronic Acid Functionalized Hydrogel-Based Optical Diffusers. *ACS Nano* **2018**, *12* (3), 2283-2291. DOI: 10.1021/acsnano.7b07082.

(5) Holtz, J. H.; Asher, S. A. Polymerized colloidal crystal hydrogel films as intelligent chemical sensing materials. *Nature* **1997**, *389* (6653), 829-832. DOI: 10.1038/39834.

(6) Nam, J.; Jung, I.-B.; Kim, B.; Lee, S.-M.; Kim, S.-E.; Lee, K.-N.; Shin, D.-S. A colorimetric hydrogel biosensor for rapid detection of nitrite ions. *Sens. Actuators B Chem.* **2018**, *270*, 112-118. DOI: doi.org/10.1016/j.snb.2018.04.171.

(7) Huang, C.; Cheng, Y.; Gao, Z.; Zhang, H.; Wei, J. Portable label-free inverse opal photonic hydrogel particles serve as facile pesticides colorimetric monitoring. *Sens. Actuators B Chem.* **2018**, *273*, 1705-1712. DOI: doi.org/10.1016/j.snb.2018.07.050.

(8) Jia, X.; Zhang, T.; Wang, J.; Wang, K.; Tan, H.; Hu, Y.; Zhang, L.; Zhu, J. Responsive Photonic Hydrogel-Based Colorimetric Sensors for Detection of Aldehydes in Aqueous Solution. *Langmuir* **2018**, *34* (13), 3987-3992. DOI: 10.1021/acs.langmuir.8b00186.

(9) Zhou, M.; Guo, J.; Yang, C. Ratiometric fluorescence sensor for Fe3+ ions detection based on quantum dot-doped hydrogel optical fiber. *Sens. Actuators B Chem.* **2018**, *264*, 52-58. DOI: doi.org/10.1016/j.snb.2018.02.119.

(10) Sun, X.; Agate, S.; Salem, K. S.; Lucia, L.; Pal, L. Hydrogel-Based Sensor Networks : Compositions , Properties , and Applications: A Review. 2021.

(11) Zhang, Y.-X.; Chen, Y.-F.; Shen, X.-Y.; Hu, J.-J.; Jan, J.-S. Reduction- and pH-Sensitive lipoic acid-modified Poly(l-lysine) and polypeptide/silica hybrid hydrogels/nanogels. *Polymer* **2016**, *86*, 32-41. DOI: doi.org/10.1016/j.polymer.2016.01.030.

(12) Zhang, N.; Chen, H.; Fan, Y.; Zhou, L.; Trépout, S.; Guo, J.; Li, M. H. Fluorescent Polymersomes with Aggregation-Induced Emission. In *ACS Nano*, 2018; Vol. 12, pp 4025-4035.

(13) Zhang, Q.; Lei, L.; Zhu, S. Gas-Responsive Polymers. In *ACS Macro Letters*, 2017; Vol. 6, pp 515-522.

(14) Tian, J.; Huang, B.; Xiao, C.; Vana, P. Intelligent CO2- and photo-dual-responsive polymer vesicles with tunable wall thickness. *Polym. Chem.* **2019**, *10* (13), 1610-1618. DOI: 10.1039/c8py01743c.

(15) Rezk, M. Y.; Sharma, J.; Gartia, M. R. Nanomaterial-Based CO_2 Sensors. *Nanomaterials* **2020**, *10* (11), 2251. DOI: 10.3390/nano10112251.

(16) Qiu, L.; Zhang, H.; Wang, B.; Zhan, Y.; Xing, C.; Pan, C.-Y. CO2-Responsive Nano-Objects with Assembly-Related Aggregation-Induced Emission and Tunable Morphologies. *ACS Appl. Mater. Interfaces* **2020**, *12* (1), 1348-1358. DOI: 10.1021/acsami.9b18792.

(17) Wang, H.; Vagin, S. I.; Rieger, B.; Meldrum, A. An Ultrasensitive Fluorescent Paper-Based CO_2 Sensor. *ACS Appl. Mater. Interfaces* **2020**, *12* (18), 20507-20513. DOI: 10.1021/acsami.0c03405.

(18) Chevalier, Y.; Pichot, C.; Graillat, C.; Joanicot, M.; Wong, K.; Maquet, J.; Lindner, P.; Cabane, B. Film formation with latex particles. *Colloid. Polym. Sci.* **1992**, *270* (8), 806-821. DOI: 10.1007/BF00776153.

(19) Kanduč, M.; Kim, W. K.; Roa, R.; Dzubiella, J. How the Shape and Chemistry of Molecular Penetrants Control Responsive Hydrogel Permeability. *ACS Nano* **2021**, *15* (1), 614-624. DOI: 10.1021/acsnano.0c06319.

(20) Warren, N. J.; Mykhaylyk, O. O.; Ryan, A. J.; Williams, M.; Doussineau, T.; Dugourd, P.; Antoine, R.; Portale, G.; Armes, S. P. Testing the Vesicular Morphology to Destruction: Birth and Death of Diblock Copolymer Vesicles Prepared via Polymerization-Induced Self-Assembly. *J. Am. Chem. Soc.* **2015**, *137* (5), 1929-1937. DOI: 10.1021/ja511423m.

(21) Hetzler, Z.; Wang, Y.; Krafft, D.; Jamalzadegan, S.; Overton, L.; Kudenov, M. W.; Ligler, F. S.; Wei, Q. Flexible sensor patch for continuous carbon dioxide monitoring. *Frontiers in Chemistry* **2022**, *Volume 10 - 2022*, Original Research. DOI: 10.3389/fchem.2022.983523.

(22) Wu, T.; Oake, J.; Liu, Z.; Bohne, C.; Branda, N. R. Probing the Microenvironments in a Polymer-Wrapped Core–Shell Nanoassembly Using Pyrene Chromophores. *ACS Omega* **2018**, *3* (7), 7673-7680. DOI: 10.1021/acsomega.8b00953.
(23) Wu, Z.; Ding, Q.; Wang, H.; Ye, J.; Luo, Y.; Yu, J.; Zhan, R.; Zhang, H.; Tao, K.; Liu, C.; et al. A Humidity-Resistant, Sensitive, and Stretchable Hydrogel-Based Oxygen Sensor for Wireless Health and Environmental Monitoring. *Adv. Funct. Mater.* **2024**, *34* (6), 2308280. DOI: https://doi.org/10.1002/adfm.202308280

5 Conclusion and Outlook

The primary goal of this project was to explore the synthesis of fluorescent pH-responsive polymers and examine how CO_2 in an aqueous environment affects these polymers. This involved studying pH changes, size characteristics, and optical properties across various systems, including linear polymers, self-assembled nanoparticles, and hydrogels.

In Chapter 1, fundamental concepts related to synthetic polymers and polymerization techniques were introduced, with a focus on reversible addition-fragmentation chain transfer (RAFT) polymerization, the main method used in this research for copolymer synthesis. The chapter also covered polymerization-induced self-assembly (PISA), as well as the principles of photoluminescence and fluorescence emission. Fluorescent pH-responsive polymers were then presented, highlighting their design, current examples, and potential applications in CO_2 sensing.

Chapter 2 detailed the synthesis of four distinct CO_2-responsive polymeric nanoparticles, all produced via RAFT emulsion polymerization. These systems shared common elements such as a pH-responsive unit (DEAEMA), a crosslinker (EGDMA), and a macro-CTA (PDMAPs), but each contained a different fluorescent dye. When CO_2 was introduced into the aqueous environment, the pH of the nanoparticles decreased due to the interaction between the tertiary amine groups and the in-situ formation of HCO_3^-. Among the fluorescent dyes evaluated, the NBDMA fluorophore emerged as the most effective for CO_2 sensing, demonstrating a fluorescence turn-on and an ultra-fast response time (15 seconds) under CO_2 bubbling, while also reversible to N_2 for at least 6 cycles. In contrast, systems incorporating ACMMA, SPMA, and TPEMA faced issues with stability, interference in fluorescence response, or slower response rates. While the

NBDMA nanoparticles showed promise for real-time CO_2 sensing, further research is needed to enhance their fluorescence turn-off for greater sensitivity.

In Chapter 3, building on the challenges encountered in Chapter 2 with both quantitative and qualitative fluorescence emission, we adopted a combined polymer and molecular-based approach. To achieve this, we synthesized a pH-responsive pyrene monomer (DEAPyMA) capable of switching its fluorescence ON and OFF in response to CO_2 interaction. This dye-based sensor demonstrated noticeable changes in fluorescence, effectively detecting CO_2-induced pH variations at dye concentrations as low as parts per billion. The pyrene-modified unit was then incorporated into PDMAm-based linear polymers, resulting in a system that exhibited a dramatic response to pH changes. Notably, this marked a significant breakthrough, as it was the first instance where the fluorescence of pyrene was completely quenched within a polymeric system in aqueous solution by disrupting excimer bonds in the presence of CO_2. Moreover, the fluorescence quenching effect was fully reversible, with the system recovering upon exposure to atmospheric air for at least five cycles. With its rapid response time, high sensitivity, and reversibility, this polymer system shows great promise for real-time CO_2 detection and could be further developed for integration into smart surface technologies.

In Chapter 4, we introduced the DEAPyMA monomer into two distinct systems, both of which could serve as potential delivery methods. These systems not only exhibited behaviors like the linear polymer analogue discussed in Chapter 3 but also showed unique characteristics depending on the surrounding environment. The P(DMAm-co-DEAPyMA-co-EGDMA) hydrogels, were synthesized via free radical polymerization, using $PDMA_m$ as backbone and EGDMA as crosslinker, that for instance, demonstrated significant changes in both quantitative and qualitative fluorescence when exposed to pH, CO_2, and air in a semi-dry state, likely due to the improved CO_2 permeation. In contrast,

the pyrene moiety within the core of nanoparticles synthesized via RAFT-PISA polymerization, using a $PGMA_{35}$ macroCTA as solvophilic block and chain extending with HPMA as solvophobic monomer. Nanoparticle formation at 70ºC was shown *via* DLS and TEM measurements. This nanoparticle formation responded more slowly to CO_2 and more rapidly to air compared to the linear system, a result of its location within the hydrophobic core, which restricts water and CO_2 permeation. These results highlight the remarkable and versatile performance of the DEAPyMA dye, which, despite slight variations across different systems, consistently proves to be a robust and adaptable candidate for integration into diverse polymer structures and delivery methods for live CO_2 sensing.

This project investigated various polymeric systems for CO_2 sensing, using fluorescence changes as the detection method. A key achievement was the successful synthesis of a pH-responsive pyrene monomer, whose fluorescence properties demonstrated robustness and reproducibility across different polymer architectures. This breakthrough opens the door to a wide array of pH-responsive pyrenes, where modifications to amine groups could tailor the sensors for different pH ranges, expanding their application scope, However, the synthesis of these compounds presents a challenge, particularly due to the complexity of their purification process.

Looking ahead, the focus will be on optimizing the physical and mechanical properties of these systems, particularly hydrogels, to enhance their stability, sensitivity, and responsiveness. Transitioning to more robust hydrogels with improved surface adhesion, higher swelling ratios, and greater long-term stability will be critical for adapting these systems to real-time CO_2 detection. These enhancements are essential for applications ranging from industrial and environmental monitoring to potential medical uses, where rapid and precise CO_2 measurement is vital. By refining these properties, we aim to pave

the way for advanced CO_2 sensing technologies capable of performing effectively under diverse, real-world conditions.